Applications of Reflectometry Towards the Development of MEMS Gas Sensors

by

Kissan Mistry

A thesis
presented to the University of Waterloo
in fulfillment of the
thesis requirement for the degree of
Doctor of Philosophy
in
Mechanical and Mechatronics Engineering

Waterloo, Ontario, Canada, 2021

Examining Committee Membership

The following served on the Examining Committee for this thesis. The decision of the Examining Committee is by majority vote.

External Examiner: Seonghwan Kim
Professor, Dept. of Mechanical and Manufacturing Engineering,
University of Calgary

Supervisor(s): Kevin Musselman
Professor, Dept. of Mechanical and Mechatronics Engineering
University of Waterloo
Mustafa Yavuz
Professor, Dept. of Mechanical and Mechatronics Engineering
University of Waterloo

Internal Member: Patricia Nieva
Professor, Dept. of Mechanical and Mechatronics Engineering
University of Waterloo

Internal Member: Michael Mayer
Professor, Dept. of Mechanical and Mechatronics Engineering
University of Waterloo

Internal-External Member: Eihab Abdel-Rahman
Professor, Dept. of Systems Design Engineering,
University of Waterloo

Author's Declaration

This thesis consists of material all of which I authored or co-authored: see Statement of Contributions included in the thesis. This is a true copy of the thesis, including any required final revisions, as accepted by my examiners.

I understand that my thesis may be made electronically available to the public.

Statement of Contributions

Kissan Mistry was the sole author for Chapters 1, 2, 4, 5 and 8, which were written under the supervision of Dr. Mustafa Yavuz and Dr. Kevin Musselman and were not written for publication. The thesis consists in part of two manuscripts written for publication. Exceptions to sole authorship of material are as follows:

Chapter 3

Kissan Mistry, Alexander Jones, Manfred Kao, Travis Yeow, Mustafa Yavuz, Kevin Musselman. In-Situ Observation of Nucleation and Property Evolution in Films Grown with an Atmospheric Pressure Spatial Atomic Layer Deposition System. Nano Express 2020, 1 (1), 010045.

I formulated the algorithms, implemented the in-situ reflectance technique and authored the manuscript. Alexander Jones and Manfred Kao assisted in integrating the in-situ reflectance measurement with the AP-SALD system. Travis Yeow assisted in film depositions. Dr. Mustafa Yavuz and Dr. Kevin Musselman provided editorial support and supervision.

Chapter 6

Kissan Mistry, Viet Nguyen, Khaled Ibrahim, Mohamed Arabi, Mustafa Yavuz, David Munoz-Rojas, Eihab Abdel-Rahman, Kevin Musselman. A Zinc Oxide Resonant Cantilever Gas Sensor. (Unpublished)

I designed, fabricated and tested the device. Dr. Viet Nguyen assisted in depositing the zinc oxide layer. Dr. Khaled Ibrahim assisted in obtaining the scanning electron micrographs of the devices. Mohamed Arabi assisted in testing the device. Dr. David Munoz-Rojas supervised the zinc oxide film depositions and provided guidance. Dr. Eihab Abdel-Rahman advised on the testing. Dr. Mustafa Yavuz and Dr. Kevin Musselman supervised the design, fabrication and testing of the device.

Chapter 7

Kissan Mistry, Khaled Ibrahim, Inna Novodchuk, Hyunh Thien Ngo, Gaku Imamura, Joseph Sanderson, Mustafa Yavuz, Genki Yoshikawa, Kevin Musselman. Nanomechanical Gas Sensing with Laser Treated 2D Nanomaterials Adv. Mater. Technol. 2020, 5 (12), 2000704.

I conceptualized the project, performed the device coating, tested the devices and authored the manuscript. Dr. Khaled Ibrahim and Inna Novodchuk performed the laser treatment of the two dimensional materials. Dr. Hyunh Thien Ngo assisted in the coating of the devices. Dr. Gaku Imamura and Dr. Genki Yoshikwa provided guidance and supervision of the coating process. Dr. Joseph Sanderson supervised the laser treatment process. Dr. Mustafa Yavuz and Dr. Kevin Mussleman provided editorial support and supervision.

Abstract

Reflectometry or reflectance spectroscopy is a relatively simple characterization technique based on the analysis of reflected light from a surface. Herein, reflectometry is used to attain significant insights towards the development of micro-electro-mechanical systems (MEMS) based gas sensors. Two main reflectometry applications are demonstrated which led to formation of unique MEMS gas sensor devices.

The first application, was the use of in-situ reflectance spectroscopy to characterize the growth behavior of metal oxide films grown by atmospheric pressure-spatial atomic layer deposition. The technique revealed an initial film nucleation period, where the length of the nucleation time was sensitive to the deposition process parameters. The in-situ reflectometry technique was then used to study and monitor the growth behavior of metal oxide films on various non-conventional surfaces. Doing so allowed for the accurate deposition of zinc oxide films on a variety of surfaces with desired thickness. This was instrumental, as it enabled the integration of the zinc oxide films into a novel MEMS resonant cantilever architecture for gas sensing. In this device, the zinc oxide layer serves as both the cantilever structural layer as well as the gas sensitive receptor layer. A key advantage of the approach was the reduction in overall mass of the cantilever which can lead to an enhancement in sensitivity to low quantities of analyte gases. The sensor had an outstanding sensitivity to low levels of relatively humidity(RH) when compared to other frequency shift based humidity sensors. The zinc oxide cantilever demonstrated a sensitivity of 23649 $\frac{ppm}{\%RH}$ at 5.9% RH and an average sensitivity of 1556 $\frac{ppm}{\%RH}$ in the range of 30-60% RH.

The second application of reflectometry was its use as a screening technique to find suitable gas sensitive receptor materials for static deflection type MEMS gas sensors. The reflectance intensity of various materials exposed to gases, was monitored, where changes in the intensity indicated that the material was physically changing in the presence of the gas. This expansion behavior is ideal for static deflection type MEMS gas sensors such as the nanomechanical membrane type surface stress sensor (MSS) architecture. The reflectance screening technique identified that laser treated two dimension materials such as graphene oxide, molybdenum disulfide and tungsten disulfide were suitable candidates to be integrated as the receptor layer in the MSS platform. The sensing response of the coated devices was obtained for a select group of volatile organic compounds. The results showed that the laser treatment technique was advantageous to enhancing the sensor response and sensitivity, as it introduces defects, dopants and functional groups to the receptor materials for improved gas adsorption.

Acknowledgements

First and foremorst I would like to express my deepest gratitude to my supervisors: Dr. Mustafa Yavuz and Dr. Kevin Musselman. To Dr. Yauvz, thank you for allowing me to join your research group as an undergraduate student, 5 years ago. You put me on this path and supported me along the way with your optimism and invaluable advise. To Dr. Musselman, thank you for your confidence in me to allow me to pursue my research interests and goals. You instilled in me the skills to be an effective scientific researcher and communicator. If I am successful tomorrow, it will be because of your supervision and mentorship. It was an absolute pleasure to work with you and be apart of your research group.

I am grateful for the two international collaborations I was fortunate to be apart of. Thank you to Dr. David Munoz-Rojas and Dr. Genki Yoshikawa, for allowing me to come visit your labs in Grenoble, France and Tsukuba, Japan. Thank you to Dr. Viet Huong Nguyen and Dr. Thien Ngo for making me feel welcomed in a new city, and for being great friends. These two international collaborations were the best part of my doctoral degree and I will always cherish these memories.

I was fortunate to fund my research work through grants and scholarships. Thank you to Mitacs Canada, Campus France and the Japan Society for the Promotion of Science (JSPS) for funding my research trips to France and Japan. Thank you to CMC Microsystems, for fabrication costs assistance. I am appreciative of the Waterloo Institute for Nanotechnology (WIN) Nanofellowship award, the Ontario Graduate Scholarship (OGS) and the Natural Sciences and Engineering Research Counci of Canada (NSERC) postgraduate doctoral scholarship. These scholarships lightened my financial burden, and allowed me to focus on the research.

This research would not have been productive or enjoyable, were it not for my group colleagues and friends. I am thankful to Abdullah Alshehri, Inna Novodchuk, Manfred Kao, Travis Yeow, Alex Jones, Hatameh Asgarimoghaddam, Jhi Yong Loke, and Apratim Chakraborty. It was a pleasure working with you all. I am grateful for my friendship with Khaled Ibrahim, which extends beyond research. To Kavish Kaup, I'm glad we took this 10 year journey together since undergrad. Thanks for your support and your friendship, I am extremely proud at what we have accomplished. To Uma Lad, you came into my life at exactly the right time and gave me the support and motivation to complete this doctoral degree. I know we will achieve our goals.

Table of Contents

List of Tables

List of Figures

List of Abbreviations

AFM atomic force microscopy 18, 69

ALD Atomic Layer Deposition xv, 17, 42–46, 58, 59, 63–65, 69, 70, 73, 74, 77, 78, 82, 85, 89–91, 96, 151

AP-CVD atmospheric pressure-chemical vapor deposition 65, 66, 73, 74, 76, 77, 80

AP-SALD Atmospheric Pressure-Spatial Atomic Layer Deposition x, xv, xvi, 2, 42–48, 58–60, 63–66, 68, 71, 73, 76, 80–85, 91, 93, 98, 100, 105, 106, 117, 140, 151

APTES 3-aminopropyl triethoxysilane xiv, 34–36

BET Brunauer-Emmet-Teller xxi, 151, 152

CHT combinatorial high throughput 103

CMC carboxymethylcellulose 28

CMUT capacitive micromachined ultrasonic transducer 148, 149

CPD critical point drying 130, 131

CVD chemical vapor deposition 15, 16, 43, 46, 58, 65

DEA diethylamine 31, 116

DEZ diethyl zinc 47, 66, 76, 84, 123

DFT density functional theory 103, 168, 171

DMAI dimethyaluminum isopropoxide 47

FBAR film bulk acoustic wave resonator 148, 149

GAB Guggenheim-Anderson-de Boar xxi, 150–152, 154

GO graphene oxide xviii, 24, 25, 50, 104, 108, 109, 114

GOF goodness of fit xvi, xvii, 59, 68–71, 77–79

GPC growth rate per cycle x, xvii, xviii, 69, 73, 85–95, 97, 98, 100, 101

LED light emitting diode 48, 63

LOD limit of detection 11, 23, 28, 163, 164

LPG liquefied petroleum gas 30

MBE molecular beam epitaxy 58

MEMS Micro-electro-mechanical systems xii, 1, 6, 9, 13–15, 17, 31, 51, 63, 82, 91, 100, 102–104, 106, 108, 110–114, 124, 130, 138

MFC mass flow controller 105, 106

MIM metal insulator metal 48, 63

MOCVD metal organic chemical vapor deposition 58

MSS nanomechanical Membrane type Surface stress Sensor xiii, xxi, 21–24, 157, 160–162, 175

MWCNT multi-wall carbon nanotubes xiii, 28, 29, 117, 148, 154

ORR oxygen reduction reaction 169

PAAM poly acryl amide 20

PCA Principal Component Analysis 20, 177

PDMS polydimethylsiloxane 27

PEI polyethyleneimine xiii, 20–22, 157

PEO polyethylene oxide 27

PEUT polyetherurethane 27

PEVA polyethylene-vinyl-acetate 27

PMMA poly methyl methacrylate xviii, 28, 83, 90–92, 104–108, 114

PMUT piezoresistive micromachined ultrasonic transducer 148, 149

ppm parts per million xiii, xvi, 9, 24, 27, 31, 35, 36, 60, 61, 148, 160, 162–165

ppt parts per trillion 19

PS polystyrene 28

PSS poly sodium 4-styrenesulfonate xiii, 21, 22, 157

PU polyurethane 28

PVA poly vinyl alcohol 20, 27, 28

PVC poly-vinyl-chloride 28

PVD physical vapor deposition 15, 16

PVP poly vinyl pyrrolidone 20, 28

QCM quartz crystal microbalance xv, 31, 38–41, 64, 69, 116, 148, 149

RH relative humidity xiii, xiv, xx, xxi, 24–27, 32–34, 39, 116, 117, 137, 141, 144–149, 151, 152

RIE reactive ion etching xix, 118, 123–125, 153

SAW surface acoustic wave 148, 149

SEM scanning electron microscope xii–xv, xviii–xx, 19, 22–25, 30–32, 34, 38, 40, 69, 85, 94, 95, 98, 99, 124, 126–128, 130–133, 135, 142

SPM scanning probe microscopy 18

SQFD squeeze film damping 139, 140, 153

TEM transmission electron microscope xiii, 24, 28, 29

TMA tri-methyl-aluminum 47, 48, 59, 65, 129

VI virtual interface xvii, xviii, 82, 85–87, 89, 90, 92–94, 97, 99

VOC volatile organic compound xxi, xxii, 1, 104, 116, 117, 156–158, 166, 170, 172, 176, 177

XPS x-ray photoelectron spectroscopy xxi, xxii, 159, 166–171, 173

XRD x-ray diffraction xxi, 127, 128, 159, 165, 167, 168

List of Symbols

E Young's/Elastic Modulus 8, 9, 139

Re Reynold's number 140

α Absorption coefficient 68

ρ Density 9, 139

Δd Cantilever or membrane displacement 8

ε Dielectric constant 14

$k(\lambda)$ Extinction coefficient 67, 68

Δf Frequency shift 141

f_n Natural resonance frequency 137

k Spring constant or "stiffness" 10

λ Wavelength 67

ω_n Angular natural resonance frequency 9

ν Poisson's Ratio 8

Q Quality factor 11, 138

$n(\lambda)$ Refractive index 67, 68

R^2 Coefficient of determination 68, 146

σ_{std} Standard deviation 146, 163

σ Stress 8, 9, 56, 174

η Viscosity coefficient of fluid 139

"The more that you read, the more things you will know. The more that you learn, the more places you'll go"

— Dr. Seuss

Chapter 1

Introduction

1.1 Motivation

Micro-electro-mechanical systems (MEMS), is a technology based on miniaturized mechanical and electrical components to form micro-actuators and micro-sensors. The sizes of these devices typically range from several hundreds of micrometers (µm) down to less than 1 µm, which is advantageous for their ubiquitous integration into all sorts of consumer and industrial applications. MEMS based gas sensors is one area of current interest, with an expected increase in the global market share from 151.9 billion in 2019 to 233.9 billion (USD) by 2026 [1].

Applications of chemical gas sensors include, but are not limited to, the detection of toxic gases, environmental pollutants and compounds in the breath, to name a few. For example the development of sensors for the detection of nitrogen dioxide is in demand as it is a known air pollutant emitted from vehicle exhausts and causes significant respiratory problems [2]. The sensing of the volatile organic compound (VOC), acetone, in exhaled breath is also of interest, as it can be used as a diagnostic indicator for Type 1 diabetes and monitoring of blood glucose levels [3]. In general, research into the development of gas sensor technologies aims to realize the goal of lower detection limits, quicker sensing times, and improved reliability, all within a package that continues to get smaller.

For MEMS gas sensors, two of the main areas of improvements are the development of new sensor materials (receptor) and the development of novel MEMS architectures for improved sensing performance. Receptor materials should be able to interact with a target chemical gas in a quantifiable way. This requires an understanding of their synthesis, material properties and applicability in MEMS sensors. The development of novel MEMS architectures requires an understanding of MEMS microfabrication techniques, compatibility with the receptor materials and integration with other peripherals. Materials characterization techniques are crucial to the research and development of sensor materials and novel MEMS architectures.

Reflectometry or reflectance spectroscopy is one such characterization tool that is based on the analysis of reflected light from a surface. While the technique itself is simple, it can provide significant and useful insights towards the development of new materials and architectures for MEMS gas sensors.

1.2 Thesis Overview

The objective of this research is to demonstrate the applications of reflectometry which are useful towards the development of MEMS gas sensors. The first application, is the use of reflectance to understand the growth behavior and properties of metal oxide thin films deposited by Atmospheric Pressure-Spatial Atomic Layer Deposition (AP-SALD). Reflectometry is used to observe the growth behavior of the films on various surfaces, which becomes useful when integrating said film into a MEMS structure. An understanding of the growth behavior of zinc oxide onto polymer films was beneficial towards the design and fabrication of a novel zinc oxide resonant microcantilever gas sensor.

A second application of reflectometry, was to evaluate the suitability of various materials for use as a responsive receptor layer in static type MEMS gas sensors. This technique allows for the screening of potential receptor material candidates before their integration into the MEMS structure. Laser treated two dimensional materials such as graphene oxide, molybdenum disulfide and tungsten disulfide were identified as excellent candidates for the receptor layer. These materials were integrated into a nanomechanical membrane-type surface stress sensor architecture for the detection of several volatile organic compounds.

1.3 Chapter Synopses

A synopsis of each chapter in this work is as follows:

Chapter 2 **Literature review**: An overview of MEMS gas sensors is introduced including sensing principles, actuation methods, signal readout and fabrication techniques. A review of the relevant literature in both static and resonant MEMS gas sensors is presented with a focus on nanomechanical membrane-type surface stress sensors and zinc oxide based resonant sensors. The working principle of the two primary nanomaterial synthesis techniques used in this research work are described (AP-SALD and femtosecond laser treatment). This is followed by an overview of reflectance spectroscopy, its principle of operation, models and review of relevant applications.

Chapter 3 **In-situ reflectance spectroscopy of thin films grown by atmospheric pressure spatial atomic layer deposition (AP-SALD)**: In this chapter, the implementation of in-situ reflectance spectroscopy with an AP-SALD system is described. The properties of zinc oxide and aluminum oxide films, such as thickness, refractive index and bandgap, were measured during the film deposition. The technique revealed a substrate nucleation period, where the length of the nucleation time was sensitive to the deposition parameters. Thus, in-situ reflectance spectroscopy was used to enable the accurate deposition of metal oxide films with desired thicknesses.

Chapter 4 **Observation of thin film nucleation and growth on various surfaces**: A modified version of the in-situ reflectance spectroscopy technique presented in the previous chapter was used to observe the growth behavior of ZnO onto a variety of different surfaces. This includes conventional surfaces like glass and silicon and non-conventional surfaces like metals, polymers, paper, various textiles and films of 2D nanoparticles. The main benefit here is that the optical properties of the underlying surface are not required by the reflectance model (unlike the previous chapter). The accurate deposition of ZnO films onto any surface is achieved as the nucleation periods can be accounted for. This is particularly relevant for the integration of ZnO thin films into the resonant microcantilever gas sensor architecture discussed in Chapter 6.

Chapter 5 **Reflectance screening technique for responsive gas sensor materials**: Reflectometry is used to monitor various materials as they are exposed to select vapors of volatile compounds (analytes). A change in the reflectance signal is observed as the materials are exposed to the vapors, indicating some form of interaction with the analyte. This interaction is likely an expansion or swelling of the tested material. Hence, these materials are good candidates for use as a receptor layer in static MEMS gas sensors such as the nanomechanical membrane-type surface stress sensor discussed in Chapter 7.

Chapter 6 **A zinc oxide resonant cantilever gas sensor**: The design, fabrication and testing of a ZnO thin film resonant microcantilever gas sensor is presented. The premise of this work is to produce a microcantilever structure where the structural cantilever layer, made from ZnO, also serves as the gas sensing (receptor) layer. This reducing the number of layers on the structure to improve its quality factor and its gas sensing performance.

Chapter 7 **Nanomechanical gas sensing with laser treated 2D nanomaterials**: Laser treated 2D nanomaterials were identified in Chapter 5 as excellent candidates for receptor layers in static MEMS gas sensors. Here, their integration into the nanomechanical surface-stress sensor (MSS) architecture is described. The laser treatment of 2D nanomaterials was used to introduce defects, dopants and functional groups to the materials for improved gas adsorption properties. The sensing capabilities of the 2D nanomaterial coated MSS devices were evaluated with a select group of volatile organic compounds.

Chapter 8 **Conclusions**: Summarizes the research conclusions of each chapter and proposes future work.

"If I have seen further, it is by standing on the shoulders of giants"

— Isaac Newton

Chapter 2

Literature Review

2.1 MEMS Gas Sensors

Chemical gas sensor devices are typically comprised of three main components. The first being a receptor or gas sensitive material that has a physical or chemical response to an analyte in the gas phase. The second component is a method of transduction, whereby the response of the receptor to an analyte is converted to a detectable output signal. The last component is a method to retrieve the output signal for the user [4].

The transistor based resistive gas sensor (also known as a chemiresistive or conductormetric sensor) is a typical sensor architecture that is commonly used in many commercially available gas sensors. A receptor material is placed between two electrical contacts which measure changes in electrical resistance (or conductance) of the receptor upon interaction with the chemical gas. These sensors rely on the chemical, electrical and physical properties of the receptor material to promote interactions with the target gas (adsorption/absorption, i.e., sorption) and in turn generate a significant resistance change to indicate successful detection [5]. An alternative sensor configuration is the micro-electro-mechanical system (MEMS) based gas sensor. In this sensor architecture, micro-scale or nano-scale free standing structures such as microbeams (cantilevers) and microplates are typically coated with a thin layer of the receptor material which can change the physical behavior of the structure in the presence of analyte gas [4].

2.1.1 Background

Sensing Principles

MEMS or microcantilever gas sensors have two main modes of operation: static or dynamic mode as illustrated in Figure 2.1. Static mode sensing occurs when there is a physical displacement of the cantilever structure in the presence of the analyte gas. The surface of the cantilever is typically functionalized with the receptor material which serves as sorption sites for the gas molecules. The sorption of the analyte with the receptor can either induce a surface or bulk stress on the cantilever which results in its static displacement. Dynamic mode sensing occurs by allowing the cantilever to resonate at its natural resonance frequency by typical MEMS based actuation methods. The adsorption of the target analyte on the receptor coated cantilever will result in a shift in its resonance frequency due to the increase in overall mass. Typically, resonant sensors are able to make indirect mass change estimations in the atto to zepto gram range [4].

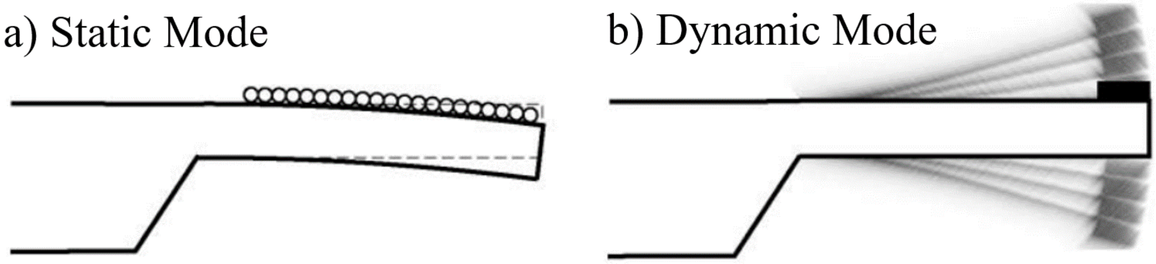

Figure 2.1: MEMS chemical gas sensor modes of operation. Adapted from ref. [6] with permission. Copyright 2001, Elsevier Science B.V.

Sensor performance is defined by its sensitivity, selectivity, responsivity, recovery time, and long-term stability (reusability). Sensor sensitivity is a quantity the describes the amount of output response (displacement or frequency shift) to an input (gas adsorption). It is desirable to have high a sensitivity which refers to large output response as a result of a small input. The sensitivity also determines the minimum detectable limits of the sensor. It identifies the minimum amount of input required to generate a significant detectable output response. One of the main goals of sensor research and development is to improve sensitivity and push minimum detectable limits of target analytes to low concentrations (parts per million/billion/trillion . . . etc.).

Selectivity or specificity pertains to the capability of the sensor to differentiate between the target analyte and other chemical compounds that may be present. Selectivity is largely dependent on the materials that comprise the receptor layer, whether it be a thin film or ligand type structure that has a high affinity to a specific analyte. Sensor responsivity characterizes the time it takes for the sensor to generate a detectable output response to the input, where fast response times are desired. The recovery time is the time it takes for the sensor to return to normal conditions after detection or attachment of a target analyte. Similar to the selectivity, response or recovery time is largely dependent on the material chosen as the sensing layer and its properties. Lastly, long term performance of the sensor is desired and therefore it is important to have high stability in that the structure does not erode or react negatively while in contact with the analytes.

Static MEMS Sensors

Gaseous analytes adsorbing onto the surface of a functionalized cantilever adds both an additional mass to the cantilever and may generate internal or surface stresses due to the interactions between the molecules and receptor layer. However, the detection of a change in mass in static mode is not practical, especially for lower limits, down to single molecules. This is largely due to the fact at the nano and micro scale, the effects of gravity and the weight of a molecule compared to a larger cantilever structure, are negligible [4]. To cause deflection of the cantilever due to an additional mass would require many molecules. Simply, the sensitivity of static mode mass sensors is poor.

Stress induced cantilever deflections is the more common static mode method. Consider a cantilever coated with a receptor layer on top. The sorption of a gas molecule onto the surface of or into the receptor layer can result in stress induced deflections of the cantilever structure. The surface stress that occurs is governed by interaction between the gas molecules and receptor layer and can result in an expansion or contraction of the layer. This imparts a compressive or tensile stress on the structural layer (cantilever) causing its deflection, as shown in Figure 2.2.

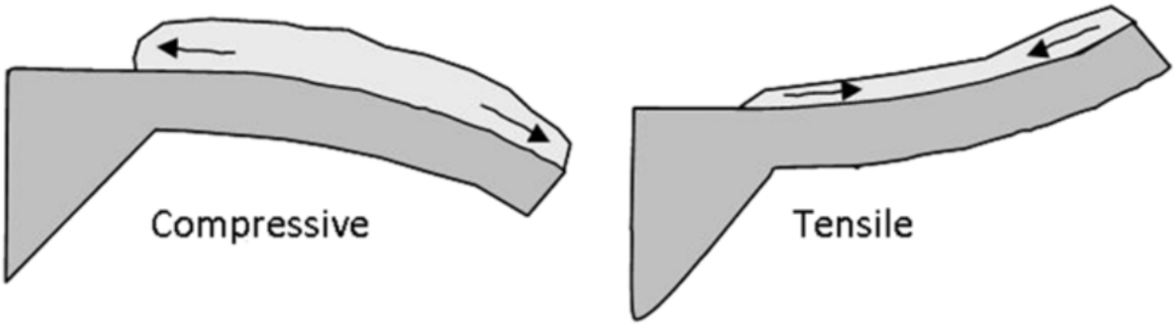

Figure 2.2: Expansion or contraction of receptor layer atop cantilever as a result of gas adsorption, imparts a compressive or tensile force on the structural layer. Adapted from ref. [4] with permission. Copyright 2011, IOP Publishing Ltd.

Generally, for a receptor layer that expands, the cantilever bends downwards until the compressive stress in the cantilever balances the tensile stress in the thin film. Similarly, for a contracting receptor layer, the cantilever bends upwards to create a tensile stress to balance out the compressive stress in the thin film. The tip deflection (Δd) of the cantilever is given by the Stoney equation modified for cantilevers (Equation 2.1) [7].

$$\Delta d = \frac{3\,(1-\nu)\,L^2}{Eh^2}\sigma, \tag{2.1}$$

Where L is the length of the cantilever, E is Young's modulus, ν is the Poisson ratio of the material, h is the thickness and σ is the imparted surface stress from gas sorption. Here it is seen that larger deflections can be obtained by maximizing the stress generated from gas adsorption, a property that will depend on the choice of receptor and structural layer materials. The sensitivity for this sensor is the ratio between the displacement and the surface stress. However, for practical gas sensing applications it is more useful to define sensitivity as the ratio between the displacement and the concentration of the gas (typically in parts per million (ppm))(Equation 2.2). Additionally, the displacement term is often replaced by an optical and electrical quantity that is equivalent to the amount of measured displacement (dependant on the choice of sensor read out method).

$$S = \frac{\Delta d}{ppm} \tag{2.2}$$

Dynamic MEMS Sensors

Dynamic MEMS gas sensors based on frequency shift are alternatively known as gravimetric, inertial or resonant sensors. The free standing structure (e.g.: microcantilever) is first actuated to its natural resonance frequency. An eigenfrequency analysis of the structure determines the resonance modes (frequencies) and mode shapes of the beam. The motion of thin beams, where rotational inertia and shear deformation have been neglected, is governed by the Euler-Bernoulli beam partial differential equation (Equation 2.3) [8].

$$\frac{\partial^2 U\left(x,t\right)}{\partial t^2}\rho\Gamma + \frac{\partial^4 U\left(x,t\right)}{\partial x^4}EI - N\frac{\partial^2 U\left(x,t\right)}{\partial x^2} = 0 \tag{2.3}$$

Where $U\left(x,t\right)$ is the displacement as a function of position on the beam (x) and time (t), ρ is the density of the material, Γ is the cross-sectional area of the cantilever, E is the Young's modulus, I is the geometric moment of inertia and N is the tensile force as a result of the residual stress (σ) in the beam $(N = \sigma\Gamma)$. The solution to the differential equation is separated into position and time dependant components (Equation 2.4).

$$U\left(x,t\right) = U_n\left(x\right)\exp\left(-i\omega_n t\right), \tag{2.4}$$

Where $U_n\left(x\right)$ are the n mode shapes of the cantilever and, ω_n are the n resonance frequencies of the beam. The first four mode shapes of a cantilever are shown in Figure 2.3. The frequency of vibration for each of the mode shapes is primarily dependent on the beam geometry and material properties. It is common to simplify the frequency to that of a spring-mass oscillator (Equation 2.5):

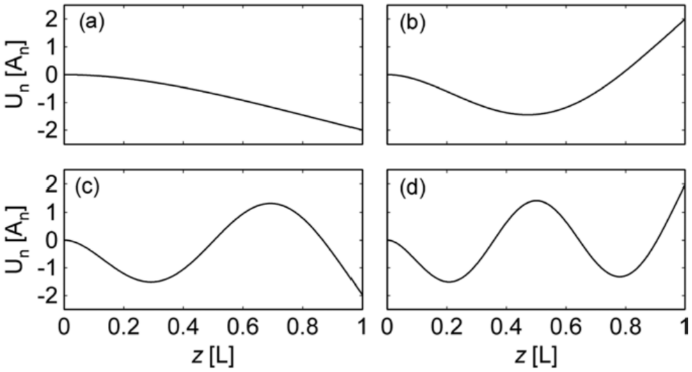

Figure 2.3: The first four modeshapes or resonance modes of a cantilever beam. a) n=1, b) n=2, c) n=3, d) n=4. Adapted from ref. [4] with permission. Copyright 2011, IOP Publishing Ltd.

$$\omega_n = \frac{\lambda_n^2}{L^2}\sqrt{\frac{EI}{\rho\Gamma}} \rightarrow \qquad \omega = \sqrt{\frac{k}{m}} \tag{2.5}$$

Where λ_n is the eigenvalue referring to a specific modeshape shown in Figure 2.3, k is the effective spring constant or stiffness of the beam and m is the effective mass. A change in mass due to the adsorption of gas molecules onto the cantilever will in turn change the resonance frequency. The sensitivity of the dynamic mass sensor can be found by differentiating with respect to the mass (Equation 2.6).

$$S = \frac{\partial\omega}{\partial m} \approx \frac{\Delta\omega}{\Delta m}. \tag{2.6}$$

To obtain high sensitivity, a beam must have a high resonant frequency. This is obtained by having a large Young's modulus, low density, small dimensions, and low mass. Higher sensitivity can also be obtained at higher resonance modes (higher frequencies). Bridge type structures (fixed-fixed beams) have higher resonance frequencies than cantilevers (fixed-free beams) of the same dimensions, however the vibrational amplitude of the mode shapes is smaller and therefore may be more difficult to readout. The minimum detectable limit is the minimum mass change required to ensure a detectable frequency change, and is given by the inverse of the sensitivity times the detectable frequency change (Equation 2.7):

$$\Delta m_{min} = S^{-1}\Delta\omega_{min}. \tag{2.7}$$

Resonating beams are subjected to damping effects resulting in a dissipation (loss) of their kinetic energy. Damping causes a broadening of the resonance peak and introduces additional frequency noise to the measurement [4]. As a result, it becomes difficult to detect smaller frequency shifts and subsequently increases the limit of detection (LOD) the sensor. Sources of energy loss include material damping, structural damping and damping due to the surrounding medium. Material damping is dependent on the stiffness or elastic modulus of the layers and residual stresses existing in the material. It is particularly dominant for multi-layer or coated cantilever beams. Structural damping arises from the geometry and dimensions of the beam. The second moment of area, dependent on the beam thickness and width, provides insight into the beams resistance to bending. The nature of the fixed/clamped end of the beam may also add damping effects known as anchor losses. The motion of the beam may be affected by viscous damping or momentum exchange with the surrounding medium. This is the dominant source of damping for sensors in atmospheric or higher-pressure conditions as well as sensors in liquid environments. Furthermore, the sensor read out method may introduce additional noise to the transduction signal. Quantitatively, the total dissipation in the system is represented by the quality factor (Q) which is inversely proportional to dissipation. Each individual source of dissipation in the system can be assigned a corresponding Q_j factor. The total quality factor for the system can be expressed in terms of the individual quality factors, similar to the equivalent resistance of parallel resistors (Equation 2.8).

$$\frac{1}{Q_{total}} = \frac{1}{Q_1} + \frac{1}{Q_2} + \ldots \sum_j \frac{1}{Q_j} \tag{2.8}$$

Q is approximately equivalent to the number of cycles the structure will oscillate in response to an external stimulus before it settles to equilibrium. It is desirable to achieve high quality factors indicative of low dissipation or damping effect.

Actuation methods

An important design criterion for dynamic mode sensing is the actuation method to vibrate the cantilever at its natural resonance frequency. The choice of actuation method can influence the type of sensor readout method required and vice versa. Figure 2.4 illustrates common cantilever actuation methods and their corresponding readout methods (discussed in next section). The use of piezoelectric materials is a common actuation method, where an applied voltage on the material induces a strain on the material [9]. An applied AC voltage would generate vibrations in the piezoelectric. At the macro scale, the chip with the fabricated cantilevers can be placed on the piezoelectric material to vibrate the whole chip at a given frequency. Alternatively, the piezoelectric material can be integrated as a layer on the cantilever.

Electrostatic actuation can be used to oscillate the cantilever to its resonant frequency [9]. It requires the cantilever to have conductive layer to act as a free electrode, while a second fixed electrode exists on the substrate underneath the cantilever. A voltage difference between the two electrodes will cause the cantilever to move toward the bottom electrode as the system tries to minimize the energy of the formed capacitor system. An AC voltage in turn creates a periodic force on the cantilever causing it to dynamically resonate. Electrostatic actuators can be combined with a capacitive readout method (described in next section) to determine the cantilever displacement or frequency shifts.

Thermal actuation takes advantage of the difference in thermal expansion of the two materials that make up a bimorph cantilever [9]. A heat source, either an external laser or a resistive heater, is used to heat up the cantilever and cause a deflection due to the bulk stress change. To oscillate the cantilever, fast heating and cooling is required at the rate of the desired frequency which may limit the achievable oscillation frequencies.

Lastly, magnetomotive actuation may be used to resonant the cantilever [10]. This principle requires a magnet to generate a magnetic field that is perpendicular to an alternative current that is run through the cantilever. The resulting Lorentz force will cause the cantilever to deflect. This method is less popular as it requires large magnetic fields and operation at low temperatures.

Sensor Readout

The last major component of a MEMS based sensor is a method to measure the displacement of the cantilever structure. This is a form of transduction where mechanical behavior is transformed to an electrical signal that can be registered. In optical read out, a laser source is focused on the top surface of a cantilever as depicted in Figure 2.4c. The cantilever may require an additional reflective coating such as thin metal layer. As the cantilever displaces, the reflected laser intensity is detected by a photodetector and is then used as an accurate estimate for cantilever displacement. The optical readout method is highly advantageous as the technique is capable of achieving 1 nm deflection resolution [4]. However, the setup does not allow for the simultaneous read-out from a reference non-functionalized cantilever. In dynamic mode the frequency of the oscillating laser intensity is correlated to the frequency of resonating cantilever.

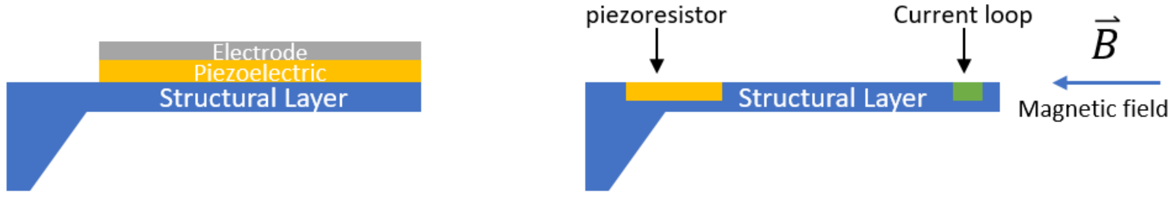

a) Piezoelectric actuation/ readout

b) Electromagnetic actuation/ piezoresistive readout

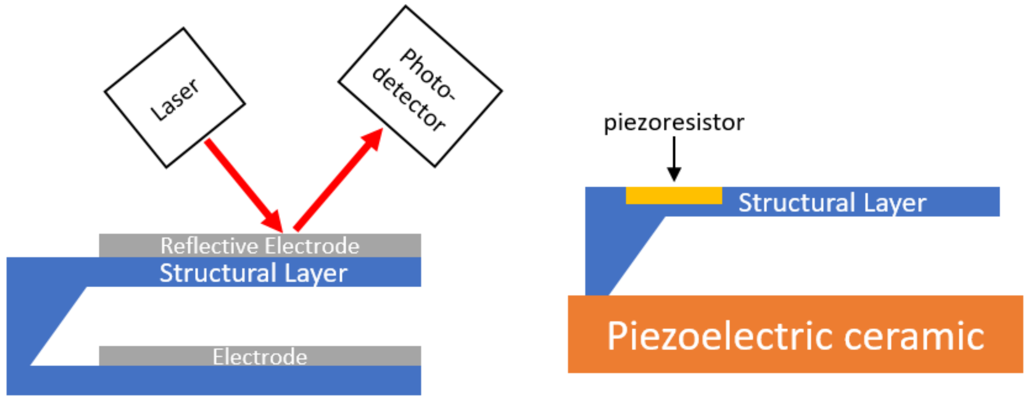

c) Electrostatic actuation/ optical readout

d) Piezoelectric actuation/ piezoresistive readout

Figure 2.4: Schematic illustration of common actuation and corresponding readout methods used in cantilever sensors.

Capacitive readout typically requires an electrostatic actuator configuration, where an electrode on the cantilever and an electrode on the substrate form a parallel capacitor. The capacitance (Equation 2.9) measured across the air gap is dependent on the dielectric constant (ε) of the gap material (air), the cross-sectional area (A) of the cantilever and the gap distance between the cantilever and the bottom electrode (d).

$$C = \frac{\varepsilon A}{d}; \tag{2.9}$$

As the cantilever deflects downward the gap distance decreases and increases the capacitance. The sensitivity of the device is thus dependent on the change in capacitance. One of its main benefits over optical readout is the fact that it can be integrated as a single packaged device. However, in miniaturizing the device, capacitance changes become very small in the picofarad (pF) region and thereby are easily drowned out in the stray capacitance of the measurement systems [4].

Piezoelectric materials can be used as a readout method, where cantilever deflections generate a strain on a piezoelectric layer and in turn produces a measurable current. Similarly, piezoresistive materials change their resistance when a mechanical strain is applied. Therefore, a piezoresistive material can be embedded onto a cantilever to capture its displacement. When the cantilever is displaced, a stress acts on the piezoresistor thus changing its resistance. Piezoelectric and piezoresistive readout methods are applicable to both static and dynamic sensing modes.

Materials and Fabrication

MEMS type structures and devices are typically made with either bulk or surface micromachining processes, as illustrated in the Figure 2.5. Silicon (both crystalline and polycrystalline) is commonly used to form the microcantilever body (structural layer) due to its compatibility with many well established micro-fabrication processes. A typical fabrication process consists of depositing and/or patterning the cantilever geometry through several thin film deposition and lithography steps. This is followed by the critical step of releasing the cantilever by etching away the material underneath the structural layer, referred to as the sacrificial layer. For cantilever gas sensing, silicon alone, is not capable of sensing chemical compounds and therefore an additional receptor layer which has an affinity for the target analyte is required. The incorporation of the receptor layer to the cantilever structure must be considered for its compatibility with the other fabrication process steps as well.

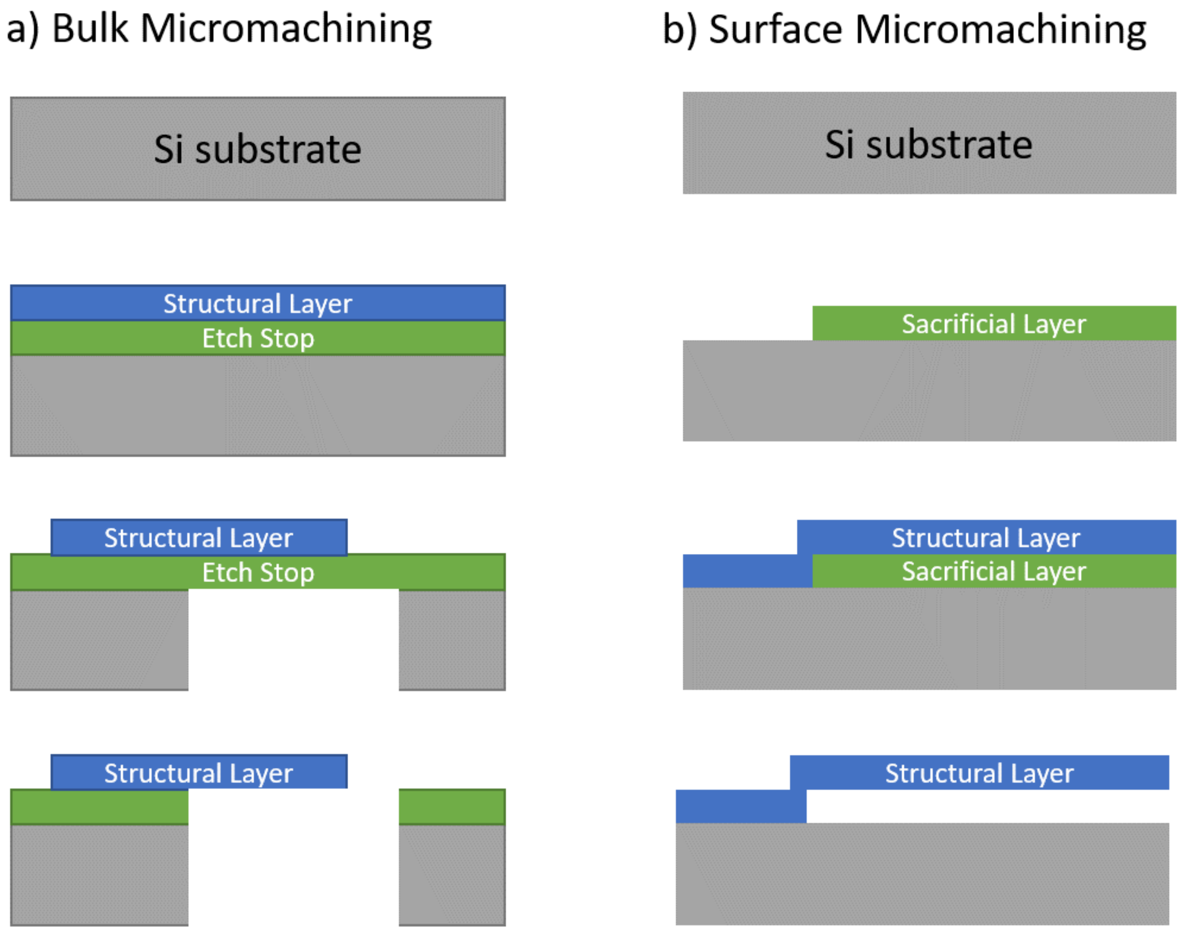

Figure 2.5: Micromachining techniques to fabricate MEMS structures. a) Bulk micromachining involving etching of the substrate. b) Surface micromachining involving a sacrificial layer and its subsequent removal. Deposited photoresist layers for lithography not shown.

Thin film layers are deposited using well established physical vapor deposition (PVD) and chemical vapor deposition (CVD) techniques. Metallic layers are often deposited by PVD techniques such DC/RF sputtering and e-beam/thermal evaporation. Dielectric materials such as polysilicon, metal oxides and nitrides can be deposited by both CVD and PVD techniques. The patterning of these layers is done by lithography followed by etching. Each step in the process must be compatible with the subsequent steps thereafter. For example, the etching step should be designed and selected so as to not remove all the previously deposited layers.

In a typical bulk micromachining process, parts of the substrate itself are removed to realize a free-standing cantilever structure. This bulk etching is illustrated in Figure 2.5a. On top a silicon wafer, an etch stop layer, the silicon based structural layer and a photoresist layer are deposited. Additional layers may be required for actuation, readout and gas sensing (receptor). A lithography process (UV for micron sized features or electron beam for nano sized features) is used to pattern the photoresist. The patterned photoresist is then used as a mask to pattern the silicon structural layer underneath into the desired cantilever geometry. This step is done by either wet or dry etching, using etchants that are selective to the structural material [4, 11, 12]. Backside wet etching of the silicon wafer is done to create the cavity/gap. To etch the silicon wafer, etchants such as potassium hydroxide (KOH) and sodium hydroxide (NaOH) are used. The etch stop layer is inert or has a slower etching rate than the silicon wafer and protects the structural layer from damage. The final step to release the cantilever is the removal of the etch stop layer by further wet etching with etchants that are selective to the etch stop material. The deposition of the gas sensing receptor layer may be done as an intermediate step before cantilever release or after cantilever release.

Surface micromachining processes, illustrated in Figure 2.5b, are also used to fabricate cantilever structures but pertain to the addition and removal of layers on top the substrate only. Here the substrate simply acts as a carrier for the device and electronics. A layer known as a sacrificial layer is deposited before the structural layer. Instead of etching through the bulk of the silicon wafer, the sacrificial layer is etched away to create the gap. This technique is used to realize both silicon and non-silicon based structural layers [13]. The sacrificial layer is etched away by wet or dry etching technique, ensuring the chosen etchant does not etch away the structural layer as well. Sacrificial layer etching or "release etching" is a slow process due to the limited access to the sacrificial layer.

Surface functionalization of the cantilever with a gas sensitive receptor layer is required to be able to attract the desired gaseous analytes. Receptor layers have consisted of various polymers, metal oxides, organic ligand type molecules, and DNA strands [4, 6, 11, 12].

Polymer receptor layers can be used for both static and dynamic MEMS gas sensing [4]. The absorption of gaseous analytes causes a swelling of the polymers. In static mode, the swelling of the polymer induces a surface stress that results in a bending of the cantilever [14]. In dynamic mode, the adsorption of analyte corresponds to a detectable mass change. These polymers are easily deposited onto the surface of the structural layer by spin-coating, dip coating, and drop casting techniques.

Metal oxide materials are also suitable for MEMS based gas sensing, however they have been more widely used in chemoresisitve gas sensors [5, 15]. The amount of available gas adsorption sites is heavily influenced by the surface morphology of the material. Nanostructured materials such as nanowire arrays or polycrystalline thin films with nanoscale roughness are advantageous due to their higher surface area-to-volume ratio [15]. Doping of the metal oxide material can improve sensitivity of the sensor by altering the surface charge of the material and can improve selectivity to certain gas analytes [15]. Atomic Layer Deposition (ALD) is one of many deposition methods for the metal oxides [5]. The most popular metal oxide material for gas sensing is tin oxide (SnO_2). Other metal oxides such as zinc oxide, titanium oxide and their doped varieties have also been used to sense a large collection different analytes [5].

A widely accepted mechanism for metal oxide based gas sensing is depicted in Figure 2.6 and is as follows. In the presence of air and absence of humidity, oxygen is "ionosorbed" (ion adsorbed) onto the surface of the metal oxide. In the presence of an oxidizing gas such as oxygen, further oxygen ions would be ionosorbed onto the surface of the metal oxide. In the presence of a reducing gas such as carbon monoxide, the ionosorbed oxygen ion would react with the reducing agent resulting in fewer oxygen species on the surface of the metal oxide. In chemiresistors, the amount of ionosorbed oxygen on the metal oxide affects its electrical conductivity and hence any changes in the amount of ionsorbed oxygen would be seen as a change in resistance [15].

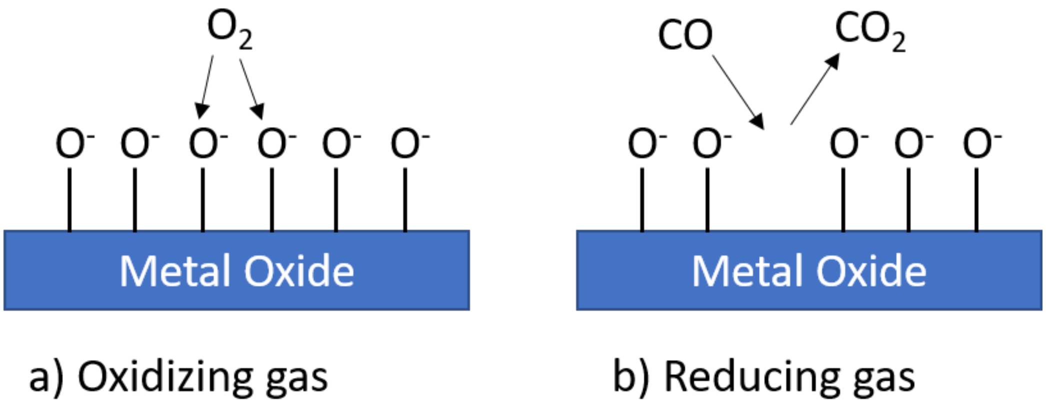

Figure 2.6: Gas adsorption on metal oxide films. In air, oxygen ions are adsorbed onto the surface of the metal oxide. a) In the presence of an oxidizing gas, additional oxygen ions are adsorbed. b) In the presence of a reducing gas, oxygen ions react with reducing agent and leave the surface.

2.1.2 Review of Static MEMS Sensors

General Review

For a while, the lone application for cantilever-type devices was for atomic force microscopy (AFM) or scanning probe microscopy (SPM) characterization of surfaces. In the 1990s, researchers began to explore alternative applications for cantilever devices, taking advantage of their reproducible bending behavior when exposed to different environments. Early research involved utilizing silicon-based cantilevers made specifically for AFM and coating them with various receptor layers for chemical sensing. In 1993, Gimzewski et al. utilized a silicon cantilever ($L \times w \times t = 400 \times 35 \times 1.5\ \mu m$) coated with a 400 nm layer of aluminum, to detect local temperature changes during the catalytic conversion of H_2 + O_2 to form H_2O [16]. The deflection in the cantilever, due to different thermal expansion coefficients of the layers, was read out by an optical method that was used for SPM at the time. In 2000, Jensenius et al., was the first to integrate a piezoresistive read out method with cantilever type devices, which allowed for miniaturization and compactness of the sensing setup [17]. Micromachined Si/SiO$_2$ cantilevers ($200 \times 50 \times 2\ \mu m$) with an embedded poly silicon piezoresistor, were coated with an AZ 5200 photoresist polymer film (∼ 10 μm thick). A reference, uncoated piezoresistive cantilever was also measured alongside the coated cantilever. The differential resistance between the two cantilevers was measured with a wheatstone bridge circuit, to obtain the equivalent bending response of the coated cantilever to vapors of ethanol, methanol and 2-propanol. Figure 2.7a, shows a scanning electron microscope (SEM) image of the uncoated (left) and coated (cantilevers), while Figure 2.7b shows the bending response of the coated cantilever to the tested alcohols. The largest response was to methanol which had the highest vapor pressure and the lowest molecular mass. The high vapor pressure corresponded to its high abundance in air, while its low molecular mass corresponds to its improved diffusivity into the polymer layer (smaller molecule).

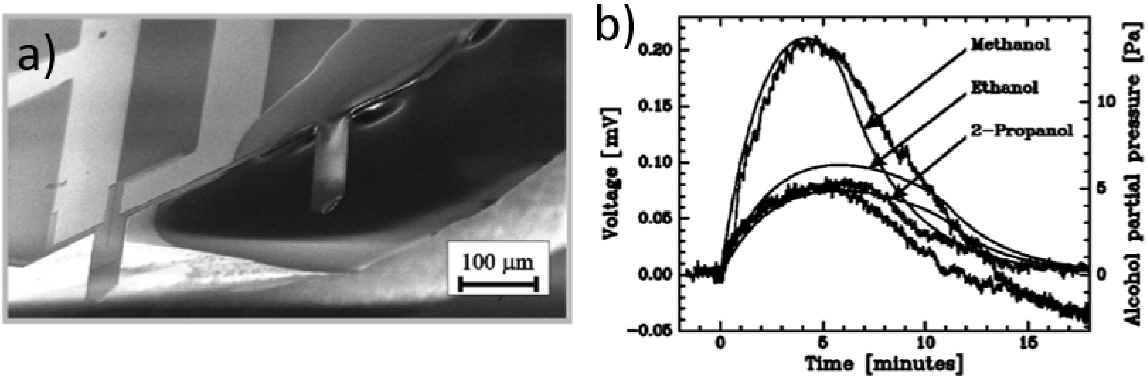

Figure 2.7: a) SEM image of uncoated (left) and polymer coated (right) cantilever. b) piezoresistive deflection response [μV] of polymer coated cantilever to methanol, ethanol and 2-propanol. Adapted from ref. [17] with permission. Copyright 2000, AIP Publishing.

In 2004 a handheld unit known as "Sniffex" was developed by researchers at Oak Ridge National Laboratory, and was able to detect vapors of plastic explosives [18]. Piezoresistive silicon cantilevers (125 × 50 × 0.5 μm) were coated with a 30 nm gold layer. The gold coated Si cantilever was coated with 4-mercaptobenzoic acid (4-MBA). Figure 2.8, shows the bending response of the coated cantilever to vapors of 10 parts per trillion (ppt) pentaerythritol tetranitrate (PETN) and 3 ppt hexahydro-1,3,5-triazine (RDX) at room temperature. The high sensitivity and repeatable detection signal of the device led to the development of a handheld unit currently used for explosives detection.

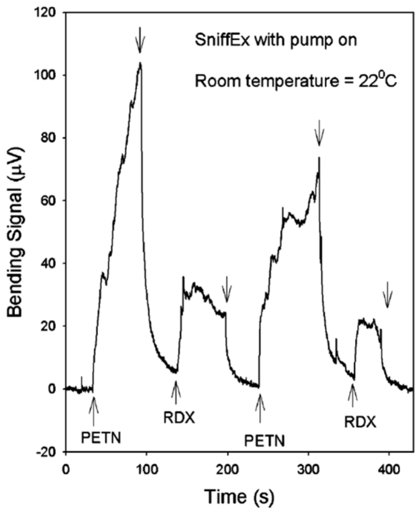

Figure 2.8: Bending signal [μV] of "SniffEx" cantilever device exposed ot PETN and RDX vapors. Adapted from ref. [18] with permission. Copyright 2004, AIP Publishing.

Yoshikawa et al. created an array of piezoresistive cantilevers to address challenges in selectivity [14]. An array of silicon cantilevers (135 × 30 × 1.5 μm) were coated with polymers such as poly vinyl alcohol (PVA), polyethyleneimine (PEI), poly acryl amide (PAAM) and poly vinyl pyrrolidone (PVP). Each coated cantilever was paired with a similar uncoated cantilever to obtain the differential piezoresistive bending signal. The bending response of each coated cantilever to vapors of water, methanol, ethanol, hexane, dimethyl either, isopropanol, pentane, hexane, heptane, nonane, decane and undecane were observed (shown in Figure 2.9a and b). The response to each analyte was measured in 5 ON/OFF cycles, for repeatability. The sorption of the analytes on the polymer layers induces a surface stress and subsequent bending of the cantilever due to the swelling of polymers. The response of each coated cantilever to each analyte, forms a "fingerprint" or identifier for that particular analyte. A Principal Component Analysis (PCA) of the data set, shown in Figure 2.9c and d, revealed unique well-defined clusters for each analyte without any overlap. This analysis demonstrates the ability of an array of piezoresistive cantilevers sensors to selectively discriminate analytes.

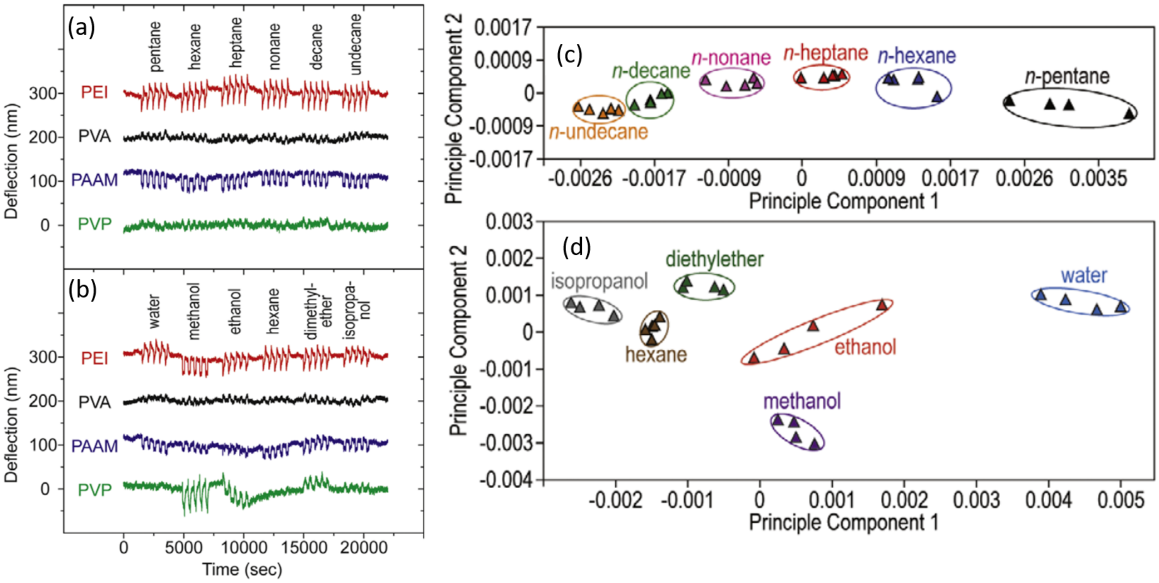

Figure 2.9: Bending/deflection response [nm] of polymer coated cantilevers to analytes tested (part a and b). Principle component analysis of bending responses reveals distinct clusters of response signals which can be used to discriminate the analytes (part c and d). Adapted from ref. [14] with permission. Copyright 2008, IOP Publishing Ltd.

Nanomechanical Membrane-type Surface Stress Sensors

Piezoresistive cantilevers suffered from poor deflection resolution when compared to optical techniques which were superior. Amplification of the piezoresistive signal was required. To address this challenge, a nanomechanical Membrane type Surface stress Sensor (MSS) was developed by Yoshikawa et al. [19]. Instead of a cantilever type structure, the device consisted of a round silicon membrane suspended by four piezoresistive beams, as depicted in Figure 2.10. The four piezoresistors were connected in a wheatstone bridge circuit configuration. In a conventional cantilever, surface stresses in one direction (along length of cantilever) are captured by a single piezoresistor. Whereas in the MSS, surface stresses in both the x and y directions are captured by 4 piezoresistors thus resulting in signal amplification. This approach has the added benefit of not requiring an additional uncoated device to obtain the differential resistance signal.

The MSS devices were coated with the polymers PEI and poly sodium 4-styrenesulfonate (PSS) and showed a response to 20% water vapor in nitrogen, shown in Figure 2.11. Coat-

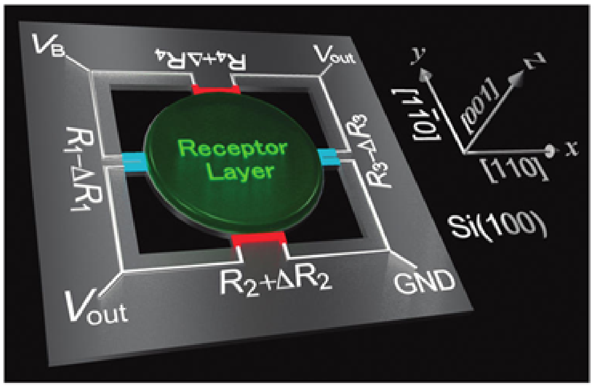

Figure 2.10: Schematic illustration of the membrane-type surface stress sensor and electrical connection to piezoresistors for measurement of bending response. Adapted from ref. [19] with permission. Copyright 2011, American Chemical Society.

ing of the membrane was done with an inkjet spotting technique, that allows for precise deposition of picolitre (pL) volumes of solution. The responses of both devices were greater than a conventional piezoresistive cantilever of similar size. These results kick-started further development of MSS devices with unique receptor layers.

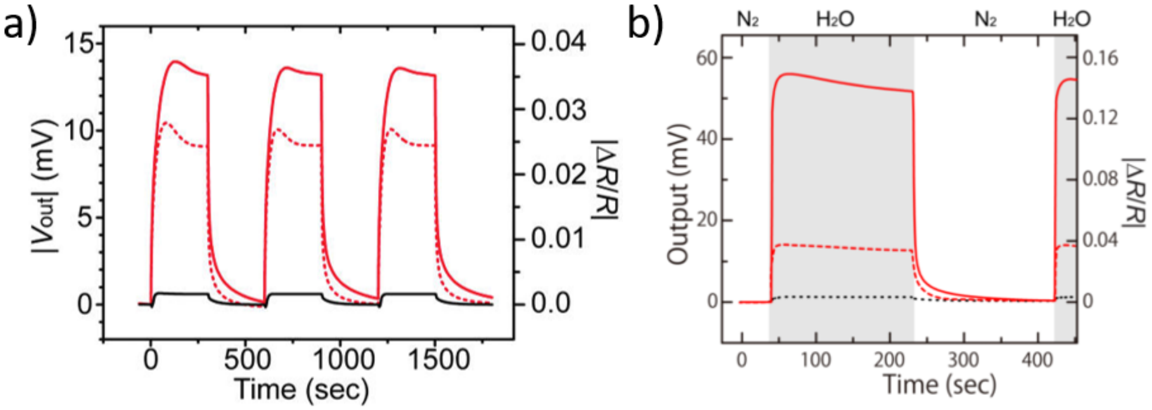

Figure 2.11: Bending response [mV] of a PEI and b)PSS coated MSS with diameters of 500 μm (solid red line) and 300 μm (dotted red line) compared a standard cantilever (black line). Adapted from ref. [19, 20] with permission. Copyright 2011, American Chemical Society.

Shiba et al. synthesized core-shell nanoparticles consisting of a porous silica core and a nanoporous titania shell [21]. The response of the coated MSS to water, ethanol, hexane, benzene and acetic acid is shown in Figure 2.12 which also includes an SEM image of the synthesized nanoparticles. Larger responses were obtained for analytes with polar groups such as water, ethanol, and acetic acid, while lower responses were obtained for nonpolar analytes such as hexane and benzene. Further analysis revealed that the surfaces of the nanoparticles were hydrophilic and therefore supports the obtained sensor response to the analytes. The origin of membrane deflection comes from the absorption of the analytes in the nanoporous titania shell resulting in its subsequent volume expansion and induced stress on the membrane. Sensor performance metrics such as sensitivity, LOD, response and recovery time were not reported.

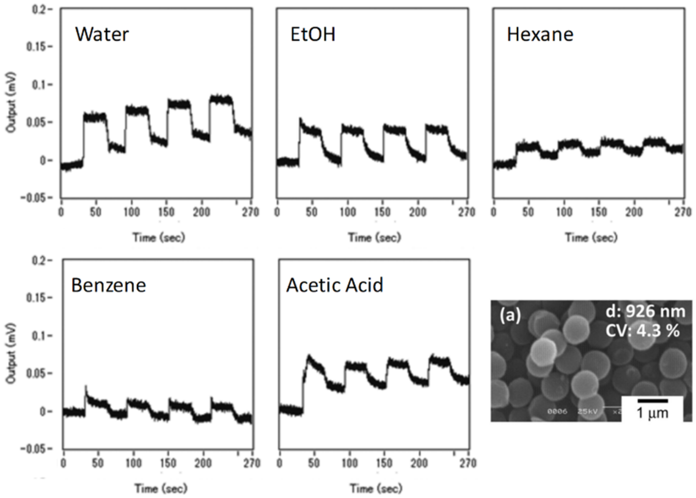

Figure 2.12: Bending response $[\mu V]$ of MSS with a titania coated silica nanoparticles receptor layer(MSS image of particles shown in bottom right figure). Responses were obtained for water, ethanol (EtOH), hexane, benzene and acetic acid vapors. Adapted from ref. [21] with permission from The Royal Society of Chemistry.

Osica et al. [22], reported MSS devices coated with a dispersion of hybrid nanostructures consisting of highly textured silica nanoparticles (named silica nanoflake-shell capsules, SFS) conjugated with metalloporphyrin molecules with different metals (cobalt, nickel, copper and zinc-based porphyrins). An illustration of the chemical structure of the metalloporphyrin and SEM image of the nanoparticle surface is shown in Figure 2.13a. The effect of the silica nanoparticle size and surface texture on the response to acetone vapors was studied and shown in Figure 2.13b. The sensor response to acetone increased as the size of the silica particle decreases and its surface texturing increased, corresponding to an increased surface area available for analyte adsorption. A limit of detection was calculated to be 0.6 ppm for acetone and 3.5 ppm for nitric oxide. Other sensor metrics such as sensitivity, response and recovery time were not reported.

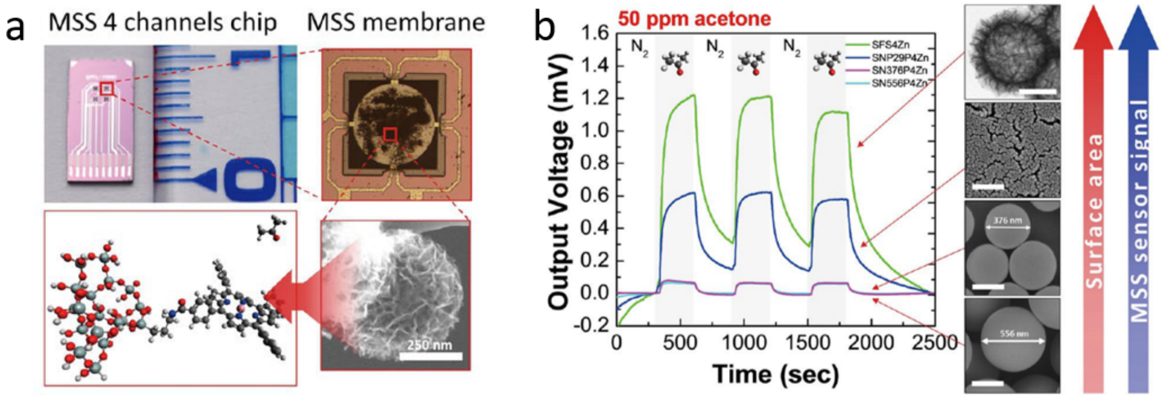

Figure 2.13: a)Array of MSS coated with metalloporphyrin conjugated textured silica nanoparticles (SEM and molecular structure shown). b) Bending response [mV] of coated MSS to 50 ppm of acetone vapor. The effect of silica nanoparticle surface texture and size (shown in SEM and transmission electron microscope (TEM) on right) on the response signal is compared. Adapted from ref. [22] with permission. Copyright 2017, American Chemical Society.

Gold nanocage (AuNC) nanoparticles were synthesized and used receptor materials for MSS and tested with water based, alkane, alcohol, aromatic, and ketone type chemical compounds. The highest responses were for water and alcohol-based analytes, which was attributed to the preferable interactions between the gold and the oxygen atom on the hydroxyl groups. The limit of detection to methanol, which had the highest sensor response, was 30 ppm. Other sensor metrics were not reported, but a larger emphasis was placed on the selective response of the sensors to the chemical groups tested.

Finally, Yao et al. fabricated a similar device structure to the MSS and coated it with graphene oxide (GO) for relative humidity (RH) sensing [23]. Figure 2.14, depicts the fabricated silicon "microbridge" structure (20 μm thickness) consisting of a square plate-like structure fixed at four piezoresistive supports. In comparison, the MSS device uses a round suspended membrane instead with a thickness of 2.5 μm. GO (synthesized via a Hummers method) was spin coated on top the silicon microbridge, to create a random distribution of GO flakes (approximately 65 nm thickness).

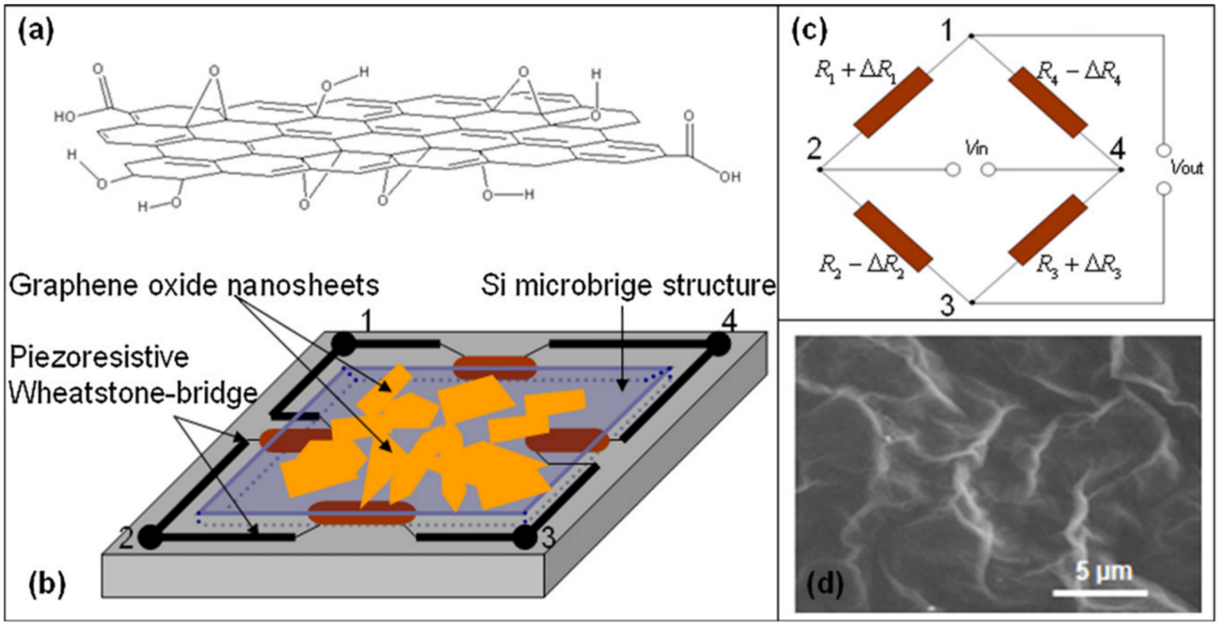

Figure 2.14: a)Illustration of graphene oxide flake functionalized with oxygen containing groups. b) schematic of fabricated piezoresistive Si microbridge structure with graphene oxide flakes receptor layer. c)circuit diagram of 4 piezoresistors connected in wheatstone bridge configuration to obtain piezoresistive bending signal. d) SEM image of the surface of the graphene oxide receptor material. Adapted from ref. [24] with permission. Copyright 2012, Elsevier B.V.

The response of the coated and uncoated device to increasing RH is shown in Figure 2.15a. It is clear the GO coating improved the sensor response to the RH changes. Here the bending response was attributed to the humidity induced deformation of GO. The oxygen functional groups on the GO such as hydroxyl, epoxy and carboxyl groups act as receptors for water molecule adsorption. This adsorption process leads to an increase in the interlayer distance between the GO flakes (i.e., swelling of the GO films). This expansion induces the surface stress on the silicon microbridge and readout by the piezoresistors. The sensitivity of the sensor was reported to be 79.3 $\mu V/\%RH$ and exhibited fast response and recovery times (although the exact time was not reported).

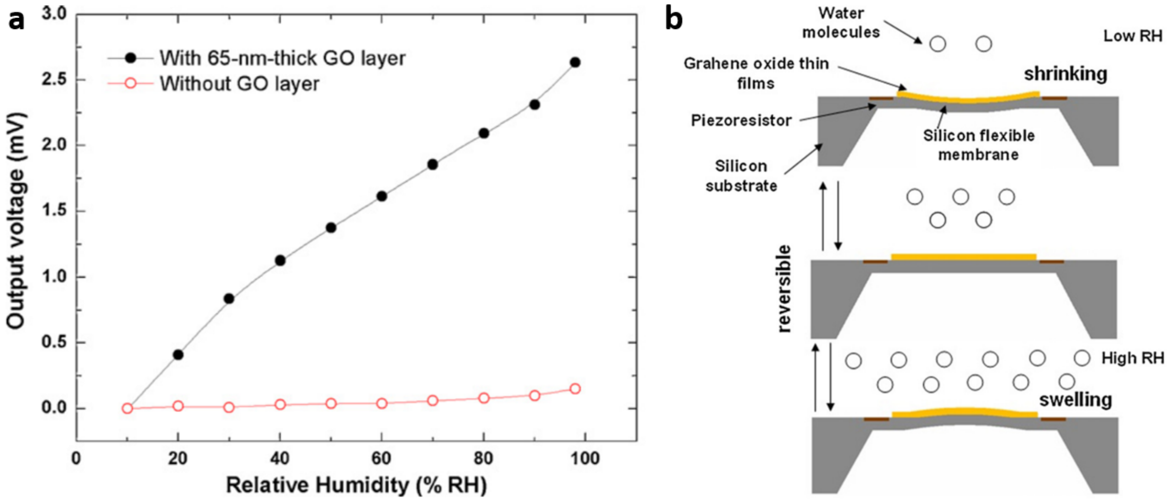

Figure 2.15: Bending response [mV] of graphene oxide coated (black) and uncoated (red) Si microbridge to increasing RH. Adapted from ref. [24] with permission. Copyright 2012, Elsevier B.V..

2.1.3 Review of Dynamic MEMS Sensors

General Review

One of the earliest reports of gas detection by a resonating microcantilever sensor was by Thundat et al. in 1995 [25]. In this study, commercially available silicon nitride cantilevers (200 μm long) were coated with a thermally evaporated layer of gold (50 nm) on one side. The coated cantilevers were used for the detection of mercury vapors. The cantilever was mounted on a piezoelectric crystal for actuation and resonant frequency was read out by optical laser vibrometry. The resonant frequency of a cantilever partially covered (only at the free end) with gold, upon exposure to mercury vapor is shown in Figure 2.16. The decrease in the resonant frequency is a result of the adsorption of mercury on the cantilever, increasing the cantilever's overall mass (see Equation 2.5). The mass sensitivity of this device was 0.7 picograms/Hz. In contrast, a cantilever that was fully covered with gold showed a frequency increase when exposed to mercury. This behavior was explained as a combination of mass loading as well as an increase in the stiffness (k) of the beam due to mercury-gold interactions.

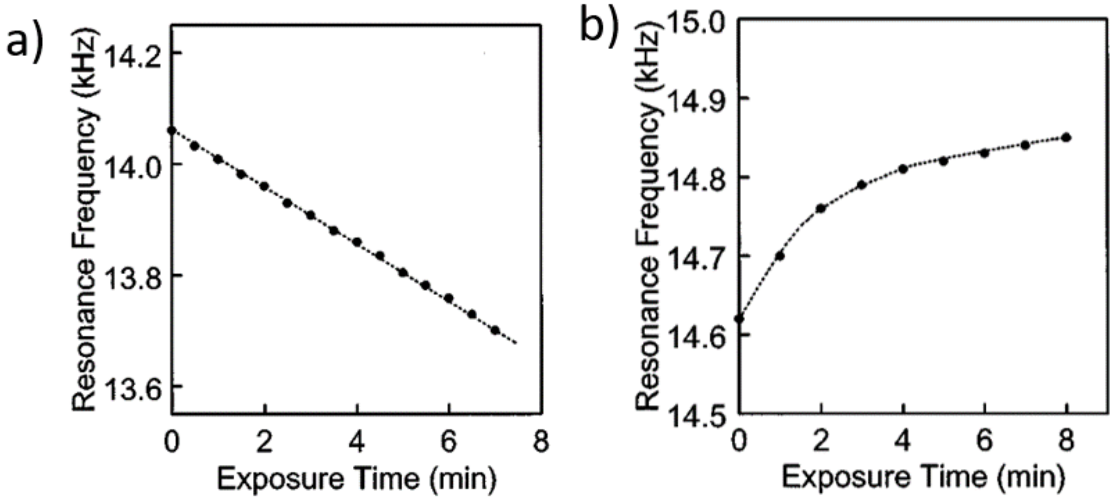

Figure 2.16: Frequency response [kHz] to mercury vapor of a silicon nitride cantilever a) partially covered with gold resulting in a decrease in frequency and, b) fully covered in gold resulting in an increase in frequency. Adapted from ref. [25] with permission. Copyright 1995, AIP Publishing.

Similar to static cantilever sensing, the coating of cantilevers with various polymers was a common technique for dynamic mode sensing as well. Maute et al. coated silicon nitride cantilevers (with reflective gold layer) with polydimethylsiloxane (PDMS) for the sensing of n-octance, toluene and n-butanole [26]. The frequency shift as a function of gas concentration (ppm) was obtained and yielded concentration sensitivities of 0.0988, 0.0409 and 0.0033 Hz/ppm for octane, toluene and butanole, respectively. Dong et al. utilized polyethylene oxide (PEO), polyethylene-vinyl-acetate (PEVA) and PVA as coatings on silicon cantilevers for the sensing of hexane, octane, toluene, benzene, acetone, ethanol and changes in RH. PEO was most sensitive to ethanol yielding a concentration sensitivity of 0.00426 Hz/ppm. PEVA was most sensitive to toluene (0.00734 Hz/ppm) while PVA was most sensitive to benzene (0.00719 Hz/ppm). Then et al. produced polyetherurethane (PEUT) on electrostatically actuated Si cantilevers [27]. Testing with butanol, toluene and octane yielded concentration sensitivities of 0.16, 0.08 and 0.05 Hz/ppm, respectively, which are large improvements over the previous report by Maute tested with the same analytes.

The ability to selectively identify and discriminate analytes is realized with the formation of cantilever arrays each functionalized with a unique polymer coating. Battiston et al. utilized 7 different polymers, which included poly methyl methacrylate (PMMA), polystyrene (PS), polyurethane (PU), poly-vinyl-chloride (PVC), PVA, PVP and carboxymethylcellulose (CMC) [6]. The frequency shifts of the coated cantilevers were measured in response to water vapor, primary alcohols (methanol, ethanol, propanol and butanol), and alkanes with different chain lengths. The individual responses of each cantilever to each analyte was used to train a feed forward neural network. The cantilever array and neural network was used in conjunction to identify the chemical composition of various perfumes. The authors did not report individual sensitivities of the coated cantilevers.

Besides polymers, various unique receptor materials have been used in dynamic cantilever sensors such as metal organic frameworks [28,29], microporous ceramic zeolite [30], peptides [31] and cyclodextrins [32–35]. Multi-wall carbon nanotubess (MWCNTs) have been implemented as a surface coating on piezoelectric cantilevers [36]. The sensors were testing with benzene, carbon monoxide and nitrogen dioxide, yielding LODs of 1, 5 and 0.05 ppm, respectively. The LODs obtained with the resonant cantilever sensors were lower than the corresponding LODs obtained for a chemoresistive sensor with the same MWCNTs receptor. The use of MWCNTs is particularly interesting as it allowed for the creation of a nanocantilever sensor comprised of a single MWCNTs as reported by Jensen et al. [37]. Figure 2.17a shows a high-resolution TEM image of the single MWCNTs cantilever fixed at one end. The frequency response of the device to evaporated gold (Figure 2.17b), showed a fairly large shift in the MHz range for an increase in mass equivalent to 51 Au atoms which corresponds to a mass sensitivity of 0.13 zeptograms/Hz.

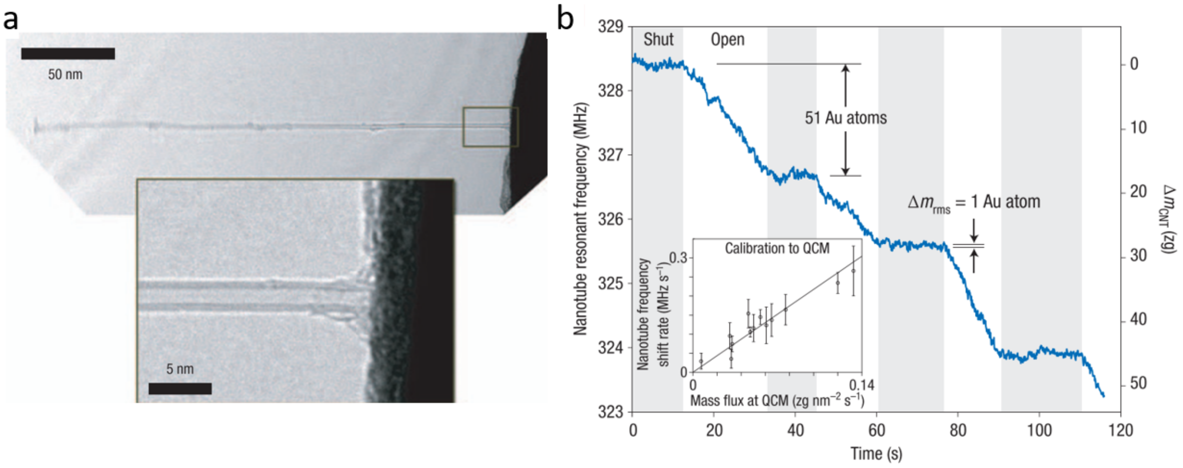

Figure 2.17: a)High resolution TEM image of a single MWCNTs nano-cantilever. b) Frequency response [MHz] of MWCNTs cantilever to evaporated gold. Adapted from ref. [37] with permission. Copyright 2008, Nature Publishing Group.

The achievement of ultra low mass sensitivity was due to the miniaturization of the cantilever structure to the nanoscale. Additionally, the single MWCNT performs the role of the structural, receptor, actuation layers all at once since it has a elastic modulus and tensile strength, many surface sites for adsorption, and is conductive. This idea of "extreme" miniaturization was further pursued by Li et al. [38] who fabricated gold coated silicon carbide (SiC) cantilevers ranging from the micro to nanoscale, shown in Figure 2.18a-d. The largest cantilever ($33 \times 5 \times 0.1$ μm) had a resonant frequency of 52 kHz while the smallest cantilever ($600 \times 400 \times 100$ nm) had a resonant frequency of 127 MHz. The nanocantilever was tested with vapors of 1,1-difluoroethane with frequency shifts that were equivalent to 1 attogram (ag) of adsorbed mass (Figure 2.18e).

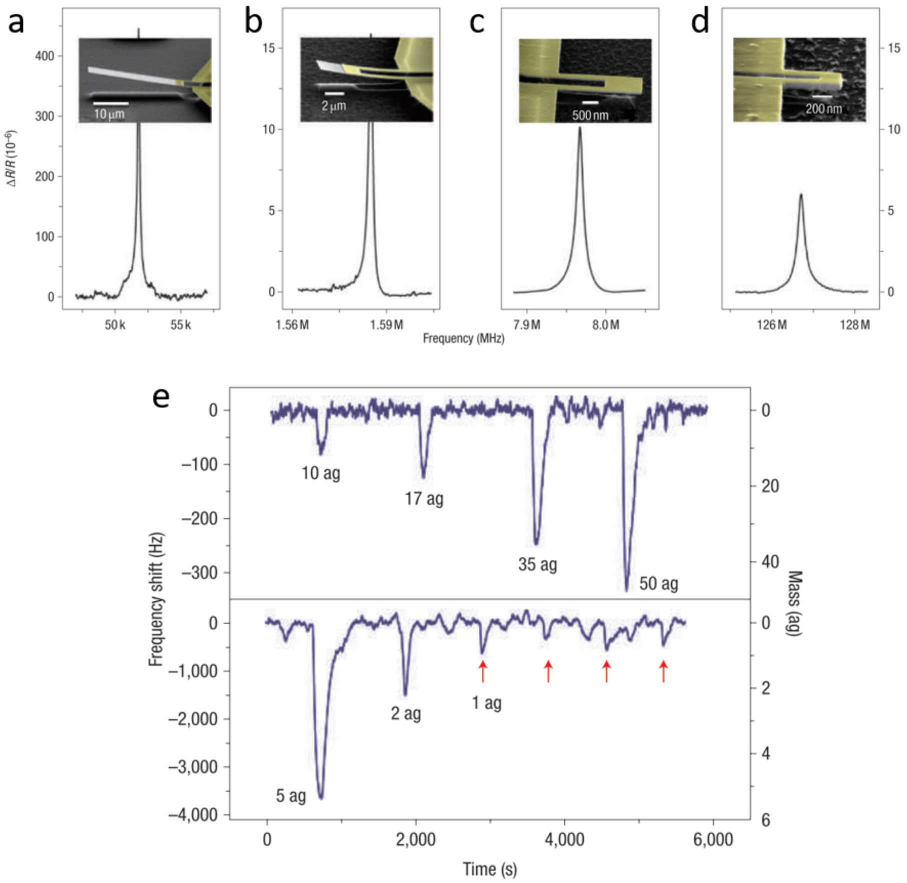

Figure 2.18: SEM images and resonant frequencies of gold coated SiC cantilevers with resonant frequencies of (dimensions in brackets) a) 52.1 kHz ($33 \times 5 \times 0.1\ \mu m$), b) 1.6 MHz ($10 \times 2 \times 0.1\ \mu m$), c) 8 MHz ($2.5 \times 0.8 \times 0.1\ \mu m$), d)127 MHz ($0.6 \times 0.4 \times 0.1\ \mu m$). e) The frequency response [Hz] of 8 MHz (top) and 127 MHz(bottom) cantilevers towards attogram amounts of 1-1 difluoroethane. Adapted from ref. [38] with permission. Copyright 2007, Nature Publishing Group.

Zinc Oxide Dynamic-mode Sensors

ZnO in chemiresistive gas sensors has been used to sense a large range of analytes such as carbon monoxide (CO), ammonia (NH_3), nitrogen dioxide (NO_2), hydrogen (H_2), liquefied petroleum gas (LPG) and Hydrogen disulfide (H_2S) [5, 39–43], to name a few. Silver doping of ZnO nanowires improved sensitivity to LPG [44], while copper doping of ZnO nanocrystalline films improved sensitivity to CO [45]. Aluminum doping of sputtered ZnO films shows selective sensitivity to NH_3 [46]. Paraguay et al. [47] studied the influence of

Al, In, Cu, Fe and Sn dopants on the ethanol sensing of ZnO thin films. Sn doped ZnO had the highest sensitivity to ethanol, followed by Al, Fe, In, undoped and finally Cu.

The implementation of semiconducting metal oxides as receptor materials in resonant cantilever sensors is fairly limited when compared to the larger number of reports of metal oxide receptors in chemiresistive gas sensors. This is likely due to the ease of fabrication of a chemiresistive sensor and the well studied metal oxide gas sensing mechanism which is primarily based on the changes in electrical conductivity of the semiconducting material. In this section, the focus is placed on the implementation of zinc oxide receptor materials in dynamic frequency shift-based gas sensors, also known as gravimetric sensors. This includes microcantilever, quartz crystal microbalance (QCM) and acoustic wave resonators, the later two are not typically categorized as MEMS devices but are still relevant for this discussion.

The first implementation of ZnO as a receptor layer in a cantilever sensor was reported by Kilinc et al. [48], who used an electro-deposition technique to grow nanorods and nanotubes on nickel cantilevers ($140 \times 20 \times 2\ \mu m$). An overview of this fabrication scheme is depicted in Figure 2.19a. An SEM of the fabricated ZnO nanorod coated Ni cantilever is shown in Figure 2.19b-d.

The cantilevers were dynamically actuated with an electromagnetic method and optically read out with a laser vibrometer and a lock-in amplifier to measure the phase variation. The phase shift of the sensors, in the presence of diethylamine (DEA) is shown in Figure 2.20a-b. For both devices the introduction of DEA results in a negative phase shift, followed by an increase when the DEA is removed. The concentration sensitivities were determined to be 0.11 m°/ppm and 1.2 m°/ppm for the nanorod and nanotube, respectively. The larger nanotube sensitivity is attributed to the increase in surface area of the nanotube structure.

The response to other analytes such as ammonia, triethylamine(TEA), toluene, acetone, isopropanol, methanol and 50% RH was observed and shown in Figure 2.20c-d. The largest phase shift was observed for ammonia, while the phase shifts for DEA and TEA were the second largest and nearly identically which suggest ZnO shows a higher response to amine

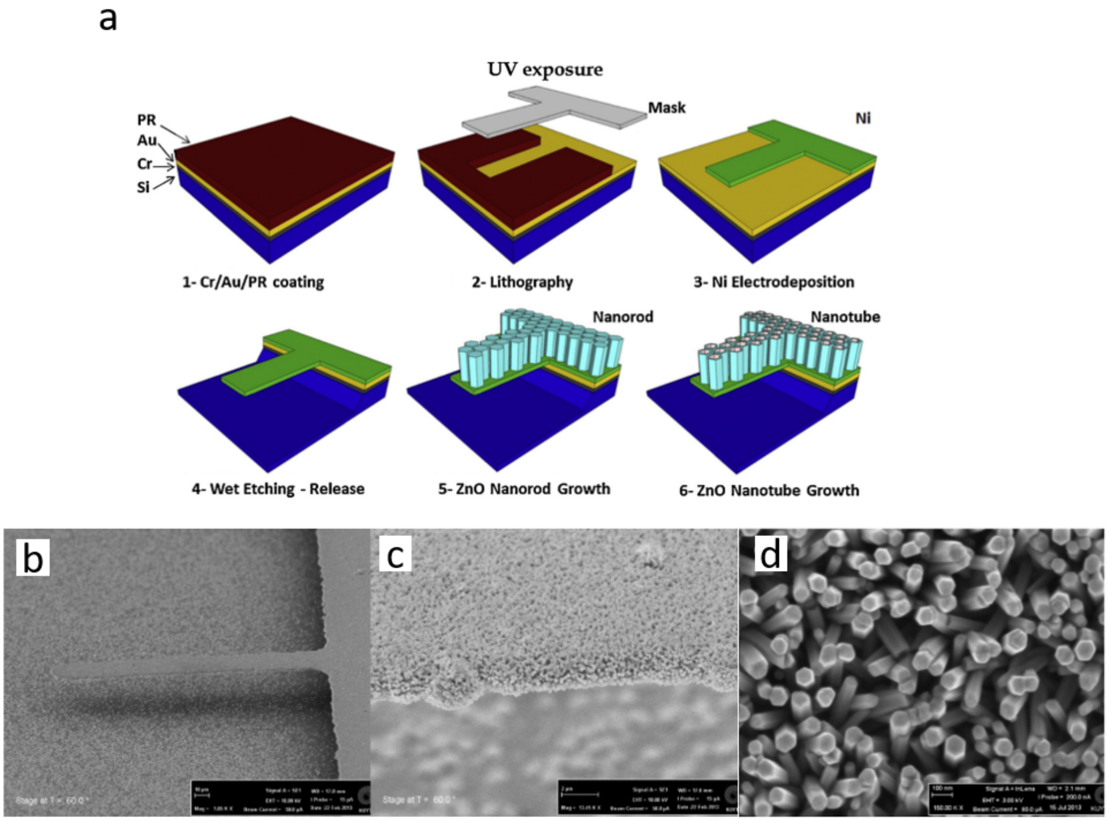

Figure 2.19: a)Schematic diagram of the fabrication process for the formation of Nickel cantilever, subsequent growth of ZnO nanorods and formation of nanotubes. SEM images of the ZnO nanotube covered Ni cantilever at b) 1kX, c) 13kX, and d) 150kX magnification. Adapted from ref. [48] with permission. Copyright 2014, Elsevier B.V.

groups.

Yang et al. [49] grew zinc oxide nanorods (via chemical bath deposition shown in Figure 2.21a) on commercially available silicon cantilevers (3 $mm \times 100\ \mu m\ \times 25\ \mu m$). The nanorod array had dimensions of $\sim 1\ \mu m$ in length and 95 nm in diameter (shown in Figure 2.21b). The substrate was placed on a piezoelectric chip for dynamic actuation and read out with a piezoresistive method.

The response of the device to changes in relative humidity is shown in Figure 2.21c-d. As the RH increased from 30% to 70%, the resonant frequency decreased from 20.98 to 20.89 kHz (a shift of $\sim 100\ Hz$), which corresponds to a sensitivity of 2.5 Hz/%RH. This shift is directly attributable to the adsorption of water onto the cantilever. Response and

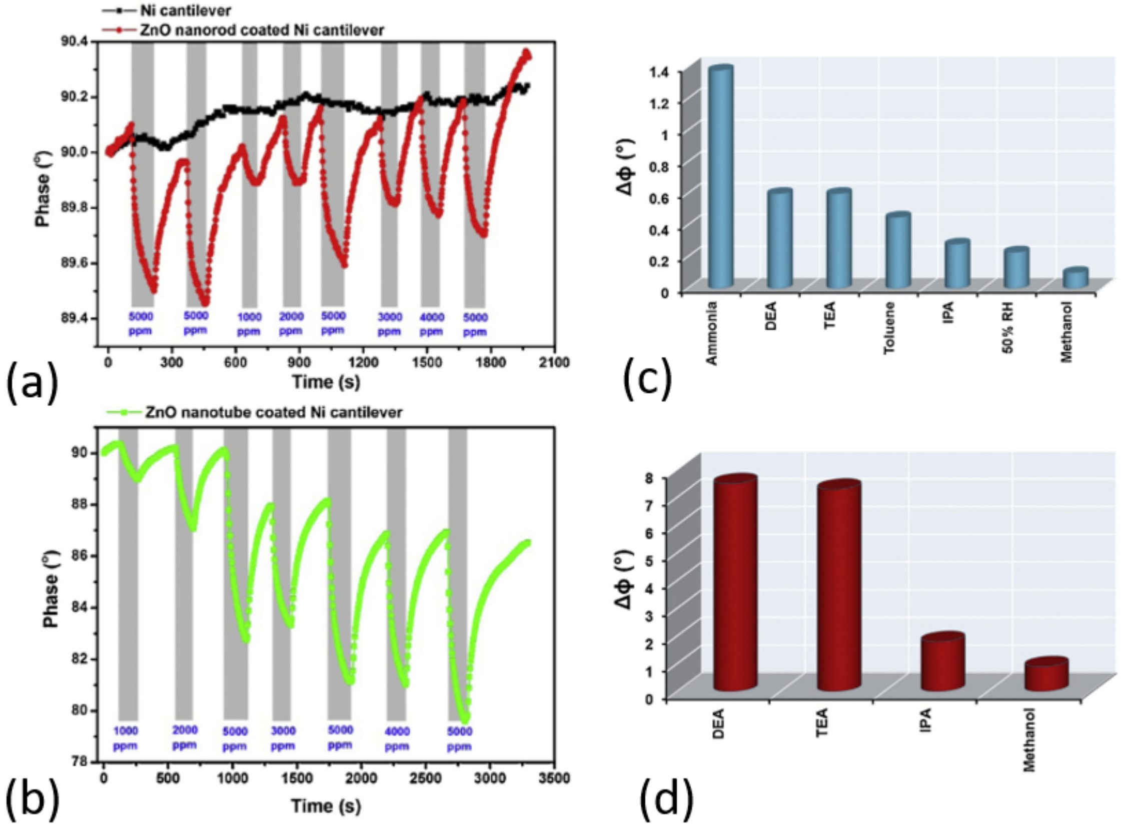

Figure 2.20: Observed phase variation of a) ZnO nanorod coated Ni cantilever (red) and uncoated Ni cantilever (black), and b) ZnO nanotube coated Ni cantilever to varying concentration of DEA vapors. The maximum phase shift to other analytes is shown in (c) for the nanorod-cantilever and (d) for the nanotube-cantilever. Adapted from ref. [48] with permission. Copyright 2014, Elsevier B.V.

recovery times were not measured.

Xu et al. [50] fabricated a similar ZnO nanorod on Si cantilever ($1\ mm \times 170\ \mu m \times 10\ \mu m$) device which was further functionalized with a chitosan coating. The structure was dynamically actuated and simultaneously read out by the embedded piezoresistor. The resonant frequency response to changes in relative humidity is shown in Figure 2.22. The chitosan coated ZnO nanorods were compared to a device without the chitosan coating. For both devices the RH increase from 30% to 70% resulted in a decrease of the resonant frequency. The chitosan coated device experienced a shift of -0.14 kHz while the device without chitosan experienced a shift of -0.025 kHz, corresponding to sensitivities of 3.5

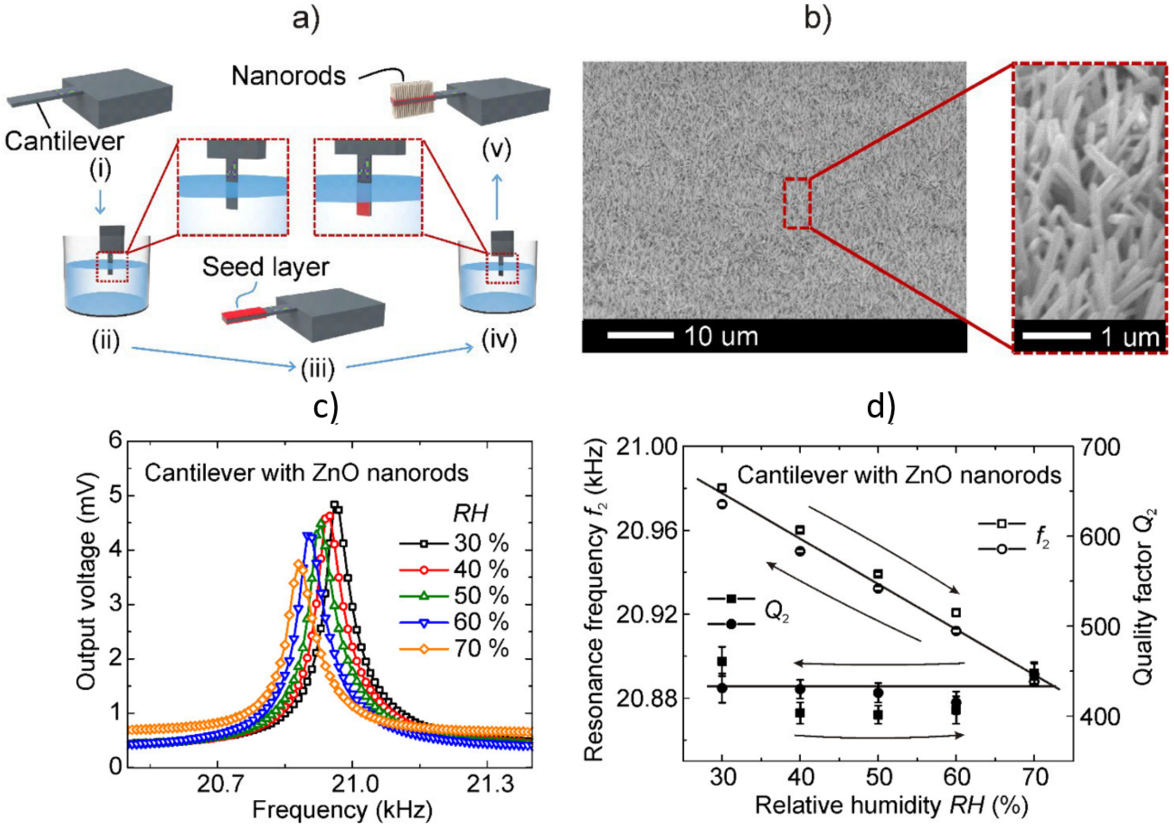

Figure 2.21: a)Schematic diagram of the growth of ZnO nanorods on Si cantilever via chemical bath deposition. b) SEM image of the ZnO nanorod features. c) Frequency sweep response of ZnO nanorod coated cantilever at 30-70% RH.d) Resonance frequency shift and cantilever quality factor (Q) as a function of %RH. Adapted from ref. [49]. Copyright 2014, Jingmei Yang, Jiushuai Xu, Wenze Wu, Maik Bertke, Hutomo Suryo Wasisto and Erwin Peiner, used under a Creative Commons Attribution-NonCommercial-NoDerivatives 4.0 International License (CC BY-NC-ND 4.0).

Hz/%RH and 0.625 Hz/%RH. While the addition of chitosan improved the sensor performance, it is not clear if the ZnO nanorods in the chitosan coated device participated in the adsorption of water or if they simply acted as a scaffold to help increase the surface area of the chitosan.

The same authors further improved their device structure by fabricating a 3D network of ZnO nanorods, on an array of silicon nanopillars, on a silicon cantilever (1 $mm \times$ 170 $\mu m \times$ 12 μm). This network was then functionalized with a self assembled layer of 3-aminopropyl triethoxysilane (APTES). An illustration of the device is shown in Figure 2.23a. The

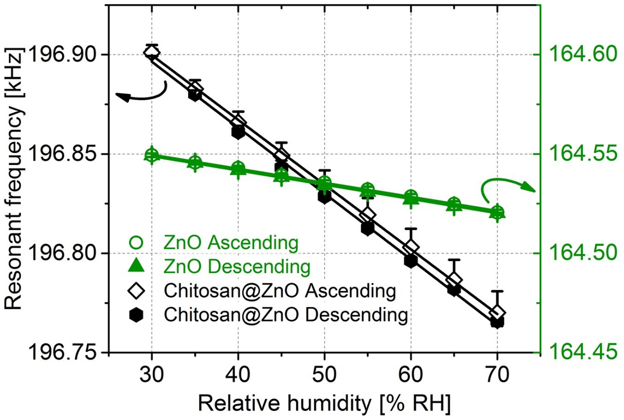

Figure 2.22: Frequency response [kHz] towards increasing %RH of chitosan coated ZnO nanorod cantilever(black) compared to bare ZnO nanorod cantilever (green). Adapted from ref. [50] with permission. Copyright 2018, Elsevier B.V.

silicon nanopillars were formed via nanoimprint lithography and deep reactive ion etching. The ZnO nanorods were grown electrochemically and subsequently functionalized with an APTES coating.

The resonant frequency shift response of the device in the presence of nitrogen dioxide (NO_2) was observed and is shown in Figure 2.23b. The APTES@ZnO@Si device (labeled S3-PMC, blue) had a frequency shift of approximately -10 Hz in the presence of 0.2 ppm of NO_2. In comparison, the device without the APTES functionalization (labeled as 3-PMC) had almost no frequency shift to 5 ppm of NO_2. A device without the silicon nanopillars (labeled S1-PMC) had a frequency shift of -0.2 Hz to 2.5 ppm of NO_2. These results seem to indicate that the ZnO nanorods and Si nanopillars did not participate in the adsorption of NO_2 but instead served as a scaffold to help increase the surface area of the APTES, similar to the previous chitosan study. The resulting concentration sensitivity of the S3-PMC device to NO_2 was 50 Hz/ppm.

Aprilia et al. [52] used a zinc nitrate precursor solution to grow ZnO nanorods on commercially available piezoresistive Si cantilevers ($400 \times 50 \times 1\ \mu m$). The frequency shift response of the device to carbon dioxide gas (at 71% RH) is shown in Figure 2.24. Here the carbon dioxide exposure resulted in a positive frequency shift of 80 Hz, from which the authors incorrectly determined an adsorbed mass of 134 picograms of CO_2 despite being a positive frequency shift.

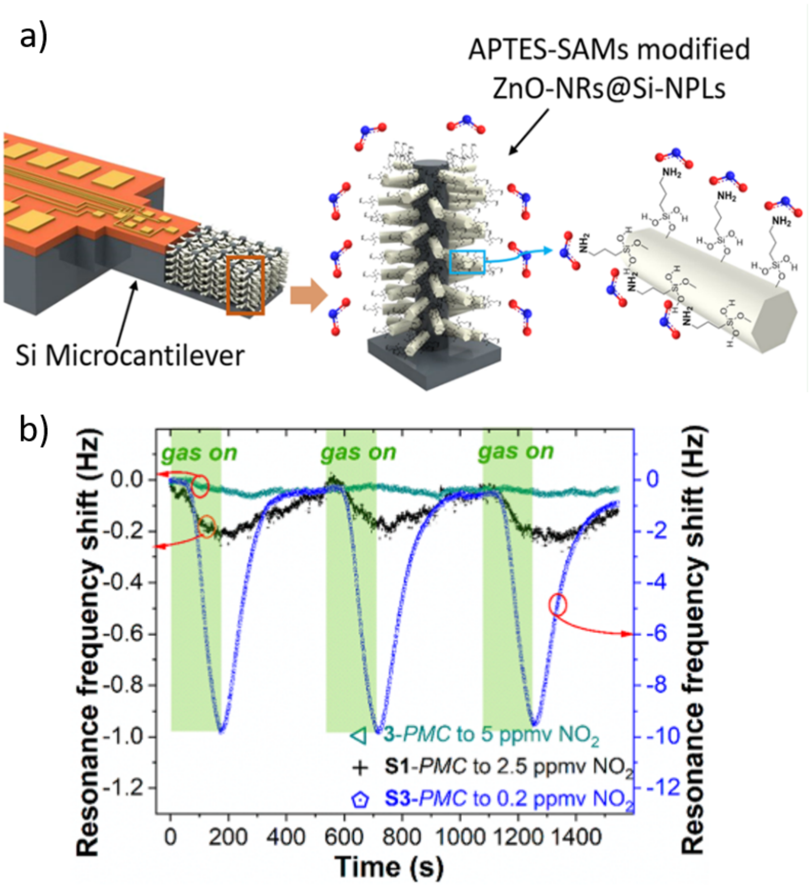

Figure 2.23: a)Illustration of APTES functionalized ZnO nanorods grown on a silicon nanopillar array, grown on a piezoresistive silicon microcantielver (APTES-ZnO-Si). b) resonance frequency shifts [Hz] towards nitrogen dioxide (NO_2), of the APTES-ZnO-Si (labeled S3-PMC, blue), a device with APTES functionalized (labeled S1-PMC, black) and a device with only ZnO nanorods (labeled (S1-PMC). Adapted from ref. [51] with permission. Copyright 2020, American Chemical Society.

In another report [53], the same authors observed the response their device to carbon monoxide gas (Figure 2.25). In the first test an air compressor was used to supply the purging gas followed by CO exposure which resulted in a negative frequency shift of about -500 Hz in 100 ppm of CO. In contrast, a second test where the air compressor was not used resulted in a positive frequency shifts of about 1.16 kHz in 126 ppm of CO. Here the authors claimed that the negative frequency shifts were due to the adsorption of CO on top of an already adsorbed layer of water from the humid air supplied by the air compressor. The frequency increase observed in the second test was a result of CO molecules directly

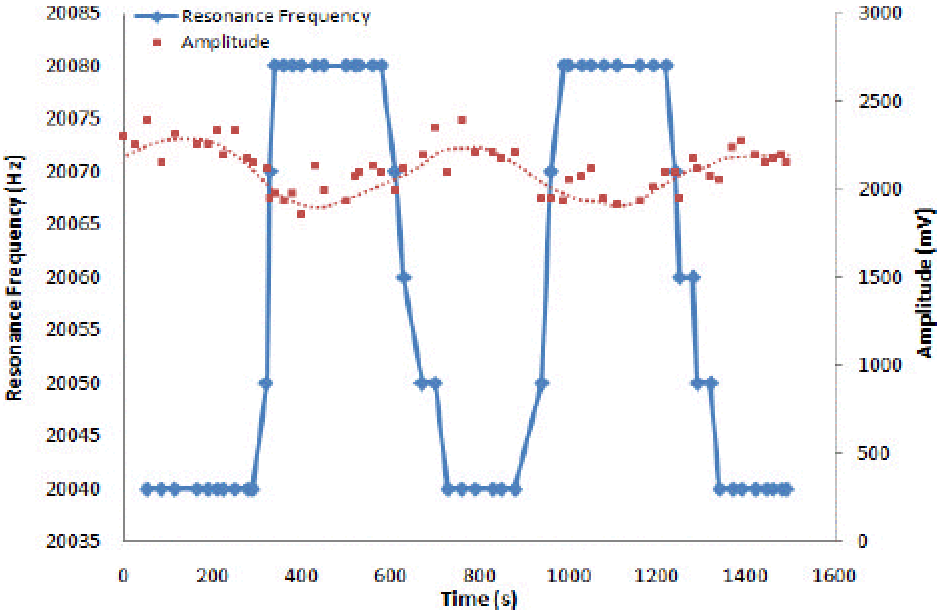

Figure 2.24: Resonance frequency [Hz] of ZnO nanorod coated commercial Si cantilever towards carbon dioxide (CO_2). Adapted from ref. [52] with permission. Copyright 2015, IEEE.

replacing previously adsorbed layer of water molecules on the surface of the ZnO resulting in a lighter mass. However, this conclusion is also questionable because the mass of a CO molecule is larger than the mass of a water molecule. The authors reported a mass sensitivity of 8.27 femtogram/Hz.

A final report from the same researchers, consisted of doping the ZnO nanorods with aluminum for the sensing of CO [54]. Surface doping of the ZnO nanorods (on the Si cantilever) was achieved by RF sputtering with an Al target at a high temperature (1500 K). The frequency response of the device to increasing concentrations of CO is shown in Figure 2.26. The introduction of CO, results in a positive frequency shift, similar to their previous result for ZnO nanorods in Figure 2.24. Interestingly, in this report the authors claimed that undoped ZnO showed no response to CO. Here the authors suggest the positive frequency shift is a result of the CO displacing adsorbed water molecules. While they acknowledge that CO is heavier than water, they suggest that less CO is adsorbed hence reducing the cantilever total mass to result in a frequency increase.

Regardless of what the specific sorption/sensing mechanism is, the above reports show

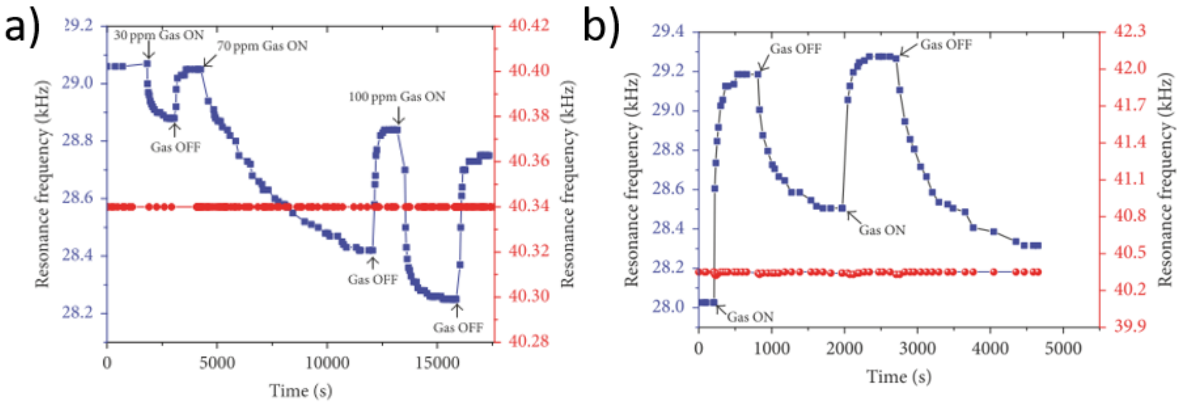

Figure 2.25: Resonance frequnecy [kHz] of ZnO nanorod coated commercial Si cantilever (blue) towards carbon monoxide (CO)using a) an air-compressor as the purge gas and, b) a second test without using the air compressor as the purge gas. Adapted from ref. [53]. Copyright 2017, Lia Aprilia , Ratno Nuryadi, Dwi Gustiono, Nurmahmudi, Arief Udhiarto, Djoko Hartanto, Brian Yuliarto, Makoto Hosoda, Yoichiro Neo, and Hidenori Mimura, used under a Creative Commons Attribution 4.0 International Licence (CC BY 4.0).

examples of both positive and negative frequency shifts for different analytes, which is certainly interesting behavior that should be studied further. To further understand these results, it is important to compare to other ZnO based gravimetric (frequency shift) sensors such as QCM. A QCM sensor consists of a piezoelectric quartz (SiO_2) crystal that resonates at its natural frequency when a voltage is applied. These devices can then be coated with various receptor materials to observe frequency shifts in the presence of chemical gases. While microcantilevers have micrometer length scales, QCMs have length scales of several millimeters.

Much early work involved synthesizing unique ZnO nanostructures to be drop casted on the surface of a QCM. This involved the formation of ZnO “nanotetrapods” [55], spherical nanoparticles [56] and nanowires [57], all for QCM based relative humidity sensing. Asar et al. compared sensors coated with nanoparticles with sensors coated with nanowires to observe the morphology dependent humidity sensing performance [58]. Figure 2.27a-b shows an SEM image of the prepared ZnO nanoparticles and nanowires, their corresponding frequency shift response to different levels of relative humidity is shown in Figure 2.27c-d. Larger shifts in resonant frequency were observed for the QCM coated with the nanopar-

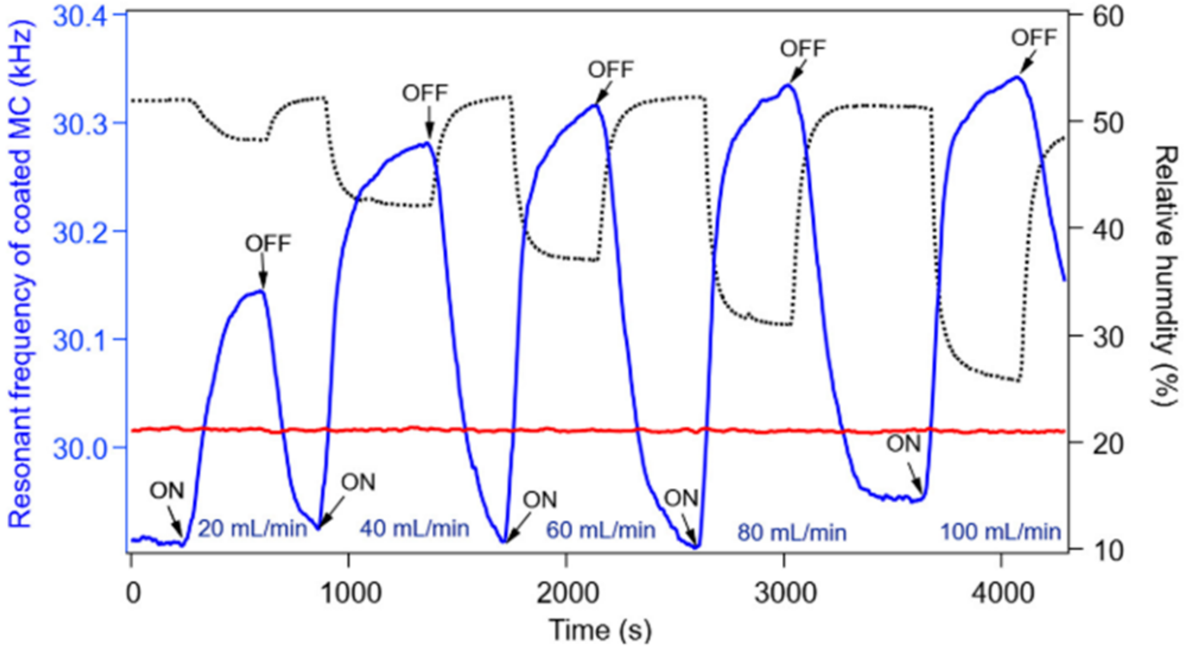

Figure 2.26: Resonance frequency [kHz] of alumunium doped ZnO nanorod coated commercial Si cantilever (blue) towards CO, compared to uncoated cantilever (red). The relative humidity of the test chamber is measured as well (dotted black line). Adapted from ref. [54]. Copyright 2020, Ratno Nuryadi, Lia Aprilia, Makoto Hosoda, Mohamad Abdul Barique, Arief Udhiarto, Djoko Hartanto, Muhammad Budi Setiawan, Yoichiro Neo and Hidenori Mimura, used under a Creative Common CC BY license.

ticles corresponding to a sensitivity of 1 Hz/%RH compared to the 0.4 Hz/%RH obtained for the nanowires. The authors attributed this difference to the higher available surface area for nanoparticles compared to nanowires.

It was observed that the response time of the sensors increased at higher relative humidity. The proposed mechanism for the phenomena is as follows. At low RH, water molecules are chemically adsorbed (chemisorbed) onto the ZnO surface by means of hydrogen bonds. At higher RH, once an initial monolayer of chemisorbed water is formed, additional layers of water form via van der waals dipole dipole interactions (physisorption), which will take a longer time to saturate all available sorption sites and come to equilibrium.

Xie et al. synthesized spherical ZnO nanoparticles 100 nm in size and drop casted them onto the surface of a QCM for the sensing of alcohols such methanol, ethanol and isopropanol [59]. At an analyte concentration of 300 ppm, the largest frequency shift was

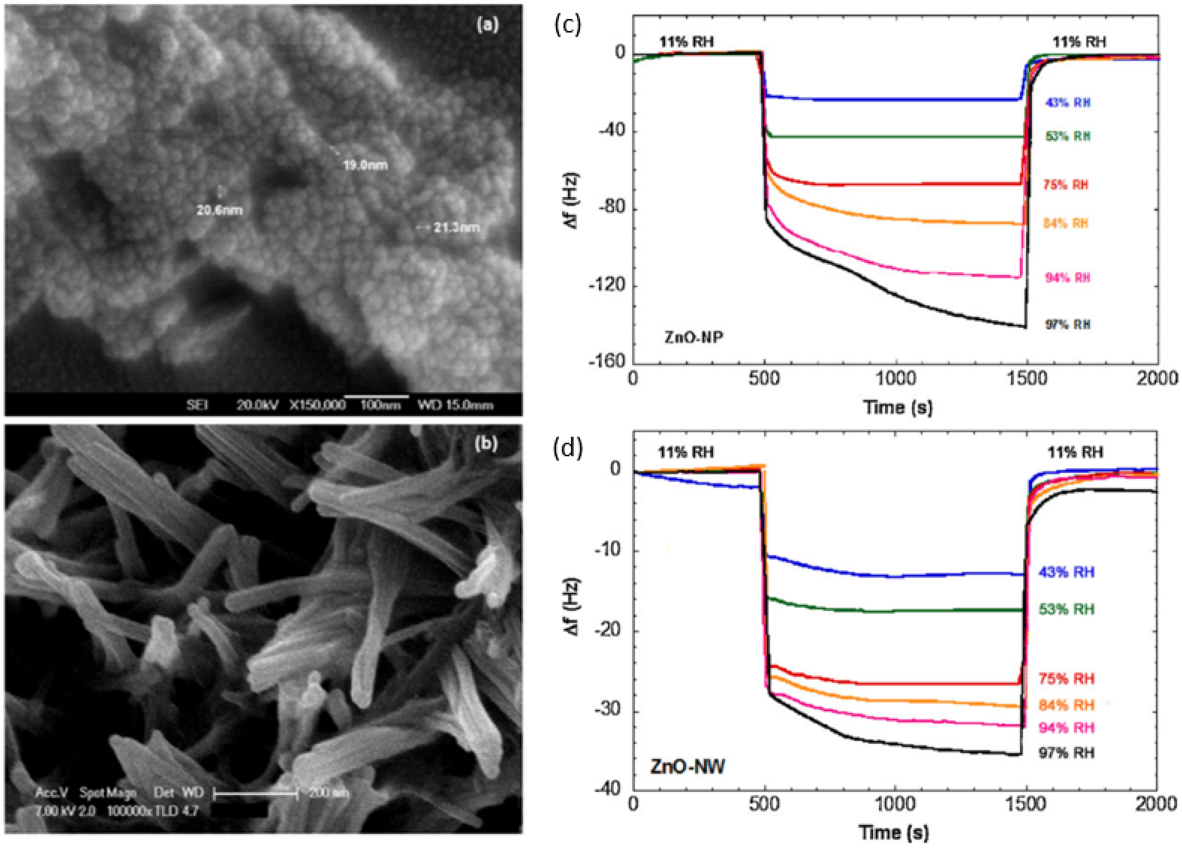

Figure 2.27: SEM image of a) ZnO nanoparticles and b) ZnO nanowires. Frequency shift response [Hz] of QCMs coated with c) ZnO nanoparticles and d) ZnO nanowires, at different %RH. Adapted from ref. [58] with permission. Copyright 2012, Elsevier B.V.

observed for methanol (-6.5 kHz), followed by ethanol (-4.2 kHz) and isopropanol (-1.4 kHz). This trend was attributed to the molecular size of the analytes, where methanol is smallest molecule and therefore more methanol molecules can adsorb onto the surface of ZnO in a compact arrangement. Isopropanol is a larger “bulkier” molecule and therefore is subject to stearic hinderance effects that limits the number of molecules that can adsorb onto the surface of ZnO.

Finally, Ozturk et al. [60] electrochemically deposited palladium (Pd) doped ZnO nanorods onto the surface of a QCM for the successful sensing of ethanol, methanol, isopropanol, xylene, toluene, acetone and chloroform. An illustration of the vertically aligned ZnO nanorods on the surface of the QCM is shown in Figure 2.28a. Figure 2.28b shows the obtained sensitivities to the analytes tested, for the ZnO nanorods with varied Pd doping levels. The lowest sensitivity was towards acetone, while the highest were obtained for xylene. The addition of Pd resulted in higher sensitivity attributed to the generation of more zinc or oxygen vacancies that contributed to chemisorption of the analyte.

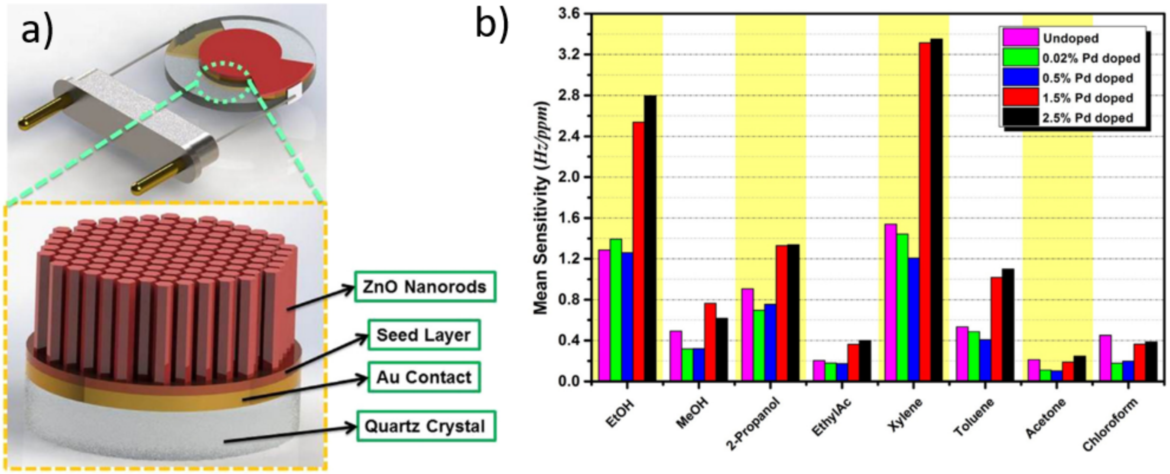

Figure 2.28: a)Illustration of alligned ZnO nanorod array grown on QCM device. b) Average sensitivity [Hz/ppm] of ZnO nanorod QCM (with varying amounts of Pd doping) towards a range of analyte vapors. Adapted from ref. [60] with permission. Copyright 2015, Elsevier B.V.

Table 2.1 summarizes all the ZnO dynamic sensors discussed in this section, both microcantilever and QCM based. A discussion on acoustic wave resonators was neglected in this section due to the slightly different sensing mechanism.

Table 2.1: Comparison of ZnO based resonant cantilever and QCM gas sensors.

Device ($L \times W \times T$)	ZnO Structure	Actuation	Readout	Analyte	Best Sensitivity	Ref.
Ni cantilever ($140\mu m \times 20\mu m \times 2\mu m$)	Nanorod/nanotube Hieght= 1 um Dia.= 100 nm	Electromagnetic (solenoid)	Laser Vibrometer	Diethylamine	$1.2\ \frac{m^{\circ}}{ppm}$	[48]
Si cantilever ($3mm \times 25\mu m \times 25\mu m$)	Nanorod Height = 1 um Dia.= 95 nm	Pieozoelectric	Piezoresistive	30-70% Relative Humidity	$2.5\ \frac{Hz}{\%RH}$	[49]
Si cantilever ($1mm \times 170\mu m \times 10\mu m$)	Chitosan coated ZnO nanorods	Thermal/Piezoresistive	Piezoresistive	30-70% Relative Humidity	$3.5\ \frac{Hz}{\%RH}$	[50]
Si cantilever ($1mm \times 170\mu m \times 12\mu m$)	APTES coated ZnO nanorods on Si nanopillars	Thermal/Piezoresistive	Piezoresistive	Nitrogen dioxide	$50\ \frac{Hz}{ppm}$	[51]
Si cantilever ($400\mu m \times 50\mu m \times 1\mu m$)	Nanorods	Piezoelectric	Piezoresistive	Carbon dioxide	$\Delta f = 40Hz$	[52]
Si cantilever ($400\mu m \times 50\mu m \times 1\mu m$)	Nanorods	Piezoelectric	Piezoresistive	Carbon monoxide	$8.27\ \frac{fg}{Hz} or\ 5\frac{Hz}{ppm}$	[53]
Si cantilever ($400\mu m \times 50\mu m \times 1\mu m$)	Al doped ZnO nanorods	Piezoelectric	Piezoresistive	Carbon dioxide	$7.57\ \frac{pg}{Hz}$	[54]
QCM	Nanotetrapods	-	-	Relative Humidity	$100\ \frac{Hz}{\%RH}$	[55]
QCM	Nanowire	-	-	Relative Humidity	$3\ \frac{Hz}{\%RH}$	[57]
QCM	Nanoparticle/Nanowire	-	-	Relative Humidity	$1\ \frac{Hz}{\%RH}$	[58]
QCM	Nanoparticles	-	-	Relative Humidity	$77\ \frac{Hz}{\%RH}$	[61]
QCM	Nanoparticles Dia. = 100 nm	-	-	Methanol	$21.6\frac{Hz}{ppm}$	[59]
QCM	Pd doped ZnO Nanorods	-	-	Xylene	$3.296\frac{Hz}{ppm}$	[60]

2.2 Nanomaterial Synthesis Methods

2.2.1 Atmospheric Pressure Spatial Atomic Layer Deposition

Atmospheric Pressure - Spatial Atomic Layer Deposition (AP-SALD) is a thin film deposition technique that has the main benefit of operating at atmospheric pressures (i.e.: open-air conditions) unlike conventional vacuum-based ALD. To understand the working principle behind AP-SALD, conventional ALD is first briefly introduced.

ALD, which is a type of CVD, is based on the use of self-limiting surface half reactions. [62] The process of thin film deposition by ALD occurs by the sequential introduction of precursor chemicals by an inert carrier gas (typically nitrogen, N_2 or argon, Ar) to the substrate surface, schematically illustrated in Figure 2.29. In Step 1, the first precursor ("Reactant A") is injected into the ultra high vacuum chamber and reacts with all available sites on the substrate surface. Excess unreacted precursor and by-products of the surface reactions in Step 1 are subsequently purged away with an inert gas in Step 2. Once the chamber has been evacuated, Step 3 consists of the injection of the second precursor ("Reactant B") into the chamber which reacts with the adsorbed layer of Reactant A to form a single monolayer of the desired binary compound. This is followed by Step 4, where similar to Step 2, unreacted precursor and by-products of the surface reactions are purged away. These 4 steps make up a single ALD "cycle", which is repeated until a desired film thickness is achieved (typically on the order of nanometers). The process described here consist of two precursors meant to form a binary film (A_xB_y), however additional precursors and steps can be added to create doped films or ternary ($A_xB_yC_z$) and quaternary films ($A_wB_xC_yD_z$).

The layer by layer technique is capable of depositing highly conformal, defect free films on surfaces with varying degrees of roughness and high aspect ratios. However, large scale production of ALD materials for commercial or industrial applications presents an inherent challenge. Layer by layer deposition to achieve a desired thickness can be time consuming. Furthermore, the process typically occurs in a vacuum environment and therefore the coated surface is limited to the size of the chamber. The deposition chamber must be pumped down (evacuation) to vacuum level pressures which can take a significant amount of time. Precursor dose times must be long enough to fill up the deposition chamber. Similarly, the purge times will also depend on the size of the chamber. Hence, the total time for thin film deposition is dependant on evacuation, dose, and purge times which can add up to a significant amount of wait time where no actual deposition is taking place. A challenge in scaling up ALD for high throughput commercial scale production of thin films

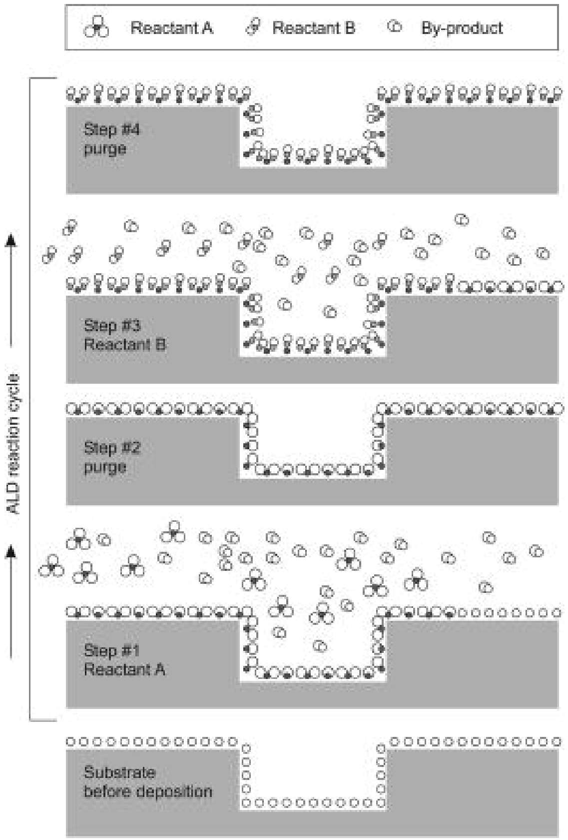

Figure 2.29: Schematic illustration of one ALD reaction cycle. Adapted from ref. [63] with permission. Copyright 2005, AIP Publishing.

is that larger deposition chambers will be required, which will lengthen the evacuation, dose and purge times [64]. Additionally, ALD of large substrate areas on the order of square feet is also limited by the size of the deposition chamber. These throughput and scalability issues have been combated by an ALD variant, AP-SALD.

AP-SALD, employs a unique gas injector ("Reactor Head") design that allows for flow of all precursor and purge gases simultaneously and continuously, though separated *spatially* as parallel flows (depicted in Figure 2.30a). The substrate is the physically moved between the precursor zones to reproduce the classical ALD cycle and half reactions, ensuring full conformal coverage.

The main difference between conventional ALD and spatial ALD is the way the precursors are delivered to the substrate. In conventional ALD the substrate position is fixed and the precursors are delivered to the entire substrate sequentially in time (Figure 2.31a).

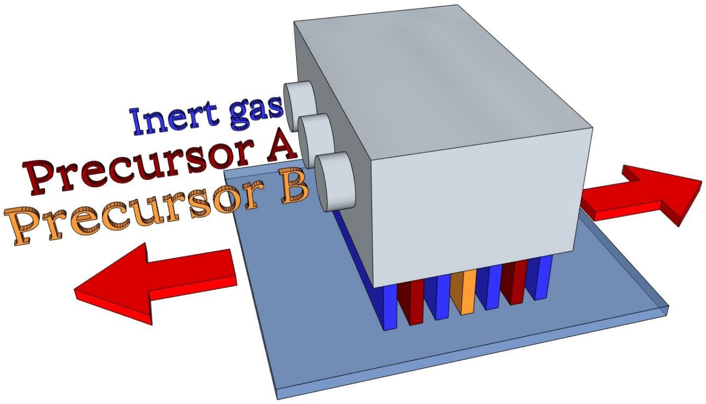

Figure 2.30: 3D illustration AP-SALD reactor head design wich allows for continuous flow of precursors separated by inert gas channels.

Whereas, in spatial ALD the substrate is moved between the precursor zones, which are continuously flowing (Figure 2.31b). By doing so, the substrate is still exposed sequentially to the different precursors thus reproducing the classical ALD cycle. The main advantage is that the net deposition rate is dependant on the substrate movement rather than the chamber evacuation and precursor dose times and thus, results in significantly quicker film growth compared to conventional ALD [64].

In an AP-SALD reactor several alternating channels of the precursors and inert gases can exist, thus a single pass of the substrate underneath the reactor can consist of more than 1 ALD cycle. For example, the configuration in Figure 2.30 above consist of 1.5 ALD cycles for a single pass through, or 2.5 ALD cycles for 1 complete AP-SALD oscillation. This approach allows for faster deposition rates than conventional ALD , as the growth rates become partially dependant on the oscillation speed and several ALD cycles can be completed in a single oscillation [65], as shown in Figure 2.31. Moreover, the elimination of lengthy vacuum pump down and purging steps, allows for the deposition of films in a shorter time span.

Furthermore, AP-SALD, as the name suggests, occurs in atmospheric pressures. In other words a vacuum chamber is not required and therefore the size of the substrates are not constrained. This makes AP-SALD compatible with high throughput commercial manufacturing techniques such as roll-to-roll processing. The use of a vacuum environment

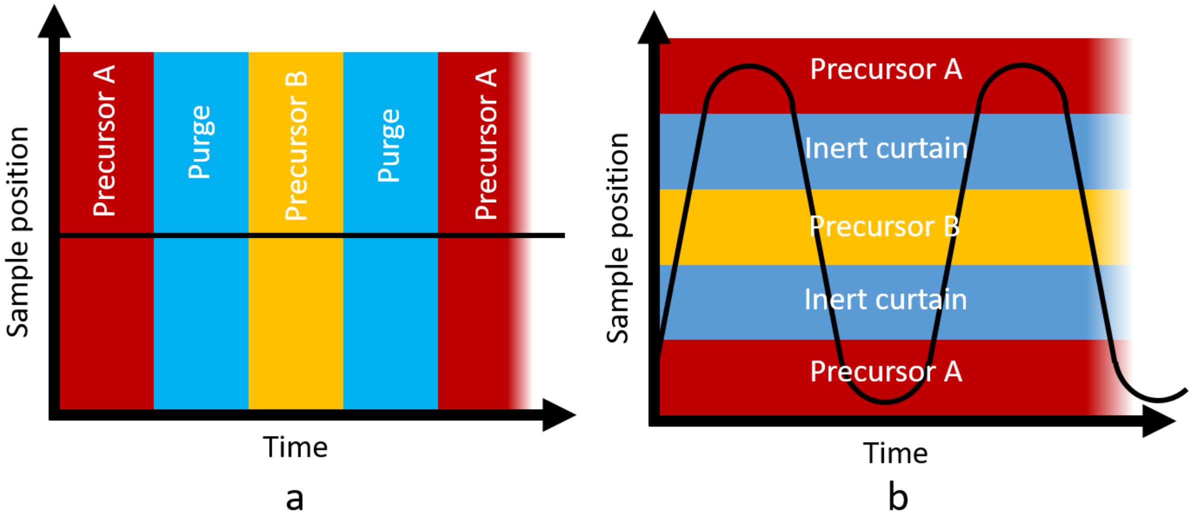

Figure 2.31: Schematic representation of conventional and spatial ALD processes as a function of substrate position (black line) and deposition time. The precursor exposures are represented by the coloured blocks. a) In conventional ALD, the substrate is at a fixed position throughout the deposition and is exposed to precursors sequentially in time. b) in spatial ALD, the substrate is moved between the different precursor zones, to reproduce the classical ALD cycle.

is avoided by the close proximity of the reactor head to the substrate. A small separation height/gap between the bottom of the reactor head and the substrate is required to maintain a "pseudo-vacuum" environment. It ensures that the substrate is only exposed to precursor from the channel directly above it and therefore maintains a true ALD process where only single monolayers of precursors are adsorbed. Should larger separation distances be used, the precursors will begin to mix and react before deposition on the substrate. This results in CVD like growth, where both precursors are introduced into a chamber at the same time. Due to the intermixing of the precursors, spatial-CVD (with larger separation distance) typically has higher growth rates than spatial-ALD [66].

Deposition by AP-SALD is affected by process parameters such as substrate movement speed, separation distance, substrate temperature, the flow rate per channel on the reactor head and the precursor concentration. If the substrate movement speed is too fast then the film coverage on the substrate will be poor as substrate exposure to the precursor is not sufficiently enough to react with all available surface sites [67].

Table 2.2: Selected reports on the deposition of Al_2O_3 by AP-SALD.

Precursors	Growth Rate (Å/cycle)	T (°C)	Application	Ref
TMA + Water	1.2	200	Thin Film Transistor	[70]
TMA + Water	1.2	200	Solar Cells	[71]
TMA + O_2 Plasma	1-2	70-200	Temperature sensitive substrates	[68, 69]
DMAI + Water	0.9-1.3	100-300	-	[72]

Table 2.3: Selected reports on the deposition ZnO by AP-SALD.

Precursors	Dopant	Growth Rate (Å/cycle)	T (°C)	Application	Ref
DEZ + Water	N (NH_3)	1.7	200	Thin Film Transistor	[70]
DEZ + Water	-	1.8	70-250	-	[73]
DEZ + Water	Al (TMA	2	200	-	[74]
DEZ + Water	Al(DMAI)	0.5-2	100-300	-	[72]
DEZ + Water	Mg ($Mg(CpEt)_2$	0.28	150	Solar Cells	[75]
DEZ + Water	In (TMIn)	1.8	200	-	[76]
DEZ + Water	S (H_2S)	0.7-1.5	100-200	Solar Cells	[77]

Till date, the two most common and well studied films deposited by AP-SALD have been Aluminum Oxide (Al_2O_3) and Zinc Oxide (ZnO). Table 2.2 summarizes selected reports on the deposition of Al_2O_3 by AP-SALD. tri-methyl-aluminum (TMA) and dimethyaluminum isopropoxide (DMAI) have been used for the aluminum precursor while water and oxygen plasma have been used for the oxygen precursor. Growth rates of 0.9-2 Å/cycle have been reported with deposition temperatures as low as 70°C up to to 300°C. The low temperature depositions are particularly useful for deposition on temperature sensitive polymer substrates [68, 69].

Table 2.3 summarizes select reports on the deposition of ZnO films by AP-SALD. Diethyl zinc (DEZ) and water were used as the Zn and oxygen precursors, respectively. Depending on its intended use, it is often advantageous to dope the ZnO to enhance its electrical conductivity (carrier mobilities) and/or alter its optical bandgap for improved light absorption. Growth rates of 0.28-2 Å/cycle have been reported with deposition temperatures of 70°C to 300°C.

Besides Al_2O_3 and ZnO, other binary oxide films such as copper (I) oxide (Cu_2O),

Table 2.4: Selected reports on other binary metal oxide films deposited by AP-SALD.

Material	Precursors	Growth Rate (Å/cycle)	T (°C)	Application	Ref
Cu_2O	Cupraselect	0.06	150-225	Solar Cells	[78]
TiO_2	$TiCl_4$	1.5	100-350	Solar Cells	[79]
SnO_2	TDMASn	1.5	80	Solar Cells	[80]

titanium dioxide (TiO_2) and tin oxide (SnO_2) have been deposited by AP-SALD. The metal precursors, reported growth rates and deposition temperatures used for these films are listed in Table 2.4.

The reports discussed above show the versatility of AP-SALD to deposit a variety of metal oxide thin films at relatively quick deposition rates and at low deposition temperatures without the need of a vacuum environment. The electronic, optical and physical properties of these films can be tuned by varying the deposition temperature, precursor partial pressure and introducing dopants). These films have been utilized in variety of applications such as solar cells [79], transparent conductors [81], light emitting diodes (LEDs) [82] and metal insulator metal (MIM) diodes [83]. Till date, a metal oxide film deposited by AP-SALD has not been used in gas sensing applications.

While it is clear that that there are many advantages to AP-SALD, it is important to note the current challenges and limitations with the technique. Thin films deposited by AP-SALD have primarily consisted of metal oxides. This is because the “open-air” or atmospheric deposition of thin films are prone to an increased incorporation of oxygen from the atmosphere [83]. This may have negative effect in the optical or electrical properties of the film. The deposition of non-oxide films by AP-SALD such as silver has been demonstrated [84] but introduces increased complexity such as the inclusion of plasma enhanced reactor. Unlocking the depositions of other non-oxide films by AP-SALD is an ongoing research effort.

Additionally, “open-air” or atmospheric deposition with highly pyrophoric precursors such as TMA are challenging to reproduce [85]. This is because ambient oxygen and variable humidity can act as an additional oxygen source and unintentionally increase the growth of the film. Furthermore, the reactor head flow channels are prone to blockages as they are directly exposed to the atmosphere and allow for deposition to occur in the channel itself. At the lab scale, further reproducibility issues arise in manual setting of the distance between the reactor head and the substrate. An unintentional non uniform spacing can lead to an over mixing of the precursors resulting in higher growth rates in certain areas of the deposition and a non-uniformity in film thickness. Lastly, precursors that have been successfully used for conventional vacuum based ALD may not necessarily translate well for use with AP-SALD due to challenges in obtaining the vapor phase of a precursor at atmospheric pressure. In these cases, additional techniques such as heating or nebulization [86] are required which increase the complexity of the system.

2.2.2 Femtosecond Laser Treatment of 2D Materials

Two-dimensional materials such as graphene, tungsten disulfide(WS_2) and molybdenum disulfide(MoS_2) have become increasingly popular over the last decade due to their excellent electrical, chemical, optical and mechanical properties. These materials typically have a flat 2D flake-like structure and have been incorporated into a variety of applications, such as bioimaging, cancer therapy, catalysis, optoelectronics, energy storage and all sorts of sensor devices [87–97]. This extreme versatility arises from the many different synthesis methods available to create these materials and the ability to easily optimize and tailor their properties for a specific application. One such synthesis method is a femtosecond laser irradiation technique reported by Ibrahim et al. in 2016 [98].

The technique consists of using high intensity femtosecond laser pulses to irradiate 2D flakes in solution. The pulses results in a coulombic explosion effect that break down the flakes into smaller flakes. The new smaller flakes have many unsatisfied edges that can form bonds with other atoms in the solution such as solvent atoms, added dopants and other freshly dissociated flakes. This phenomenon is illustrated in Figure 2.32 for the femtosecond irradiation of aqueous graphene oxide solution. When the laser focal point is placed at the air-solution interface, carboxyl and in-plane hydroxyl functional groups are removed from the flakes while the solvent (water) is evaporated, simultaneously. This results in a chemical reduction of the graphene oxide to reduced graphene oxide (rGO) as well as a reduction of the solution volume to form a high viscosity rGO gel (named "femtogel"). Varying the laser pulse energy, focal length and treatment time resulted in femtogels with different properties.

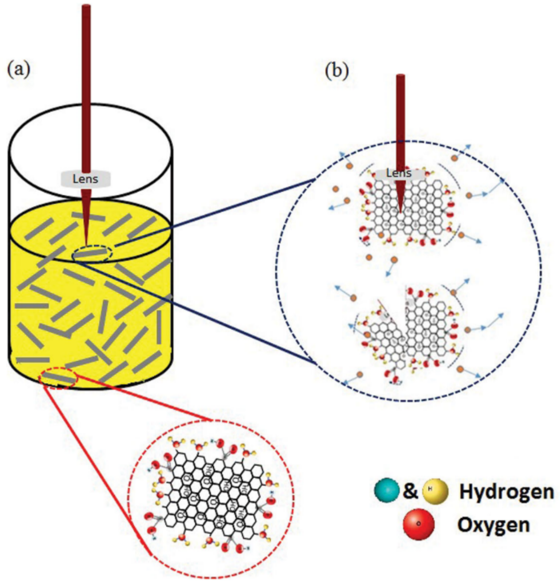

Figure 2.32: Schematic illustration of femtosecond laser treatment of graphene oxide sheets in solution, resulting in cleavage of flakes as well as edge functionalization with solvent atoms. Adapted from ref. [98] with permission. Copyright 2016, WILEY-VCH Verlag GmbH & Co. KGaA, Weinheim.

The femtosecond laser treatment technique has been used to synthesize rGO femtogels for highly responsive photodetectors [99], as well as boron nitride doped rGO gels with high mobilities approaching that of pristine graphene [100]. In 2018, the technique was used to simultaneously synthesize and functionalize nanoparticles of molybdenum disulfide, tungsten disulfide and boron nitride [101]. The laser reduces the size of the flakes from micrometers to nanometers. At the same time, the solvent molecules are dissociated and bond to the edges of the nanoparticles. In that work, a solvent mixture of water and ethanol was used to functionalize the 2D nanoparticles with carbon and oxygen groups as illustrated in Figure 2.33. Functionalization of the particles with the solvent atoms changed the optical properties of the materials with the introduction of new absorption and photoluminescence peaks.

The unique advantage of the femtosecond laser treatment technique is the ability to

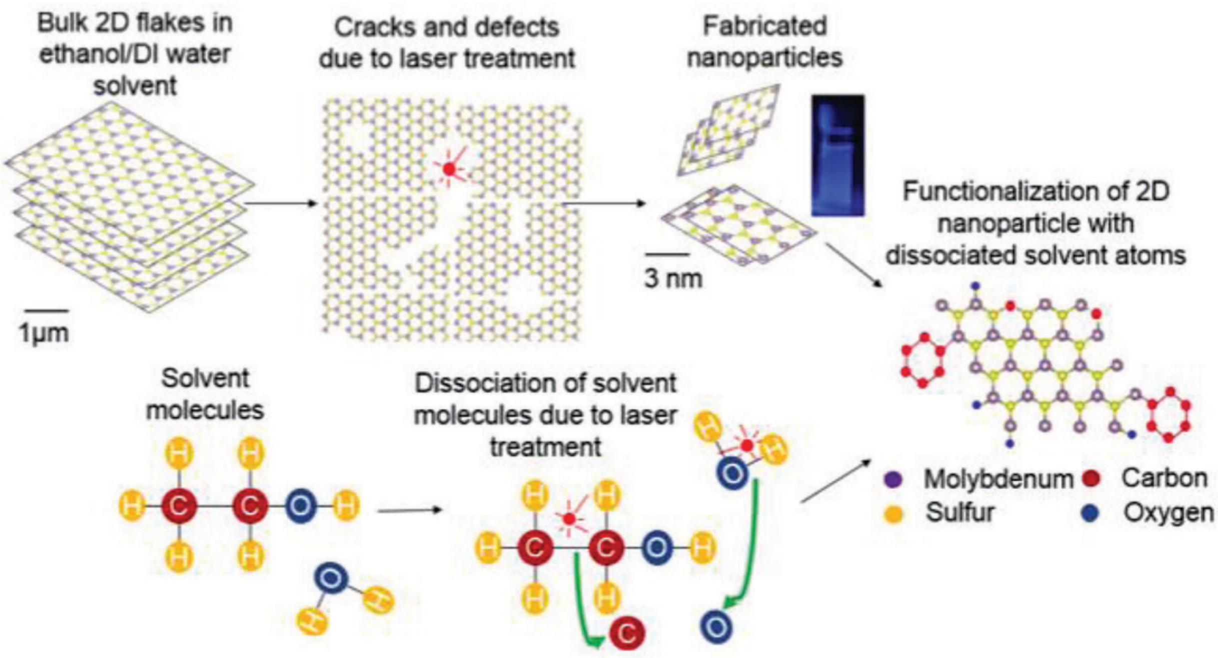

Figure 2.33: Laser treatment mechanism of molybdenum disulfide flakes in an ethanol-water solvent which simultaneously reduced the size of the flakes and functionalizes the edges with carbon and oxygen based groups. Adapted from ref. [101] with permission. Copyright 2018, WILEY-VCH Verlag GmbH & Co. KGaA, Weinheim.

synthesize highly functionalized 2D nanoparticles by choice of solvent and varying the laser treatment parameters. Thus, the technique can be used to tailor 2D materials for chemical gas sensing. In this work, functionalized 2D materials were used as the receptor material in static MEMS sensors (described in Chapter 5 and Chapter 7).

2.3 Reflectance Spectroscopy

2.3.1 Principle of Operation

In reflectance spectroscopy, a broadband light source and optical fiber are used to illuminate the sample (thin film) with unpolarized light (UV-Visible-Infrared). Reflected light is collected by a fiber optic reflectance probe and is detected by the spectrometer, as depicted in Figure 2.34a. The light is directed at a normal angle of incidence to the sample and is reflected back at the same angle [102].

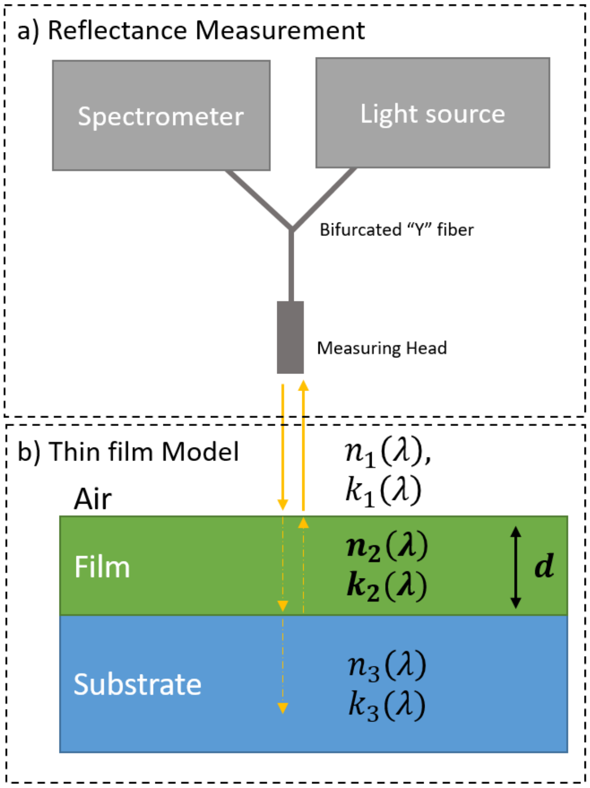

Figure 2.34: a)Schematic of reflectance measurement setup consisting of spectrometer, light source and bifurcated “Y” shaped fiber to illuminate sample and collect reflected intensity. b) Reflectance model of a single thin film on a substrate.

2.3.2 Reflectance Models

Fresnel Reflectance Model

To determine the film properties, a modelled reflectance spectrum must be fitted to the measured spectrum. The Fresnel reflectance model describes the interaction of light or electromagnetic radiation incident on an interface between different optical media [103]. Figure 2.34b depicts a three-layer model corresponding to the reflectance of a single thin film. The light is incident at the air-film interface, partially reflects and partially transmits through the film to the film-substrate interface where further reflection and transmission take place. The final reflected intensity is a combination of the individual reflected light intensities. Here it is assumed that the substrate thickness is sufficiently large that backside reflections do not occur.

The measured reflectance spectra are dependant on the complex refractive indices $\hat{n}$ of each layer (comprised of refractive index n and extinction coefficient k), as well as the thickness d of the thin film (Equation 2.10-2.12).

$$n_1 = 1, \quad k_1 = 0 \tag{2.10}$$

$$\hat{n}_2 \; (\lambda) = n_2 (\lambda) - ik_2 (\lambda) \tag{2.11}$$

$$\hat{n}_3 (\lambda) = n_3 (\lambda) - ik_3 (\lambda) \tag{2.12}$$

The refractive index and extinction coefficient of air are 1 and 0 respectively (Equation 2.10), while the values for substrates ($\hat{n}_3$) such as silicon, silicon dioxide and glass are known (Equation 2.12). The Fresnel reflection coefficients represent the reflections that occur at the air-film ($\hat{r}_{12}$, Equation 2.13) and film-substrate ($\hat{r}_{23}$, Equation 2.14) interface. The phase factor (β, Equation 2.15) accounts for the change in phase of the light wave propagating through the film medium and is dependent on its thickness.

$$\hat{r}_{12} (\lambda) = \frac{\hat{n}_2 - n_1}{\hat{n}_2 + n_1} \tag{2.13}$$

$$\hat{r}_{23} (\lambda) = \frac{\hat{n}_3 - \hat{n}_2}{\hat{n}_3 + \hat{n}_2} \tag{2.14}$$

$$\beta (\lambda) = \frac{4\pi \hat{n}_2 d}{\lambda} \tag{2.15}$$

The reflectivity $\hat{r}$, of the three-layer system is calculated and subsequently squared to obtain the reflectance spectrum as a function of wavelength ($R(\lambda)$, Equation 2.16). The Fresnel reflectance equations can be extended to thin film stacks with multiple thin films of varying thicknesses. In those cases, calculations are made easier by utilizing a transfer matrix formulism.

$$R (\lambda) = \hat{r}^2 = \left| \frac{\hat{r}_{12} (\lambda) + \hat{r}_{23} (\lambda) e^{-i\beta}}{1 + \hat{r}_{12} (\lambda) \hat{r}_{23} (\lambda) e^{-i\beta}} \right|^2 \tag{2.16}$$

The optical parameters of the thin film, refractive index n, and extinction coefficient k, are unknown values in the presented Fresnel equations above. Empirical formulas have been developed for the determination of these values based on a set of fitting parameters. Along with the thickness d, the parameters are adjusted by the fitting algorithm to closely match the calculated and measured reflectance spectra. In literature several competing empirical formulas have been presented for materials such as insulators, semiconductors and conductors. Three well known models are presented below. The Cauchy model (Equation 2.17-2.18) developed by the mathematician A.L. Cauchy is often used for amorphous insulator materials such as aluminum oxide [102, 104].

$$n\left(\lambda\right) = A + \frac{B}{\lambda^2} + \frac{C}{\lambda^4} \tag{2.17}$$

$$k\left(\lambda\right) = 0 \tag{2.18}$$

The extinction coefficient k, also called attenuation coefficient relates to the damping of an electromagnetic wave as it propagates through a material. It describes the absorption of light by the material. Insulators probed by UV-Visible light are considered to be weakly absorbing films and therefore the extinction coefficient can be set to 0. Fitting reflectance spectra of insulator materials will have 4 fitting parameters (A, B, C and thickness d).

The Tauc-Lorentz formula is used for the reflectance fitting of semiconductor materials [105, 106]. Here, the dielectric constants, which are closely related to the optical constants, are modelled and fitted as well. The model is made complex by use of a Kramers-Kronig integral that obtains the real dielectric constant (ε_1) from the imaginary component (ε_2). For amorphous semiconductors the Tauc-Lorentz equations are presented below (Equation 2.19-2.20). A one, two or three term expansion ($i = 1, 2, 3$) of the equation results in a total of 6, 10 or 14 fitting parameters for improved reflectance fitting accuracy.

$$\varepsilon_2\left(E\right) = 2nk = \sum_{i=1}^{j=1,2,3} \frac{A_i C_i E_{0i}\left(E - E_{gi}\right)^2}{\left(E^2 - E_{0i}^2\right)^2 + C_i^2 E^2} \bullet \frac{1}{E}\ if\ E > E_g,\ or = 0\ if\ E < E_g \tag{2.19}$$

$$\varepsilon_1\left(E\right) = n^2 - k^2 = \varepsilon_1\left(\infty\right) + \frac{2}{\pi} PV \int_0^\infty s \frac{\varepsilon_2\left(s\right)}{s^2 - E^2} ds \tag{2.20}$$

For crystalline semiconductors, the imaginary dielectric constant (ε_2) is simplified and can result in the use of 5,8 or 11 fitting parameters (Equation 2.21).

$$\varepsilon_2\left(E\right) = 2nk = \sum_{i=1}^{j=1,2,3} \frac{A_i}{C_i + \left(E - E_{0i}\right)^2} \tag{2.21}$$

The free conduction of electrons in a material (conductors) can be parametrized by the combination of one Drude and two Lorentz oscillators [104]. The fit parameter: ω_{pu} is the Drude plasma energy, Γ_D is the Drude damping factor while the Lorentz oscillators are located at ω_{0j}, with strength f_j, and damping factor γ_j. Here up to 7 or 10 fitting parameters can be utilized to obtain fits for a reflectance spectrum (Equation 2.22).

$$\varepsilon\ \left(\omega\right) = n^2 = \quad \varepsilon\left(\infty\right) - \frac{\omega_{pu}^2}{\omega^2 - i\omega\Gamma_D} + \sum_{j=1}^{2} \frac{f_j\omega_{0j}^2}{\omega_{0j}^2 - \omega^2 + i\omega\gamma_j} \tag{2.22}$$

Virtual Interface Model

The Fresnel reflectance model presented in the previous section requires prior knowledge of the substrate optical properties (refractive index n, and extinction coefficient k). Breiland and Killeen reported an in-situ reflectance model, named the Virtual Interface Method, that does not require prior knowledge of the underling film/substrate [107]. In the VI method, the reflectance intensity at a single wavelength is observed as a function of time, $R(t)$. This is in contrast to the Fresnel model where the whole reflectance spectrum, $R\left(\lambda\right)$, is observed at a single point in time.

The observable reflectance intensity (at a given wavelength) as a function of time is modelled by the following Equation 2.23.

$$R\left(t\right) = \frac{R_\infty - 2\sqrt{R_\infty R_i}e^{-\gamma t}\cos\left(\delta t - \sigma - \varphi\right) + R_i e^{-2\gamma t}}{1 - 2\sqrt{R_\infty R_i}e^{-\gamma t}\cos\left(\delta t - \sigma + \varphi\right) + R_\infty R_i e^{-2\gamma t}} \tag{2.23}$$

Where the following definitions are used (Equation 2.24-2.29):

$$R_\infty = \left|r_\infty\right|^2 = \frac{\left(1-n\right)^2 + k^2}{\left(1+n\right)^2 + k^2} \tag{2.24}$$

$$\varphi = \tan^{-1}\left(\frac{2k}{n^2 + k^2 - 1}\right) \tag{2.25}$$

$$R_i = |r_i|^2 = \frac{(n - n_s)^2 + (k - k_s)}{(n + n_s)^2 + (k + k_s)^2} \tag{2.26}$$

$$\sigma = \tan^{-1}\left(\frac{2(nk_s - n_s k}{n^2 - n_s^2 + k^2 - k_s^2}\right) \tag{2.27}$$

$$\gamma = \frac{4\pi k G}{\lambda} \tag{2.28}$$

$$\delta = \frac{4\pi n G}{\lambda} \tag{2.29}$$

Where R_∞ is the reflectance of a infinitely thick film, dependent on n and k of the film. R_i is the reflectance of the underlying film/substrate dependant on n and k for the film and substrate (n_s and k_s). G is the growth rate of the film in nm/s. When Equation 2.24-2.29 are substituted into Equation 2.23, $R(t)$ becomes dependant on n, k, G, R_i and σ. Of the five unknowns, the first three parameters are of interest while the last two represent the optical response of the underlying layer but can be treated as fitting parameters to obtain the first three parameters. This avoids the need to know the underlying layer's optical properties.

As evident by the cosine and exponential terms in Equation 2.23, the $R(t)$ produces a damped oscillatory pattern shown in Figure 2.35. Characteristic features of this oscillatory pattern can be used as estimators for the five unknowns.

First an estimate for R_∞ (Equation 2.30), is obtained as the mean value of $R(t)$. The frequency, δ (Equation 2.31), is obtained by the half period of the oscillation, T. The decay constant, γ (Equation 2.32), is determined by the amplitudes of the first two maxima and the time between them. Equation 2.33-2.35 can then be used to estimate G, n and k. Estimators for σ and R_i are obtained from the initial reflectance, $R(t = 0)$ and its derivative $R'(t = 0)$ (Equation 2.36-2.37).

$$R_\infty \cong \langle R(t) \rangle_t \tag{2.30}$$

$$\delta \cong \frac{\pi}{T} \tag{2.31}$$

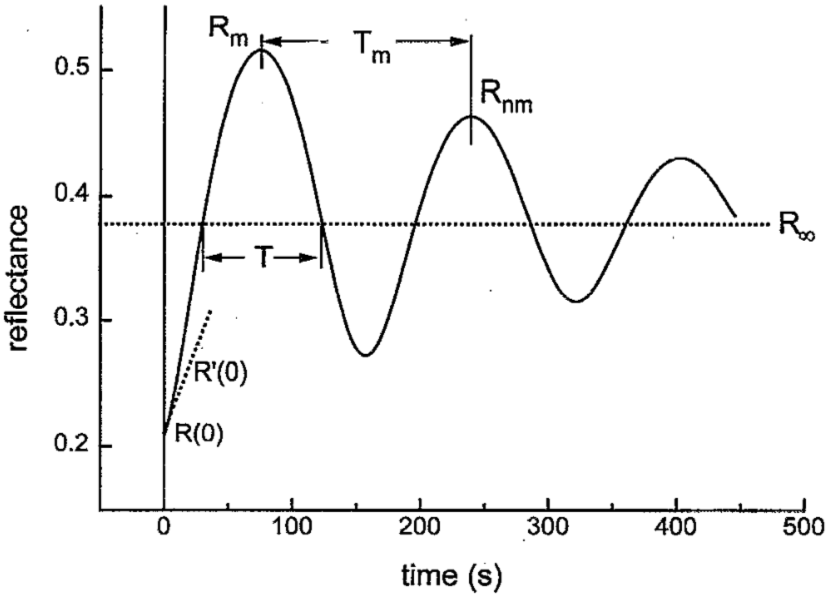

Figure 2.35: Example reflectance-time, $R(t)$, measurement from which quantities R_m, R_{nm}, T, T_m, $R(t=0)$, and $R'(t=0)$ can be extracted to obtain initial estimates for G, n, k, σ, and R_i. Adapted from ref. [107] with permission. Copyright 1995, AIP Publishing.

$$\gamma \cong \frac{\ln\left(\frac{R_m}{R_{nm}}\right)}{T_m} \tag{2.32}$$

$$G \cong \frac{\lambda\delta}{4\pi}\left[\frac{1+R_\infty}{1-R_\infty} - \sqrt{\left(\frac{1+R_\infty}{1-R_\infty}\right)^2 - \frac{\gamma^2+\delta^2}{\delta^2}}\right] \tag{2.33}$$

$$n \cong \frac{\delta}{G} \tag{2.34}$$

$$k \cong \frac{\gamma}{G} \tag{2.35}$$

$$\sigma \cong \tan^{-1}\left(\frac{-\frac{R'(0)}{\delta}}{R_\infty - R\,(0)}\right) \tag{2.36}$$

$$R_i = \frac{(R_\infty - R(0))^2 + \left(\frac{R'(0)}{\delta}\right)^2}{4R_\infty(1-R_\infty)^2} \tag{2.37}$$

The estimators are used as initial values in a nonlinear-least square fitting method such as Levengberg-Marquardt algorithm to obtain the true value of the parameters of interest n, k and G of the thin film. It is important to note here that at least two oscillation amplitudes must be measured (to obtain an estimate for γ) before the VI method can be used accurately. This method has been widely used to extract the growth rate of thin films deposited by CVD or molecular beam epitaxy (MBE) methods, particularly when the optical properties of the film or substrate are not known beforehand.

2.3.3 Review of Relevant Applications

The most common application of reflectance spectroscopy is for the determination of thin film thickness. This was first reported by Larson et al. [103] in 1973, who utilized fiber coupled reflectometry for the thickness determination of uranium oxide (UO_2) thin films. The first implementation of in-situ spectral reflectometry was by Killeen and Brieland [108], who monitored the real time growth of AlAs, GaAs and AlGaAs films grown by metal organic chemical vapor deposition (MOCVD). However, in-situ reflectance spectroscopy was never practically adopted for widespread use in conventional ALD and other thin film deposition systems. This was because spectroscopic ellipsometry was preferred due to its ability to measure more data than reflectance spectroscopy which allows for the determination of film properties and thickness with higher accuracy. However, it requires a unique spatial arrangement of the light source and detector (at an angle) and the data analysis also involves more complexity than the data analysis of reflectance spectroscopy.

Despite its lack of use in vacuum based ALD systems, the use of optical fibers to measure and collect the light as well as its simplicity makes reflectance spectroscopy suitable for implementation in AP-SALD systems. This was done by Yersak et al. [109] in 2013 and is till date, the lone report on the in-situ reflectance spectroscopy characterization of AP-SALD films. Al_2O_3 was deposited by AP-SALD on a continuous web of polyethylene napththalate (PEN) at 100°C, depicted in Figure 2.36a. A Filmetrics F20-UV reflectometry system was used to measure reflectance spectra of the growing film. The optical fiber was placed over the web and focused on the matte black web roller that minimized backside reflections. Proprietary Filmetrics analysis software was used to fit the measured spectra and obtain the thickness of the growing film shown in Figure 2.36b. Growth rates of 0.11-0.13 nm/cycle were determined by using the Cauchy model (described in Chapter 2.3.2) for insulator materials. The analysis software attempts to fit the model to the measured spectra requiring an initial guess for the refractive index and returns a goodness of fit (GOF) value. Obtained thickness values with $GOF < 0.98$ were omitted from the growth rate per cycle determination which was particularly evident at low cycle numbers. Additionally, the authors were able to observe a nucleation period of 48 ALD cycles before film growth occurred which follows previous reports on the growth of Al_2O_3.

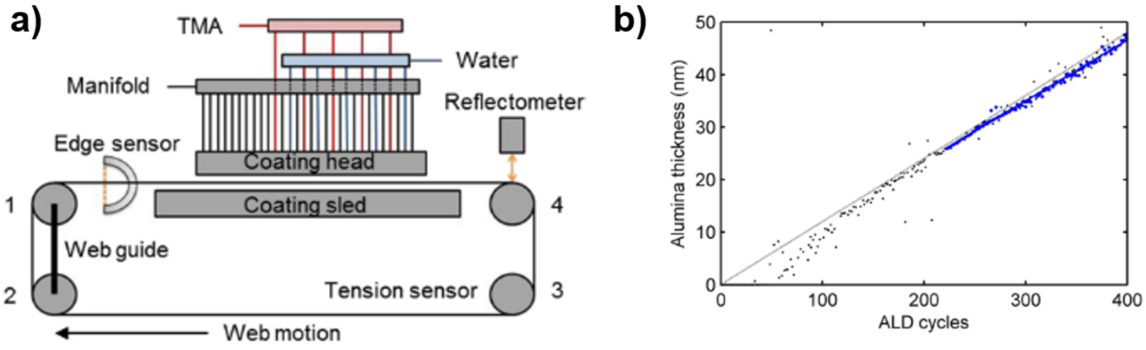

Figure 2.36: a)implementation of in-situ reflectometry on a continuous web coater AP-SALD system. b) thickness of Al_2O_3 deposited with the continuous web coater, determined by in-situ reflectometry. Adapted from ref. [109] with permission. Copyright 2014, AIP Publishing.

The authors were able to demonstrate the use of in situ reflectance spectroscopy to explore the immediate effect of process parameters on the growth. In a single deposition of more than 1600 ALD cycles, the authors varied the TMA bubbling rate from 0.025 to 0.25 slpm (standard liter per minute) and observed its real time effect on the growth rate per cycle, shown as the slopes in Figure 2.37. A second experiment observed the effect of web speed on the growth rate, where web speeds of 0.5, 1.0 and 2.0 m/s yielded growth rates of 0.14, 0.12 and 0.08 nm/cycle. The web speed is inversely proportional to the residence time of the precursors on the substrate and therefore at slower web speeds larger growth rates are observed due to inefficient purging and mixing of the precursors. The authors have demonstrated the ability of in-situ reflectometry to monitor and control the growth process in AP-SALD systems. It is important to note that the propriety analysis software used here was provided by the vendor (Filmetrics) and is only capable of determining thickness from the measured reflectance spectra. As evidenced by this article, the implementation of in-situ reflectance spectroscopy with AP-SALD is achievable.

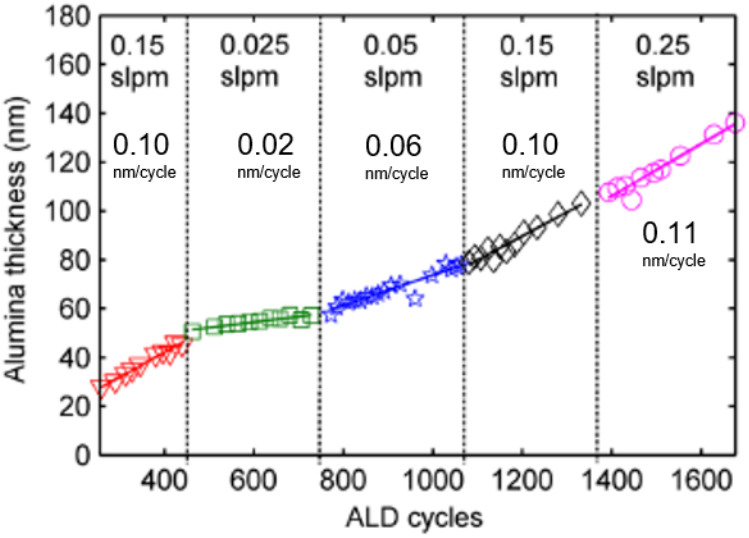

Figure 2.37: In-situ reflectometry determination of growth rate per cycle [nm/cycle] as the precursor bubbling rate is varied. Adapted from ref. [109] with permission. Copyright 2014, AIP Publishing.

A unique application of reflectance spectroscopy relevant to gas sensor materials was reported by Degler et al. [110]. Operando (In operation) UV/VIS reflectance spectroscopy was used to monitor tin oxide (SnO_2) based chemiresistive gas sensors as they were exposed to various gases. The SnO_2 powder was synthesized using a ball milling method, mixed with a solvent and then drop casted as a thick film on an interdigitated platinum electrode substrate. The sensor was placed in a test chamber with a quartz window which allowed for the measurement of the reflectance spectra (wavelength range of 300-1100 nm). Reflectance spectra (shown in Figure 2.38) were recorded for the sensor in different atmospheres such as dry air, dry nitrogen, 300 ppm of CO in dry air, 300 ppm of CO in dry nitrogen and 3000 ppm of O_2 in dry nitrogen. For all experiments, the sensor was heated up to 300°C.

As can be seen from the figure, a reduction of the reflectance intensity is observed in different atmospheres, where the largest reduction was obtained in 300 ppm of CO in dry nitrogen (green). The decrease in the reflectance intensity was attributed to increased light absorption of the sample and not a change in film thickness. The increased absorption arises from the chemical reduction of the SnO_2 grains by the gas and the formation of oxygen

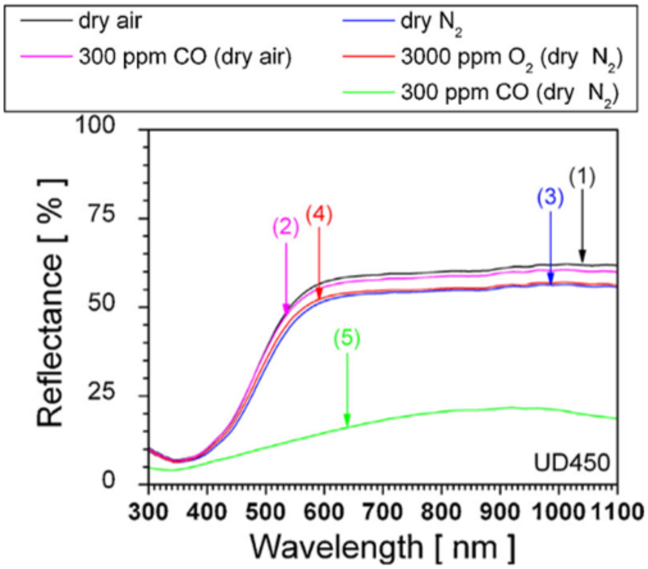

Figure 2.38: Reflectance spectra of SnO_2films (heated at 300°C), in different atmospheres: dry air (black), dry nitrogen (blue), 300 ppm CO in dry air (pink), 3000 ppm O_2in dry nitrogen (red) and 300 ppm of CO in dry nitrogen (green). Adapted from ref. [110] with permission. Copyright 2015, Elsevier B.V.

vacancies. The reflectance for CO in dry oxygen did not decrease as much as it did for CO in dry nitrogen, due to the quick chemical re-oxidation of SnO_2 in an oxygen abundant atmosphere.

A similar study was done by Elger et al. [111]. who measured the reflectance spectra of SnO_2 chemiresistive gas sensors in ethanol gas environments. The sensor was placed in a test chamber with multiple windows for the simultaneous measurement of FTIR, Raman and UV-vis reflectance spectra. Measurements were done at a temperature of 325°C. Figure 2.39 shows the obtained reflectance spectra (250 to 550 nm) of the SnO_2 sensor exposed in sequence to air, 250 ppm ethanol in air, purge nitrogen, ethanol in nitrogen and pure nitrogen. Exposure to ethanol gas resulted in a decrease in the reflectance intensity, where the large decrease in intensity was obtained in the absence of oxygen (pure nitrogen). This behavior was similar to the results obtained in the previous study for SnO_2 exposure to CO gas. Similarly, the authors here, attributed the change in reflectance intensity to increased by the same due to an increased generation of oxygen vacancies from chemical reduction of SnO_2. Interestingly, upon switching to pure nitrogen flow, the reflectance intensity increases as the sample reoxidizes (chemically)

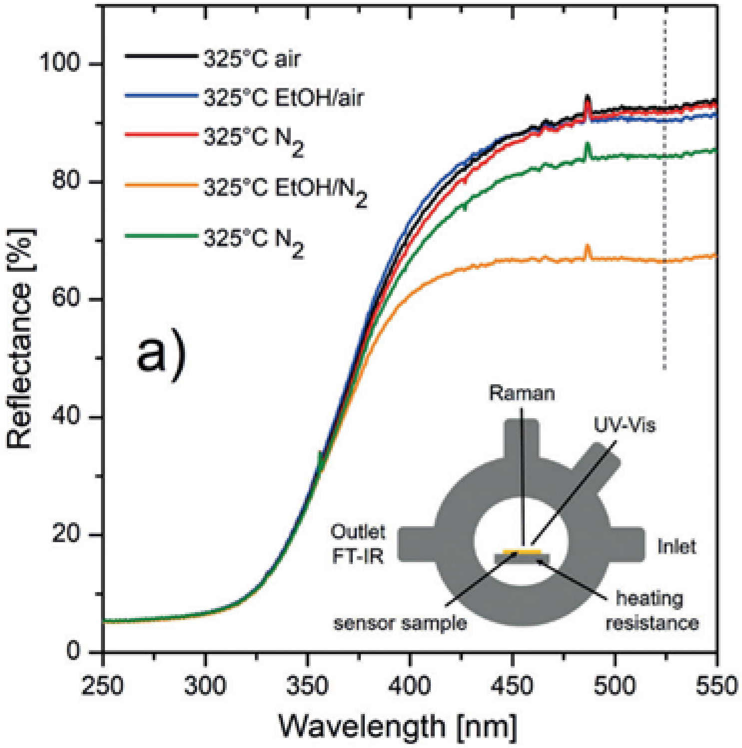

Figure 2.39: Reflectance spectra of SnO_2 film (heated at 325°C) exposed to a sequence of gases: air, ethanol in air, nitrogen, ethanol in nitrogen and pure nitrogen. The inset shows the characterization setup. Adapted from ref. [111] with permission. Copyright 2016, Christian Hess and Ann-Kathrin Elger, used under Creative Commons License (CC-BY-NC).

The above two reports show the capability of reflectance spectroscopy to probe the sensing behavior of semiconductor metal oxide (SnO_2) receptor layers for chemiresistive gas sensing. The reflectance intensity decreases when the metal oxide is chemically reduced as a result of surface interactions with the gas species. Other metal oxides and receptor materials have not yet been experimentally tested in this manner. Should a receptor material have a physical response when interacting with a chemical gas, such as a change in volume, then this change in volume or thickness can be reflected as a change in the reflectance spectrum (see Chapter 5).

> *"Happiness can be found, even in the darkest of times, if one only remembers to turn on the light."*
>
> — Albus Dumbledore

Chapter 3

In-Situ Reflectance Spectroscopy of Thin Films Grown by AP-SALD[1]

3.1 Introduction

AP-SALD is an emerging technique that is capable of producing conformal, pinhole-free films in open-air. The technique and its principle of operation are described in Chapter 2.2.1. Films deposited by the AP-SALD technique have been utilized in thin film transistors [70, 74], MIM diodes [83], photovoltaic devices [71, 77, 80, 113–117], and LEDs [75, 118, 119]. Their implementation in gas sensor devices, in particular MEMS based devices, has not yet been realized.

Little has been done to characterize the nucleation and property evolution of these nanoscale films grown with AP-SALD. This may follow, in part, from the expectation that the chemistry and film formation is identical to conventional ALD, which neglects the

---

[1] This chapter has been adapted from the published manuscript titled "In-situ observation of nucleatoin and property evolution in films growth with an atmospheric pressure spatial atomic layer deposition system" by Mistry et al. [112], used under a CC-BY 4.0 International License.

influence of atmospheric conditions (i.e., open-air). It was recently shown, for example, that the periodic exposure of Al:ZnO films to oxygen during deposition in an AP-SALD system results in a higher trap density at grain boundaries, which limits the electron mobility [120]. As for other nanoscale film deposition methods, an understanding of film nucleation and property evolution is necessary to permit the fabrication of AP-SALD films with specific properties and desired thickness and morphology.

In-situ characterization techniques are typically used to study film nucleation and evolution. Quartz crystal microbalances (QCM) are commonly used to measure film deposition rates, as are reflection high energy electron diffraction (RHEED) methods employed in ultra-high vacuum environments [121–124]. Conventional ALD systems typically employ spectroscopic ellipsometry for the determination of film thickness and optical properties [104]. However, the arrangement of the optics involved tend to be "bulky" and is not ideal to make multiple real time measurements across the substrate area. Other optical spectroscopy techniques can be more easily integrated into AP-SALD systems. Mione et al. [125] recently used infrared and optical emission spectroscopy to study the gas-phase chemistry of aluminum oxide (Al_2O_3) deposition in an atmospheric-pressure plasma-enhanced SALD system. As described in Chapter 2.3.3, Yersak et al. [109] used in-situ reflectance spectroscopy to monitor the growth of insulating Al_2O_3 films deposited by a continuous web AP-SALD system. A reflectance probe was mounted above the polymer web substrate and continuously captured reflectance spectra throughout the growth. Known Al_2O_3 refractive index values were inputted into commercial software which used the Cauchy dispersion model to determine the thickness of the deposited film, although accurate thicknesses below 20 nm could not be measured and hence this technique could not be used to study the nucleation behavior of films.

In this work, an advanced reflectance spectroscopy characterization tool is developed and implemented into an AP-SALD system. Using this characterization tool, the nucleation and property evolution of insulating (Aluminum Oxide, Al_2O_3) and semiconducting (Zinc Oxide, ZnO) thin films deposited with an AP-SALD system are observed for the first time. Superior measurements at low thicknesses enable the direct observation of a substrate nucleation phase prior to film deposition, as well as the effect of different deposition parameters on this nucleation phase. The evolution of the complex refractive index can be observed throughout film deposition, and it is found that by changing the deposition parameters, the film nucleation can be controlled to produce ZnO films with different bandgaps and Al_2O_3 films with different refractive indices.

3.2 Experimental

Film deposition was performed using a custom-built AP-SALD system, which employs a close-proximity reactor head configuration as described in Chapter 2.2.1. Briefly, liquid precursors are bubbled with an inert gas (Nitrogen, N_2) that carries the precursor vapors to the reactor head. Before they arrive at the reactor head, they combine with additional streams of inert gas at higher flow rates that serve to push the precursors to the reactor (carrier lines). The ratio between the flow rate of the bubbler and the flow rate of the carrier line is used to represent the concentration of the precursor in the line, however, the actual concentration would be lower. As illustrated by the "Open-Air Deposition" section of Figure 3.1, flows of metallic and oxygen precursors are fed into the reactor head which subsequently distributes the flows into an alternating sequence of spatially separated parallel channels. In between the precursor channels exists N_2 purging and exhaust (not shown) channels. A vacuum pump was connected to the exhaust channels to actively exhaust any unreacted precursor. The reactor head is held a set distance above the heated substrate stage. Larger reactor-substrate separation heights reduce the effectiveness of the purging and exhaust channels and therefore allow intermixing of the precursors before deposition onto the substrate, analogous to CVD or atmospheric pressure-chemical vapor deposition (AP-CVD) mode. A single deposition cycle by AP-SALD consists of one complete oscillation (back and forth movement) of the substrate stage. This represents 2 conventional ALD cycles.

Insulating Al_2O_3 films were deposited on silicon wafers, using TMA as the metallic precursor and water as the oxygen precursor. The outlet channel flow rate was set to 125

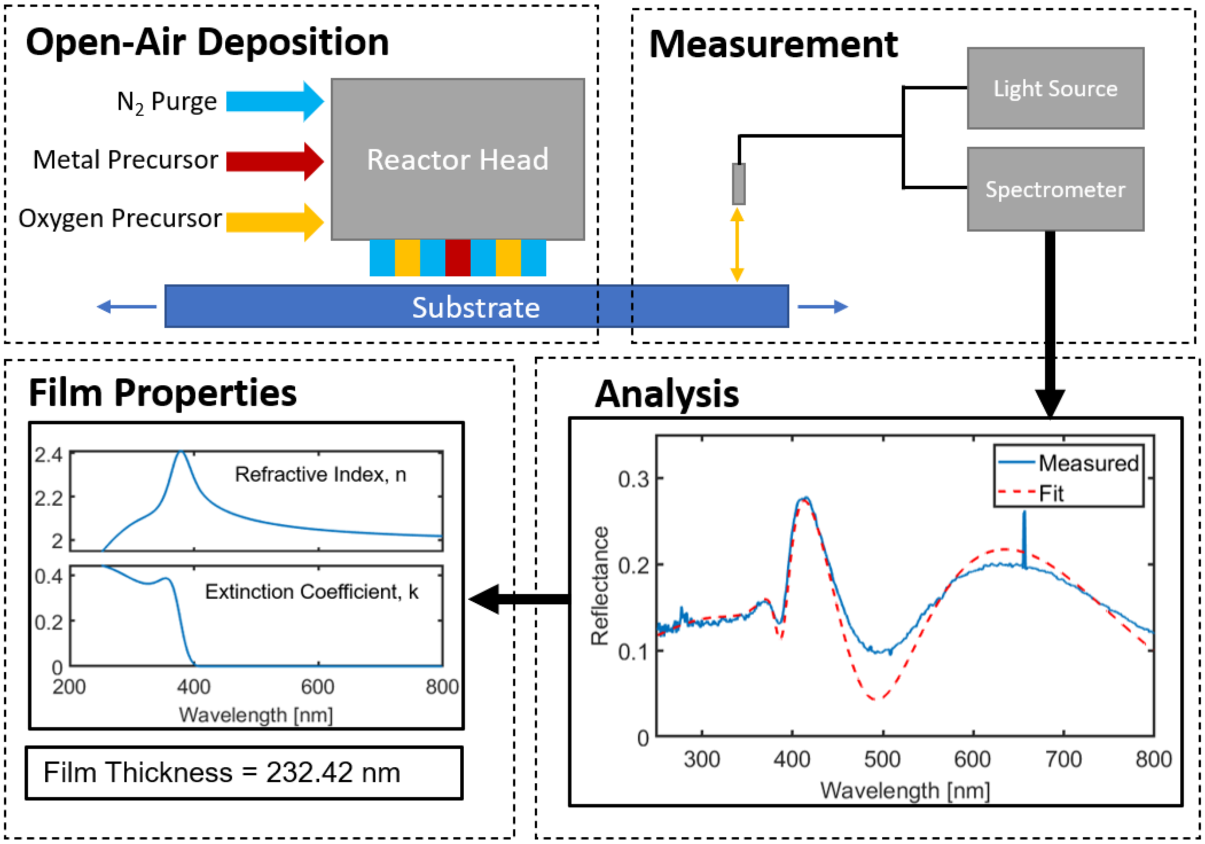

Figure 3.1: Schematic overview (not to scale) of the implemented method consisting of thin film deposition, measurement, analysis, and determination of film properties. Deposition in open-air was performed by AP-SALD utilizing a "close-proximity" reactor head. The film is grown on the substrate that oscillates underneath the reactor head. Concurrently, reflectance spectra of the growing film are captured by the mounted reflectance probe and spectrometer. Each spectrum is fitted to optical models to obtain the film thickness and the refractive index (n) and extinction coefficient (imaginary part of refractive index, k).

SCCM with a metal precursor concentration of 30% and an oxygen precursor concentration of 60%. The substrate temperature was varied from 100-250°C in increments of 50°C and the oscillation speed was varied from 15-50 mm/s. Semiconducting ZnO films were deposited on borosilicate glass, using DEZ as the metallic precursor and water as the oxygen precursor. The outlet channel flow rate was set to 150 SCCM with both the metallic and oxygen precursor concentrations set to 15% unless otherwise specified. These deposition conditions are similar to those previously reported to result in AP-CVD film growth [113]. The substrates were rinsed with isopropyl alcohol and dried with compressed air before placing on the heated substrate stage for 2 minutes to arrive at the correct deposition temperature. The substrate temperature was varied from 50-200°C in increments of 50°C and the substrate oscillation speed was varied from 5-50 mm/s. In both cases, the reactor-substrate separation was set to 100 µm.

As shown in the "Measurement" section of Figure 3.1, a bifurcated reflectance probe is mounted above the substrate stage at normal incidence (Ocean Optics QR600). A UV-Visible light source (Ocean Optics DH-2000) coupled to the reflectance probe was used to illuminate the surface of substrate. Reflected light is directed back to the reflectance probe and captured by the UV-Visible spectrometer (Ocean Optics HDX-UV-VIS) with a range of 250-800 nm. Calibration of the reflectance measurement requires the measurement of the background (bare substrate), the noise in the system (dark measurement) and the measurement of a known standard (silicon). For measurements of films grown on borosilicate glass, a matte black tape was used to cover the metallic stage to remove unwanted backside reflections. The spectrometer acquisition time was set using a modified exponential search algorithm to optimize the light intensity range for the spectrometer's detector [126], resulting in acquisition times that were typically less than 6 milliseconds. Reflectance spectra were captured every two deposition cycles in the same spot.

The determination of film properties is done by fitting the measured reflectance spectrum to an optical reflectance model. This model, which is described in Chapter 2.3.2, consists of a three-layer stack (air-film-substrate) whose total reflectance is governed by the Fresnel reflectance equations (Equation 2.10-2.16). Parameters of importance are the complex refractive indices of each layer and thickness of the growing film [102]. The complex refractive index is comprised of the real component $n(\lambda)$ and the imaginary component $k(\lambda)$, also referred to as the extinction coefficient. The refractive indices of air and the substrate are known parameters, while the wavelength(λ) dependent complex refractive index and the thickness of the film are unknowns. For Al_2O_3 and other non absorbing films, the refractive index can be described by the Cauchy dispersion model [102] where $n(\lambda)$ is a function of 3 fitting parameters and $k(\lambda) = 0$ (Equation 2.17-2.18). Including thickness, there are a total of 4 fitting parameters used to fit the measured spectrum to the reflectance model. The Tauc-Lorentz dispersion model is used for polycrystalline semiconductors such as ZnO [105,106]. Here, 9 fitting parameters are used to determine the film's complex dielectric function from which $n(\lambda)$ and $k(\lambda)$ can be obtained and results in a total of 10 fitting parameters to fit the measured reflectance spectrum (Equation 2.19-2.20).

A Levenberg-Marquardt (LM) fitting algorithm is used to fit the previously unknown parameters in the reflectance models to the measured reflectance spectra to simultaneously determine both the film's complex refractive index and thickness. The built-in function *lsqcurvefit* in MATLAB was used to perform the Levenberg-Marquardt (LM) fitting [127]. The function returns a GOF which is simply the R^2 value. Where other implementations of reflectance fitting require previous knowledge of the film's optical properties to be used as initial guesses, the implementation discussed here makes use of several guesses in a range inputted in parallel into the LM algorithm, such that previous knowledge of the film's optical properties is not used. For both the Cauchy and Tauc-Lorentz fit parameters an initial guess value of 1 was used. For the thickness parameter, several guesses in a range centred around the deposition cycle number were inputted in parallel to the *lsqcurvefit* function, from which the fit with the highest GOF was selected. This was done to account for the tendency of LM fitting programs to minimize to the local minima instead of the global minima resulting in erroneous values. This method is found to be quite successful in measuring the overall growth behavior of a deposited film. However, inaccurate fitting results occasionally occur and are represented by large spikes in the thickness values that deviate from the overall growth rate. For these cases, the incorrect thickness is corrected by refitting the spectrum using the fit parameters of the deposition cycles before and after the incorrect point. Furthermore, to improve accuracy of low thickness fits, a smaller range of parallel guesses was used (± 5nm) until the film thickness reached 30nm after which the range was extended (± 50nm). The thickness of films, as determined by reflectance spectroscopy, matched closely with the thickness measured by spectroscopic ellipsometry (J.A. Woollam M-2000DI). This validated the method described herein for the in-situ thickness measurement of films deposited by AP-SALD. As shown in the "Film Properties" section of Figure 3.1, the LM fitting algorithm returns the film's thickness, and refractive index, as well as the extinction coefficient for semiconductors. Consequentially, the absorption coefficient (α) can be determined and the optical bandgap identified using the well known

Tauc equation [128,129] (Equation 3.1-3.2). A direct bandgap ($r = 1/2$) was assumed for ZnO films [130,131].

$$\alpha(\lambda) = \frac{4\pi \; k(\lambda)}{\lambda} \tag{3.1}$$

$$\alpha \; h\nu = B \, (h\nu - E_g)^r \tag{3.2}$$

3.3 Results and Discussion

Figure 3.2 illustrates the measurement of successive ZnO and Al_2O_3 reflectance spectra during their deposition, and the evolution of the obtained film thickness and optical properties. Measured reflectance spectra are shown in Figure 3.2a and d, for ZnO and Al_2O_3, respectively. The thickness of the film at each measured cycle is plotted (Figure 3.2b and e) and can be used to determine the growth rate per cycle (GPC). The GOF is also shown. The real part of the refractive index at a wavelength of 600 nm is shown as a function of deposition cycles and is relatively consistent throughout the deposition (Figure 3.2c and f). For ZnO, the bandgap of the growing film is also shown (Figure 3.2c).

3.3.1 Film Nucleation and Growth

Figure 3.3a shows the obtained thickness of ZnO films deposited at three different substrate oscillation speeds (15, 30 and 50 mm/s). Here, substrate oscillation speed is inversely related to the precursor dose or exposure time that is typically referenced in conventional ALD literature. The substrate stage moving at a lower speed gives the precursors more time to adsorb and react on the surface of the substrate. As depicted in Figure 3.3a, film growth is found to occur in two stages: a nonlinear surface nucleation/incubation stage and a linear growth stage. This growth behavior is consistent with that of conventional vacuum based ALD, which has been verified by in situ crystal microgravimetry(QCM) [121], SEM [132], AFM [133], and surface profilometry [134]. The lack of growth during the initial deposition cycles is attributed to the nucleation time to form ZnO nuclei on the bare substrate [121].

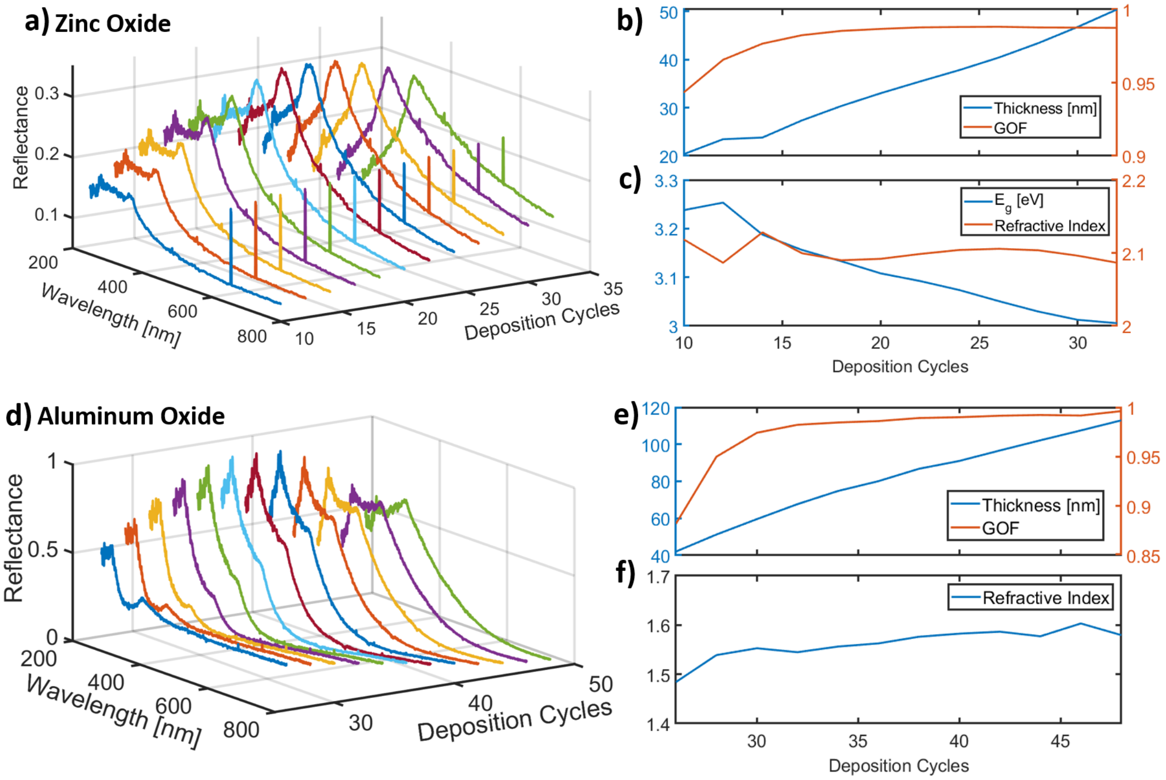

Figure 3.2: Reflectance spectra measured every 2 deposition cycles and the respective determined thickness and optical properties. (a) ZnO reflectance spectra from 10-30 cycles. (b) ZnO film thickness (left) and GOF (right). (c) ZnO optical bandgap, E_g [eV] (left), and refractive index at 600 nm (right). (d) Al_2O_3 reflectance spectra from 20-50 cycles. (e) Al_2O_3 film thickness (left) and GOF (right). (f) Al_2O_3 refractive index at 600 nm.

The density of ZnO nuclei created is related to the amount of adsorbed hydroxyl groups on the surface. The precursors will readily adsorb and react with the ZnO nuclei (active sites) resulting in an island-like growth. This continues until the islands eventually coalesce forming a complete layer, after which layer by layer growth behavior occurs in a linear fashion. This two-stage growth mechanism has been extensively reviewed by R.L. Puurunen who states that many ALD growth studies inaccurately claim a full monolayer per cycle growth from the start but that this has never been experimentally verified [63]. Methods to decrease nucleation time have included substrate pre-treatment with oxygen plasma [132] or acid cleaning [134] to increase the hydroxyl density on the surface. More commonly, increasing the length of the precursor dose time results in an increase in ZnO nuclei formation consequently decreasing the nucleation time [133]. This effect has been reproduced by AP-SALD here, where it is seen in Figure 3.3a that depositions done with quicker oscillation speeds and hence lower precursor dose times, require more deposition cycles to populate the surface with ZnO nuclei that subsequently grow into a continuous film and enter the linear growth regime.

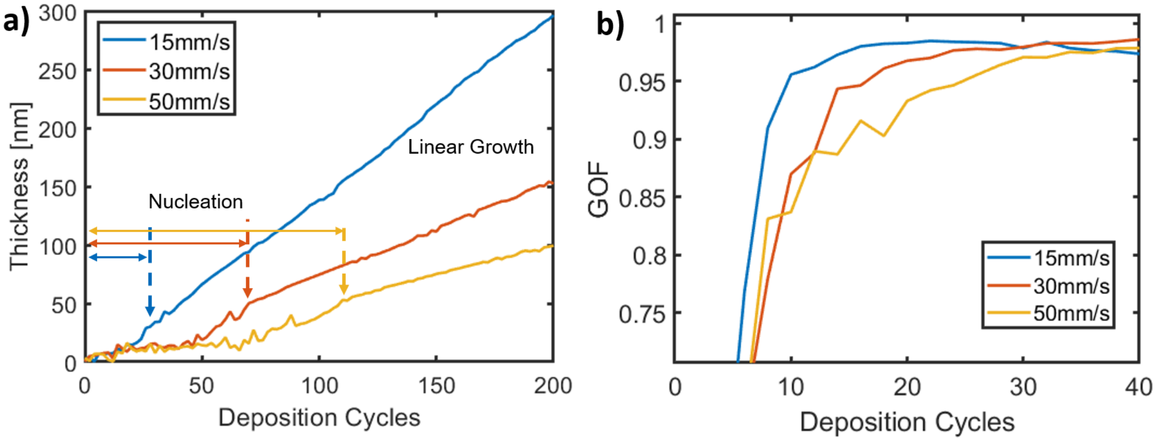

Figure 3.3: Growth of ZnO thin films at T=150°C at three different stage oscillation speeds. (a) Thickness of ZnO as a function of deposition cycles. Arrows indicate the length of the "surface nucleation" window for each oscillation speed. (b) GOF for ZnO reflectance spectra measured for the first 40 deposition cycles.

The GOF of the obtained reflectance spectra is shown in Figure 3.3b where a similar trend is observed in that quicker oscillation speeds require more deposition cycles to obtain a high GOF (>0.9) corresponding to the formation of a complete film layer on the substrate. The GOF represents the uncertainty of the reflectance measurement. In most cases a GOF (>0.9) is first achieved for a film of $\approx 10\ nm$ thickness, which corresponds to the minimum thickness required for accurate thickness determination. These results show that linear growth rates cannot be assumed from the first deposition cycle, which becomes particularly relevant in thin film applications such as passivation layers and transparent coatings. The in-situ reflectance spectroscopy technique introduced in this work enables the deposition of nanoscale films with accurate thickness.

Control of the ZnO film nucleation and growth rates was further explored by introducing the deposition temperature as an additional parameter. ZnO films were deposited on borosilicate glass at temperatures of 50, 100, 150 and 200°C, with substrate oscillation

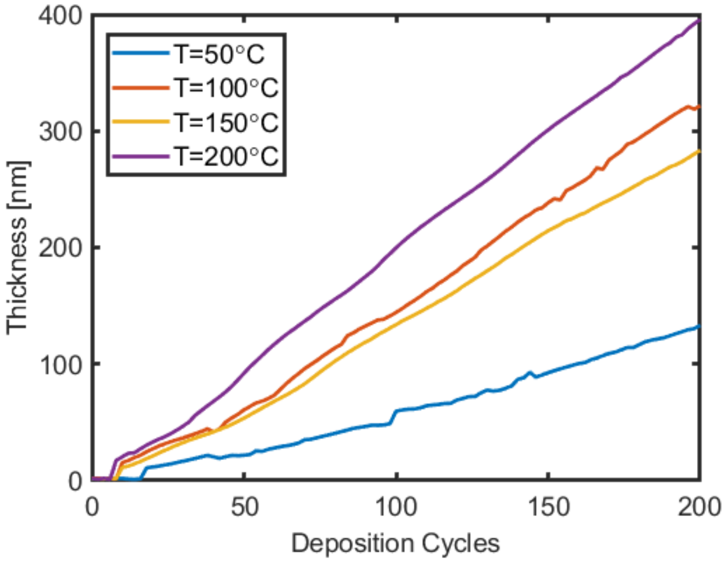

Figure 3.4: ZnO film thickness at varying deposition temperatures with a substrate oscillation speed of 5 mm/s. Similar plots for other substrate oscillation speeds are presented in Figure A.1 in Appendix A. The results are summarized in Table 3.1 and Table 3.2.

Table 3.1: Nucleation period (number of cycles) for ZnO thin films deposited with varying temperatures and substrate oscillation speeds.

	50°C	100°C	150°C	200°C
5 [mm s^{-1}]	34	14	10	8
15 [mm s^{-1}]	70	32	24	18
30 [mm s^{-1}]	98	46	40	34
50 [mm s^{-1}]	120	64	58	44

speeds of 5,15, 30 and 50 mm/s for a total of 16 ZnO samples in the study. Each film was deposited for 200 cycles, with in-situ reflectance measurements taken every 2 cycles. To obtain the same dataset by an ex-situ measurement technique would require the deposition of 1600 individual ZnO samples. Figure 3.4 compares the measured thicknesses of ZnO films deposited at different temperatures for an oscillation speed of 5 mm/s. Similar thickness plots for other oscillation speeds are presented in Figure A.1 in Appendix A. The growth behavior results of the total study are summarized in Table 3.1 (nucleation period) and Table 3.2 (linear growth rates).

Table 3.1 shows that an increase in deposition temperature results in a decrease in the number of cycles to saturate the surface of the substrate. This is in contrast to the nu-

Table 3.2: Linear growth rates per cycle (nm/cycle) for ZnO thin films deposited with varying temperatures and substrate oscillation speeds. One AP-SALD cycle corresponds to 2 conventional ALD cycles.

	50°C	100°C	150°C	200°C
5 [mm s^{-1}]	0.62	1.68	1.48	2.03
15 [mm s^{-1}]	0.27	0.51	0.62	1.47
30 [mm s^{-1}]	0.18	0.30	0.35	0.32
50 [mm s^{-1}]	0.10	0.18	0.35	0.29

cleation behavior of ZnO in conventional chamber-based ALD, where higher temperatures result in desorption of the precursors from the substrate and therefore require longer nucleation times [63]. The deviation from this behavior is attributable to the high-pressure open-air environment of AP-SALD which has an abundance of oxygen and hydroxyls, as well as the use of parameters that are expected to result in chemical vapor deposition. In agreement with the results obtained here, AP-CVD of ZnO films by Biswas et al showed that substrate coverage can be significantly improved by increasing growth temperatures [135]. This is because the elevated temperatures accelerate precursor gas phase reaction in air, rather than adsorption on the substrate, resulting in shorter nucleation times and quicker growth rates [136]. The data presented in Table 3.2 demonstrate that a wide range of growth rates of 0.1-2 nm/cycle (corresponding to 0.05-1 nm per conventional ALD cycle) are achievable. The lowest growth rate of 0.1 nm/cycle represents the resolution of the in-situ thickness measurement by reflectance spectroscopy. An increase in deposition temperature generally results in an increase in growth rate per cycle. This is in agreement with the shorter nucleation times observed at higher temperature. The growth rate is seen to decrease as the substrate oscillation speed increases (dose time decreases). Despite operating with parameters that are expected to result in AP-CVD, the growth rates at oscillation speeds of 30 and 50 mm/s are comparable to ZnO growth rates achieved by conventional ALD of 0.1-0.3 nm per ALD cycle [73, 79, 137]. Decreasing the oscillation speed to 15 or 5 mm/s resulted in an increase in growth rates up to 2 nm/cycle (1 nm per ALD cycle), consistent with AP-CVD, where the slower oscillation speed allows for a longer AP-CVD reaction [136]. There are a few minor deviations from the noted trends in Table 3.2: GPC at 100°C vs 150°C for an oscillation speed of 5mm/s, and, 150°C vs 200°C for oscillation speeds of 30mm/s and 50mm/s. Since many of these depositions occurred one after another, one possible explanation to the higher growth rate at a lower temperature can be due to an accumulation of precursor in the line. Additionally, the spacing between the stainless-steel reactor head and the substrate was manually set to 100 µm at the start of the study. It is possible that at the lower temperature the substrate thermally expanded less and therefore resulted in a spacing that was larger than 100 µm and promoted more precursor mixing resulting in the higher growth rate. Another possible explanation lies in classical ALD theory, where higher deposition temperatures outside of the "ALD window" result in desorption of the precursor from the substrate [138–141]. This phenomena may be more relevant to higher growth rates at 150°C than 200°C for both 30 and 50 mm/s oscillation speeds, whereas the anomaly observed at 100°C vs 150°C is most likely due to the previous two explanations.

A similar study to examine the influence of deposition parameters was done for Al_2O_3 films. Al_2O_3 films were deposited at temperatures of 100, 150, 200 and 250°C with oscillation speeds of 15, 30 and 50 mm/s on silicon substrates (12 samples in total, 100 cycles each). Figure 3.5 compares the measured thickness of films deposited at 200°C for different oscillation speeds. Similar thickness plots for other deposition temperatures are presented in Figure A.2 in Appendix A. The growth behavior results of the total study are summarized in Table 3.3 (nucleation period) and Table 3.4 (linear growth rate). While the growth behavior for ZnO closely followed the expected trends, this is not the case for Al_2O_3. For example, as shown in Figure 3.5, the nucleation period is larger for an oscillation speed of 15mm/s compared to 30 mm/s, where the opposite would be expected. There are no clear trends in the nucleation period, as presented in Table 3.3. Additionally, the rates presented in Table 3.4 do not exhibit clear trends in growth behavior. As reported previously, the atmospheric ("open-air") deposition of Al_2O_3 using the highly pyrophoric precursor TMA, can be challenging to reproduce [85]. The ambient oxygen and water in the air (humid conditions) can act as an additional oxygen source that can increase growth rates [65]. Human error in adjusting the reactor head spacing can lead to an overmixing of the precursors (AP-CVD) and deposition with high rates [82]. Jur and Parsons concluded that the high pressures of atmospheric deposition will typically increase Al_2O_3 growth rates by

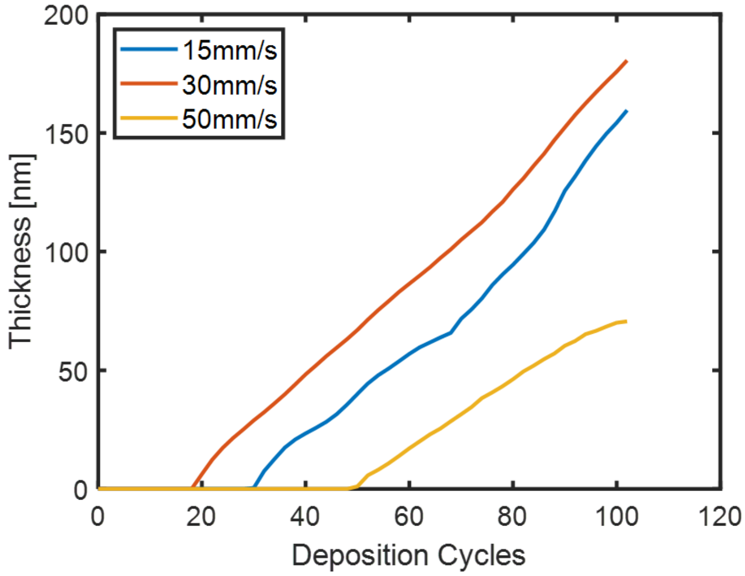

Figure 3.5: Thickness of deposited Al_2O_3 film at varying substrate oscillation speeds with a deposition temperature of 200°C. Thickness plots of Al_2O_3 films deposited at other temperatures are presented in Figure A.2 in Appendix A. The results are summarized in Table 3.3 and Table 3.4.

Table 3.3: Nucleation period (number of cycles) for Al_2O_3 thin films deposited with varying temperatures and substrate oscillation speeds.

	100°C	150°C	200°C	250 °C
15 [mm s^{-1}]	18	24	30	16
30 [mm s^{-1}]	10	52	18	24
50 [mm s^{-1}]	74	22	50	18

$\approx 25-30\%$ [142]. More importantly, Mousa et al. noted that at high atmospheric pressures the growth of Al_2O_3 with TMA is largely independent of temperature [143]. It is therefore difficult to observe the influence of temperature and oscillation speed on the Al_2O_3 growth. However, it strongly supports the need for an in-situ thickness characterization tool for Al_2O_3 grown in atmospheric conditions using this technique.

Added benefits of monitoring the film thickness in-situ include the ability to monitor for deposition errors and to control the deposition rate. Figure 3.6a depicts an example of error monitoring during the deposition of an Al_2O_3 thin film. The linear growth regime starts after 20 deposition cycles and after 36 cycles the vacuum pump for the exhaust channels was turned on which immediately reduced the growth rate. In this case, the lack of vacuum

Table 3.4: Linear growth rates per cycle (nm/cycle) for Al_2O_3 thin films deposited with varying temperatures and substrate oscillation speeds. One AP-SALD cycle corresponds to 2 conventional ALD cycles.

	100°C	150°C	200°C	250 °C
15 [mm s^{-1}]	1.68	1.47	2.28	2.92
30 [mm s^{-1}]	1.13	1.21	2.11	1.57
50 [mm s^{-1}]	1.09	0.83	1.44	0.78

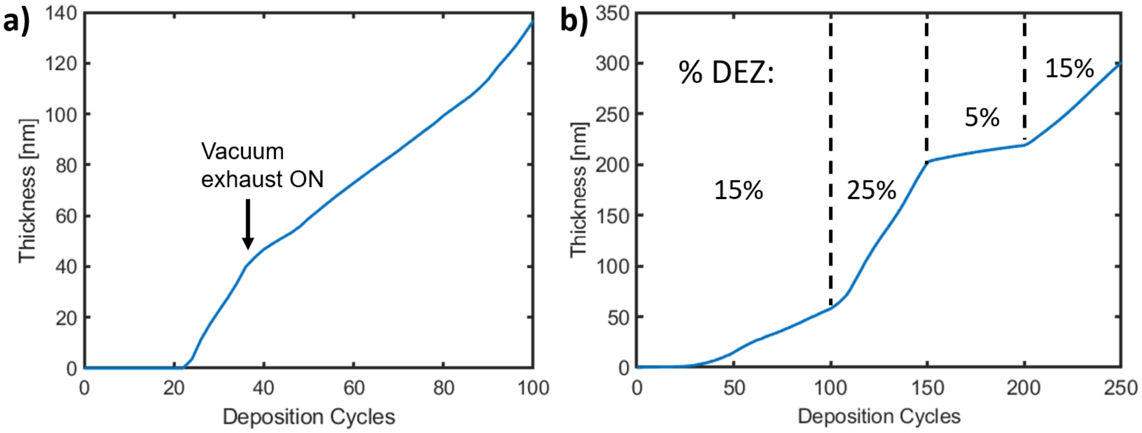

Figure 3.6: Real time monitoring of deposition errors and rate. (a) Thickness of a deposited Al_2O_3 film (T=150°C), the vacuum pump for the exhaust channels was not turned on for the first 36 deposition cycles. (b) Different deposition rates for a ZnO film (T=200°C), the DEZ flow rates were varied.

exhaust during the initial growth period resulted in a higher amount of precursor mixing and consequentially a higher growth rate. Figure 3.6b illustrates the ability to control the deposition rate of a ZnO thin film by varying the precursor (DEZ) flow rate. The initial 100 deposition cycles were done at a concentration of 15% to first saturate the surface and subsequently enter the linear growth regime. After 100 cycles the concentration was increased to 25% resulting in a stark increase in the growth rate per cycle. After another 50 cycles the concentration was decreased to 5% resulting in a decrease in growth rate which was followed by an increase in growth rate once the concentration was set back to 15%. The large variation in growth rate is consistent with AP-CVD type growth as discussed earlier.

3.3.2 Evolution of Optical Properties

As previously described, the bandgap (E_g) of semiconducting films can be obtained from in-situ reflectance spectroscopy and thus can be monitored over the deposition period. Figure 3.7 shows the bandgap evolution of growing ZnO films deposited at different temperatures. The E_g data was taken after the completion of the nucleation period and when high GOF was achieved. As observed in the figure, the obtained bandgaps range from 3.39-2.95 eV, where films deposited at a lower temperature have a higher initial bandgap. This is consistent with previous reports, where three reasons are presented. The first attributes the bandgap temperature dependence to the thermal expansion of the ZnO lattice and its direct effect on the relative position of the valence and conduction band [144]. The second is the temperature dependence of the electron-phonon interactions and their affect on the band energies [145]. Lastly, it is known that the higher deposition temperatures result in an increased crystallinity for ZnO films grown by this method, and the decrease in bandgap has been attributed to the improved crystallinity [146]. The bandgap then decreases from the initial value as the film grows which is attributed to the size of the grains as well as the porosity in the nanocrystalline film. The early stages of film growth will consist of smaller crystallite sizes corresponding to higher film porosity. As the film grows the crystallite sizes become larger, the film becomes more compact and the overall film porosity decreases. Like quantum dots, the optical bandgap of a nanocrystalline ZnO film will decrease as the grain size increases [131, 147]. Similarly, the bandgap is expected to decrease as the porosity of the film decreases as well [148, 149]. The general trend of decreasing bandgap as deposition temperature increases has been shown for ZnO films grown by conventional ALD methods [150, 151]. However, values as low as 2.9 eV (deposited at 200°C) have not, to our knowledge, been reported for ZnO grown by ALD. As described by the Varshini equation [152], the bandgap of semiconductors tends to decrease as a function of the measurement temperature. The sample grown at 200°C was re-measured at room temperature and had a bandgap of 3.07 eV which is still low when compared to that of ALD grown ZnO. This may be attributed to the deposition done in atmospheric conditions, as AP-CVD grown ZnO has reported bandgaps as low as 2.8 eV [153].

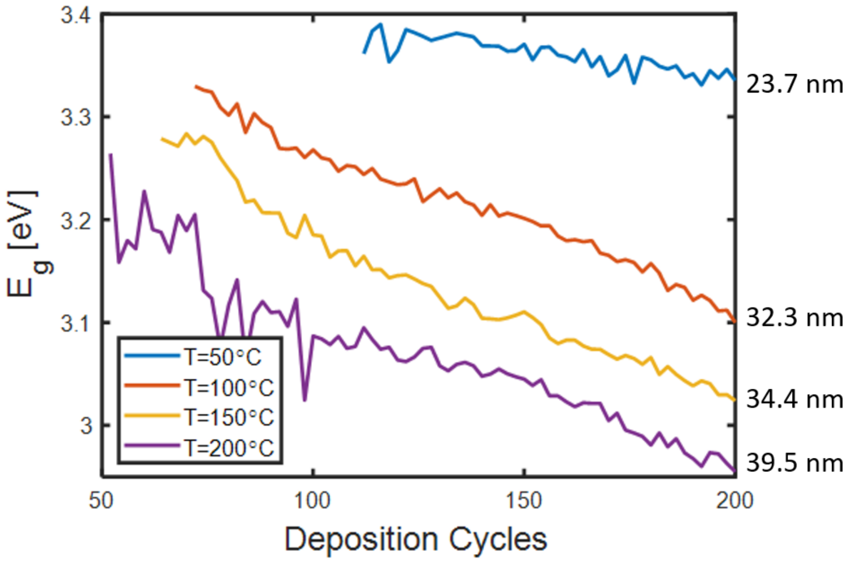

Figure 3.7: The optical bandgap E_g [eV] of ZnO films obtained from in-situ reflectance spectroscopy measurements. The influence of deposition temperature on the bandgap is examined throughout the course of film deposition at an oscillation speed of 50 mm/s. Values are taken after completion of the nucleation period and when high GOF was achieved. Final film thicknesses are listed on the right.

The refractive index of a thin film can give an indication of film quality and density. Figure 3.8 shows the refractive index (at 600nm) of Al_2O_3 films deposited at different temperatures. Values obtained before the completion of the nucleation period were ignored. The initial formation of the films is observed as the refractive index starts at zero or near zero values and increases to a value of 1.4-1.5, which is the expected refractive index range for Al_2O_3 grown by conventional ALD [72, 154]. It is clear that the refractive index of the film grown at 100°C is lower compared to the films grown at higher temperatures. This is attributed to the decreased density and increased impurity levels of Al_2O_3 grown at lower temperatures [69, 154, 155]. It is expected that higher temperatures would promote a higher degree of crystallinity and higher density resulting in an increase in refractive index approaching a value of 1.76, that of sapphire (α-Al_2O_3).

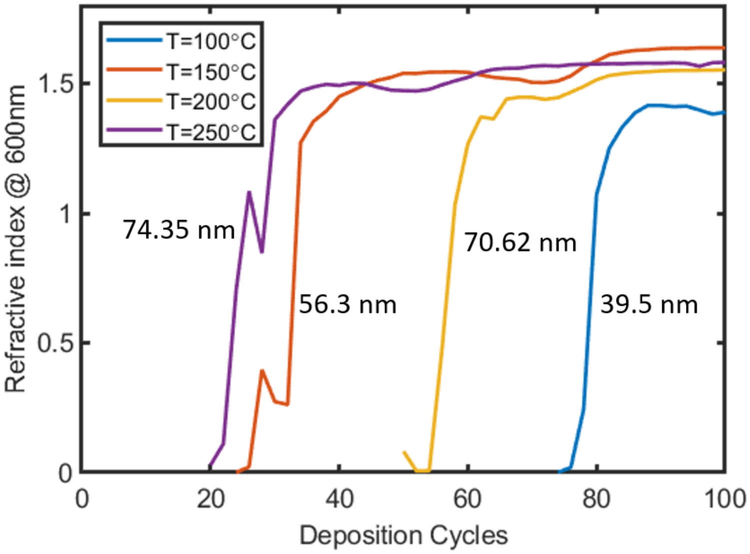

Figure 3.8: Comparison of refractive index of Al_2O_3 films at different deposition temperatures, as determined by in situ reflectance spectroscopy. The refractive index value was taken at 600 nm. Data obtained before the completion of the nucleation period was ignored. Final film thicknesses after 100 deposition cycles are listed.

3.4 Conclusion

An in-situ reflectance spectroscopy tool was developed and implemented with an atmospheric pressure-spatial atomic layer deposition system. A reflectance probe mounted above the deposition stage was able to capture reflectance spectra every two deposition cycles of growing insulating (Al_2O_3) and semiconducting (ZnO) metal oxide thin films. The spectra were fitted to optical reflectance models in real-time to obtain properties such as thickness, refractive index and optical bandgap (for semiconductors). GOF values for each fitted spectrum were obtained to indicate the level of confidence in the obtained properties.

The approach works well to study the nucleation and property evolution of metal oxide films deposited with this open-air technique. A two-stage growth mechanism was observed, consistent with previous reports of an initial nucleation period to saturate the surface with metal oxide nuclei that eventually grow into a continuous film after which, linear growth occurs. In-situ thickness characterization is therefore crucial to enable to the accurate deposition of films with a desired thickness, as linear growth rates cannot be assumed from the start.

The influence of deposition parameters such as substrate oscillation speed, temperature and precursor concentration, on the growth behavior of the films was studied. The length of the nucleation period for ZnO depositions was sensitive to the oscillation speed and temperature. Faster oscillation speeds resulted in a longer nucleation period and higher deposition temperatures shortened the nucleation period, which was consistent with AP-CVD growth. Similarly, a wide range of growth rates were achievable (0.1-3nm per AP-SALD cycle) by varying the deposition parameters. Furthermore, the high reactivity of pyrophoric precursors deposited in open atmosphere can result in errors that appear as sudden changes in growth rate during a deposition. The real time monitoring of growth rate allows the user to ensure film growth is occurring as expected.

The evolution of optical properties such as bandgap and refractive index of the growing film was observed and followed expected behavior relating to the crystallinity and density of the thin films. It was clear the deposition temperature influenced the optical properties of the film. The bandgap of ZnO films decreased as a function of deposition cycles and increasing temperature. The low bandgap of ZnO obtained at higher deposition temperatures was consistent with reported atmospheric CVD grown ZnO. The trend of increasing Al_2O_3 refractive index as a function of deposition temperature was similar to that of films grown by conventional ALD. An ex-situ characterization technique such as x-ray photoelectron spectroscopy is warranted to study variation in the film's chemical composition and its effect on the optical properties.

The nucleation and property evolution for films deposited with an AP-SALD system has not been studied in detail previously. By implementing in-situ reflectance spectroscopy, the growth behavior and film properties can be obtained and monitored in real time during a deposition. This becomes particularly useful when implementing films in specific applications such as the resonant cantilever gas sensors discussed in Chapter 6.

"To Infinity and Beyond!"

— Buzz Lightyear

Chapter 4

Observation of Thin Film Nucleation and Growth on Various Materials

4.1 Introduction

In the previous chapter, the in-situ reflectance spectroscopy technique for films grown by AP-SALD was introduced. One of the major findings of this study was the occurrence of the nucleation period in the initial stages of film growth. It was shown that the growth of the films were delayed for a number of deposition cycles until enough metal oxide nuclei are formed for complete surface coverage. After this stage, the film growth continues in a linear fashion. It was concluded that the in-situ reflectance technique was particularly beneficial for the accurate and reproducible deposition of sub 50 nm thin films, as the nucleation delay could be observed and accounted for. However, the technique was only demonstrated for depositions on conventional substrates such as a glass and silicon wafers.

In practical metal oxide gas sensor applications, metal oxide films are often deposited on surfaces that are not glass or silicon. For example in resistive gas sensor devices based on interdigitated electrodes, the film is often deposited on top of the electrode layer consisting of a metal such as gold or aluminum. In MEMS based sensors, thin film sensing layers are deposited on structural layers (metals, silicon, oxides, and nitrides), which are deposited on top of sacrificial layers (polymers and oxides). Thin film deposition on fabrics has recently become prominent due to the COVID-19 outbreak and the push for the development of facial masks with antiviral coatings. Metal oxides such as zinc oxide and cuprous oxide have known antiviral and antibacterial efficacy [156–158] and therefore their deposition on the polypropylene fabrics used to make N95 masks is beneficial.

In all of these applications, there is a need to achieve reproducible film deposition with accurate thicknesses. For metal oxide coatings on textiles by ALD, the thickness of the coating is often estimated by determining the thickness of the film deposited on silicon with the same deposition conditions [159, 160]. However, this estimation is fairly inaccurate as it assumes the growth behavior on the textile to be same as on silicon which is not the case. It was shown that the nucleation and growth behavior of ALD ZnO on silicon, galium nitride (GaN) and sapphire (α-Al2O3) substrates all varied due to their different surface morphologies [133]. Thus, it is expected that the nucleation and growth behavior on textiles and other surfaces would also vary. This motivated the use of in-situ reflectometry, as described in Chapter 3, to quantify the nucleation and growth behavior of AP-SALD films deposited on various surfaces.

The Fresnel reflectance model used to determine the growing film thickness in Chapter 3, requires prior knowledge of the underlying layer's (substrate) optical properties (refractive index n, and extinction coefficient k). These values are known for conventional substrates such as glass and silicon but are generally not available for other materials such as textiles, proprietary polymers and plastics. To circumvent this issue, a reflectance model known as the Virtual Interface virtual interface (VI) method was used [107]. As described in Chapter 2.3.2, the reflectance intensity at a single wavelength over the duration of the deposition is analyzed instead of the complete reflectance spectrum (all wavelengths) at each cycle. The VI method is able to extract growth rates without any prior knowledge of the underlying surface. Additionally, the length of the nucleation period can be obtained by observing the number of deposition cycles until the first change in reflectance intensity is observed. With this method the minimum number of cycles required for film deposition on various surfaces is obtained and as well as their respective growth rates which allows for accurate and reproducible film deposition.

In this work, AP-SALD is used to deposit zinc oxide on a variety of different surfaces and monitored by in-situ reflectometry. The nucleation period (number of cycles) and growth rates are determined by analysis of the reflectance intensity as a function of deposition time. The method is first demonstrated for conventional substrates such as glass and silicon and then followed by ZnO depositions on metals, polymer layers, flexible substrates, polypropylene fabric and on drop casted solutions of laser treated 2D nanoparticles.

4.2 Experimental Section

4.2.1 Materials

The glass substrates were square (7 cm) borosilicate glass pieces obtained from Abrisa Technologies. Silicon substrates were 3" wafers obtained from University Wafer. Gold and copper substrates were fabricated by electron beam and thermal evaporation onto borosilicate glass and silicon substrates. PMMA drop casted onto silicon substrates were prepared by Rishard Rameez, a PhD student at the University of Waterloo. Shipley S1811 photoresist was spin coated onto silicon substrates at 5000 RPM for 60s and baked at 110°C for 90s. Kapton tape (polyimide) was taped onto borosilicate glass substrates. Transparent polystyrene plastic was taped onto borosilicate glass. Paper with an adhesive backing (sticky note) was placed onto borosilicate glass. Spunbound polypropylene fabric with a density of 50 g/m^2 was obtained from Eclipse Automation and was cut into rectangular pieces (2 x 5 cm) and affixed onto borosilicate glass substrates in tension.

A highly concentrated (6.2 mg/ml) graphene solution (GO) and ultrafine powders of molybdenum disulfide (MoS_2), and tungsten disulfide (WS_2) were purchased from Graphene Supermarket and were treated with a femtosecond laser method as described in Chapter 2.2.2. The laser treatment process was done by Dr. Khaled Ibrahim, former doctoral student at the University of Waterloo. The laser was produced with a Ti:Sapphire regenerative amplifier, producing a central wavelength of 800 nm, pulse duration of 35 fs, average power of 2 W, and a repetition rate of 1 kHz. The 2D material solutions were placed in 5 mL vials and irradiated with the laser. The incident laser beam was focused with a 5 cm off axis parabolic mirror. The focal point was set at depth 0.5 cm below the air/solution interface. During the irradiation process, the solutions were constantly stirred by a magnetic stirrer at 250 RPM. The graphene oxide solution was laser treated for 20 minutes. MoS_2 dispensed in DI water at a concentration of 1 mg/mL was laser treated for 70 minutes, while WS_2 in DI water at a concentration of 0.5 mg/mL was treated for 70 minutes. The 2D material solutions were drop casted onto silicon substrates and dried at 60° C until the solvent evaporated. Prior to deposition all samples were placed on the heated substrate stage for 2 minutes to arrive at the correct deposition temperature.

4.2.2 Film Deposition and Reflectance Measurement

Zinc oxide (ZnO) films were deposited on all samples by the AP-SALD technique as described in Chapter 2.2.1. DEZ and water were used as the metallic and oxygen precursors. The total outlet channel flow rate was set to 150 SCCM with both the metallic and oxygen precursor concentrations set to 30%, which is higher than the concentration used in Chapter 3 (15%). The higher concentration was used in this work to promote shorter nucleation times. The deposition temperature was set to 100°C which is below the melting temperature of all the materials deposited on. The substrate oscillation speed was set to 15 mm/s. The separation distance between the bottom of the reactor head and the sample was kept at approximately 100 µm.

In-situ reflectance measurements were done in the same manner as described in Chapter 3. As shown in Figure 3.1, a bifurcated reflectance probe was mounted over the substrate stage at normal incidence. A UV-visible light source (Ocean Optics DH-2000) was used to illuminate the surface of the samples. Reflected light was captured by the UV-visible spectrometer (Ocean Optics HDX) with a range of 250-800 nm. Reflectance signals were captured every two AP-SALD deposition cycles near the centre of the deposition area. As described previously, a single deposition cycle by AP-SALD conssist of one complete oscillation (back and forth movement) of the substrate state, equivalent to 2 conventional ALD cycles. SEM images of the polypropylene and WS_2 samples were obtained with a JEOL JSM-7200F SEM, with an acceleration voltage of 5kV.

4.2.3 Analysis of Reflectance

While the method above captures the full reflectance spectra (at each wavelength), the monitoring of nucleation period and growth rates by the VI method requires only the reflectance intensity at a single wavelength in time. Here, deposition time in seconds is replaced by deposition cycles. Unless otherwise, the reflectance intensity as a function of deposition cycles was monitored at a wavelength of 400 nm, R(cyc). The nucleation period of the film growth was determined by observing the number of deposition cycles until a significant change in reflectance intensity and the start of an oscillatory pattern, is observed.

The VI method (as described in Chapter 2.3.2), is used to determined the growth rate per cycle. Equation 2.30-2.37 are used to extract initial estimates for the fitting parameters from the measured oscillatory reflectance signal, R(cyc). This required film depositions to be sufficiently long in order to observe at minimum two oscillation amplitudes in the R(cyc) signal. A nonlinear-least squares fitting method (MATLAB built-in function, “lsqcurvefit”), is used to to fit the measured R(cyc) data to the VI model, Equation 2.23. From the fitted model, Equation 2.24-2.29 are used to obtain the growth rate per cycle, GPC (or “G” in Equation 2.28).

4.3 Results and Discussion

4.3.1 Deposition on Conventional Substrates

To validate the virtual-interface method used in this work, the model was first applied to previously collected reflectance data for ZnO films grown on borosilicate glass, shown in Chapter 3. The reflectance intensity at a wavelength of 400 nm, as a function of deposition cycles is shown in Figure 4.1, for ZnO films grown with an oscillation speed of 5 mm/s and at different temperatures (50-200°C). The length of the nucleation period was determined by observing the number of deposition cycles until a significant change in the reflectance intensity and an oscillatory pattern, is observed (depicted with an orange double-headed arrow). The VI method was used to fit the reflectance intensity data thereafter (shown in blue) to obtain the GPC. As the deposition temperature increased from 50°C to 200°C the length of the nucleation period decreased from 24 cycles to 6 cycles, while the GPC increased from 0.68 nm/cyc to 2.02 nm/cyc. GPCs determined at other wavelengths returned similar values. However, estimates for the nucleation period obtained at larger wavelengths(> 400 nm) were slightly greater the nucleation periods determined at shorter wavelengths. This is because at low thicknesses (≤ 20 nm), the film is optically transparent in the visible to near infrared range [102]. Hence the nucleation period will be "delayed" when determined at these wavelengths. The nucleation periods estimated with lower wavelengths (≤ 400 nm) returned the same values.

Table 4.1 compares the nucleation period and GPC data obtained by the VI method to the data obtained by the fresnel reflectance model (Table 3.1 and Table 3.2). For the ZnO grown at 50°C, there is a fairly close match for the obtained GPCs (0.68 and 0.62 nm/cyc) while the nucleation periods differ (24 and 34 cycles). This difference may be a result of the lower goodness of fit (GOF) achieved by the Fresnel model at low thicknesses resulting in an inaccurate determination of the nucleation period length. All other obtained values by both methods do show a close match which validates the use of the reflectance-time method for nucleation period and GPC estimation.

As observed in Figure 4.1, as the thin film grows the reflectance intensity at a single

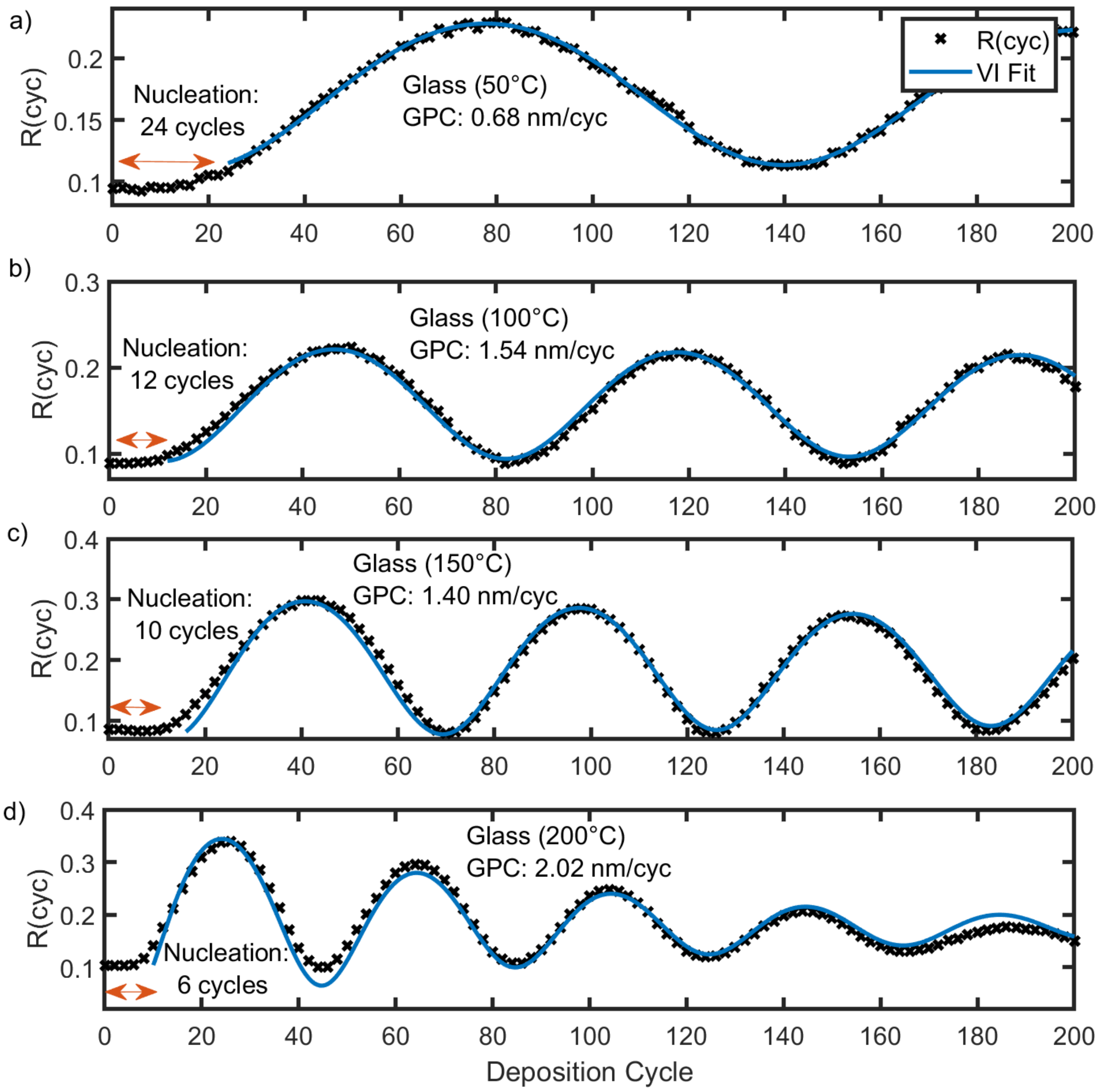

Figure 4.1: Measured reflectance intensity (black crosses) at a wavelength of 400 nm as a function of time (deposition cycles) for ZnO films grown on borosilicate glass with an oscillation speed of 5 mm/s at different temperatures: a) 50°C, b) 100°C, c) 150°C and d) 200°C. The data was fitted to the VI Method (blue) to obtain the GPC.

wavelength will oscillate. The origin of this oscillation is due to thin film interference effects [102]. Light waves reflecting off of the air-film and film-substrate interfaces undergo a phase change. Light waves that travel through the film and reflect off of the film-substrate interface have an additional travel distance that will alter its phase and constructively or destructively interfere with the other reflected waves. Constructive interference occurs when the film thickness is $\frac{1}{4}\lambda$, $\frac{3}{4}\lambda$, $\frac{5}{4}\lambda$...etc, whereas destructive interference occurs when

Table 4.1: Comparison of the nucleation (number of cycles) and GPC (nm/cycle) obtained by the R-t method and the Fresnel reflectance model in Chapter 3.

	Nucleation Period		GPC	
	R-t	Fresnel	R-t	Fresnel
50°C	24	34	0.68	0.62
100°C	12	14	1.54	1.68
150°C	10	10	1.40	1.48
200°C	6	8	2.02	2.03

the film thickness is $\frac{1}{2}\lambda$, 1λ, $\frac{3}{2}\lambda$...etc. Therefore, as the film thickness increases, the reflected waves will switch between constructive and destructive interference and cause an oscillatory pattern in the overall film reflectance as a function of time. It is evident that the frequency of this oscillation is related to the growth rate of the film.

For comparison of growth behavior for all other substrates in this study, the metal precursor concentration was increased to 30% instead of the 15% previously used to promote shorter nucleation times on the non conventional substrates. The deposition temperature was set to 100°C, to stay below the melting temperatures of some of the substrates used. With these conditions, ZnO was deposited on borosilicate glass and silicon. The measured and fitted reflectance-time data are shown in Figure 4.2. The higher precursor concentration results in almost immediate nucleation on glass (within 2 deposition cycles) followed by a fairly high GPC of 1.79 nm/cycle. For deposition on silicon, the nucleation period was 12 cycles with a GPC of 0.63 nm/cyc. When compared to glass, the longer nucleation time on silicon is expected. Glass is an oxide (SiO_2) whose top surface is saturated with hydroxyl (OH) groups available for reaction with the metal precursor. Whereas, the surface of silicon is less populated with hydroxyl groups and thus requires more time for a film to have complete surface coverage.

4.3.2 Deposition on Non-conventional Substrates

Deposition on Metal Layers

As shown in Figure 4.3, the nucleation period and GPC were obtained for ZnO deposited on metal substrates such as gold, copper and aluminum foil. Aluminum foil had the shortest

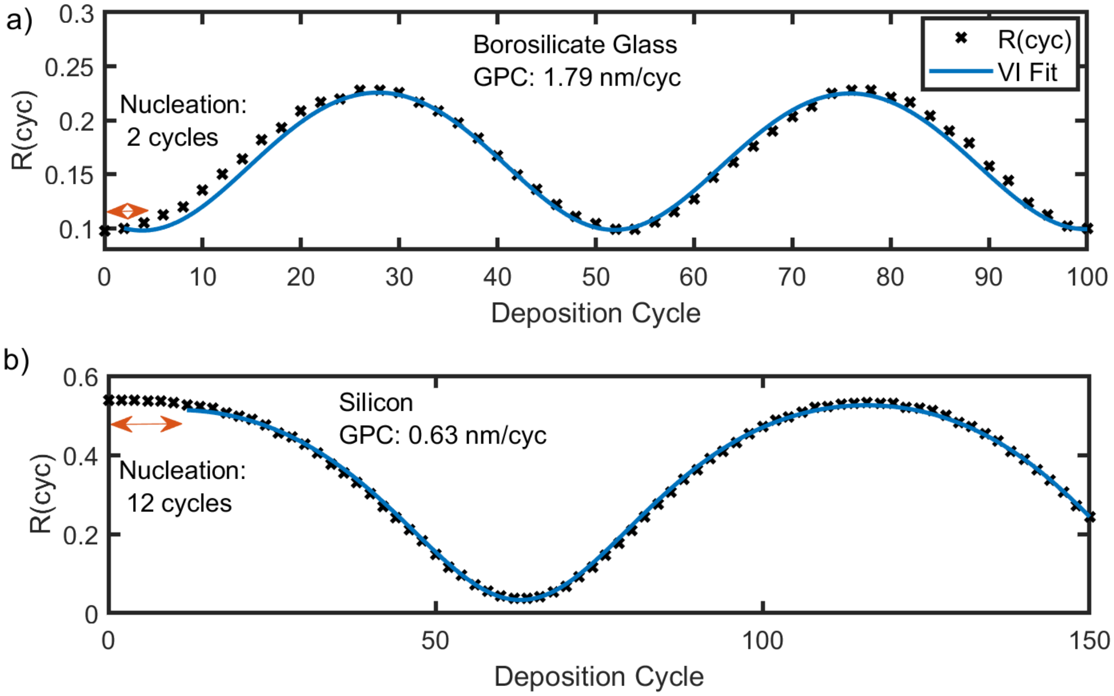

Figure 4.2: Measured reflectance intensity (black crosses) at a wavelength of 400 nm as a function of time (deposition cycles) for ZnO films grown on a) borosilicate glass and b) silicon. The data was fitted to the VI model (blue) to obtain the GPC.

nucleation period of 12 cycles, while copper had the the largest at 34 cycles and gold had a nucleation time of 18 cycles. Based on the reactivity series of metals, aluminum is the most reactive, followed by copper and gold [161]. This means that aluminum is more easily oxidized and therefore requires fewer deposition cycles to create a thin oxide layer (Al_2O_3) to populate the surface with hydroxyl groups. Once the the surface is sufficiently hydroxylated, the reaction with the metal (Zn) precursor can proceed for ZnO growth. A similar mechanism is expected for copper but requiring a longer nucleation period as it is less reactive than aluminum. Gold is the least reactive metal out of the three and therefore should have the longest nucleation period. In fact, since it is a noble metal and is chemically inert, thin film growth was not expected at all but that was not the case here. Despite this expected behavior, metal oxide growth on gold by ALD has been previously reported but the specific nucleation mechanisms were not studied [121, 162]. Deposition on gold did however, result in the lowest GPC of 0.28 nm/cyc which may be due to the substrate influencing growth with a particular surface morphology or crystal direction that is slower compared to the growth on aluminum and copper [133]. X-ray diffraction measurements are recommended to further investigate these mechanisms.

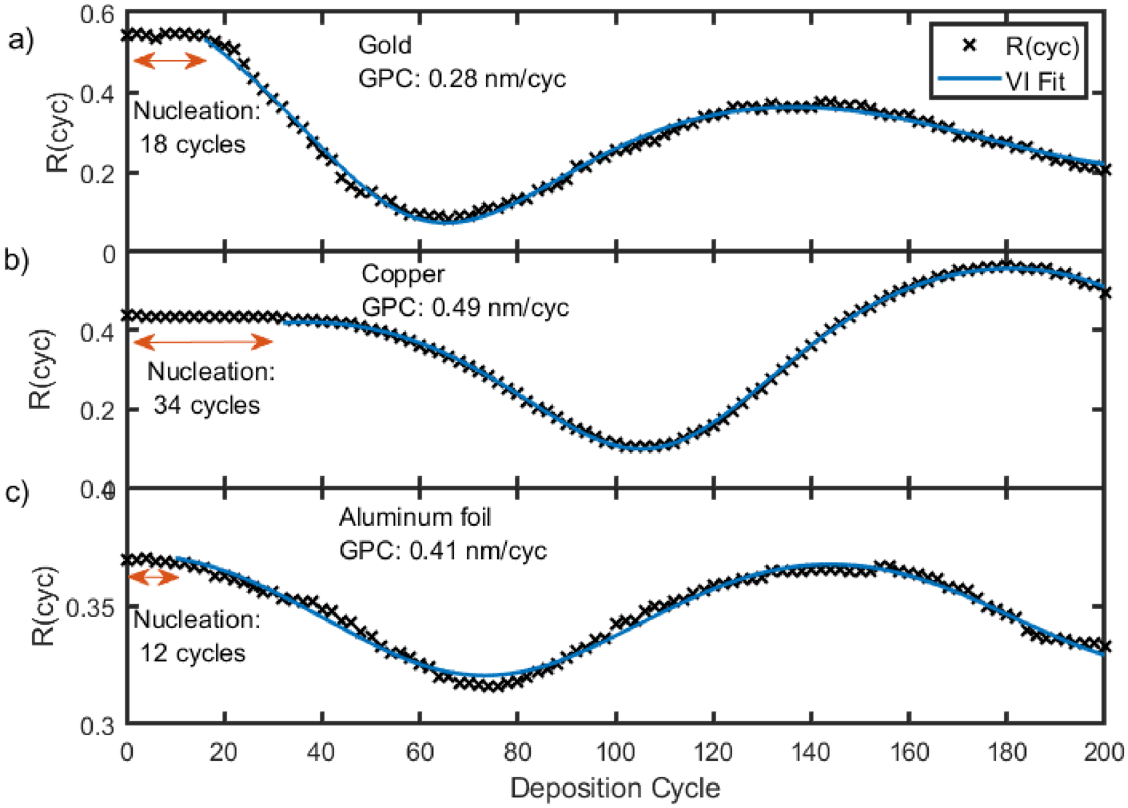

Figure 4.3: Measured reflectance intensity (black crosses) at $\lambda = 400\ nm$ as a function time (deposition cycles) for ZnO films grown on a) gold, b) copper and c) aluminum foil. The data was fitted to the VI model (blue) to obtain the GPC (nm/cyc).

Deposition on Polymer Layers

The growth behavior of ZnO films on PMMA and photoresist (Shipley S1800) layers are shown in Figure 4.4. The ALD growth mechanism on polymer layers is dependant on the chemical structure of the polymer and the permeability of the polymer films. For polymers that have functional groups such as hydroxyls, the ALD growth occurs similar to the growth on conventional substrates like glass [163]. However, for polymers that do not have suitable reactive species, it was shown that the precursors diffuse and embed into the sub-surface of the polymer film and form metal oxide clusters or nuclei. After further ALD cycles, the nuclei eventually coalesce into a continuous film that grows above the surface of the polymer which corresponds to the end of the nucleation period [62, 164]. Despite the different growth mechanism, deposition on polymer layers is still characterized by an initial nucleation period followed by a linear growth period. For PMMA, a polymer without suitable reactive species, a nucleation period of 18 cycles was observed with a GPC of 0.53 nm/cyc.

In microfabrication, one of the more useful applications of polymers is for the patterning of thin films and formation of unique nano/micro structures. In the fabrication of MEMS based devices, polymers can be used as sacrificial layers that are removed to create free-standing structures. In Chapter 6, micro-cantilever structural layers made up of zinc oxide are deposited by AP-SALD on top of Shipley S1800 photoresist sacrificial layers. The zinc oxide was deposited at three different deposition temperatures to obtain unique film morphologies (50°C, 120°C and 200°C). The nucleation period and GPC of the ZnO grown on photoresist at the three temperatures is obtained in Figure 4.4b-d. It is seen from the figure that as the deposition temperature increased the nucleation period decreased and the GPC increased, which is the same behavior that was observed for the depositions on glass. The growth behavior data obtained here, specifically the nucleation periods, allows for the accurate deposition of the cantilever structural layers with the desired thickness.

Deposition on Flexible Substrates

Observation of the nucleation period and GPC for depositions on flexible substrates such as polyimide (Kapton tape) and paper were also demonstrated as seen in Figure 4.5. ZnO growth on the polyimide substrate had a nucleation period of 10 cycles and a GPC of 1.36 nm/cyc. Here, the growth mechanism on polyimide is similar to growth on PMMA. Since polyimide does not have the suitable reactive species for surface growth, the nucleation phase is expected to occur in the subsurface. After which the film grows above the surface in a linear fashion. The nucleation and growth rates are both quicker for polyimide than PMMA. This difference in the growth behaviors may be related to porosity of the polymer

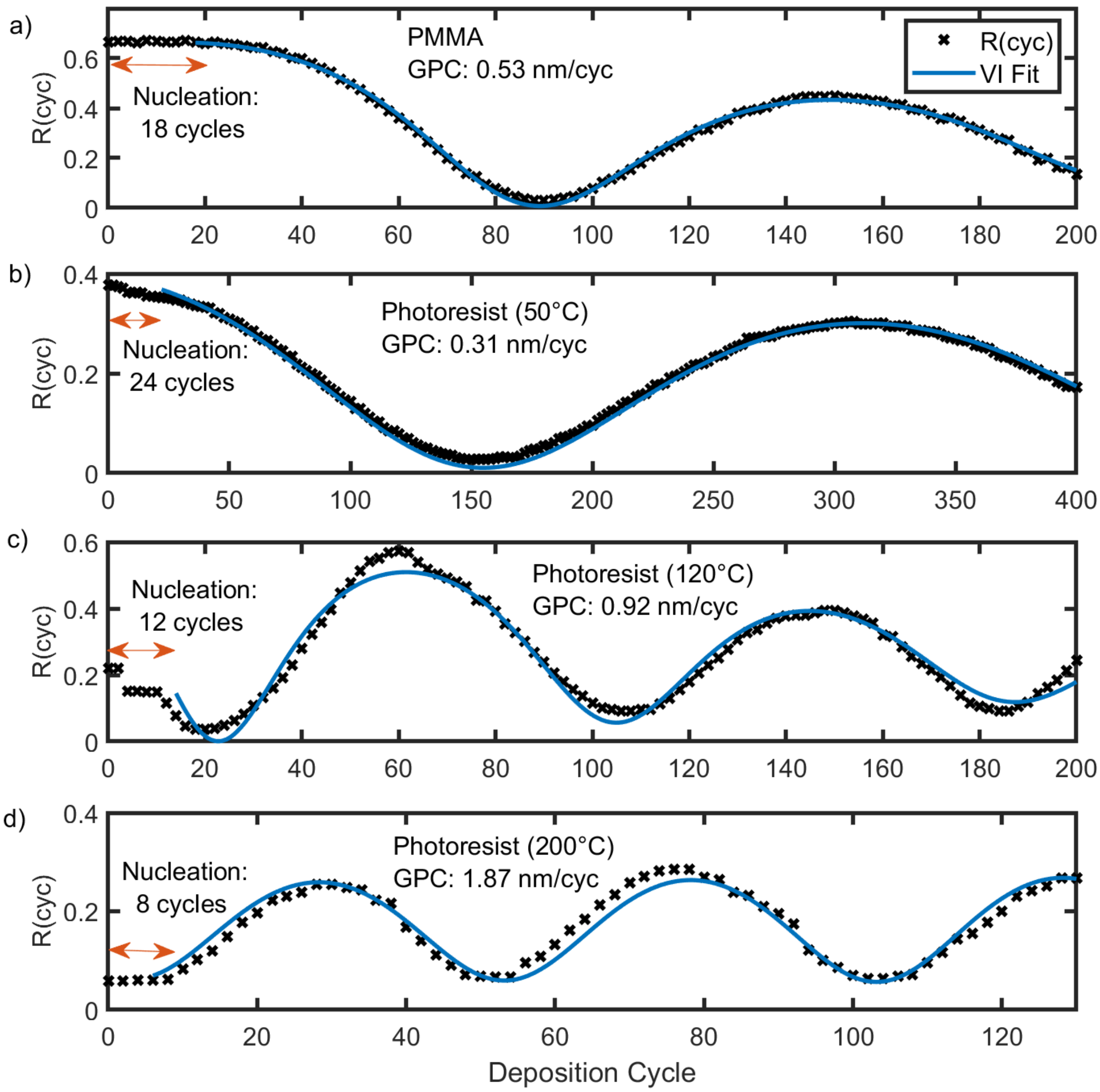

Figure 4.4: Measured reflectance intensity (black crosses) at λ = 400 nm as a function time (deposition cycles) for ZnO films grown on a) PMMA, and Shipley S1800 photoresist at a deposition temperature of b) 50°C, c) 120°C and d) 200°C. The data was fitted to the VI model (blue) to obtain the GPC (nm/cyc).

layers, size of the monomer (and molecular weight) and arrangement of the polymer chains.

For the deposition on paper substrates, fairly noisy reflectance intensities were observed (Figure 4.5b). This is because paper has a matte finish and is comprised of a random network of cellulose fibers with several air gaps (as opposed to a compact solid film), which results in poor reflectivity. Nevertheless, an oscillatory pattern in the reflectance-time data is still observed. Deposition on paper had a nucleation period of 48 cycles and a growth rate of 0.43 nm/cyc. Here, the nucleation is facilitated by the hydroxyl groups on the surface of the cellulose fibers [165]. The successful demonstration of nucleation period and GPC determination by reflectance, suggests that this method could be extended to other fiber based textile materials such as the polypropylene based fabrics in the next section.

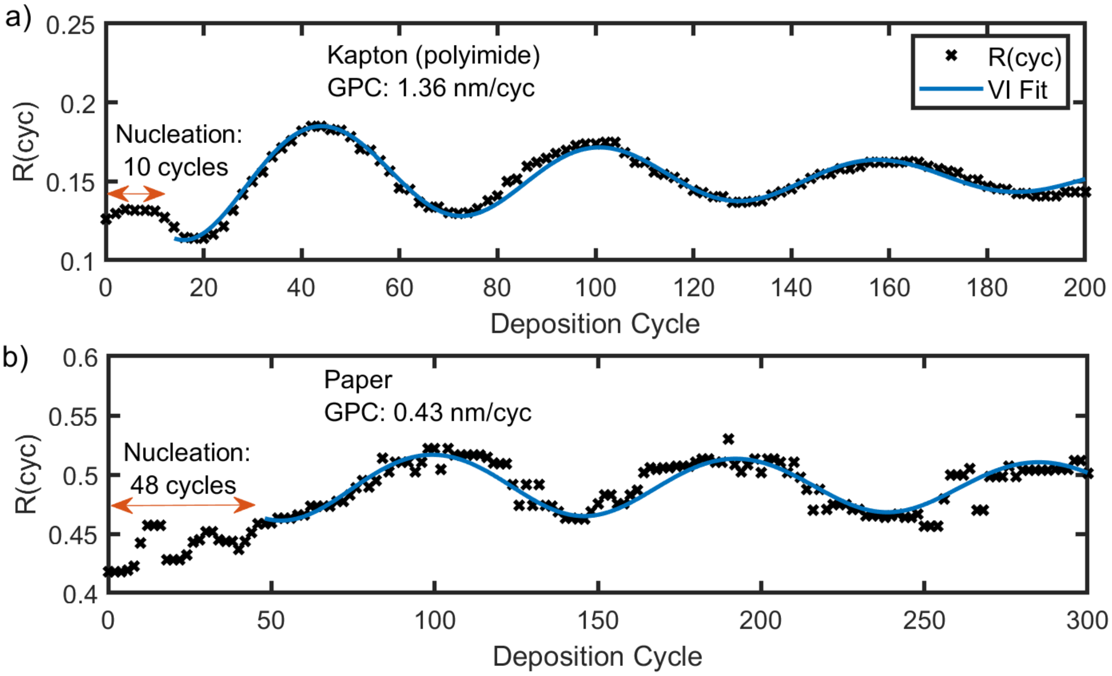

Figure 4.5: Measured reflectance intensity (black crosses) at $\lambda = 400nm$ as a function time (deposition cycles) for ZnO films grown on a) kapton (polyimide) and b) paper (sticky note). The data was fitted to the VI model (blue) to obtain the GPC (nm/cyc).

Deposition on Fabrics

The onset of the COVID-19 pandemic has spurred huge interest towards the development of antiviral coatings for personal protective equipment such as facial masks and other high contact surfaces. Some metal oxides have shown antiviral properties and therefore it is advantageous to use an atmospheric and scalable technique such as AP-SALD to coat large rolls of polypropylene fabrics utilized in N95 masks. Figure 4.6, demonstrates the ability of the in-situ reflectometry technique to observe the nucleation period and growth of ZnO on polypropylene fabrics utilized in N95 masks. Like paper, the fabrics are comprised of a random network of spunbound polyproylene fibers of varying densities. The growth behavior of ZnO on both the low density and high density fabrics is shown in Figure 4.6a and Figure 4.6b, respectively. Nucleation periods of 70 and 60 cycles were obtained for the low and high density fabric. This fairly long nucleation period likely is due to the lack of suitable reactive species (e.g. oxygen functional groups) in the polymer chain. This is followed by similar GPCs of 0.14 and 0.16 nm/cyc for the low and high density fabrics respectively.

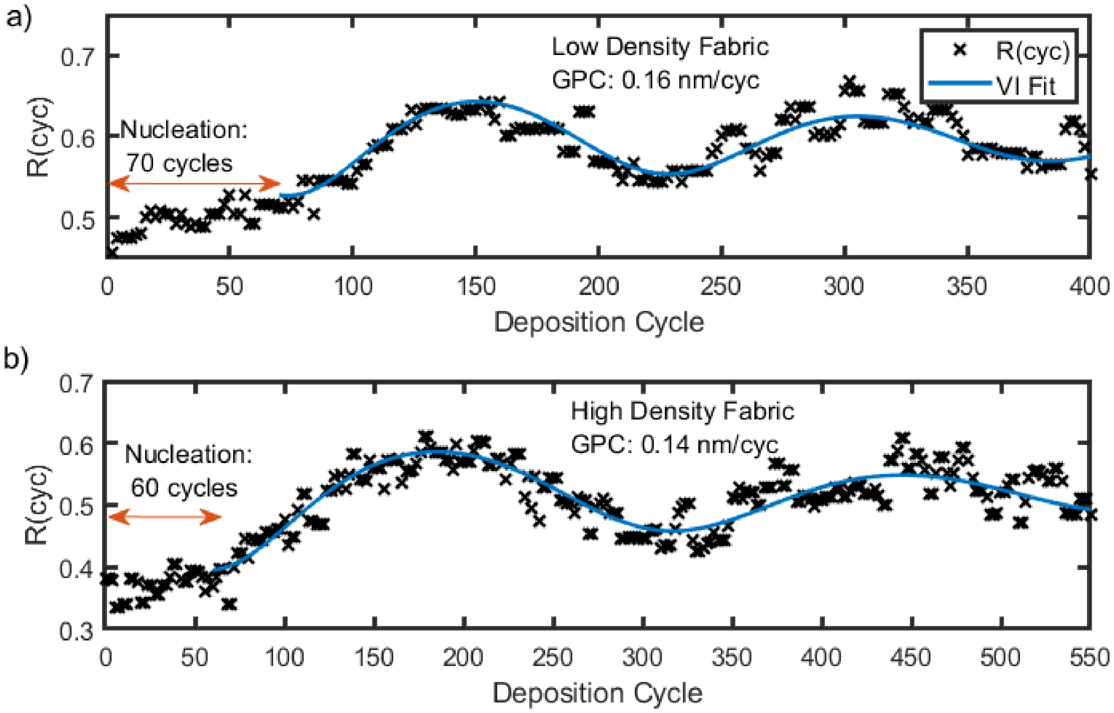

Figure 4.6: Measured reflectance intensity (black crosses) at $\lambda = 400nm$ as a function time (deposition cycles) for ZnO films grown on spunbound polypropylene fabrics of a) low fiber density and b) high fiber density. The data was fitted to the VI model (blue) to obtain the GPC (nm/cyc).

SEM was used to confirm the presence of film formation on the fabrics, shown in Figure 4.7. The uncoated fabric is shown in part a (100x) and c (2000x), while the fabric coated with 100 cycles of ZnO is shown in part b (100x) and d (2000x). Successful deposition of the ZnO film on the polypropylene fiber is confirmed by the matte-like surface appearance seen in part d compared to the metallic finish seen in part c which comes from surface charging effects of the organic compounds under SEM. Notably, the images show the conformality of the ZnO coating around a fiber as well as the ability to deposit on fibers that are within the fabric (as opposed to just fibers located on the outer surface of the fabric). Unfortunately the thickness of the ZnO coating could not accurately be determined from the SEM images due to the large variability in the fiber diameters (of several micrometers). Further investigation is warranted to determine the thickness of the coating and verify the obtained GPCs. One potential method for thickness determination is encasing the fabric in an epoxy and cutting the sample in half with low temperature ion milling to reveal its cross section for SEM imaging.

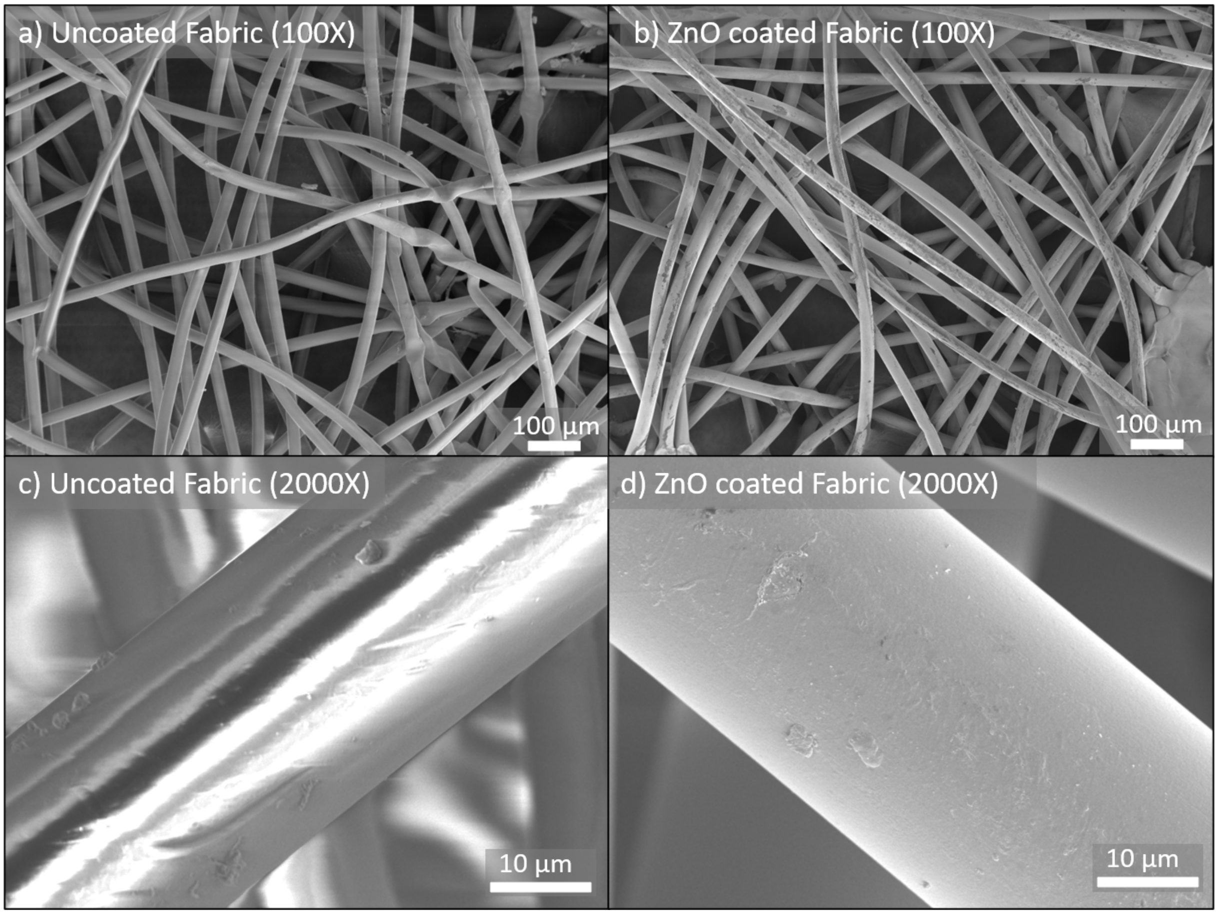

Figure 4.7: Scanning electron microscope (SEM) images of the uncoated (a and c) and ZnO coated (b and d) polypropylene fibers after 100 deposition cycles.

Deposition on 2D Materials

Finally, the nucleation period and growth of ZnO deposited on drop casted solutions of 2D materials is observed in Figure 4.8. The 2D materials were treated with a femtosecond laser as previously described in Chapter 2.2.2. Briefly, the laser treatment results in a reduction of the 2D flake size from microns to nanometers. Along with the reduction in size, the laser treatment introduces defects, dopants and functional groups to the flakes. This treatment process makes these 2D materials exciting for a variety of different applications including but not limited to solar cells, transistors and sensors. Coating these materials with a metal oxide layer to form hybrid nanostructures has shown to be beneficial for chemiresistive gas sensing [166] and therefore an understanding and accurate control of the metal oxide growth behavior on 2D materials, is of importance.

As seen in Figure 4.9a, the drop casted graphene oxide solution forms an opaque film. An optical microscope image (at 100x magnification) of the film (Figure 4.9b), shows that the graphene oxide forms a wrinkled but connected film. Images of the film after ZnO deposition are seen in Figure 4.9c-d. The optical microscope image shows a homogeneous coloration of the film surface indicative of ZnO coverage. The growth behavior of ZnO on graphene oxide is shown in Figure 4.8a. A short nucleation period of 6 cycles and a high growth rate of 1.18 nm/cyc was observed. Here, the ALD growth of ZnO on graphene oxide is easily done because of the oxygen functional groups and defect sites on the GO [167] This is in contrast to pristine graphene, which is chemically inert, does not contain defects and functional groups and therefore, must be oxidized first before a metal oxides can be grown. The growth is expected to occur in an island like fashion, where ZnO nuclei first form at the oxygen functional groups (primarily hydroxyl groups, OH). Subsequent deposition cycles serve to grow those individual islands until a continuous film is formed (after 6 cycles in this case). In some applications it is advantageous to have a discontinuous metal oxide film on graphene. This was demonstrated by Mu et al. who showed that a 0.5 nm discontinuous ZnO film on graphene had a higher detection sensitivity to formaldehyde gas than a continuous 3 nm ZnO film on graphene [168]. In this case, it is useful to use this reflectance technique presented here to reproducibly obtain the discontinuous metal oxide

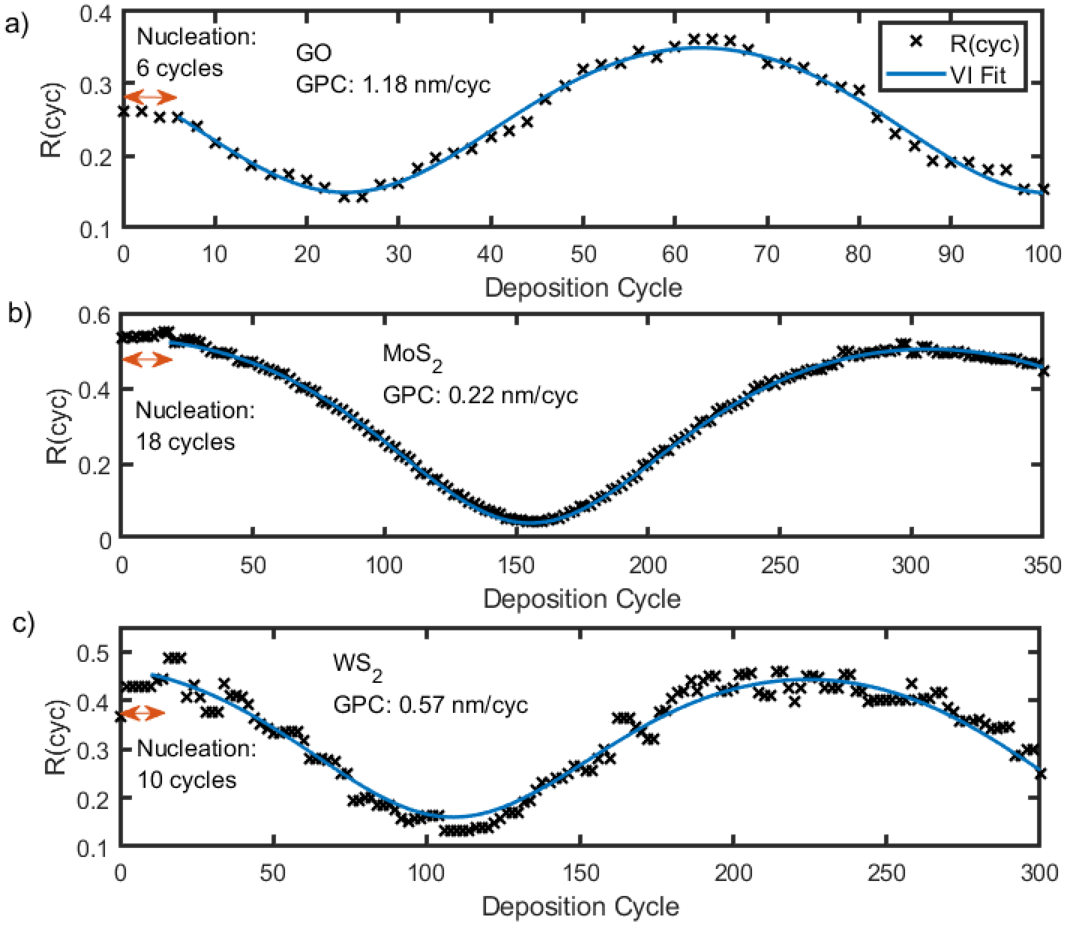

Figure 4.8: Measured reflectance intensity (black crosses) at $\lambda = 400\ nm$ as a function time (deposition cycles) for ZnO films grown on drop casted solutions of femtosecond laser treated a) graphene oxide, b) molybdenum disulfide (MoS_2) and c) tungsten disulfide (WS_2). The data was fitted to the VI model (blue) to obtain the GPC (nm/cyc).

film.

The ZnO growth on molybdenum disulfide (MoS_2) and tungsten disulfide (WS_2) is presented in Figure 4.8b and c. Images of the WS_2 film is shown in Figure 4.10. A semi continuous film of WS_2 nanoparticles is formed as seen from the optical microscope image in Figure 4.10b. The nucleation periods of 18 and 10 cycles for the MoS_2 and WS_2 respectively, were longer than the nucleation period for graphene oxide. Similar to pristine graphene, the deposition on the MoS_2/WS_2 basal plane is expected to be strongly inhibited and instead occurs at the grain boundaries or edges of the flakes which have higher chemical reactivity [169]. Possible nucleation sites on the edges of the flakes include

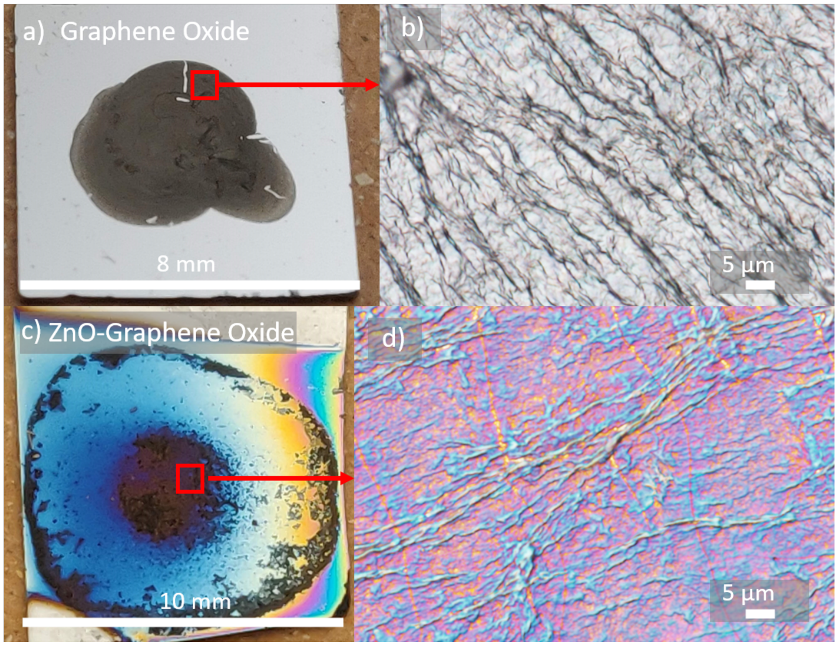

Figure 4.9: a)Drop casted GO film on silicon. b) Optical microscope image (100x) of GO film. c) ZnO deposited on drop casted GO film. d) Optical microscope image (100x) of ZnO deposited on GO film.

oxidized metal (Mo-O or W-O), oxidized sulfur (S-O) as well as edge sulfur sites that can react directly with the metal precursor (resulting in S-Zn bonds in this case) [170]. The shorter nucleation period for GO compared to MoS_2/WS_2 is likely due to the higher number of available oxygen nucleation sites. Correspondingly, both materials had lower GPCs than GO (0.22nm/cyc and 0.57nm/cyc for MoS_2 and WS_2, respectively). An SEM image of the ZnO deposited on WS_2 is shown in Figure 4.10d. The bare WS_2 particles are not observed, instead replaced by ZnO particles with a hexagonal type shape. This suggests that the WS_2 served as nucleation sites for the ZnO, which continued to grow until it fully encompassed the WS_2 particles. Similar images are expected for the uncoated and ZnO coated MoS_2 samples, due to structural similarities of MoS_2 and WS_2.

4.4 Conclusion

In this chapter, the in-situ reflectometry technique was used to observe the growth behavior of ZnO films, deposited by AP-SALD, onto various surfaces. The reflectance intensity at

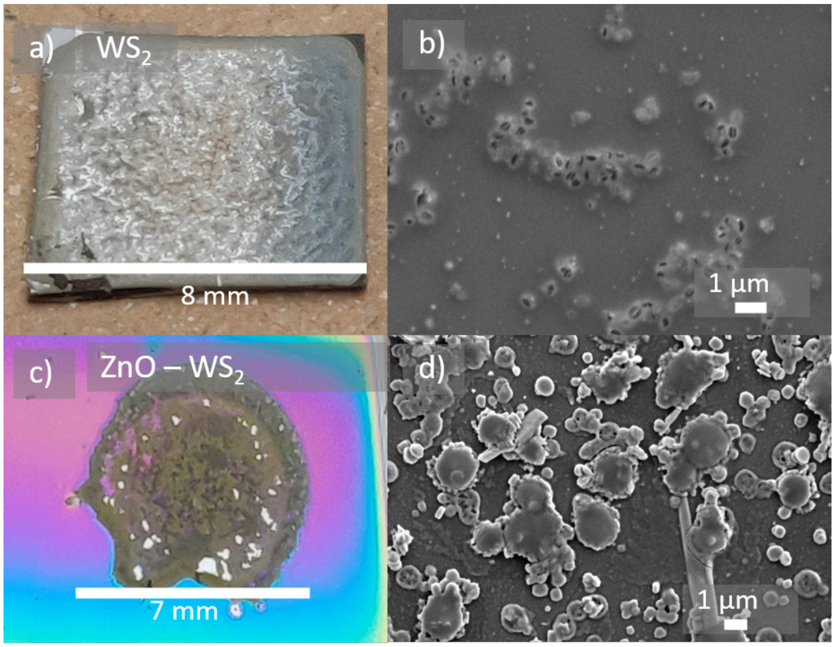

Figure 4.10: a) Drop casted WS_2 film on silicon. b) SEM image (7000x) of drop casted WS_2. c) ZnO deposited on drop casted WS_2 film. d) SEM image (5000x) of ZnO deposited on WS_2.

a single wavelength was obtained in time (deposition cycles) and fitted to the VI model to determine the growth rate per cycle. Nucleation times were obtained by observing the number of cycles until a significant change in reflectance intensity was observed. This approach addresses a weakness of the Fresnel reflectance model (used in Chapter 3) where the optical properties of the underlying substrate need to be known beforehand. The growth behavior of ZnO was determined on various conventional and non-conventional substrates where the optical properties of the substrate where unknown. This includes surfaces like polymer films, flexible plastics, fabrics comprised of a random network of fibers and drop casted solutions of two dimensional nanoparticles. The chemical composition of the different surfaces greatly influences the nucleation behavior of ZnO and therefore produces different nucleation times and growth rates.

The monitoring of nucleation time, allows for the accurate deposition of thin films on various surfaces which may have implications on their intended application. This is relevant because many applications require the deposition of metal oxide films on non-conventional surfaces. For example, ZnO was deposited on polypropylene fabrics utilized to make N95 masks with antibacterial or antiviral capabilities. The suitability of a ZnO/WS_2 hybrid for use in a MEMS type gas sensor is evaluated in Chapter 5. In both of these applications the nucleation period must be accounted for during the deposition of ZnO on these surfaces to ensure adequate coverage.

It's clear that the obtained reflectance data is for a single spot on the substrate. For that single measurement spot, the nucleation period and GPC are determined. The applicability of the obtained results to the rest of the substrate depends on the substrate itself and the AP-SALD technique. For flat uniform substrates such as glass, metals and polymer films, the film growth is expected to be uniform throughout. Although, there will be a small degree of non-uniformity which may come from uneven reactor head spacing (i.e., human error) or the increased incorporation of oxygen on the outer edges of the substrate which is readily accessible by atmospheric oxygen [171]. For porous substrates such as the polypropylene fabrics used in this work, the porosity or density of the fabric is consistent throughout the material. Therefore, the measured growth behavior of ZnO on those substrates is applicable for the entirety of the deposition area. However, as shown in Figure 4.9 and Figure 4.10, drop casted samples of the laser treated 2D materials produce a non-uniform distribution of material on the silicon substrate. This is due to the agglomeration of the particles and their movement during solvent evaporation. In this case the obtained growth behavior of ZnO on those samples is only applicable to the measurement spot itself. The density of these particles varies throughout the deposition area which would likely result in different ZnO growth behaviors. Here the objective was to simply demonstrate the ability of the reflectance technique to observe the growth behavior of ZnO on 2D materials. If the particles were uniformly dispersed on the substrate (via spin coating or other synthesis methods), then the obtain growth data of the single spot would be applicable throughout the sample.

Similarly, in Chapter 6 ZnO is deposited onto photoresist sacrificial layers to form a cantilever structural layer. The thickness of the ZnO layer is critical to the structural integrity of the beam, its natural resonance frequency and ultimately its performance as a sensor. Therefore the GPC should be monitored to achieve precise ZnO thicknesses for the cantilever. This growth behavior should not be estimated from the growth behavior on conventional substrates like glass or silicon, which had different nucleation times and GPCs than ZnO growth on photoresist.

“Do you smell it? That smell, a kind of smelly smell. A smelly smell that smells…smelly”

— Mr.Krabs

Chapter 5

Reflectance Screening Technique for Responsive Gas Sensor Materials

5.1 Introduction

A key component of gas sensor devices is the receptor material, which interacts with a gas and produces a measurable response (signal transduction) indicating successful detection of a chemical. In resistive based gas sensors, gas adsorption on a receptor material results in a change in its electrical properties (e.g., resistivity/conductivity). Whereas receptor materials in MEMS gas sensors typically take advantage of a physical change in material properties when interacting with a chemical gas such as film expansion, stress changes and mass changes [4]. Extensive research efforts have gone into discovering and developing novel materials that are able to sense various gases with high sensitivity and selectivity. Ultimately, to evaluate a material’s sensing capabilities, it needs to be integrated into a fabricated gas sensor device and tested under the appropriate conditions. However, the fabrication of MEMS devices can be quite lengthy and costly.

As discussed in Chapter 2.1.1, the fabrication of MEMS sensors often involves many steps which contributes to its complexity and cost. The process involves the deposition of several layers, that are patterned through lithographic and etching techniques followed by a release etching step to realize freestanding structures. These efforts could be outsourced to a MEMS foundry but can be costly especially if many different receptor materials need to be tested. In some cases the receptor material must be incorporated into the MEMS structure at an intermediate step instead and therefore a custom fabrication process is required. Essentially, the prototyping and testing of many different receptor materials with MEMS sensors could be considered infeasible. For these reasons, a screening technique may be preferred to identify those materials which have a positive response to target gases before incorporation into the fabricated MEMS devices.

Simulation methods such as density functional theory (DFT) calculations, can be used as a screening tool for responsive gas sensor materials. In DFT studies, the adsorption behavior of a single molecule (of the target analyte) on a receptor material is determined. The simulation outputs adsorption energies, bonding distance and the spatially distributed charge density. Higher adsorption energies and short bonding distances are indicative of high adsorption strength which can often be correlated to its performance as a gas sensor [172–175]. However, DFT studies do not provide much information about signal transduction upon gas adsorption, such as the change in electrical properties for resistive gas sensors or change in physical properties for MEMS sensors. Furthermore, the simulation is done with a single molecule of the target gas and a finite area of the receptor material which evidently does not reflect the real conditions the gas sensor is tested under. To this end, experimental screening techniques are required.

For the screening of receptor materials for resistive gas sensors, a combinatorial high throughput (CHT) approach has been reported. In these CHT studies, a custom multi-electrode substrate was used where many receptor materials (up to 64) can be deposited and measured in parallel under the appropriate testing conditions [176–178]. By doing so, the screening of receptor materials is accelerated. However, this approach is only valid for resistive gas sensors and still requires the fabrication of the gas sensor electrodes. It would be challenging to adopt a similar approach for MEMS sensors, for the reasons discussed above.

The use of optical techniques such as operando UV/vis diffuse reflectance spectroscopy was introduced by Degler et al. to study tin oxide (SnO_2) resistive gas sensors [110]. The UV/vis reflectance spectra of a SnO_2 film was monitored in dry nitrogen and during exposure to carbon monoxide (CO) and oxygen (O_2) gases. Upon exposure to the gases, a clear change in the reflectance spectra was observed. Similar results were presented by Elger et al. who demonstrated a change in the SnO_2 reflectance spectra upon exposure to an ethanol/nitrogen gas mixture [111]. In both cases, the change in reflectance spectra was attributed to the formation of oxygen vacancies and the chemical reduction of the individual SnO_2 grains causing a change the film's overall photon absorption behavior. In this case, reflectance spectroscopy can be used to screen metal oxides as receptor materials in resistive gas sensors. As was demonstrated in Chapter 3 and Chapter 4, in situ reflectometry can be used to monitor changes in thin film thickness. Thus it is also expected that reflectometry can be utilized to screen for receptor materials that change in volume when exposed to a gas. These materials can then be incorporated into MEMS type structures that take advantage of this phenomena for gas sensing.

In this work, the reflectance signal of various potential receptor materials is monitored as they are exposed to VOC vapors such as water, acetone, and ethanol. First the method is tested with PMMA, a receptor material that is known to expand or swell in the presence of VOC vapors, to validate the ability of reflectance method to capture the swelling behavior. The technique is then used to monitor the response of 2D materials such as graphene oxide (GO), MoS_2 and WS_2, which are produced by a femtosecond laser treatment method. Finally the the response of metal oxide thin films produced by AP-SALD is monitored to evaluate their suitability as receptor materials in MEMS sensors.

5.2 Experimental Section

5.2.1 Materials

All receptor materials tested in this work were prepared on silicon wafer pieces. PMMA prepared by Rishard Rameez, a PhD student at the university of Waterloo was drop casted onto a silicon substrate and dried. Solutions of graphene oxide, molybdenum disulifde (MoS_2) and tungsten disulfide (WS_2) were treated with a femtosecond laser treatment technique described in Chapter 2.2.2. The laser treatment was done by Dr. Khaled Ibrahim, a former doctoral student at the University of Waterloo. The experimental details of the laser treatment are described in Chapter 4.2.1. The solutions were drop casted (1 μL volume) onto the silicon substrate and dried at 60°C. ZnO coated WS_2 is prepared by AP-SALD as described in Chapter 4. Similarly, bare metal oxide films of ZnO and SnO_2 (100 nm thickness) are deposited on silicon by AP-SALD. ZnO deposition by AP-SALD have been described in Chapter 3. The AP-SALD of SnO_2 was done by Louis Delumeau, a masters student at the University of Waterloo. The precursors tetrakis-(dimethylamino) tin(IV) (TDMASn) and ozone were used as the Sn and oxygen precursor, respectively.

5.2.2 Experimental Setup

Figure 5.1 depicts the gas delivery system and reflectance measurement setup. The prepared receptor material samples were placed in a sealed enclosure (5.4 $in.$ × 4 $in.$ × 3 $in.$) with openings for a gas inlet and outlet line as well as a quartz window for reflectance measurements. A bifurcated reflectance probe was mounted above the quartz window and connected to a UV-vis spectrometer (Ocean Optics HDX) and light source (Ocean Optics DH-2000). Reflectance spectra are captured every second and stored. For most of the receptor materials tested the reflectance intensity at a wavelength of 655 nm was used, which is the location of the deuterium alpha emission peak which provides a high signal to noise ratio.

The gas delivery system comprised of two mass flow controllers (MFCs), compressed nitrogen gas, analyte and mixing vials is shown on left side of Figure 5.1. The analytes used in this study (water, ethanol and acetone) were placed in the analyte vial. Similar to bubbling of precursors for AP-SALD, the analytes are carried by the compressed nitrogen gas (controlled by MFC 1). Pure nitrogen for purging the chamber before and after the analyte exposure is controlled by MFC 2. Both the analyte stream and the nitrogen stream are fed to a mixing vial and then fed to inlet connection of the enclosure. Unless otherwise stated, each receptor material tested was exposed to analyte solvent vapors for 10 minutes at a flow rate of 1000 SCCM (MFC 1). 10 minutes of pure nitrogen at 1000 SCCM (MFC 2) was injected into the chamber before and after the analyte exposure for purging.

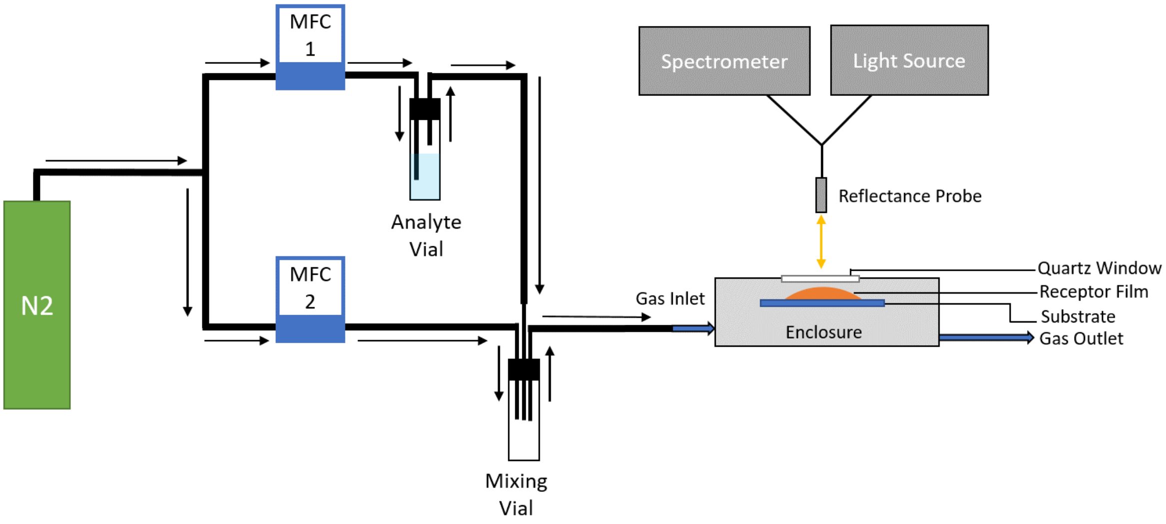

Figure 5.1: Schematic of gas delivery system and reflectance measurement setup.

5.3 Results and Discussion

As discussed in Chapter 2.1.2, PMMA has been used a receptor material in MEMS gas sensors due to the innate swelling behavior of polymers when exposed to various gases [179]. This behavior was captured by reflectance measurements, as shown in Figure 5.2, for a PMMA film deposited on silicon exposed to water, acetone and ethanol vapors.

The change in reflectance intensity at 655 nm is shown for the PMMA film on silicon. The first 10 minutes (600s) corresponds to purging the test chamber with a nitrogen purge

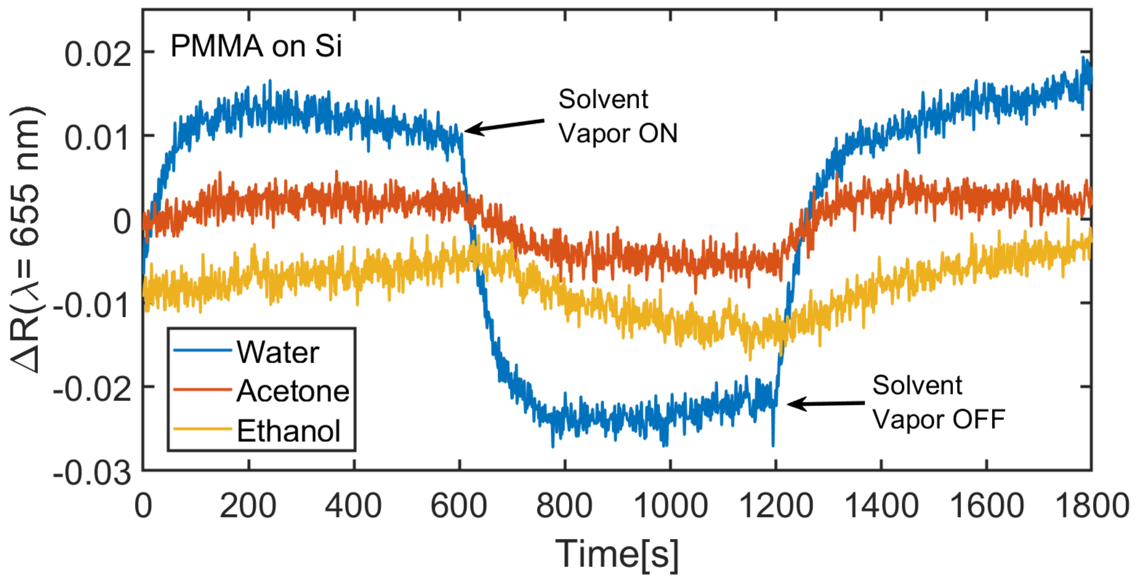

Figure 5.2: Change in reflectance intensity (at $\lambda = 655$nm) of a PMMA film drop casted on silicon. The film was exposed to vapors of water (blue), acetone (red), and ethanol (yellow). Data is intentionally staggered along y-axis.

gas, followed by separate exposures to water(blue), acetone(red) and ethanol(yellow) vapors for 10 minutes and a subsequent 10 minute nitrogen purge. Here, the reflectance intensities are decreasing when exposed to the solvent vapors which indicates film expansion. Changes in the reflectance intensity correspond to a change in film thickness. However, it is not clear if the film is expanding or contracting. This is because both positive or negative changes in the reflectance intensity can indicate an increase and or decrease in the film thickness as observed in Chapter 4 where the reflectance of a growing film was shown to oscillate in time. However, based on the mechanism of gas interaction with the materials tested (as reported in literature), it is likely the films are expanding or "swelling". This change in reflectance intensity is observed at all measured wavelengths, but the reflectance at 655 nm is chosen as it has the highest signal-to-noise ratio due to the deuterium alpha emission peak from the light source. Once the solvent vapor was removed, the reflectance intensity starts to recover back to its original value which is suggests film contraction. The largest change in reflectance intensity was for the water vapor, while smaller changes were observed for acetone and ethanol. The reflectance intensity for water also reaches a saturated value which suggest that no further water absorption can take place. The behavior is seen for acetone as well, although less pronounced. It appears the response for ethanol never reaches saturation (within 10 minutes of exposure), and it is also the slowest to recover. It is possible that the slower recovery observed for ethanol is due to a stronger sorption affinity of this specific PMMA formulation to ethanol. The higher response for water may be due to its smaller molecular size compared to acetone and ethanol which allows it to have a higher diffusivity into the polymer. It is important to note that the due to the high variability in the composition of PMMA films (different molecular weights, solvents and processing) reported in literature it is difficult to compare the gas sensing response shown here to the gas sensing response of PMMA reported elsewhere. Despite this, these results verify that the reflectance method can be used to observe the expansion/swelling behavior of receptor materials when exposed to a gas.

The reflectance method is now used towards the experimental discovery of receptor materials that can be potentially used in MEMS gas sensors. The first of which is graphene oxide that was produced with a femtosecond laser treatment method. The laser treatment simultaneously reduces the size of the graphene oxide flakes and introduces defects and functional groups from the solvent it was processed in. Here the graphene oxide was treated in the 1:1 ethanol:water solution. Figure 5.3 shows the reflectance response of the GO (drop casted on silicon) to solvent vapors tested. Interestingly, the largest response was observed for ethanol, while the lowest response was observed for water. Likewise, the response to ethanol reached a saturated value while it did not for water (within 10 minutes of exposure). While the response to water recovered fully to near its original value, the responses for ethanol and acetone never did fully recovery to their original value and instead recovered to a new point. The swelling behavior of graphene oxide films in the presence of water [23, 180] and various alcohols [181, 182] has been previously reported. The deposited GO film is comprised of several layers of overlapping flakes. Similar to polymer materials, it is expected that the analyte molecules infiltrate this layered structure and go into the gaps between the flakes pushing them outwards which causes an expansion of the overall film. Functional groups on the surface of the graphene oxide may favor the sorption of ethanol over acetone and water. Further investigation into these mechanisms for GO is presented in Chapter 7.

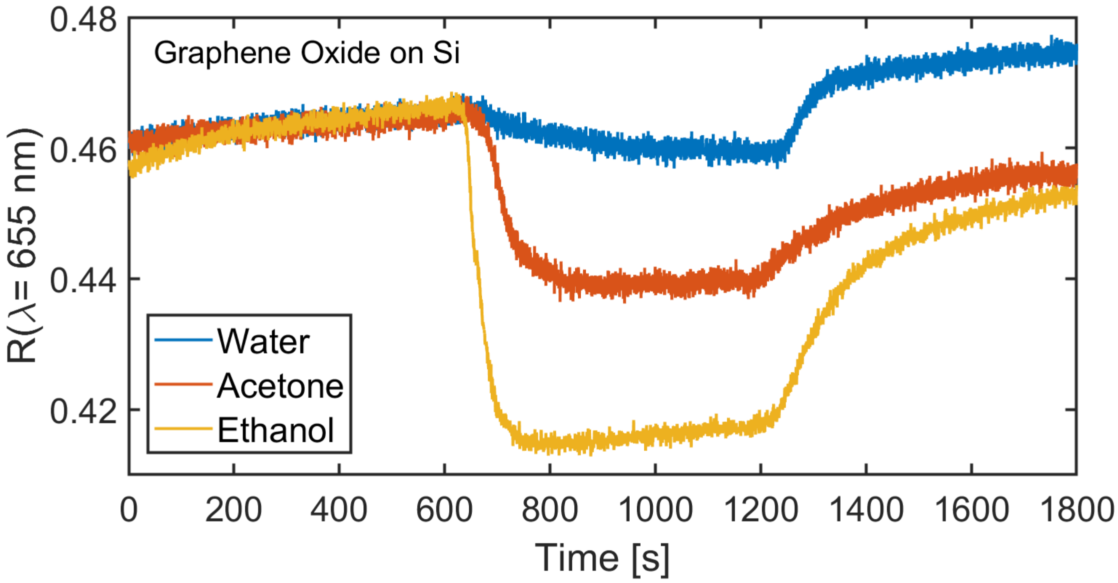

Figure 5.3: Reflectance intensity (at λ = 655nm) of Graphene Oxide (GO) drop casted on silicon. The sample was exposed to vapors of water (blue), acetone (red), and ethanol (yellow).

The response of the laser treated MoS_2 and WS_2 (drop casted on silicon) is shown in Figure 5.4 and Figure 5.5, respectively. The largest response for both receptor materials was obtained for water. Clear responses to acetone and ethanol were obtained for WS_2 unlike MoS_2, which had a near-negligible change in intensity for the same solvents. For WS_2, a quicker response time is observed for acetone compared to water. While the response to ethanol vapor resulted in an initial small decrease in intensity before increasing. This probable swelling behavior, in the presence of a gas, for MoS_2 and WS_2 has not been reported previously, but it is expected to follow the same mechanism as graphene oxide due to their similar flat flake-like structures. Further investigation into these adsorption mechanisms for MoS_2 and WS_2 is presented in Chapter 7.

Hybrid heterojunction nanostructures comprised of a metal oxide and a 2D material have been used as receptor materials in chemiresistive gas sensors. In these composite type materials, the sensing advantage primarily comes from the interface between the two materials where a charge carrier depletion zone exists. The conductivity of this area is strongly modulated by gas adsorption and desorption, hence making these hybrid materials suitable for chemiresistive gas sensors [166]. The benefits of a metal oxide/2D material receptor for

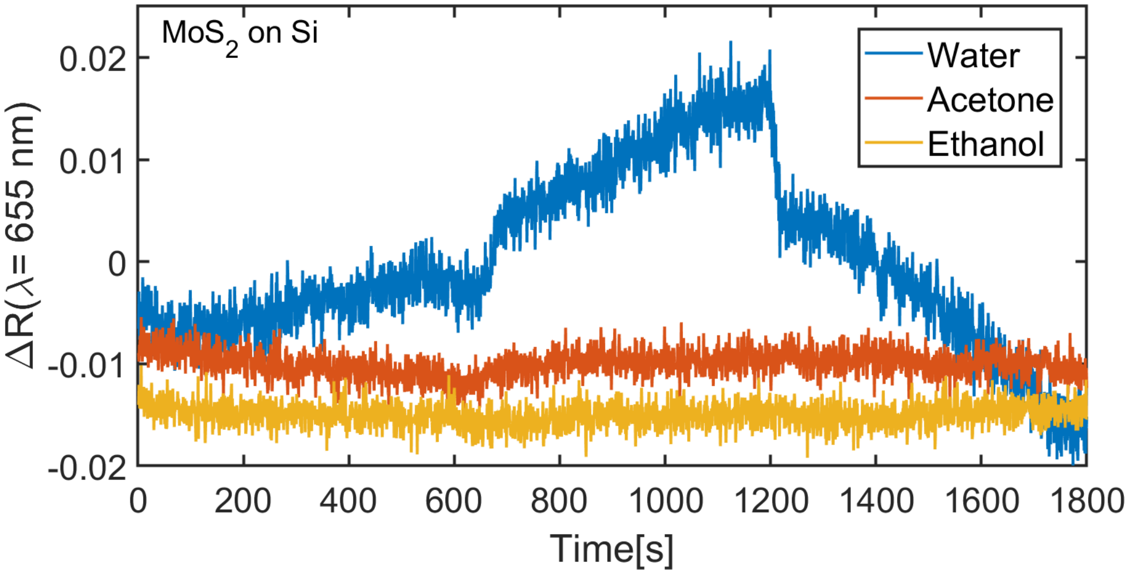

Figure 5.4: Change in reflectance intensity (at $\lambda = 655$nm) of MoS_2 drop casted on silicon. The sample was exposed to vapors of water (blue), acetone (red), and ethanol (yellow). Data is intentionally staggered along y-axis.

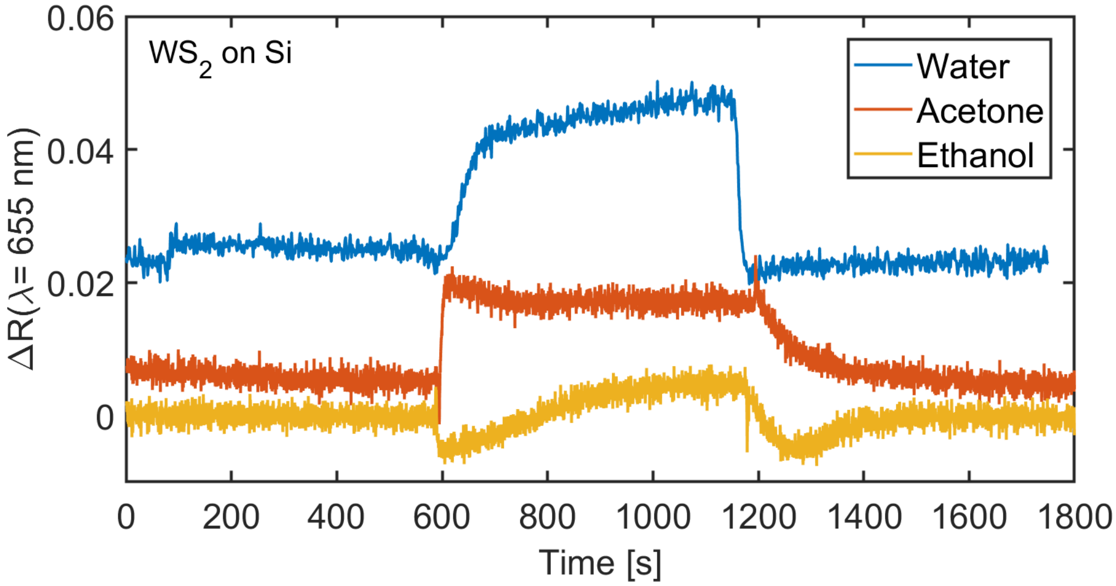

Figure 5.5: Change in reflectance intensity (at $\lambda = 655$nm) of WS_2 drop casted on silicon. The sample was exposed to vapors of water (blue), acetone (red), and ethanol (yellow). Data is intentionally staggered along y-axis.

MEMS gas sensors have not yet been realized but is studied here with reflectance. Zinc oxide was deposited onto a drop casted sample of WS_2, by the AP-SALD technique described in Chapter 3 and its growth was monitored by the technique describe in Chapter 4. The reflectance response of the ZnO/WS_2 hybrid structure is shown in Figure 5.6.

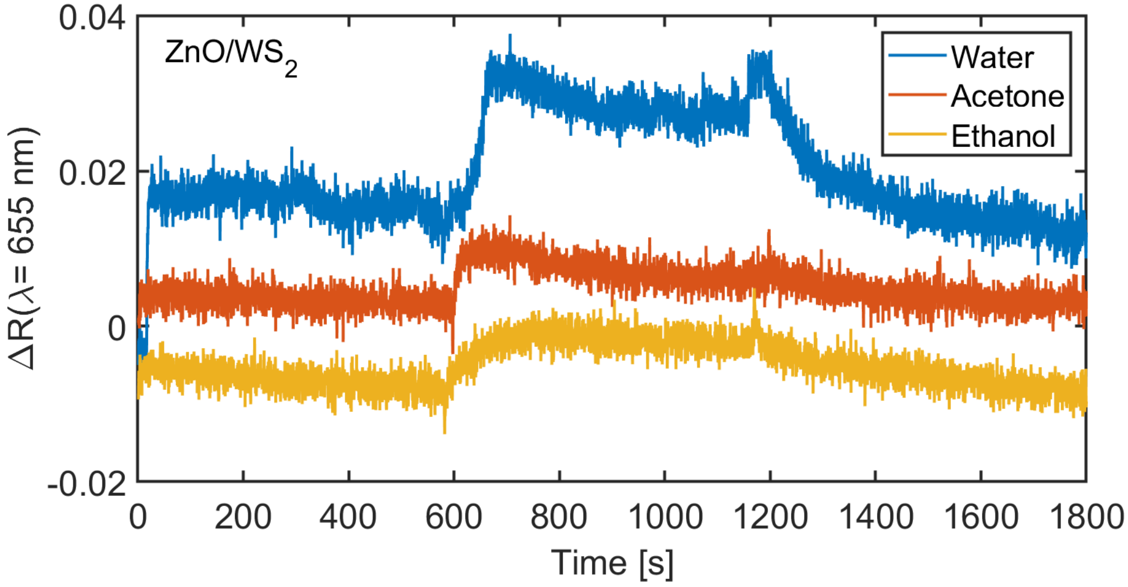

Figure 5.6: Change in reflectance intensity (at $\lambda = 655$nm) of ZnO coated WS_2 drop casted on silicon. The sample was exposed to vapors of water (blue), acetone (red), and ethanol (yellow). Data is intentionally staggered along y-axis.

Evidently, the response of the ZnO/WS_2 material to the solvent vapors is not improved compared to the response of WS_2 alone. While the responses to water are comparable, the responses to acetone and ethanol are lower for the hybrid material. These results suggest that the ZnO may be limiting the expansion behavior of the WS_2. Therefore despite being promising receptor materials for chemiresistive sensors, ZnO/WS_2 hybrids appears less promising for MEMS sensors.

Next, the reflectance response of metal oxide thin films (deposited by AP-SALD) was measured when exposed to the solvent vapors. Figure 5.7a shows the response of a ZnO thin film to water, acetone and ethanol vapors and Figure 5.7b shows the response of a SnO_2 thin film to acetone and ethanol vapors. No measurable change in the reflectance spectra (at all wavelengths) was observed for the ZnO thin film. In contrast, a change in reflectance spectra was detected for the SnO_2 film, but notably only occurred at larger wavelengths corresponding to the near-infrared range ($\lambda \geq 760$ nm). In this wavelength range, the SnO_2 reflectance intensity decreased when exposed to ethanol and acetone.

Since this shift in intensity was not observed at other wavelengths (UV-Vis), it can be concluded that the thickness of the ZnO and SnO_2 films is not changing. Metal oxide films deposited by ALD are often used as non-permeable diffusion barriers for moisture or oxygen sensitive materials [183]. This is because ALD produces compact, dense films. The ZnO and SnO_2 film used here were deposited by AP-SALD and are of comparable quality in terms of density and compactness. Thus, no analyte absorption or infiltration into the films is expected and correspondingly, no volume expansion or increase in thickness.

The decrease in the reflectance intensity for SnO_2 in the near-IR range may be attributable to chemical reduction of the SnO_2 by the analyte molecules which in turn changes the free charge carrier concentration in the film. The free charge carrier concentration influences the IR absorption properties of the film. As discussed previously, similar results for an SnO_2 film exposed to carbon monoxide and ethanol (at a temperature of 300°C) were reported by Degler [110] and Elger [111], respectively.

The SnO_2 exposure to acetone was repeated at an elevated temperature of 200°C. This was done by placing the test chamber on a hotplate. The obtained reflectance response is compared to the room temperature measurement in Figure 5.8. It is evident that the heated film had a larger decrease in the reflectance intensity than the RT film. This shows that the SnO_2 response to chemical analytes is greater when when heated, which follows why metal oxide based gas sensors are often heated (200°C-400°C). The higher operation temperature facilitates larger chemical reduction of the metal oxide material, promotes adsorption of the analyte and enhances the conductive properties of the metal oxide [15]. Conversely, the zinc oxide film heated to 200°C showed no observable reflectance response to the vapors tested. Hence, the reflectance screening technique is used here to show that SnO_2 may be a favorable receptor material for chemiresistive gas sensors while ZnO may not be. It follows that much of the literature in metal oxide chemiresistive gas sensors utilizes SnO_2 and it is widely used in commercial chemiresistive gas sensor products as well [5, 15]. Whereas implementation of ZnO in chemiresistive gas sensors often requires doping to enhance the response. Ultimately, in the scope of this work, it appears that both of the metal oxides tested here are not suitable for MEMS sensors that take advantage of

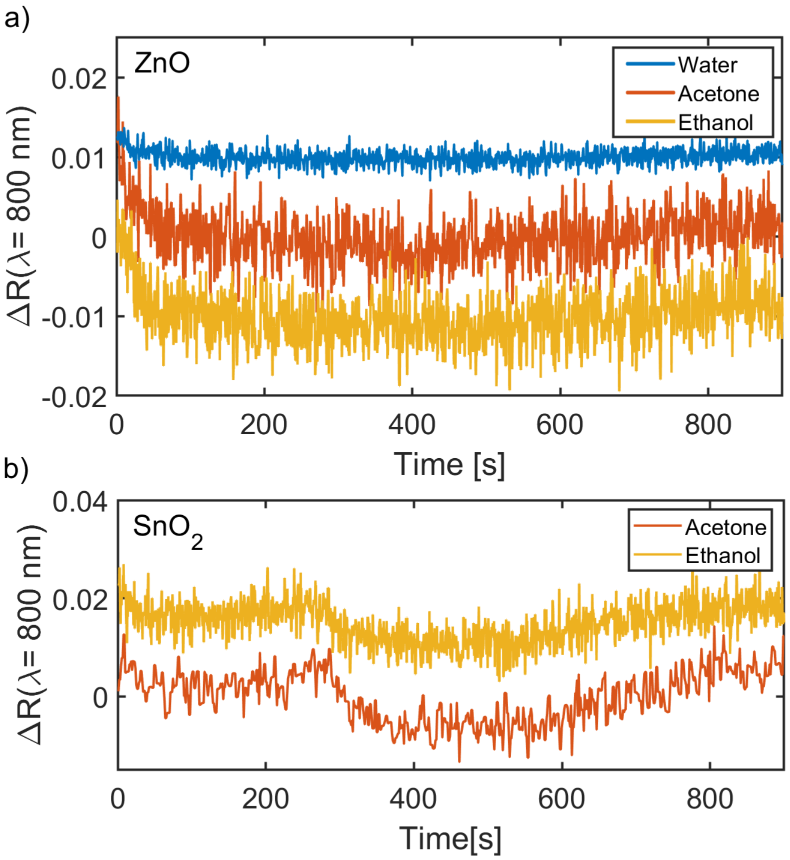

Figure 5.7: Change in reflectance intensity (at λ = 800nm) of thin films of a) Zinc Oxide (ZnO) and b) Tin Oxide (SnO_2) deposited on silicon. The films were exposed to vapors of acetone (blue), and ethanol (red).Data is intentionally staggered along y-axis.

volume expansion or swelling such as the static MEMS sensors discussed in Chapter 2.1.1 and Chapter 7.

5.4 Conclusions

An optical method based on reflectance was used to screen for potential receptor materials for use in static deflection type MEMS gas sensors. Films of potential receptor materials were prepared on silicon substrates and exposed to vapors of water, ethanol and acetone in a sealed chamber. The reflectance of the receptor materials exposed to vapors was obtained. A clear reversible change in reflectance intensity is observed upon exposure to the analyte vapors which is indicative of film expansion or swelling. This behavior was observed for

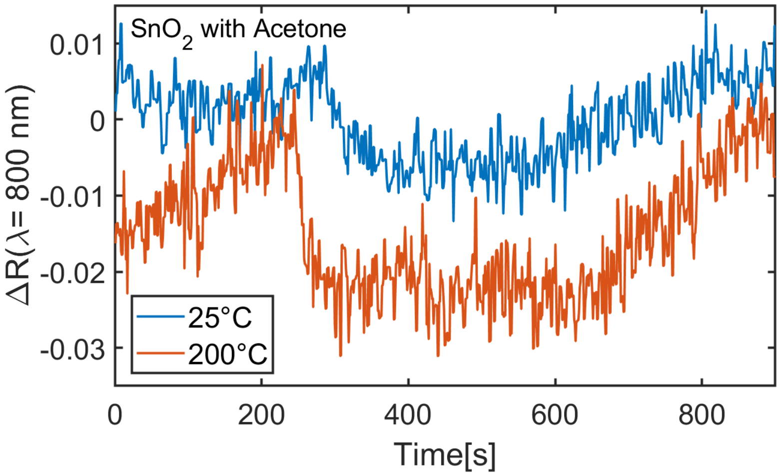

Figure 5.8: Change in reflectance intensity (at $\lambda = 800$nm) of thin films of tin Oxide (SnO_2) deposited on silicon. The film were exposed to vapors of acetone at a chamber temperature of a) 25°C and b) 200°C.

PMMA, laser treated graphene oxide, MoS_2 and WS_2, where the analyte molecules are allowed to infiltrate into the porous structure of the films and cause expansion. This behavior was not observed for ZnO films deposited by AP-SALD which are compact in nature. However, a change in the reflectance at IR wavelengths was observed for SnO_2 likely due to the high carrier concentration in the film which can interact with IR wavelengths. The response of SnO_2 to acetone was further enhanced when the substrate was heated to 200°C.

The results suggests that PMMA and laser treated 2D materials are suitable receptor materials for static deflection MEMS gas sensors, while the metal oxide films are not. Furthermore, the coating of WS_2 with ZnO did not improve its "swelling" behavior compared to uncoated WS_2. So while hybrid ZnO/WS_2 receptor materials have advantages in chemiresistive gas sensing, they are not ideal for MEMS static deflection sensors. In Chapter 7, the laser treated GO, MoS_2 and WS_2 are coated onto a nanomechanical membrane type surface stress sensor (described in Chapter 2.1.2), for the sensing of various volatile organic compounds.

"Everything in life is vibration"

— Albert Einstein

Chapter 6

A Zinc Oxide Resonant Cantilever Gas Sensor

6.1 Introduction

Resonant microcantilever sensors are known for their high sensitivity to single molecules and the ability to make indirect mass estimations in the atto- and zepto-gram range. These type of devices can therefore be used as gas sensors for the detection of toxic gases and environmental pollutants in low quantities. As described in Chapter 2.1.1, cantilever gas sensors are typically comprised of a structural layer, which makes up the main cantilever body, and a sensing or receptor layer that has an affinity for a target gas analyte. Zinc oxide is one such receptor material, popular for chemiresistive gas sensing due to its large density of surface vacancies which can act as active sites for chemisorption. For these reasons, many researchers have explored the benefits of combining resonant microcantilever sensors with zinc oxide receptors, as discussed in Chapter 2.1.3.

In general, approaches have consisted of growing a "forest" of vertical 1D ZnO nanostructures (e.g., nanowires or nanorods), onto the surface of a cantilever structural layer (typically silicon). The main advantage to using 1D nanostructures is the higher surface area available for analyte adsorption. These devices have been used for RH sensing and towards the detection of DEA [48], nitrogen dioxide [51] and carbon monoxide [52–54]. ZnO nanomaterials have also been implemented into QCM resonant gas sensors for RH (RH) sensing and the detection of various VOCs. The details of these reported devices and their sensitivities are listed in Table 2.1. For RH sensing, the best performing ZnO based QCM sensor [55] had a sensitivity of $100 \frac{Hz}{\%RH}$ while the best performing ZnO based cantilever sensor [50] had a sensitivity of $3.5 \frac{Hz}{\%RH}$. Due to the high quality factors typically associated with microcantilevers, it is expected that their sensitivities would generally outperform a QCM based sensor but that is not the case here. Of course a direct comparison cannot be made due to the differences in the ZnO material used however, it is clear that there is room for improvement for ZnO based cantilever sensors.

A general strategy to improve resonant cantilever sensor sensitivity is by reducing its mass while maintaining high natural resonance frequencies [37]. Both of these criteria can be accomplished by reducing the size (i.e., volume) of the cantilever. Reducing the cantilever mass closer towards the mass of analyte molecules, makes the cantilever more susceptible to small mass changes from analyte adsorption. Moreover, cantilevers comprised of multiple layers generally have reduced quality factors due to intrinsic damping effects that come from the mismatch between the layers. In the reports listed in Table 2.1, the growth of 1D ZnO nanostructures (receptor layer) onto the surface of the cantilever structural layer can be a source of intrinsic damping which can reduce the gas sensing performance of the sensor. In most cases, additional layers and components are required for cantilever actuation and readout, which further contributes negatively to the quality factor. Hence, simplicity in the cantilever design, in terms of number of layers is preferred.

Indeed, these strategies for improving the resonant cantilever performance have been implemented in previous literature. As described in Chapter 2.1.3, ultra low mass sensitivity was achieved as a result of miniaturization of the cantilever structure. Li et al. [38], achieved mass resolution of less than 1 attogram with a silicon carbide nanocantilever with a length of 600 nm, a width of 400nm and a thickness of 100 nm. Jensen et al. [37] created a nanocantilever structure out of an ultra thin strand of a MWCNT which was able to detect the mass of a single gold atom (zeptogram range). Here, the single MWCNT acts as both the receptor and the structural layer for the sensor device, a concept which can be leveraged in order to improve the quality factor and device sensitivity.

Conventional microcantilever structural layers comprised of polysilicon, silicon dioxide, silicon nitride or various metals are not capable of sensing analytes on their own. Cantilevers made purely out of polymers for the sensing of VOCs have been reported [184]. However, there are significant challenges in their implementation, outlined by Li et al. such as low stiffness, substrate adhesion, incompatibility with other fabrication processes, electrical charging during actuation, susceptibility to residual stresses and poor long term stability [185]. Metal oxides such as ZnO, are excellent candidates to serve this dual role due to their comparable strength (elastic modulus) to silicon [186–188] and ability to interact with analyte gases, which is evident from the many metal oxide based gas sensor articles discussed in Chapter 2.1.3.

In this chapter, a microcantilever device is fabricated primarily out of ZnO which serves as both the structural layer and the receptor layer. AP-SALD is used to deposit the ZnO layer with thicknesses of 100-300 nm which is an order of magnitude lower than the thicknesses of conventional microcantilevers, thereby reducing its overall mass. The frequency shift response of the ZnO cantilever to changes in RH was measured. The results showed comparatively higher sensitivities (for the RH range tested) than other frequency shift based RH sensors.

6.2 Design

6.2.1 Design Considerations

As described above, the primary design element of the resonant microcantilever is the use of a ZnO layer as both the receptor layer and the structural layer. ZnO was chosen due to its extensive use as a gas sensor receptor material as reported in literature (described in Chapter 2.1.3). More importantly, the deposition of ZnO by AP-SALD is a well established process as seen in Chapter 2.2.1. In Chapter 3, a more thorough understanding of its growth behavior and optical properties is presented. A second design element is the use of optical readout method known as laser vibrometry to measure the frequency response of the device (described in Chapter 2.1.1). This method requires a reflective surface on the top side of the cantilever and therefore requires a thin metallic layer. Additionally, the minimum width of the cantilever beam must be 10 μm to focus the laser spot.

The third design element is the use of an electrostatic actuation method to actuate the cantilever structure to its natural resonance frequency (described in Chapter 2.1.1). Electrostatic actuation is implemented by using a parallel plate capacitor configuration where one electrode exists on the cantilever and the other is fixed on the substrate. This requires the deposition of a bottom metal contact on the substrate. The reflective metal layer for optical read out serves as the top electrode. The thicknesses of these metal electrode layers are 50-100 nm, which is thinner than the structural ZnO layer thickness of 100-300 nm.

The choice of electrostatic actuation which requires a bottom electrode, limits the fabrication scheme to surface micromachining techniques. Bulk micromachining techniques such as through wafer etching cannot be used. The choice of metal for the top electrode must be compatible with other fabrication processes. For example, gold is not compatible with the reactive ion etching (RIE) process. Finally, an air gap of 1 μm underneath the structural layer is used. This gap is defined by the deposition of a sacrificial layer which is removed in the release etching step at the end (see Chapter 2.1.1). The material for the sacrificial layer must be carefully selected so that its etchant does not remove other layers of the structure. Polymers like photoresist, are good candidates for the sacrificial layer as they can be easily removed by oxygen plasma or solvents, which do not react with the other layers. Metal oxides (besides ZnO) can be used as well, as the etchant for one oxide is not necessarily a good etchant for another. For example, porous aluminum oxide membranes have been used for the formation of ZnO nanowires which grow inside the Al_2O_3

pores. The Al_2O_3 membrane is subsequently etched by NaOH leaving behind unaffected ZnO nanowires. Therefore Al_2O_3 might also be a good candidate for the sacrificial layer. With these design considerations accounted for, the proposed ZnO cantilever structure (cross-sectional view) is illustrated in Figure 6.1.

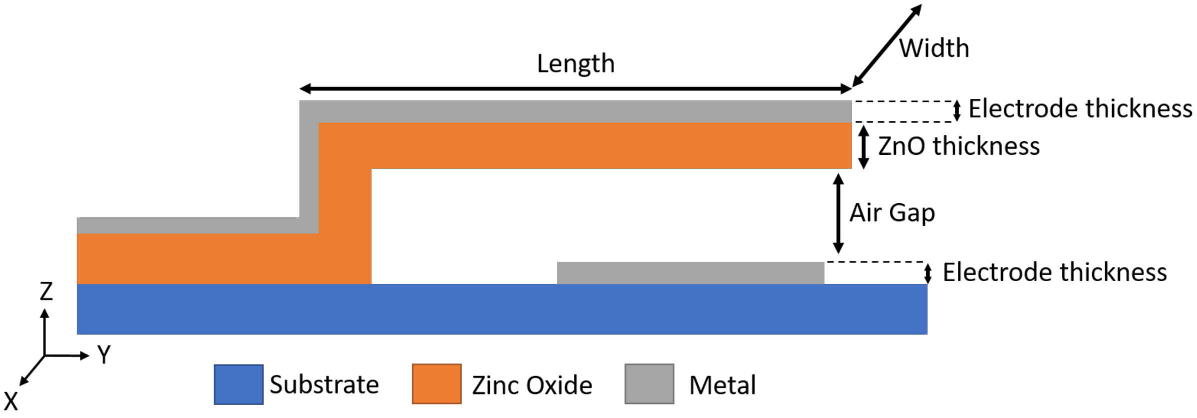

Figure 6.1: Cross sectional schematic of the proposed ZnO cantilever structure with relevant dimensions.

6.2.2 Mask Layout

The proposed cantilever architecture required the use of three photolithography masks to pattern the deposited layers. A fourth mask was added at a later date to address challenges in wirebonding (discussed in the following sections). The first mask patterns the deposited metal layer to form the bottom electrode and its corresponding electrical trace and bonding pad. The second mask, patterns the sacrificial layer. The third mask, patterns both the ZnO and the top electrode layers, while the fourth mask, patterns an additional metal layer intended to increase the thickness of the bonding pads. As defined by the criteria for laser vibrometry, the smallest feature size was 10 μm which necessitates the use of UV lithography as opposed to e-beam lithography.

The mask geometries are depicted in Figure 6.2a. Mask 3 defines the cantilever geometry. Several sets of devices were made with varying cantilever widths (10/25/50 μm) and lengths (50/100/200/300 μm). An array of release holes (2 μm squares) were designed into the top metal electrode for beams that were wider than 10 μm, to allow for the release etchant to get underneath the cantilever structure and remove the sacrificial layer.

Mask 2, which defines the sacrificial layer underneath the structural layer, is simply a rectangular box with dimensions 5 μm larger than the cantilever geometry, on all sides. The additional area is a tolerance for errors in mask alignment which is done manually. Similarly, the bottom electrode, defined by Mask 1, is also a rectangular box with the same tolerance of 5 μm on all sides. Both the top and bottom electrodes are connected to a trace ($width = 10\ \mu m$) comprised of the same metal. The trace extends out to the bonding pad with dimensions of 100 $\times$ 100 μm.

An overlay of the 3 masks to form the cantilever structure is shown in Figure 6.2b. In addition to cantilever structures, bridge type structures with the same dimensions as the cantilevers were also fabricated. Devices consisting of a square plate (with area of 100/200 μm^2) held with either a single arm, two arms on opposite sides, two arms on the same side and four arms were designed as well.

Each device geometry was repeated several times to form an array of devices within a die size of 9×9 mm, shown in Figure 6.3. The arrays were arranged to fit on a 3" wafer. Alignment marks/crosses are placed around the individual dies comprised of the 3 mask layers, which aid in the manual mask alignment. 31 unique device geometries were designed, resulting in over 500 devices on a single wafer although.

6.3 Fabrication

6.3.1 Fabrication Process

The starting substrate is a 3 inch silicon wafer with a top layer of thermal oxide (SiO_2) approximately 300 nm thick. A lift-off process is used to pattern the bottom metal electrode, illustrated in Figure 6.4. First a negative photoresist (ma-N 1410) is spin coated on to substrate at 3000 RPM for 60 seconds to result in a 1275 nm thick film. UV lithography (MA6 mask aligner) with mask 1, is done to selectively expose the photoresist to a dose

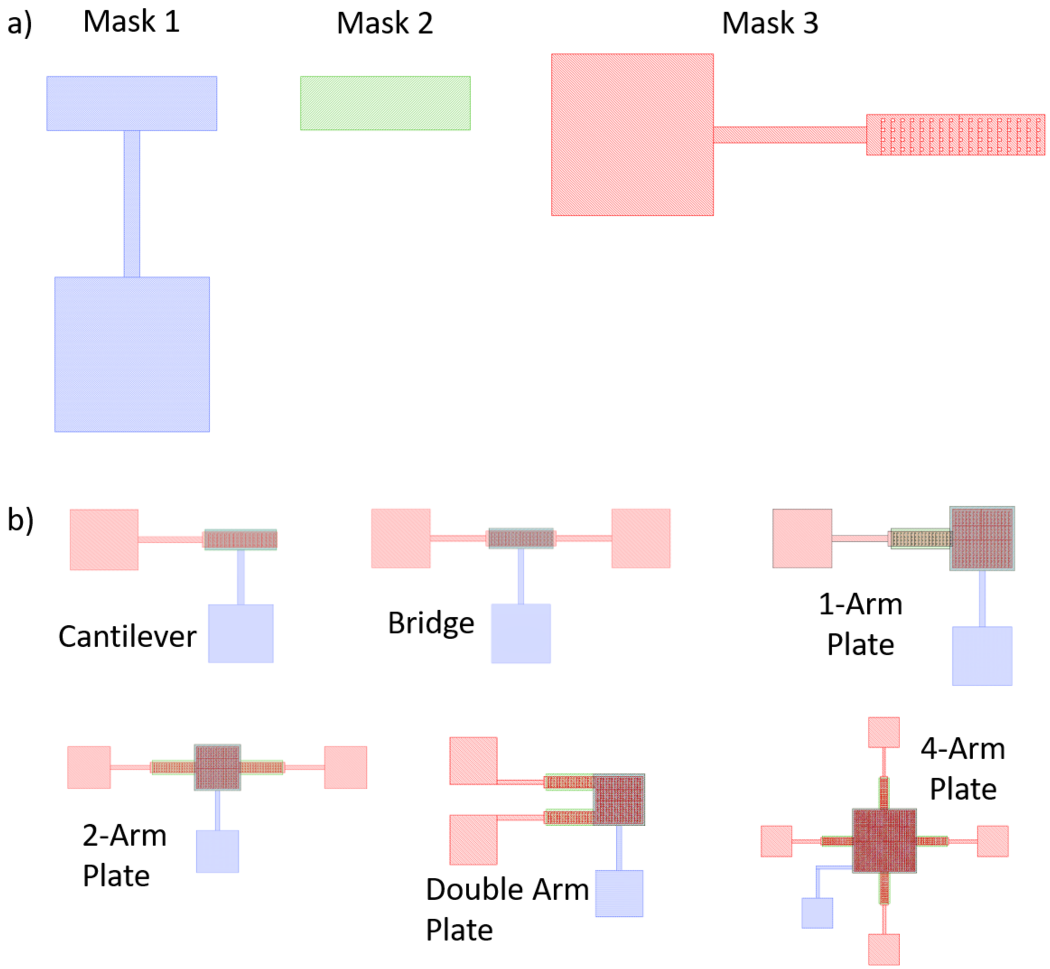

Figure 6.2: a)Three photolithography masks to define the bottom electrode (blue), the sacrificial layer (green) and the top electrode/cantilever structure (red). b) Overlay of the 3 masks to form cantilever, bridge, and plate type structures.

of 350 $\frac{mJ}{cm^2}$ of UV light with a wavelength of 365 nm. The layer is placed in a developer solution (ma-D 533/S) and rinsed with DI water to reveal openings in the photoresist layer in the shape of the bottom electrodes. Aluminum is deposited by sputter deposition (AJA Magnetron). Thicknesses of 50-100 nm were achieved with a sputter deposition time of 359-719 seconds. Finally, the photoresist is removed with successive 5 minute baths in acetone, isopropanol, remover PG and DI water, leaving behind the patterned metal electrode.

Photoresist was used as the sacrificial layer, illustrated in Figure 6.5. Positive pho-

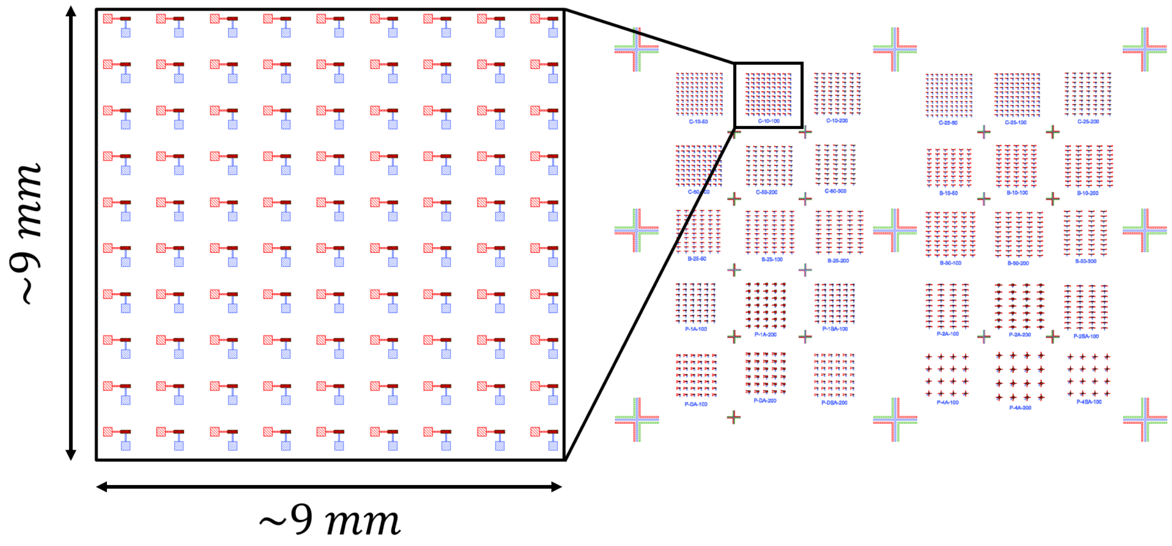

Figure 6.3: Wafer level arrangement of designed devices. Arrays of each unique device geometry were arranged into die sizes of 9 × 9 mm.

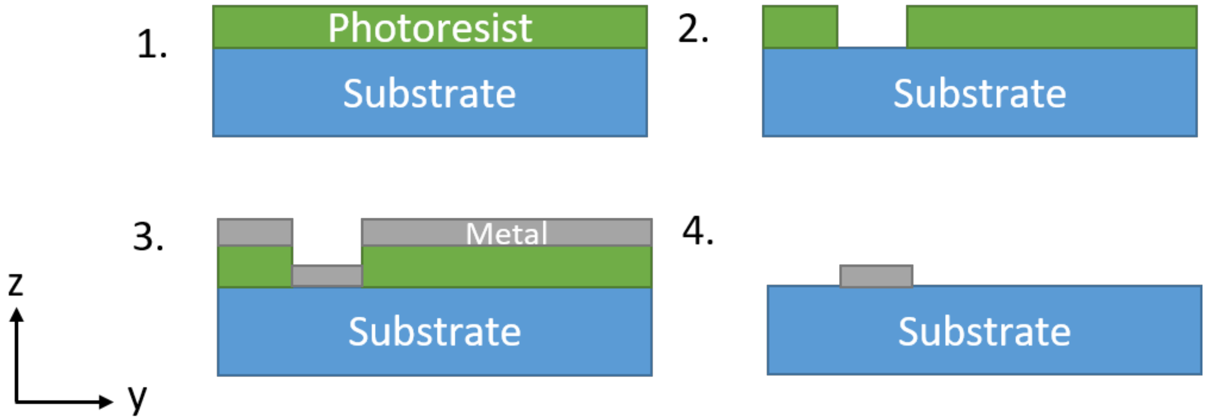

Figure 6.4: Schematic of bottom metal electrode fabrication. The sputtered aluminum layer (grey) is patterned by UV lithography with mask 1 and liftoff process with negative photoresist (green).

toresist (Shipley S1811) was spin coated onto the sample at 5000 RPM for 60 seconds to result in a 1 μm thick film. UV lithography (MA6 mask aligner) with mask 2, is done to selectively expose the photoresist to a dose of 125 $\frac{mJ}{cm^2}$ of UV light at a wavelength of 405 nm. The sample was placed in MF-319 developer solution and rinsed with DI water to reveal the sacrificial layer.

Figure 6.5: Photoresist (PR) sacrificial layer(green) patterned by UV lithography with mask 2.

The ZnO structural (and receptor) layer is deposited by the AP-SALD technique described in Chapter 2.2.1 and Chapter 3. DEZ and water are used as the precursors. The film conformally covers the entire surface of the sample, including the sides of the sacrificial photoresist layer. Conformal coverage is critical to ensure that the structural layer is anchored to the substrate. Deposition was done on several wafers (all with the bottom electrode and sacrificial layer) to vary the properties of the ZnO film. Deposition cycles of 50, 100, 150, 200 and 300 cycles were used to vary the thickness of the ZnO film between 60-450 nm, with deposition temperatures of 50°C, 120°C, 200°C. The ZnO films are discussed further in the following section, Chapter 6.3.2.

After deposition of the ZnO film, the liftoff process is used again to deposit and pattern the top metal electrode, shown in Figure 6.6. The same process that was used to form the bottom metal electrode was used, this time with mask 3. The thickness of the top aluminum layer is 50-100 nm. The aluminum layer also defines the cantilever geometry and is used as an etch mask for the RIE of the ZnO layer, shown in Figure 6.7a. Before this etch step, the wafers are diced to form individual dies for separate processing. RIE of the ZnO is done with an Oxford Plasmalab system. The etch gases were methane (CH_4) and hydrogen (H_2), with a chamber temperature of 60°C. The RIE process results in an anisotropic (directional) etch which only removes the exposed ZnO, leaving behind the ZnO structural layer underneath the aluminum top layer. The etch time is dependant on the thickness of the ZnO film. For example the 150 cycle ZnO film, which had a thickness of 200 nm, required an etch time of 3.5 minutes which was verified experimentally by profilometry.

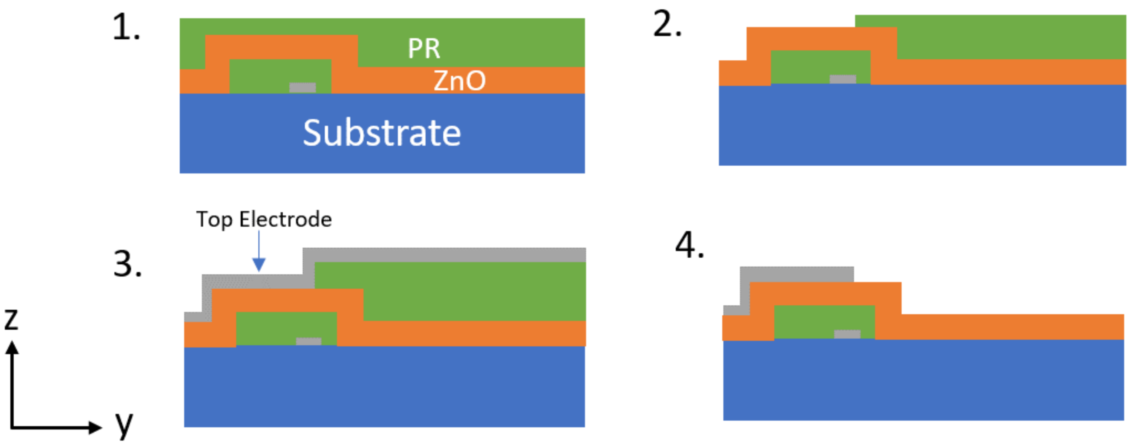

Figure 6.6: Schematic of top metal electrode fabrication. The sputtered aluminum layer (grey) is patterned by UV lithography with mask 3 and liftoff process with negative photoresist (green). ZnO layer deposited by AP-SALD is shown in orange.

The critical step in a MEMS fabrication process is the removal of the sacrificial layer to release the freestanding structural layer. As previously described, the release etchant must selectively removed the sacrificial layer and leave the structural layer intact and therefore chemical compatabilities must be considered. In this fabrication process the photoresist Shipley S1811, is used successfully as the sacrificial layer. The use of Al_2O_3 as an alternative sacrificial layer candidate was investigated and is discussed in Chapter 6.3.3. For the selective removal of the photoresist sacrificial layer, both wet and dry etching methods were investigated. Initial wet release experiments were unsuccessful which is elaborated in Chapter 6.3.3. Ultimately, a dry etching technique known as oxygen plasma ashing was able to successfully release the cantilever (depicted in Figure 6.7b). A CV-200RFS plasma ashing system (Yield Engineering Systems) was used, which like RIE, generally produces an anisotropic oxygen plasma etch. To achieve a lateral etch, an elevated pressure is used (700 mTorr) and a low power (300 W) to promote scattering of the etchant (oxgyen plasma/ions). The process was done in repeated 20 minute durations, until the photoresist was removed and the cantilever was successfully release, which was visually confirmed by SEM .

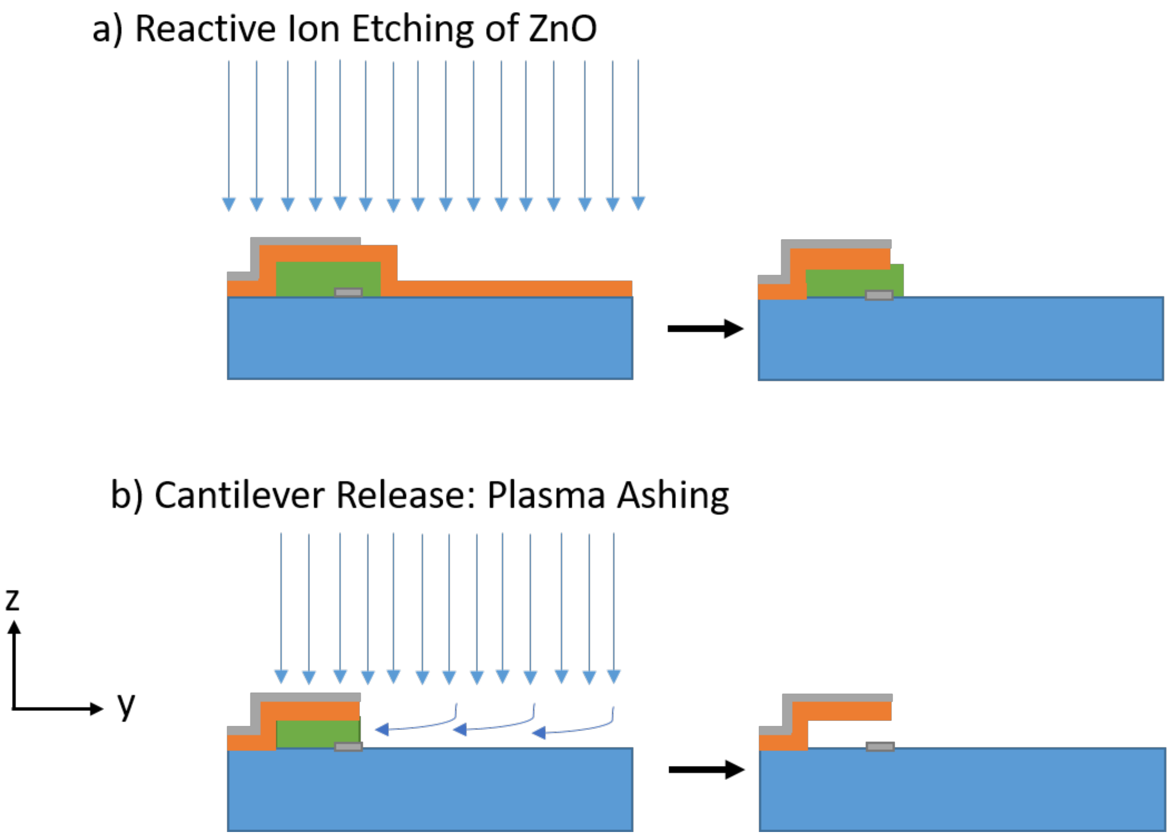

Figure 6.7: a)RIE of ZnO (orange) with CH_4 and H_2 etchant gases. b) Cantilever release etching by oxygen plasma ashing.

Successfully released cantilever devices can be tested using micromanipulator probes to directly apply the actuation voltage onto the contact pads. However, to test the devices as gas sensors, they must be placed in an enclosure (i.e.: test chamber) and therefore require wire bonding to a chip carrier package. Devices were wire bonded to a 40 pin C-DIP style chip carrier, with a Westbond 747677E manual wirebonder. Gold wire with a diameter of 75 μm is ball-bonded to the aluminum pads on the device and the gold pads on the chip carrier. This process had a low yield rate, resulting in 10/100 useful devices on a single chip. Attempts to improve this yield are discussed in Chapter 6.3.3

6.3.2 Zinc Oxide Thin Film

The ZnO film was deposited by AP-SALD onto the wafer surface which at the time was comprised of areas of silicon oxide (substrate), sacrificial photoresist and aluminium. In

Chapter 4, in-situ reflectance measurements revealed that the nucleation period and growth rate of ZnO on these three different surfaces are different. The thickness of the cantilever is a critical parameter that affects the natural resonance frequency of the cantilever beam and by extension also affects the sensor sensitivity. Hence, the in-situ reflectance technique demonstrated in Chapter 4 is advantageous for the accurate deposition of ZnO structural layers on a polymer sacrificial layer. Furthermore, in this study, ZnO structural layers were deposited at different temperatures. The growth behavior of the ZnO on the sacrificial layer at these temperatures was shown in Figure 4.4b-d. It was observed that depositions at lower temperatures resulted in longer nucleation times and slower growth rates. Here, the in-situ reflectance technique is useful to achieve the same structural layer thickness amongst the samples for comparison.

By varying the AP-SALD process parameters, the morphology and other properties of the ZnO film can be controlled and optimized for gas sensing. The morphology of the film is of interest here, as it directly influences the interaction with analyte gases (i.e., sorption). Figure 6.8 shows SEM images of ZnO films at different thicknesses deposited by AP-SALD. The length of deposition was varied from 50-300 cycles, at a deposition temperature of 200° C. It is clear from the images that the grain size increases as the cycle number is increased, while the number of grains or grain density appears to decrease, indicating that smaller grains are coalescing to form larger ones. The smaller feature size of the 50-cycle film is expected to have a larger surface area for gas adsorption however, it may not have the structural integrity to stand on its own as a cantilever. Whereas, thicker films with larger grains are expected to have less surface area available for gas adsorption.

Similarly, Figure 6.9 shows the SEM images of the ZnO films deposited at different temperatures (all with 150 deposition cycles). The change in morphology due to deposition temperature is clear. ZnO deposited at 50°C has a loosely packed surface with empty gaps (dark spots). The film at 120 °C formed a spherical type morphology, while the film at 200 °C formed a textured faceted morphology. While the films deposited at lower temperatures may have higher surface area, their low packing density may result in a loss of structural integrity for the cantilever structure.

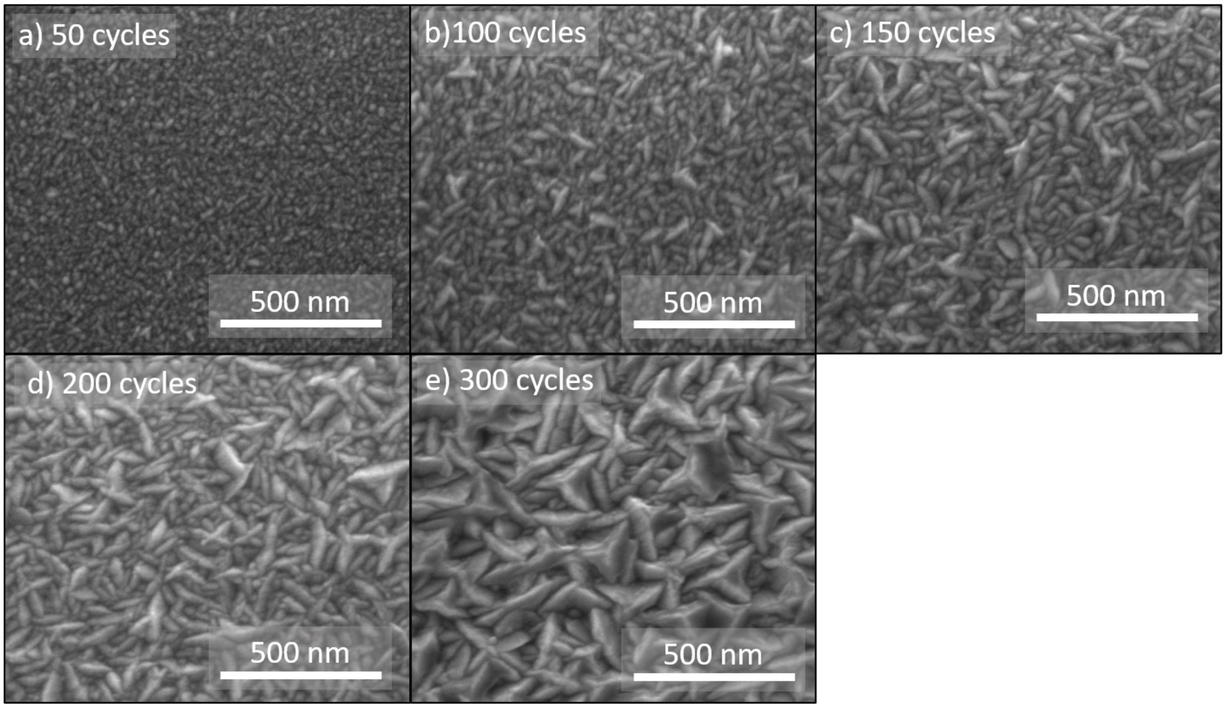

Figure 6.8: SEM images (100kX magnification) of ZnO films deposited by AP-SALD at 200°C with varying number of deposition cycles. a) 50 cycles, b) 100 cycles, c) 150 cycles, d)200 cycles, e) 300 cycles.

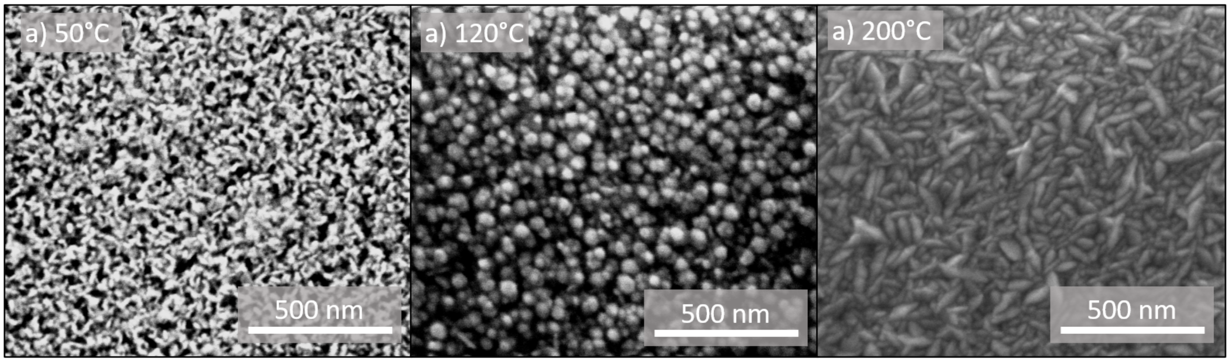

Figure 6.9: SEM images (100kX magnification) of ZnO films deposited by AP-SALD (150 cycles) at different deposition temperatures. a) 50 °C, b) 120 °C, c) 200 °C.

A cross sectional SEM image of the ZnO cantilever before the sacrificial layer release step is shown in Figure 6.10. The image shows the compact 200 nm thick ZnO film (150 AP-SALD deposition cycles at 200°C) atop the 1 μm sacrificial layer.

The observed changes in the material structure are further explored with x-ray diffraction (XRD). The diffraction pattern of the samples with varying thicknesses (50-300 deposition cycles) are shown in Figure 6.11a. Diffraction peaks are observed at $\sim$ 31°, 34° and

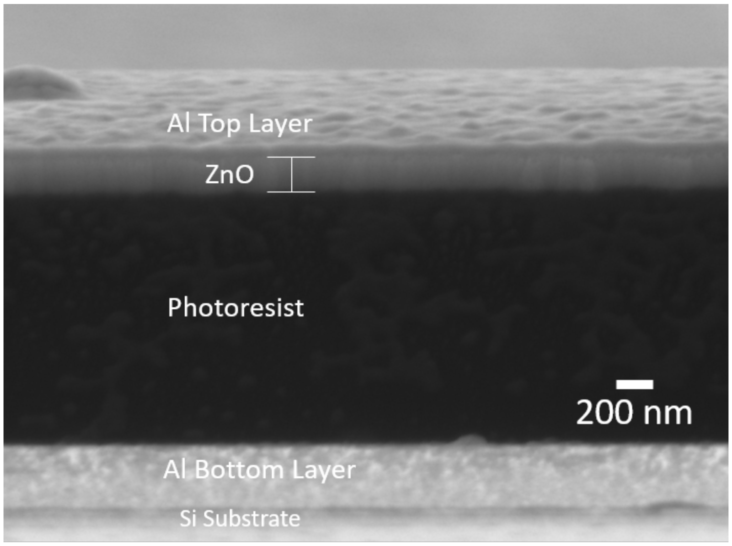

Figure 6.10: Cross sectional SEM image (30kX magnification) of deposited cantilever layers, before sacrificial layer release. ZnO layer thickness is approximately 200 nm (150 AP-SALD deposition cycles).

56° corresponding to the (100), (002) and (110) planes, respectively. The 50 cycle sample is fairly amorphous but has a small (002) peak. The (002) peak is dominant for the samples with 100-200 deposition cycles, but is reduced for the sample with 300 deposition cycles. The crystallite size calculated by the Scherrer equation [146] for the (002) peak is listed in the figure. As the film grows the (002) crystallite size increases and reaches a maximum of 55 nm at 150-200 cycles. The diffraction peaks for the ZnO samples deposited at different temperatures is shown in Figure 6.11b. The sample grown at 50°C is amorphous. The sample deposited at 120 °C, has a single (002) peak, while the sample deposited at 200°C has all three peaks. In ZnO based chemiresistive gas sensors, films with a dominant (002) peak showed improved sensitivities to analyte gases [189]. From the overall XRD data obtained here, it can be concluded that preferential growth in the [002] direction is possible by varying the deposition temperature. However, the the duration of deposition or its thickness is another factor that can influence the film orientation, and too large of a thickness may reduce its sensitivity to an analyte. At the same time, it is important to ensure the packing density of film is adequate enough to hold itself up as a cantilever beam. So while the deposition at 120 °C might be preferred to achieve the (002) face, its packing (as shown in the SEM image) may not be adequate.

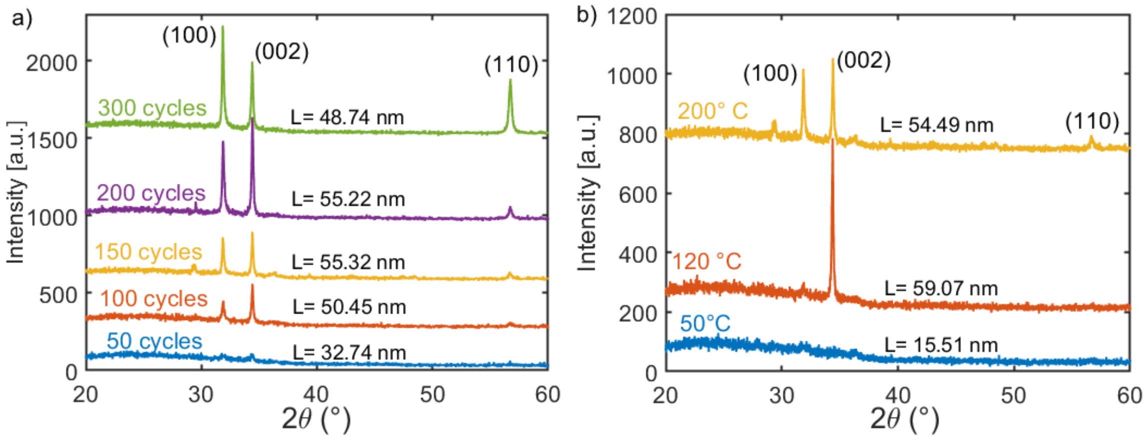

Figure 6.11: X-ray diffraction patterns obtained for ZnO films deposited by AP-SALD with a) 50-300 deposition cycles and b) 50-200°C deposition temperatures.

Lastly, Aluminum doped Zinc Oxide (AZO) films were deposited (150 cycles at 200°C) with varying aluminum concentrations. The precursor TMA was used as the aluminum dopant, and was injected into the metal precursor flow line every 10, 16 or 22 cycles of Zn precursor, creating three unique films of varying Al quantity. It is expected the the introduction of the Al dopant to the ZnO film would change the quantity of oxygen vacancies in the film. These oxygen vacancies promote adsorption analytes onto the surface of the film [46, 47]. Hence, there is potential for improved sensor sensitivities through Al doping.

6.3.3 Fabrication Challenges

Incompatible Materials

As described previously, Al_2O_3 and polymer based materials such as photoresist were candidates for the sacrificial layer. This is because their removal with their respective etchants would not affect the ZnO structural layer. The effectiveness of Al_2O_3 as a sacrificial layer in these fabrication process was explored. The 1 μm thick photoresist layer (Shipley S1811) was replaced with a Al_2O_3 layer deposited by AP-SALD, with approximately the same thickness. The film was deposited at a temperature of 200°C and required 1000 deposition cycles. The total deposition time was approximately 50 minutes. However, after deposition the film delaminated or "peeled off" the surface of the substrate, thus making it unusable. This may be a result of the build up of residual stresses in the Al_2O_3 film which are amplified at large thicknesses. Hence, the use of a 1 μm Al_2O_3 sacrifcial layer is not successful and the use of a photoresist sacrificial layer was the preferred method.

ZnO structural layers with varying morphologies were deposited, as discussed in the previous section. It was clear from the SEM images shown in Figure 6.9 that the films deposited at 50 °C and 120 °C had a loosely packed or porous morphology. Ultimately, these morphologies were detrimental to the fabrication of the device. This issue was observed during the patterning of the top metal electrode, shown in Figure 6.6. After deposition of the Al layer, the final step is the lift off process to pattern the layer. This involves successive baths in acetone, isopropanol, remover PG and DI water, to remove the photoresist and excess aluminum. However, after this step, the ZnO structural layer and photoresist sacrificial layers were removed as well. This result suggests that the porosity of the ZnO allowed the solutions to get through the structural layer and remove the sacrificial layer, thus removing everything on top as well. The ZnO structural layers deposited at 200 °C, did not have this issue likely due to their higher packing density which was impenetrable by the liftoff solutions. Therefore the compactness of the ZnO structural layer is another requirement that must be considered. The diffraction pattern of the ZnO films (shown in Figure 6.11b) indicates that the 120 °C film had a dominant (002) peak which was preferred for gas adsorption. This presents a tradeoff between the compactness of the ZnO layer and its gas adsorption behavior. A thicker film ($>$ 150 deposition cycles) may resolve this issue.

Cantilever Release

The use of both wet and dry etching methods for the removal of the sacrificial photoresist layer was explored. The wet release method is often preferred in MEMS fabrication as it typically takes less time than the dry release method and it does not alter the structural layer. The wet release method has to be combined with critical point drying (CPD) to prevent the cantilever from collapsing down as the etchant evaporates from the sacrificial layer gap. Here, a wet release recipe was adapted from [190] which comprised of a long bath (4 hours) in a photoresist remover solution (remover PG) with gentle agitation followed by CPD. Figure 6.12 is an optical microscope image of a 10 $\times 200$ μm cantilever after the wet release attempt. A crack at the beam's anchor point is observed with only a partial reduction in the sacrificial photoresist layer. As labeled on the figure, more photoresist is removed near the anchor point. This suggests that the photoresist at the anchor point may have been removed to release the beam only at the anchor point, while the rest of the the beam remained adhered to the unremoved photoresist. The residual stresses in the structural layer likely resulted in a bending moment at the anchor point that was larger than the force of adhesion of the beam to the substrate, resulting in a crack. This wet release method was repeated for 25 $\times 100$ μm and 50 $\times 100$ μm cantilevers and also resulted in cracks at the anchor points. It is likely that these issues could be resolved through further optimization of the wet release recipe, but this was not feasible at the time.

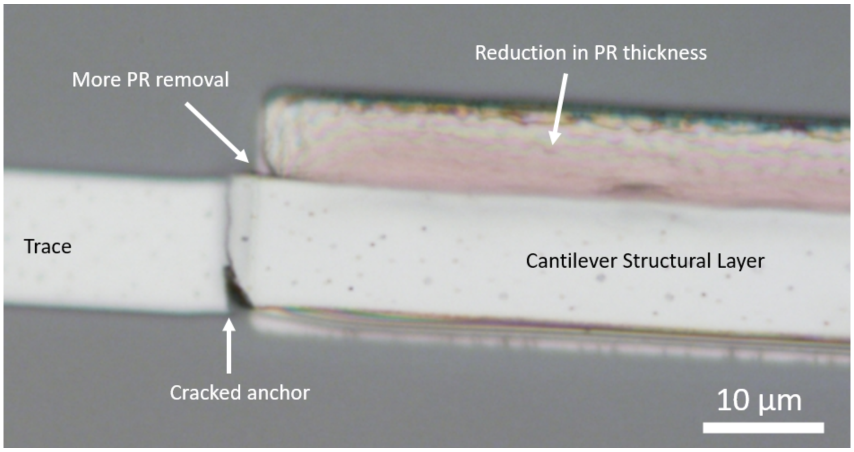

Figure 6.12: Optical microscope image of $10x100x0.25\mu m$ cantilever subjected to wet release method and critical point drying ultimately resulting in a crack. Partial reduction of the sacrificial photoresist (PR) layer is also observed.

A dry release method by oxygen plasma ashing proved to be most successful in releasing the ZnO cantilever structures. The parameters of the plasma ashing process are described in Chapter 6.3.1. SEM was used to observe the removal of the photoresist sacrificial layer. Samples were mounted on a variable angle SEM mount to observe the cross-sectional profile. Cantilever devices with a 150 cycle ZnO film (≈ 200 nm thickness) were used to validate the release process. Figure 6.13 shows the cantilever structure before and after a single ashing step of 20 minutes. It confirms that the release process does remove the sacrificial layer. Additionally, it shows that the cantilever structure is conformal to the shape of the photoresist layer underneath resulting in structures with a slight dip at its free end.

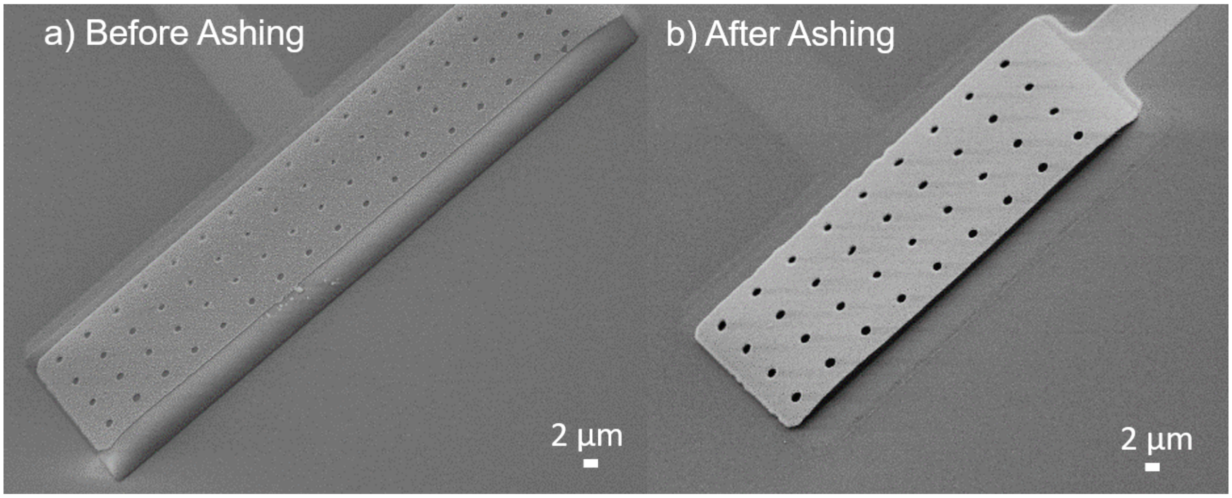

Figure 6.13: Angled SEM images of cantilever before (a) and after (b) a single plasma ashing cycle of 20 minutes.

Figure 6.14 shows the tilted SEM view of a cantilever device with a width of 10 μm and a length of 200 μm at different times during the plasma aching. It can be seen that the photoresist layer is receding as the release process time is increased. However, after the 2-hour mark, this particular device collapsed. One reason for its loss of structural integrity is that the device length to width ratio was relatively large, that is the length was too large and the width was too small.

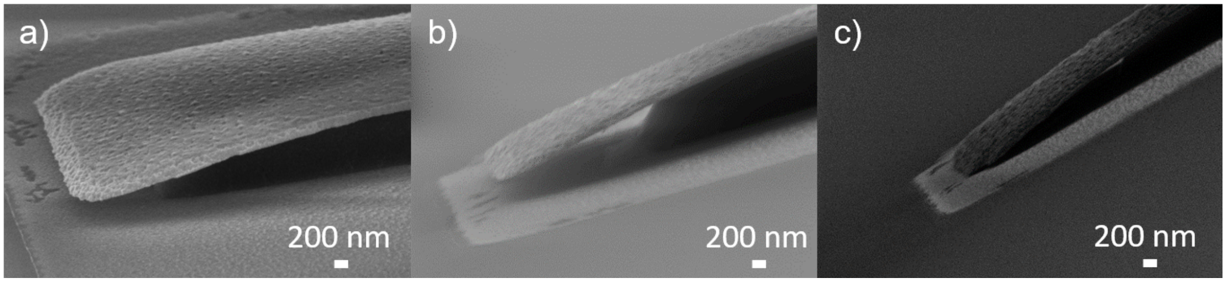

Figure 6.14: Angled SEM images of cantilever $10x200\mu m$ at different stages of the release process. a) 52 minutes, b) 1 hour and 20 minutes, c) 2 hour and 20 minutes.

Wider beams (25 × 50 μm) required the inclusion of release holes in the design to accelerate the release process. Figure 6.15 shows the removal of the photoresist through the release holes, leaving behind pyramid-like patterns in the remaining photoresist. This shows that the plasma ashing process is in fact isotropic. The plasma ashing process is repeated until cantilevers are fully released, as confirmed visually by tilted SEM .

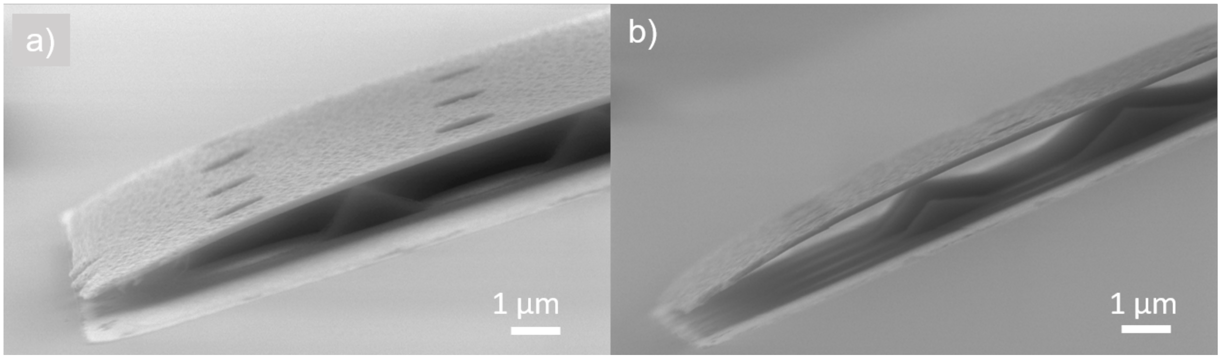

Figure 6.15: Isotropic etching of the photoresist sacrificial layer through the release holes on a $25x100\mu m$ cantilever. Shown for etch times: a) 1 hour 46 minute and b) 2 hours 46 minutes.

A major artifact of this process is that the resulting cantilevers are curved upward and in some cases warped, as seen in Figure 6.16. The source of the curvature is likely due to residual stresses in the ZnO and/or Al layers. The residual stresses in the films impart a bending moment on the cantilever in order to relax. This is further supported by the observation of the cracked beam after the wet release method, suggesting that the films were inherently stressed. Another reason for the curvature may be due to the prolonged exposure to an elevated temperature (180°C) and high energy ion bombardment of the plasma ashing process which may have resulted thermal expansion of the aluminum and zinc oxide layers on the cantilever. The two films expanding at different rates can further build up residual stresses in the film. The curvature of the beam becomes an issue for optical readout by laser vibrometry, as the reflected light would not be directed at the photodetector. The curvature was prominent for beam lengths of 100 and 200 μm while it was minimal for devices with a beam length of $50\mu m$. Additionally, the curvature was minimized by allowing cool down periods in between the 20 minute ashing cycles.

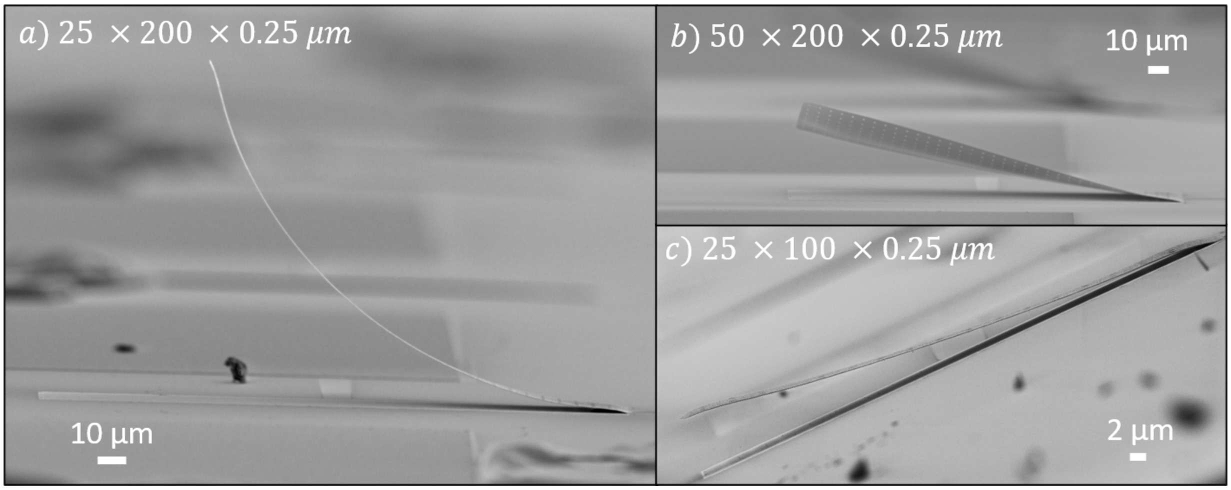

Figure 6.16: Fully released curved ZnO cantilever beams with beam dimensions: a) 25 × 200 × 0.25 μm, b) 50 × 200 × 0.25 μm and c) 25 × 100 × 0.25 μm.

Wirebonding

Wirebonding is necessary to be able to apply an actuation voltage to the device for gas sensing measurements. 75 μm gold wires were ball-bonding onto the aluminum contact pads which were approximately 50 nm thick with a size of 100 × 100 μm. In many instances, the first attempts at placing the wirebond scratches off the entire pad. As seen in the optical microscope images of the devices (Figure 6.17), the aluminum pads have significantly deteriorated, evident by the visible roughness. This roughness arises from the high temperature (T=180°C) and long duration of the plasma ashing release process which likely oxidizes the aluminum. Additionally, the thin thickness of the aluminum layers is less than the ideal bonding pad thickness of 1 μm. The thin layer is more susceptible to oxidation, as well. The top aluminum contact is deposited on the ZnO film which has a distinct surface morphology and roughness (shown in Figure 6.8) which may contribute to the poor adhesion of the wire bond. Due to the small size of the bonding pads, an unsuccessful bonding attempt (seen in Figure 6.17b) made the entire device unusable. The pads should be larger to allow for more than one bond to be made.

The first attempt to improve wirebond adhesion is to vary the process parameters of the Westbond wirebonding tool. This includes the ultrasonic power, ultrasonic time and temperature. Increasing the ultrasonic power and time can improve the adhesion of the

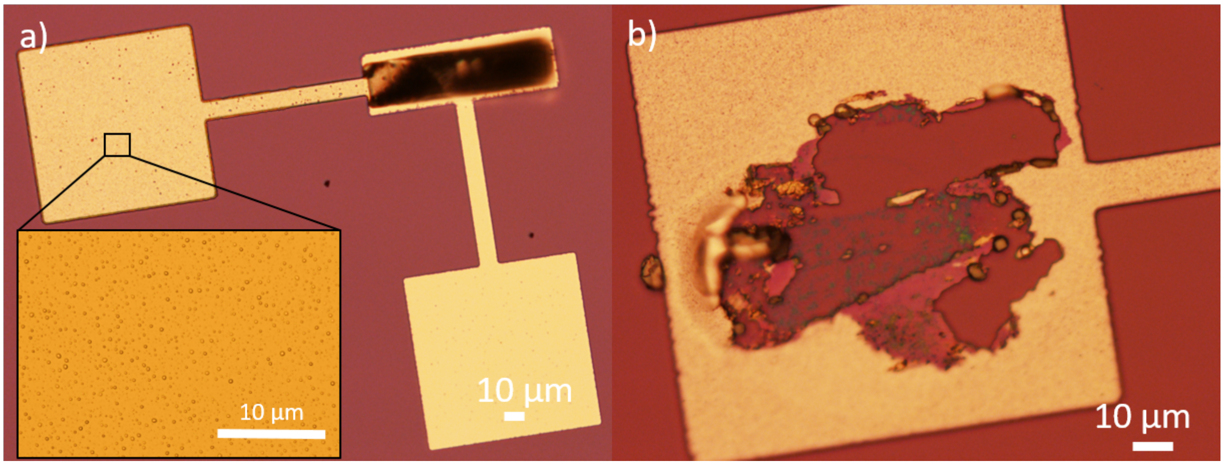

Figure 6.17: Optical microscope images of the aluminum contact pads for the device. a) A 20x image of a $25x100x0.25\mu m$ device.The inset shows a further magnified image of the surface of the pad. b) An aluminum contact pad after an unsuccessful wire-bonding attempt.

wirebond. Additionaly, hydrogen plasma cleaning is often done to remove organic residues from the surface before wirebonding. However, no set of process parameters or plasma cleaning improved the bonding process which suggests the poor surface quality of the pads was the limiting factor. To rectify this issue, a fourth UV lithography mask was designed specifically to allow for further deposition of aluminum to increase the pad thickness and size. The design of the fourth lithography mask is shown in Figure 6.18. Metal deposition was done by thermal evaporation and patterned by lift off similar to the previous metal deposition steps. The deposition time was set to deposit a 300 nm Al layer. The resulting thickness and larger pad size improved the reliability of the wirebonding process.

6.4 Experimental Results

6.4.1 Successfully Released Structures

Figure 6.19 shows the SEM images of the successfully released and relatively flat cantilever beams. The $25 \times 50\ \mu m$ device (shown in Figure 6.19a), required a total plasma ashing time of 4 hours while the $10 \times 50\ \mu m$ device (shown in Figure 6.19b), required a total ashing time of 8 hours. The longer release time for the smaller width device may be due to its lack

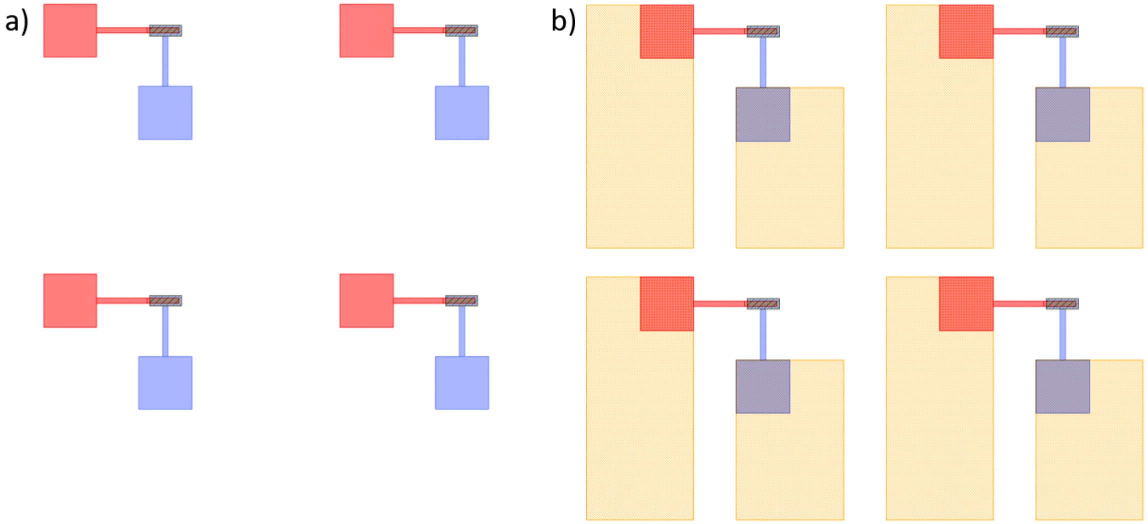

Figure 6.18: Overlay of process lithography masks for an array of 10 × 500 × 0.25 μm cantilevers. a) the first three lithography masks are shown in blue (bottom contact), green (sacrificial layer) and red (top contact). b) the fourth lithography mask shown in orange is overlayed over the first three.

of release holes. The smaller beam length of 50 μm resulted in minimal curvature in the beams when compared to the larger curvatures obtained for beam lengths of 100 μm and 200 μm (shown in Figure 6.16). However, it is clear that there is some degree of warpage in the 50 μm length beams, as well as a non uniform separation gap to the bottom electrode. All experimental results discussed in the following sections are for the 10 × 50 μm device.

6.4.2 Resonance Frequency Measurement

Experimental Setup

A laser Doppler vibrometer (Polytech MSV 400) is used to measure the velocity of the cantilever oscillations. A fast Fourier transform (FFT) is applied to the velocity-time signal to obtain the frequency response of the cantilever. Figure 6.20 shows the measurement setup. The cantilever devices, wirebonded to a dip style chip carrier are placed inside a metal enclosure with a quartz window. The laser is focused onto the top surface of the cantilever. Delivery of gases to the test chamber was done in a similar fashion to the

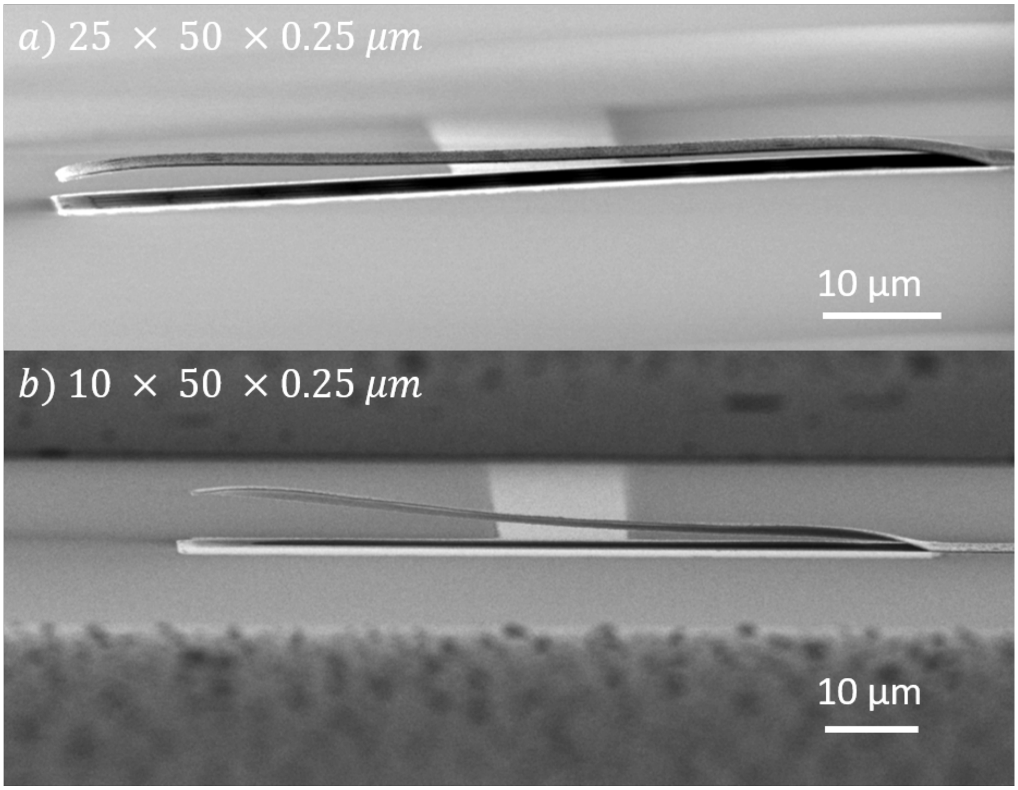

Figure 6.19: Fully released and relatively flat ZnO cantilever beams with dimensions of a)25 × 50 μm and b) 10 × 50 μm.

experimental setup described in Chapter 5.2.2 (schematically illustrated in Figure 5.1). Gases used in this work include nitrogen, compressed dry air and water vapor/humidity (produced by bubbling water with dry air). A wireless humidity sensor (SensorPush HT1) was placed inside the test chamber to obtain accurate RH levels. For measurements done in a vacuum environment, the test chamber is replaced with a vacuum enclosure (with an optical window) and is pumped to a vacuum level of 3 mTorr.

Natural Resonance Frequency Determination

The natural resonance frequency (f_n) of the ZnO cantilever is determined by measuring its response in a vacuum environment (3 mTorr). In this environment, the effects of damping due to the surrounding medium are removed, which isolates the damping effects to the material or the structure itself. Measurement in vacuum generally allows determination of the natural resonance frequency without an applied actuation voltage, since external

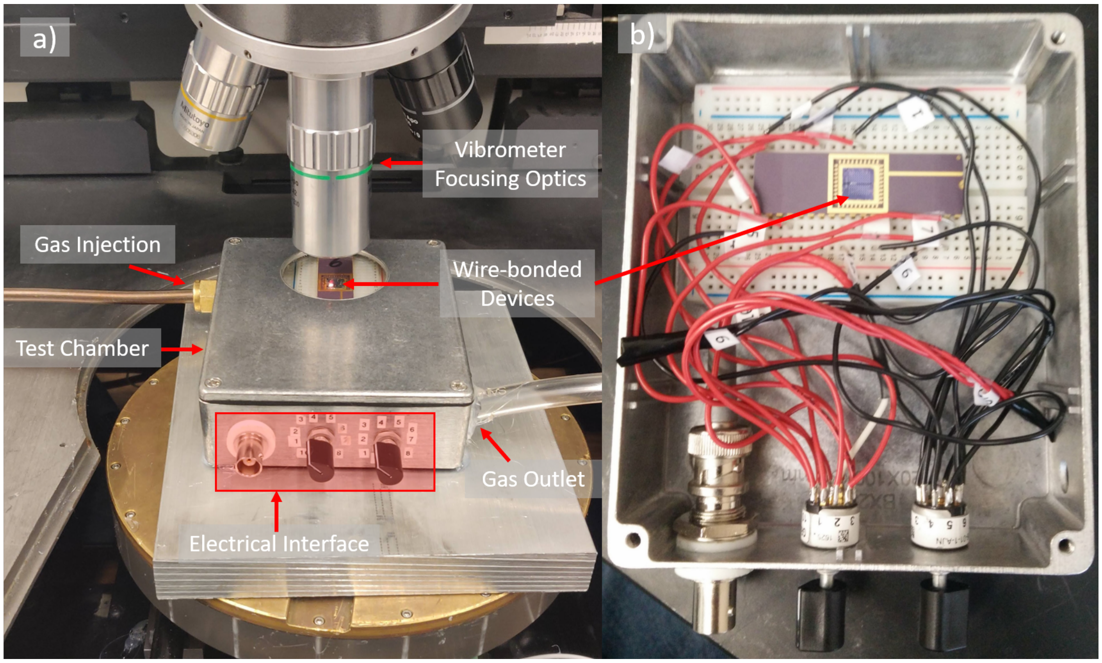

Figure 6.20: Experimental setup for resonance frequency measurement. a)Laser vibrometer focused on cantilever chip placed in gas enclosure. b) internal assembly of gas enclosure.

damping effects are removed. Figure 6.21 shows the natural resonance frequency of the ZnO cantilever measured in vacuum (red line) and in ambient room conditions (atmospheric pressure, blue line). The quality factors (Q), were determined by the dividing the peak frequency by the half power bandwidth [8]. The measurement in vacuum yielded a resonance frequency of 243.69 kHz and a quality factor of 487, while the measurement in ambient conditions yielded a resonance frequency 177.75 kHz and quality factor of 5. The change in measurement environment resulted in a frequency shift of 66 kHz with significant damping at atmospheric pressure. Notably, no actuation voltage was required for the measurement in ambient conditions. That is, the cantilever "self-actuates" in air, despite significant damping as indicated by the low quality factor. This self-actuation behavior may be attributable to the low thickness of the cantilever layers ($\approx$ 250 nm) and corresponding low mass, which allows it to be thermally excited by the collisions with the Brownian motion of the fluid(air) molecules [191, 192].

At atmospheric pressure, MEMS structures are subjected to viscous damping effects from the surrounding medium (air). These effects are further amplified if large surface area structures are in close proximity to each other (e.g., a cantilever beam and the substrate),

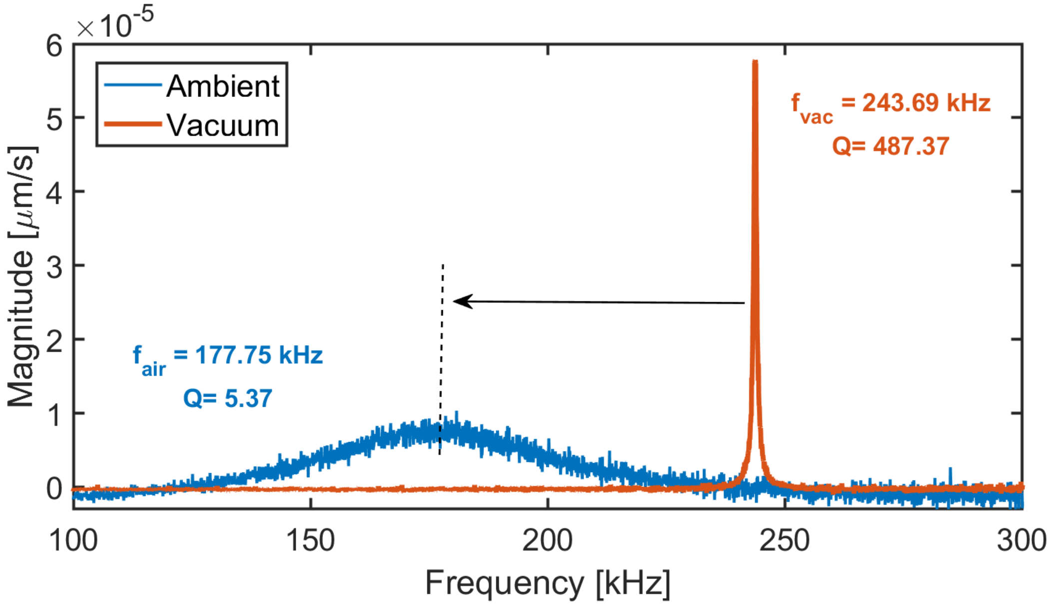

Figure 6.21: Fast Fourier transform of the cantilever oscillation velocity [$\mu m/s$] when measured in 3 mTorr vacuum (red line) and in ambient conditions (blue line). Peak frequencies (f_{vac} *and* f_{air}) and corresponding quality factors (Q) are listed on the figure.

in a phenomenon known as squeeze film damping (SQFD). An expression to predict the quality factor when SQFD is dominant is given in Equation 6.1 [8]. Where, w, t, L, E and ρ are the cantilever width, thickness, length, Young's modulus and density, respectively. d is the separation distance between the cantilever and the other surface (substrate) and η is the viscosity coefficient of the fluid (air).

$$Q = \frac{w\sqrt{E\rho}}{\eta}\left(\frac{t}{L}\right)^2\left(\frac{d}{w}\right)^3 \tag{6.1}$$

The expression is valid for $d < 1/3w$, which is the case for the measured ZnO cantilever ($d = 1\ \mu m, w = 10\ \mu m$). Using values reported in literature for the Young's modulus [193] and bulk density [194] of ZnO ($E = 159.4\ GPa$ and $\rho_{ZnO} = 5.61\ g/cm^3$), and air viscosity [195] ($\eta = 1.849 \times 10^-5\ \frac{kg}{ms}$), the quality factor for the device in air is estimated to be 2.58. The estimate is comparable to the obtained Q factor of 5.87 which suggests that the dominant source of damping for the ZnO cantilever in air is in fact SQFD. The difference between the two values is likely due to the non-uniform gap of the ZnO cantilever as well as differences in the actual Young's modulus and density of the ZnO film deposited by

AP-SALD. From Equation 6.1, the Q factor has a cubic dependence on the gap distance. Thus an increase in the gap distance can greatly decrease the effects of SQFD.

The origin of the of the 66 kHz frequency shift (from vacuum to ambient) is investigated. Green and Sader reported a numerical model to determine the frequency response of a cantilever beam immersed in a viscous fluid (i.e., air) in proximity to a solid surface (i.e., substrate) [191]. This model accounts for the dissipative and inertial loads experienced by the cantilever in a viscous fluid. The inputs to the model are given in Equation 6.2-6.4. $\bar{H}$ is the ratio between the gap distance (h_0) and the width of the cantilever (b). $\bar{T}$ is the ratio of the added mass due to the fluid inertia to the cantilever mass and is dependent on the density of the fluid (ρ_f), the density of the cantilever ($\rho_c = \rho_{ZnO}$), the cantilever width (b) and thickness (h). Re is the Reynolds number, dependent on ρ_f, b, the fluid viscosity (η) and the radial resonance frequency of the beam in vacuum (f_{vac}) which accounts for its intrinsic stiffness.

$$\bar{H} = \frac{h_0}{b} \tag{6.2}$$

$$\bar{T} = \frac{\rho_f b}{\rho_c h} \tag{6.3}$$

$$\bar{Re} = \frac{\rho \omega_{vac} b^2}{4\ \eta} \tag{6.4}$$

Based on the calculated parameters above, an estimate for the resonance frequency of the ZnO cantilever in ambient air was determined to be within 80-90% of its resonance frequency measured in vacuum. That is, for $f_{vac} = 243.69\ kHz$, the expected frequency in air is within 194-219 kHz corresponding to a shift of $\Delta f = 24 - 49\ kHz$. This expected frequency in air from the model is distant from the measured frequency in air of 177.75 kHz.

According to Equation 6.5, the remaining decrease in frequency may be attributable to either a decrease in the stiffness (k) of the cantilever or an increase in its mass (m). k

depends on the elastic modulus of the material as well as the cantilever dimensions. The cantilever dimensions are not expected to be different in a vacuum environment. It was shown that that the sorption of water (humidity) on ZnO nanobelts increased the elastic modulus of the ZnO [196]. Based on this report, the sorption of water from the ambient atmosphere on the ZnO cantilever should result in a frequency increase, but that is not the case. Hence, it is likely that the remaining decrease in frequency is not primarily attributable to the changing stiffness. The discrepancy in frequency shift is therefore assumed to be as a result of an increase in mass of the cantilever, due to the adsorption of species present in the air such as oxygen and water (humidity).

$$f_n = \sqrt{\frac{k}{m}} \tag{6.5}$$

Figure 6.22, shows the resonance frequency shift (Δf) and the quality factor as the vacuum pressure was slowly increased from 3 mTorr to 1 Torr. As the pressure is increased the frequency decreases towards the frequency measured in ambient atmosphere. This is expected behavior, based on the adsorption of oxygen and water (humidity) on the ZnO surface as air is introduced back into the chamber. The quality factors decrease from 421 (obtained at 3 mTorr) to 10 (obtained at 1 Torr). This trend follows a $Q \propto 1/P$ dependence, which is in agreement with the molecular air damping regime, described by Newell [8]. While the frequency shifts are associated with the adsorption of mass, the change in quality factor can be associated with a change in pressure level and hence may have potential applications in pressure sensing [197].

Measurement of the ZnO cantilever resonance frequencies in ambient and vacuum conditions were done over a period of 75 days, shown in Figure 6.23a. The RH of the room was within 25-30% on the days tested. As seen from the figure, the resonance frequency of the ZnO cantilever decreases over time. The trend is similar for both measurements in air and vacuum. The corresponding Q factor for each measurement is shown in Figure 6.23b-c. The trend observed in part a, is also observed for the Q factors in vacuum which suggests that the stiffness of the beam is changing over time and is a source of further intrinsic damping. The same trend was not observed for the Q factors determined in air, likely due

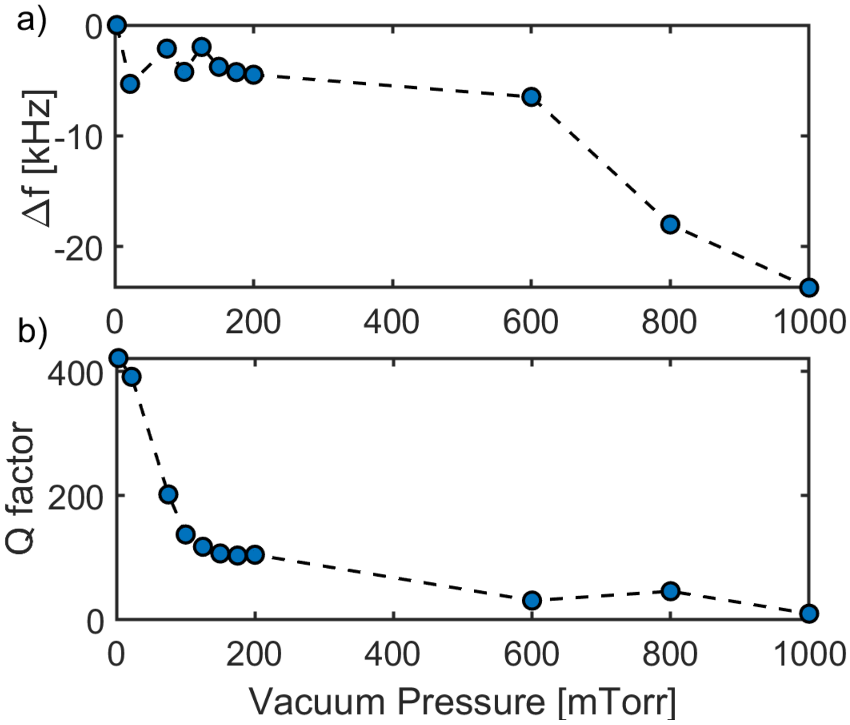

Figure 6.22: a) Measured resonance frequency shift (Δf) and b) quality factor of ZnO cantilever as the vacuum pressure is increased from 3 mTorr to 1 Torr.

to dominant air damping effects. The changing stiffness of the beam is likely due to the relaxation of residual stresses in the cantilever layers, a phenomenon observed in polymer cantilevers [185]. As discussed previously, the fabrication process yielded curved beams which is indicative of residual stresses in the ZnO and/or Al layers. While the curvature was minimized for the beam lengths of 50 μm, it is evident from the non-uniform gap observed in the SEM images (Figure 6.19) that the beam was still stressed. This instability in the resonance frequency over time is not ideal, however, the difference between frequencies measured in vacuum and in air remains the same. This suggests that the magnitude of the frequency shift (Δf) for the adsorption or desorption of an amount of gas will not change over time.

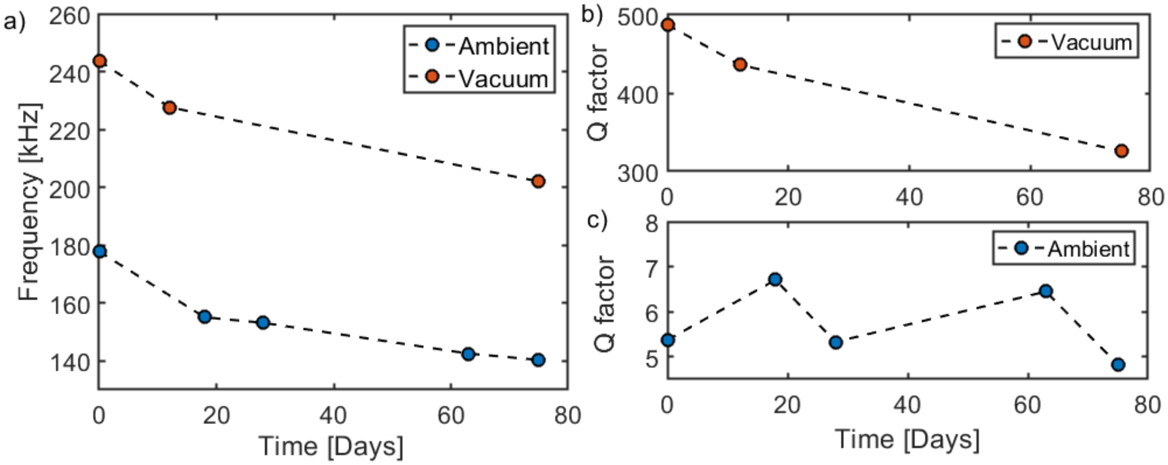

Figure 6.23: a)Measurement of resonance frequencies of ZnO cantilever in ambient (blue) and vacuum conditions (red) over time (days). b) Q factors determined in vacuum. c) Q factors determined in ambient atmosphere.

6.4.3 Frequency Response to Humidity

The previous results indicate that the ZnO cantilever is adsorbing species present in air (likely oxygen and water). The effect of purging the test chamber with nitrogen is shown in Figure 6.24a. Nitrogen was introduced to the chamber at flow rate of 100 SCCM, over a span of 16 hours. The resonance frequency was measured every 15 minutes for the first three hours, and the last hour. As seen in the figure, a positive frequency shift (Δf) is observed as the nitrogen is introduced which corresponds to a decrease in cantilever mass and desorption of oxygen and/or water from the surface of the cantilever. After 16 hours in nitrogen, a total shift of $\Delta f = +34.38\ kHz$ is observed and the last three measurements appear to be stabilized. At 1000 minutes the nitrogen is turned off and the lid of the test chamber is opened which results in a rapid decrease in frequency corresponding to the re-adsorption of oxygen and water from air. A frequency shift of 66 kHz corresponding to complete desorption of oxygen and water was never attained, likely due to the imperfect seals of the test chamber which allowed air to leak back in.

To isolate the water and oxygen desorption processes, dry air (comprised of 78.9% nitrogen and 20.95% oxygen) was injected into the test chamber at a flow rate of 100 SCCM, shown in Figure 6.24b. The frequency response is compared to the nitrogen experiment.

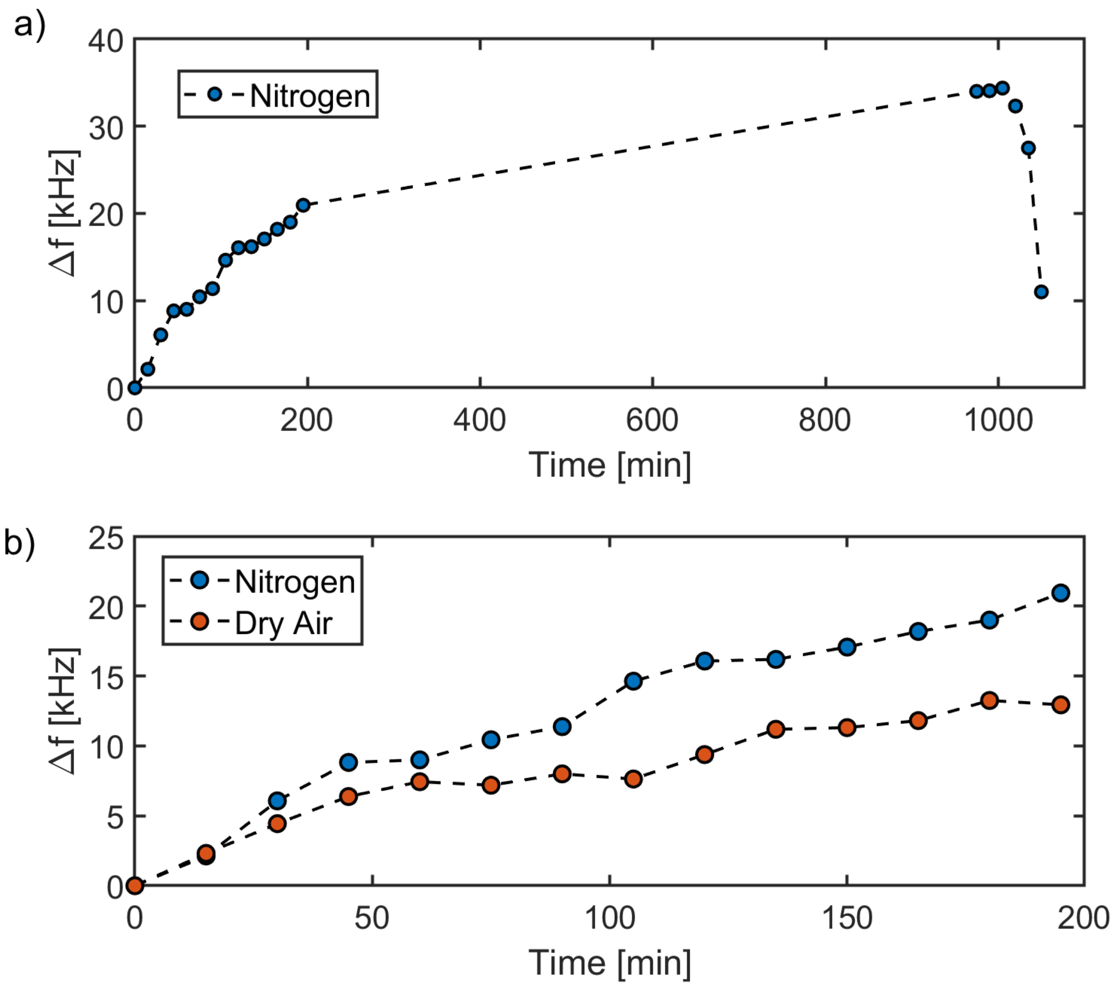

Figure 6.24: a) Measured resonance frequency shift (Δf) of ZnO cantilever in nitrogen over a span of 16 hours. b) Measured Δf in nitrogen (blue) compared to dry air (red) over 3 hours.

From the figure, it is evident that Δf_{N2} is larger than Δf_{Dryair}. The larger shift in nitrogen is attributed to the desorption of both oxygen and water while the shift in air is attributed to the desorption of water only.

The frequency response of the ZnO cantilever in varied RH conditions is obtained. The dry air humidity desorption experiment is repeated over a span of 16 hours. A commercial wireless RH sensor (Sensorpush HT1) with an accuracy of ±4.5% below 20% RH and ±3% above 20RH, was placed in the test chamber to record the RH level. Figure 6.25a shows the measured frequency response to dry air (blue, measured every 10 minutes). The RH level reported by the commercial sensor is shown as well (red line). It is seen from the figure that total shift was $\Delta f = +27.75\ kHz$ after 16 hours of dry air (100 SCCM flow rate). The humidity level of the test chamber decreased from 22.1 %RH to 5.8 %RH during the testing span. The frequency shift curve of the ZnO cantilever and the RH response of the commercial sensor appear to be mirrored images of each other, which may signify the suitability of the ZnO cantilever for commercial RH sensing applications.

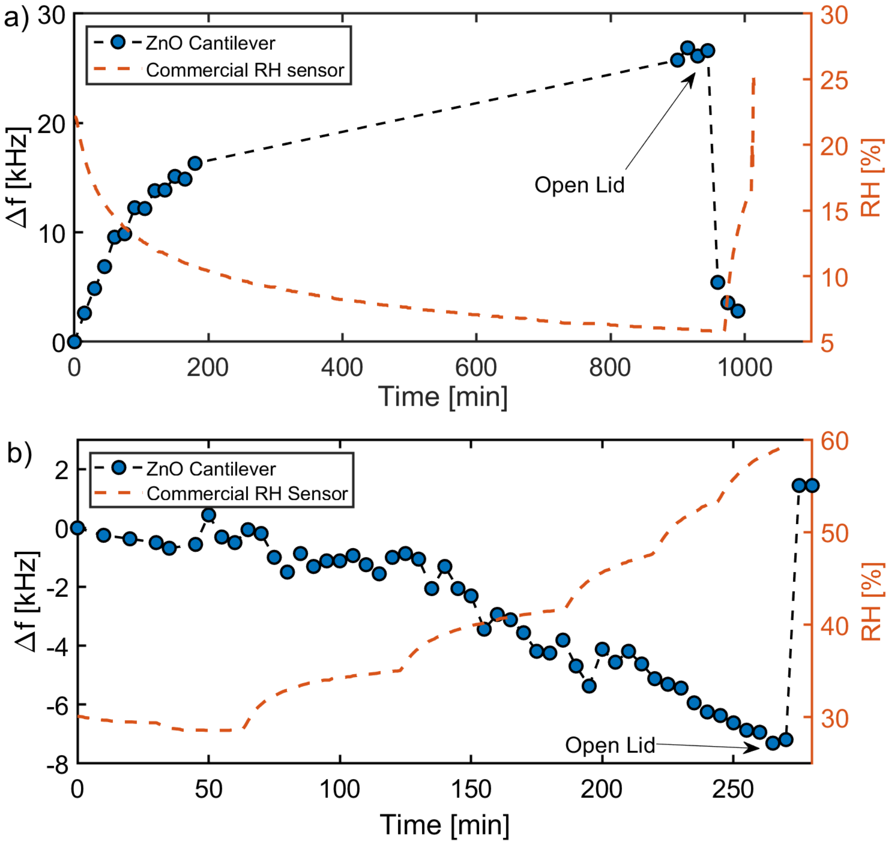

Figure 6.25: Measured resonance frequency shift (Δf) of ZnO cantilever in a) decreasing RH levels over a span of 16 hours and b) increased RH levels over a space of 4 hours. The RH of the test chamber is monitored during the test (red line).

The gas delivery system was used to increase the humidity level of the test chamber from ambient conditions. This was done by “bubbling” water with the dry air carrier gas to produce humidified air. The stream of humidified air was combined with an additional stream of dry air before injection into the test chamber. The flow rate ratio between the humidified air and dry air was varied to set the RH level of the injected gas (with a combined flow rate of 100 SCCM). Figure 6.25b, shows the frequency response of the ZnO cantilever (blue) as the RH level was increased from 28.6% to 59% in steps (red line). The RH level as determined by the commercial sensor are well resolved, which is likely due to on board signal processing and averaging over many measurements. In comparison, the frequency measurements of the ZnO cantilever are single measurements (not averaged) and are unprocessed for noise reduction. A negative Δf is observed which indicates the adsorption of humidity onto the ZnO cantilever. A total shift of $\Delta f = -6.69\ kHz$ was observed. Opening the lid of the test chamber at 270 minutes resulted in an immediate positive shift towards the f measured in ambient atmosphere, which indicates relatively quick humidity desorption .

The measured Δf from the humidity desorption/adsorption experiments in Figure 6.25 were combined and plotted as a function of the RH level of the test chamber, shown in Figure 6.26a. The combined plot shows a non-linear, exponential relationship between Δf and RH%. The data was fitted to a two term exponential equation with 4 fit parameters resulting in a R^2 value of 0.9898. Figure 6.26b, shows the data with the inclusion of error bars to account for errors in the measurements. The frequency measurement error or "noise" was determined by obtaining the standard deviation (σ_{std}) of 31 frequency measurements of the ZnO cantilever held in ambient air conditions over the course of 1 hour, yielding $\sigma_{std} = 0.231\ kHz$. The error in relative humidity measurements was obtained from the reported accuracy of the SensorPush HT1 relative humidity sensor (±4.5% below 20% RH and ±3% above 20RH).

The sensitivity (S) was determined by obtaining the derivative [51] of the fit of the $frequency\ vs.\ RH$ data (Equation 6.6). The calculated sensitivities were plotted as function of RH, shown in Figure 6.27. This shows the dependence of the sensitivity on the RH level. The average sensitivity in the 30-60 %RH range was 251.9 $\frac{Hz}{\%RH}$, while significantly higher sensitivities were obtained at low %RH. A maximum sensitivity of 3382 $\frac{Hz}{\%RH}$ was obtained at 5.8 %RH.

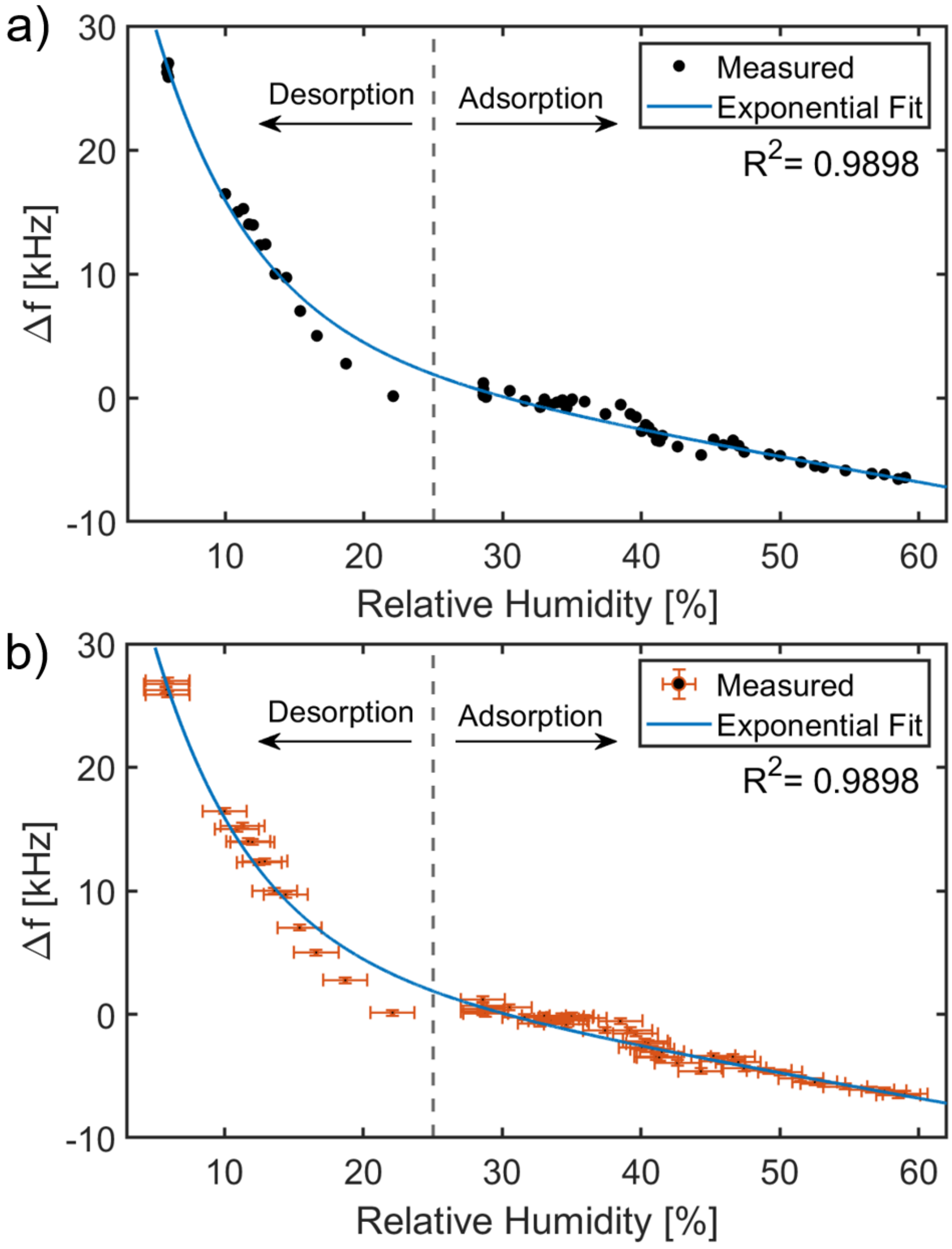

Figure 6.26: a) Measured resonance frequency shift (Δf) of ZnO cantilever as a function of RH level of the test chamber. The data was fitted to a two term exponential equation to give a R^2 value of 0.9898. b) Same figure with inclusion of experimental error of 0.23 kHz in frequency axis and 3-4.5% in relative humidity axis.

$$S = \frac{\partial f}{\partial RH} \tag{6.6}$$

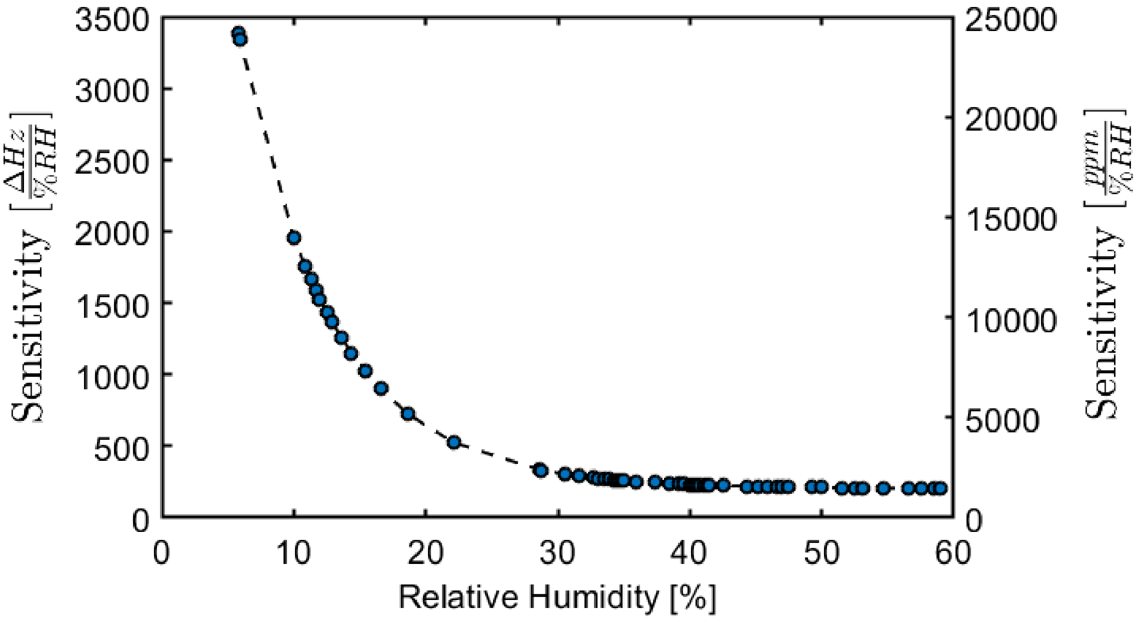

Figure 6.27: Calculated sensitivity of the ZnO cantilever as a function of RH. The sensitivity is given in $\frac{Hz}{\%RH}$ (left) and $\frac{ppm}{\%RH}$ (right).

For comparison to other gravimetric (frequency shift) based humidity sensors in literature, the sensitivity was determined in parts per million units (ppm), given in Equation 6.7. These values are shown on the second y-axis in Figure 6.27. The maximum sensitivity at 5.8 %RH was 23649 $\frac{ppm}{\%RH}$, while the average sensitivity in the 30-60 %RH range was 1556 $\frac{ppm}{\%RH}$.

$$S = \frac{ppm}{\%RH} \qquad \rightarrow \qquad ppm = \frac{\Delta f}{f_n} \times 10^6 \tag{6.7}$$

Table 6.1 is a comprehensive list of other gravimetric RH sensors reported in literature. The type of devices includes quartz crystal microbalances (QCM), capacitive micromachined ultrasonic transducer (CMUT), piezoresistive micromachined ultrasonic transducer (PMUT), film bulk acoustic wave resonator (FBAR), surface acoustic wave (SAW) resonators and microcantilevers. The ppm sensitivities and corresponding humidity ranges are compared to the ZnO cantilever from this work. The highest reported sensitivity of $S = 1530\ \frac{ppm}{\%RH}$ was obtained for the graphene oxide coated CMUT in the 43-94% RH range [198]. The second highest sensitivity of $S = 924\ \frac{ppm}{\%RH}$ was obtained for the MWCNT/nafion SAW device in the range of 11-75% [199].

Table 6.1: Comparison of gravimetric (frequency shift based) relative humidity sensors in literature.

Device	Receptor Material	Sensitivity $[\frac{ppm}{\%RH}]$	Humidity Range [%]	Ref
QCM	ZnO nanotretrapods	9.94	40-80	[55]
	ZnO nanowires	0.37	48-88	[57]
	ZnO nanoparticle/nanowire	0.12	11-97	[58]
	ZnO nanoparticles	15.60	33-95	[61]
	ZnO nanoneedles	0.7-2.14	11-95	[200]
	TiO2 nanoparticles	0.75	0-25	[201]
	PEDOT/PSS nanofibers	8.69	38-59	[202]
	GO/PEI film	2.73	11.3-97.3	[203]
	GO	2.87	6.4-97.3	[23]
	Cellulose nanocrystal	5.5 28	11-54 54-97	[204]
	Graphene QD-chitosan	3.9	11-95	[205]
CMUT/PMUT	Mesoporous silica	462.2	0-80	[206]
	Mesoporous silica	24	0-20	[207]
	Guanidine polymer	52	0-20	
	GO	560 1530	11-43 43-94	[198]
	GO	271.17	10-90	[208]
FBAR	GO film	5.9	3-83	[209]
	ZnO	5.94	22-82	[210]
SAW	MWCNT/nafion	924	11-75	[199]
	ZnO film	27	5-87	[211]
	GO film	235.6	3-83	[212]
	GO	29.62	10-90	[213]
	CeO2/PVP	17.55	11-95	[214]
	PVA	10.41	0-99	[215]
	GO/PVA/SiO2	4.85 11.9	5-55 55-90	[216]
Microcantilever	CMOS Metal	265	15-85	[217]
	Hydrogel	640-850	10-50	[218]
	PMMA	192	10-50	[219]
	Chitosan/ZnO nanorods	16.9-83.3	30-80	[50]
	ZnO nanorods	4.4	30-80	
	GO	40	10-90	[220]
	ZnO thin film	**2378-23649** **1556**	**5.8-28** **30-60**	**This work**

In comparison, the ZnO cantilever in this work achieves record high sensitivity in the low RH range, which is several orders of magnitude larger than the values listed for other devices. The sensitivity achieved in the 30-60 %RH range is also larger than the highest reported sensitivity as well. The enhanced sensitivity of the ZnO cantilever may be attributable to its low overall mass as well as the dual role of the ZnO layer as both the sensing and structural layer.

The adsorption mechanics of gases onto a surface can be described by an adsorption isotherm model. The isotherm describes the amount (mass or volume) of adsorbate (gas molecule) on the adsorbent (sensing surface) as a function of the gas concentration. Table 6.2 lists 8 different isotherm models relevant for the adsorption of humidity onto various surfaces. The expressions are given as an amount of adsorbed mass (X) as a function of water activity $a_w = \frac{\%RH}{100}$ [221]. All other parameters are left as fitting parameters.

Table 6.2: Adsorption isotherm expressions.

Model	Expression
Langmuir [222]	$X = \frac{X_m K a_w}{1 + K a_w}$
Freundlich [223]	$X = K a_w^{1/n}$
BET [224]	$X = \frac{X_m C a_w}{(1 - a_w)(a_w(c-1)+1)}$
GAB [221]	$X = \frac{X_m C K a_w}{(1 - K a_w)(1 - K a_w + C K a_w)}$
Oswin [221]	$X = A \left[\frac{a_w}{1 - a_w}\right]^B$
Henderson [221]	$X = \left[-\frac{log(1 - a_w)}{A}\right]^{\frac{1}{B}}$
Peleg [221]	$X = A a_w^{n_1} + B a_w^{n_2}$
Smith [221]	$X = A + B\ log(1 - a_w)$

The ZnO cantilever frequency shift (Δf) response was converted to a relative change in mass $\frac{\Delta m}{m_c}$ as seen in Equation 6.8. This was subsequently fitted to the isotherm models listed in Table 6.2, as shown in Figure 6.28.

$$\begin{gathered} \Delta m = -2\frac{\Delta f}{f_n} m_c \\ X = \frac{\Delta m}{m_c} = -2\frac{\Delta f}{f_n} \end{gathered} \tag{6.8}$$

As seen from the figure, the best fit was obtained for the Langmuir and Guggenheim-

Anderson-de Boar (GAB) isotherms, with a $R^2 = 0.99889$. The Langmuir isotherm assumes that adsorption occurs until a complete monolayer of the gas is adsorbed, after which no further adsorption takes place. The Brunauer-Emmet-Teller (BET) isotherm assumes adsorption occurs in a multilayer fashion. The GAB isotherm is a refinement of both the Langmuir and BET models and combines both monolayer and multilayer theory [221]. Good fits with the Langmuir and GAB isotherms and poor fitting with the BET isotherm suggests that humidity adsorption on the ZnO cantilever takes place in a monolayer fashion for the RH range tested here.

6.5 Design Recommendations

The promising results presented here, warrant a second design iteration to address areas of concern. The first issue to address is the instability of the ZnO cantilever resonance frequency over a timescale of weeks or months, shown in Figure 6.23. The decrease of the resonance frequency over days was attributed to the relaxation of residual stresses in the layers of the cantilever. One source of these residual stresses is the lattice mismatch between Al and ZnO layers, which yielded curved beams for longer beam lengths. A design where the top Al layer is not required would rectify this issue. Another solution is to the optimize the residual stresses in the ZnO layer by varying the AP-SALD deposition parameters. For conventional ALD, it was shown that the deposition process parameters influences the amount of residual stress in deposited metal oxide films [225, 226], and therefore a similar effect is expected for films deposited by AP-SALD. However, optimization of the film's residual stresses should not be done at the expense of its structural integrity.

The second design recommendation is the removal of the top aluminum layer, which has implications on actuation and read out method. As discussed previously, the removal of the top aluminum layer is expected to prevent residual stress issues within the cantilever beam. Removal of the Al layer also increases the ZnO surface area available for gas sorption. More importantly, removal of this layer further reduces the number of layers on the cantilever to 1 which should improve the quality factor as well as reduce the overall mass, making it

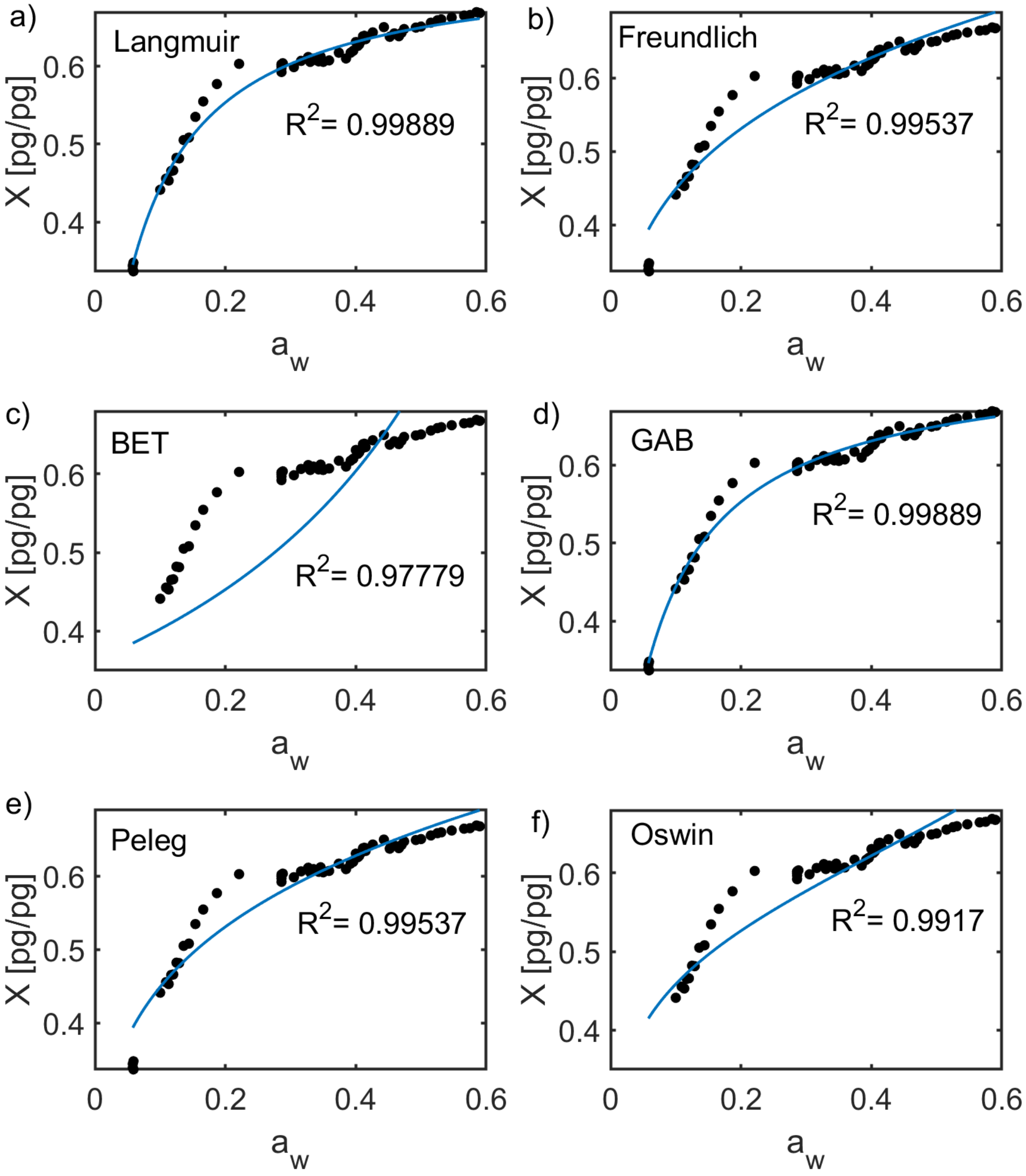

Figure 6.28: ZnO cantilever RH response fitted to sorption isotherm models. a) Langmuir, b) Freundlich, c) Brunauer-Emmett-Teller (BET), c) Guggenheim-Anderson-de Boar (GAB), d) Peleg, and f) Oswin. The Henderson ($R^2 = 0.92327$) and Smith ($R^2 = 0.978849$) isotherms are not shown.

more sensitive to analytes. Suitable replacements for the actuation and readout method are required. For the actuation method, it is advantageous to utilize the piezoelectric properties of the ZnO layer. An actuation voltage would need be applied across two electrodes however, it is unclear if their placement on the cantilever itself is required. Electrodes for actuation is avoided altogether by utilizing the inherent "self-actuation" behavior of the ZnO cantilever observed in ambient atmosphere (Figure 6.21).

With the removal of the top Al layer, readout via laser vibrometry or capacitance is ruled out. Instead, piezoresistive elements can be placed at the anchor of the ZnO cantilever to obtain its displacement signal. Doing so allows for a single ZnO layer cantilever to be used as a gas sensor. However, the placement of the piezoresistor may introduce additional damping or may prevent the self-actuation behavior. It is also possible that piezoresistive readout may not be able to pick up the self-actuated oscillations.

The removal of the top Al layer also removes the requirement for the bottom electrode layer. The effects of SQFD can be eliminated by creating a larger gap underneath the cantilever. This can be done by a bulk etch of the substrate itself (bulk micromachining).

In the case that a top metal electrode is a necessity, an alternative metal that does not oxidize easily should be used such as gold. However, implementation of gold requires further changes to the fabrication process as it was not compatible to use as an etch mask for the RIE of ZnO. Therefore, for the use of gold as a top electrode an additional lithography step would be required to form a protective sacrificial polymer layer on top of the gold so that is is compatible with the subsequent RIE process. Gold is also preferred for wire-bonding. Moreover, larger pad sizes and pad thicknesses are required for improved wire-bond adhesion. As discussed previously, the increase in the bonding pad thickness requires an additional lithography step. Another consideration is the placement of the bonding pads relative to the cantilever device. In the current design the pads are placed 100 μm away from the device which is not ideal. In a new layout design, it is recommended that the pads are placed further away on one side of the chip. Other electrical interface techniques can be used to avoid wire-bonding altogether, such as the use of ribbon connector style contacts.

The final design recommendation is to further miniaturize the ZnO cantilever by utilizing 1D nanostructures such as nanowires, nanorods and nanobelts. Similar to the single

MWCNT cantilever reported previously [37], a single 1D ZnO nanostructure can be utilized as a cantilever for enhanced sensitivity potentially towards atomic mass resolution. However, the complexity of such device and its readout systems would likely make it not practical for use.

6.6 Conclusions

A novel zinc oxide resonant microcantilever device was fabricated and its humidity sensing performance was evaluated. In this cantilever architecture, the ZnO layer served as both the cantilever structural layer and the gas sensitive receptor layer. In doing so, the number of layers on the cantilever was reduced to minimize potential interlayer damping effects. Additionally, the overall cantilever mass was reduced by utilizing a thin ZnO layer thickness of 200 nm, deposited by the AP-SALD technique. These design aspects were instrumental to achieving record high sensitivities to water vapor or humidity when compared to other frequency shift based humidity sensors. The ZnO cantilever demonstrated a remarkable sensitivity of 23649 $\frac{ppm}{\%RH}$ at 5.9%RH and an average sensitivity of 1556 $\frac{ppm}{\%RH}$ in the range of 30-60%RH. Notably, no actuation voltage was required to actuate the ZnO cantilever, as it exhibited a “self-actuation” behavior in air. Adorption isotherm modeling revealed that the humidity adsorption on the ZnO cantilever took place in a monolayer fashion, based on the Langmuir and GAB isotherm models.

The ultra high sensitivity obtained at low %RH is particularly beneficial for applications where low humidity or moisture levels have detrimental implications. Additionally, the self-actuation behavior is advantageous for low-power consumption type devices. While the results are promising, there are some areas of improvement. Notably, the instability of the ZnO cantilever natural resonance frequency over several weeks. This was attributed to the relaxation of residual stresses in the beam, and would likely require further optimization of the fabrication process. Other design recommendations include: removal of the top aluminum layer, utilize self-actuation behavior instead of electrostatic actuation coupled with piezoresistive readout and improvements to the design of the contact pads for wirebonding. The response of the ZnO cantilever to other gases is proposed as future work.

"The bamboo that bends is stronger than the oak that resists."

— Japanese Proverb

Chapter 7

Nanomechanical Gas Sensing with Laser Treated 2D Nanomaterials [1]

7.1 Introduction

In recent years there has been a great interest in the development of 2D nanomaterials for the detection of toxic gases, environmental pollutants and VOCs, which is reflected in the sheer number of review articles on the topic [91–97]. Detection of VOCs in exhaled breath has been particularly useful for the diagnosis of a broad range of diseases such as diabetes, liver and lung disorders, and different forms of cancer [228]. Two dimensional (2D) nanomaterials such as graphene oxide (GO), molybdenum disulfide (MoS_2) and tungsten disulfide (WS_2), are viable candidates for use in chemical gas sensors due to their large specific surface area that can be tailored for analyte adsorption.

2D nanomaterials have been primarily used for the detection of toxic gases and pollutants such as nitrogen dioxide (NO_2), hydrogen disulfide (H_2S), carbon monoxide (CO)

---

[1] This chapter has been adapted with permission from the published manuscript of the same title by Mistry et al. [227], Copyright 2020, Wiley-VCH

and carbon dioxide (CO_2) [91,92,229], while the detection of VOCs by these materials has been limited. GO [24,230], MoS_2 [231,232] and WS_2 [233,234] have all shown a response to water vapor or relative humidity changes. Without the aid of other compounds or dopants, graphene oxide has shown a response to ethanol [235,236] and toluene vapors [237]. Similarly, MoS_2 and WS_2 have shown a response to vapors of ethanol, acetone, hexane, toluene and benzene [173,238,239]. In most of these reports, the sensing material is casted over a set of interdigitated electrodes to form a chemo-resistive sensor. The interaction between analyte vapors and the sensing material (i.e. through adsorption) results in charge transfer and in turn changes the electrical response of the material (resistance, voltage, current or impedance) and thus makes uses of the high theoretical conductivity of 2D materials.

To achieve high sensor response and sensitivity, resistive sensors require sensing materials with high conductance [96] and analyte adsorption properties. Graphene and other 2D materials have excellent conductive properties, but despite their large surface area, they have weak adsorption properties with various analytes due to their naturally passivated surfaces. The introduction of defects, dopants or functional groups improves analyte adsorption [172,240–242] but may reduce the conductivity of the material [243,244] which can have a negative effect on the response and sensitivity of a resistive sensor.

In this work, this tradeoff in the performance of sensors based on 2D materials is avoided by utilizing a piezoresistive nanomechanical Membrane-type Surface stress Sensor (MSS) [19,20] as a sensing platform instead of a resistive sensor. The MEMS-based MSS consists of a round silicon membrane suspended by four supports with embedded piezoresistors. The membrane is coated with a gas sensitive material known as a receptor layer, which interacts with a target analyte resulting in a deflection of the membrane. This deflection imparts a strain on the piezoresistors producing a change in their resistance. It is important to note here that while the output of the MSS is still an electrical signal (resistance change of piezoresistors), it is not dependent on the electrical properties of the receptor layer. As described in Chapter 2.1.2, receptor layer materials that have been incorporated into a MSS include PEI [19], PSS [20], silica-porphyrin hybrid nanostructures [22], titania coated silica particles [21,245], porphine molecules with different center metal ions (zinc, nickel, iron) [246], gold nanocages [247], and recently nanoparticles based on metal organic frameworks (MOF) [248].

Herein, graphene oxide (GO), molybdenum disulfide (MoS_2) and tungsten disulfide (WS_2) are treated with a femtosecond laser treatment process to introduce defects, dopants, and functional groups for improved gas adsorption properties. In Chapter 5, it was demonstrated that the laser treated 2D materials showed a change in reflectance intensity when exposed to vapors of water, acetone and ethanol due to film expansion. It is therefore advantageous to integrate these materials onto a MSS platform and observe the sensing signals and sensitivities to a variety of VOCs. By doing so, the suitability of 2D materials for applications in piezoresistive gas sensing is evaluated. 2D materials typically have a high Young's modulus [249, 250] which has been shown to be advantageous for receptor materials incorporated into an MSS [251, 252]. The MSS platform eliminates the need for highly conductive 2D materials, allowing the materials to be freely modified to improve their gas adsorption properties. Additionally, the mechanisms that contribute to increased sensor response of the 2D materials are experimentally investigated.

7.2 Experimental Section

7.2.1 Laser Treatment Process

The laser was produced with a Ti:Sapphire regenerative amplifier, producing a central wavelength of 800 nm, pulse duration of 35 fs, average power of 2 W, and a repetition rate of 1 kHz. These parameters were used in the treatment of all the 2D materials, unless otherwise stated. The 2D material solutions were placed in 5ml vials and irradiated with the laser. The incident laser beam was focused with a 5 cm off axis parabolic mirror. The focal point was set at depth 0.5cm below the air/solution interface. During the irradiation process the solutions were constantly stirred by a magnetic stirrer at 250 RPM.

7.2.2 2D Material Solution Preparation

A highly concentrated (6.2 mg ml^{-1}) graphene oxide (GO) solution and ultrafine powders of hexagonal boron nitride (BN), molybdenum disulfide (MoS_2) and tungsten disulfide (WS_2) were purchased from Graphene Supermarket. Using the previously reported process [98], 4 ml of the highly concentrated GO solution was treated for 1 and 1.5 hours, respectively to produce the undoped GO solutions utilized in this work. BN doped GO solutions were prepared as previously reported [253]. 1.24 mg ml^{-1} hexagonal boron nitride in a 1:1 deionized ethanol:water solution was laser treated for 55 min. The treated BN solution and the highly concentrated GO solution (6.2 mg ml 1) were mixed at different volume percentages: 5 vol% BN and 95 vol% GO, and 15 vol% BN and 85 vol% GO, and further laser treated with a 1 W beam power for 50 minutes. The MoS_2 and WS_2 powders were laser treated in a deionized water solution and a 1:1 deionized ethanol:water solution following a previously reported recipe [101]. MoS_2 solutions at a concentration of 1 mg ml^{-1} were treated for 2 hours while WS_2 solutions at a concentration of 0.5 mg ml^{-1} were treated for 20 minutes.

7.2.3 Materials Characterization

Characterization samples were prepared by drop casting 250 µL of the laser treated solutions on silicon substrates and drying at room temperature. Raman spectroscopy was carried out with a Renishaw micro-Raman spectrometer with an excitation wavelength of 632.8 nm and power of 20 mW. X-ray diffraction (XRD) was performed using an X'Pert Pro Panalytical diffractometer system with the Kα1 wavelength of 1.524 Åat 45 kV and 35 mA. x-ray photoelectron spectroscopy (XPS) was done with a Thermo ESCALAB 250 with an incident energy of 1486.6 eV. The peak corresponding to the Si 2p transition was used to calibrate the binding energies. Spectral analysis was performed by deconvoluting Gaussian multipeak fits.

7.2.4 MSS Fabrication and Receptor Layer Coating

The fabrication of the nanomechanical Membrane-type Surface stress Sensor has been previously reported elsewhere [19, 20]. Coating of the membranes with the 2D materials was carried out with an inkjet spotting unit (LaboJet-500SP, MICROJET Corporation) equipped with a nozzle (IJHBS-300, MICROJET Corporation). This instrument is capable of drop casting picolitre (pL) sized droplets with micrometer precision. The casting speed, volume and number of droplets were fixed at approximately 5 m s^{-1}, 300 pL and 300 droplets, respectively. The sample stage was heated to 60°C to evaporate the solvent. Optical microscope images of the uncoated and coated MSS devices are shown in Figure B.1.

7.2.5 Analyte Vapor Sensing

The coated MSS were placed in a Teflon enclosure kept at room temperature. The enclosure was connected to an automated gas flow system consisting of a nitrogen cylinder, two mass flow controllers and vials to hold the analytes to be tested. Nitrogen was used as a purge and carrier gas. The total flow rate into the enclosure was set to 100 sccm. Vapors of each analyte were produced by bubbling with the carrier gas at flow rates of 2%, 5% and 10% of the total flow rate to vary the concentration of the analyte. The remaining balance was nitrogen. The analytes used in this study were: water, ethanol, hexanol, hexanal, heptane, methylcyclohexane, toluene, ethyl acetate and acetone. Table B.1 in Appendix B shows the vapor pressure of the analytes and the calculated saturation concentration (100%) in parts per million (ppm). The corresponding analyte concentrations (ppm) at 2%, 5% and 10% relative vapor pressures were determined from the saturation concentration and used for sensor sensitivity calculation. At the start of the measurement, pure nitrogen was introduced into the enclosure for 1 minute as a purging step. The analyte vapor flow was introduced in 10 second ON/OFF cycles for 10 cycles for a total of 200 seconds, followed by nitrogen purging. The measurement process was repeated for each analyte at each relative vapor pressure. The resistances of the four piezoresistors were measured with a Wheatstone bridge circuit as described elsewhere [251]. The data were recorded at the bridge voltage of -0.5 V and a sampling rate of 10 Hz. The last 5 cycles were used for analysis and baseline corrected.

7.3 Results and Discussion

Solutions of multilayered 2D nanoparticles were fabricated using a previously reported femtosecond laser treatment process [98, 101, 253, 254]. The laser focal point interacts with the untreated 2D flakes and the solvent molecules, whereby a multiphoton-absorption ionization phenomenon occurs. The intense electric field of the laser extricates the electrons from the molecule cluster, resulting in the constituents of the cluster to become highly ionized with a mutually repulsive charge effectively breaking the bonds. This phenomenon is known as Coulomb explosion. Leveraging this concept, the 2D flakes are broken into smaller particles with highly active edge sites which may bond with the dissociated solvent atoms, as illustrated in Figure 7.1. Due to the high power used in this process, several laser-induced scenarios may occur including vacancy formation in the basal plane, introduction of substitutional impurities from the solvent species, defect sites, dangling bonds, and unsatisfied edges. All of these have the potential to enhance the adsorption properties of the 2D material.

Fabrication of the MSS and its working principle have been reported previously [19,20]. The diameter of the membrane is 300 µm with a thickness of 2.5 µm. As depicted in Figure 7.1, laser treated 2D materials were deposited as the receptor layer on the sensor membrane. The coating of the sensors was carried out with an inkjet spotting system, which deposited 300 droplets of solution (300 picolitres each) onto the membrane. The coatings are expected to appear similar to the SEM images of drop casted GO and WS_2 films shown in Figure 4.9 and Figure 4.10. The interaction of an analyte with the 2D material receptor results in a deflection of the membrane, as illustrated in the lower portion of Figure 7.1, which imparts a strain on four piezoresistors (illustrated in red in Figure 7.1; refer to previous report [19] for detailed structure of each piezoresistor) embedded at the fixed supports of the membrane. The strain induced in the piezoresistors by the introduction of

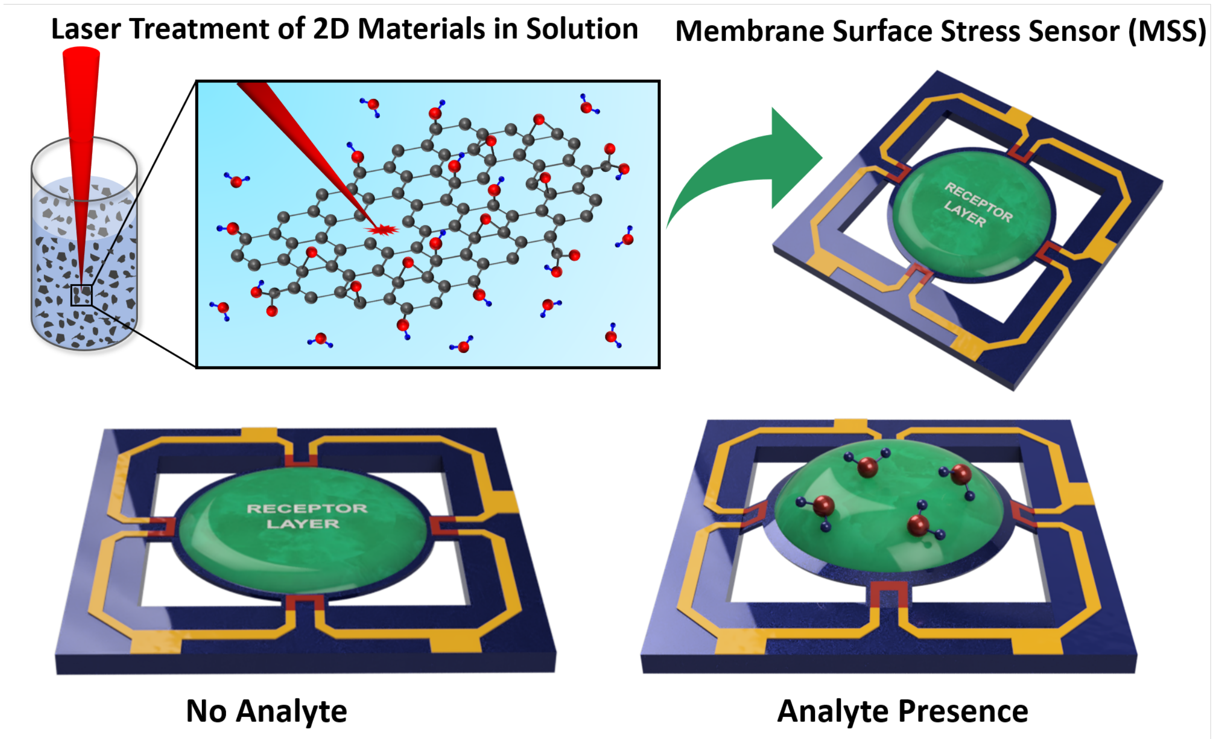

Figure 7.1: Laser treatment of 2D materials in solution and their application as the receptor layer in the nanomechanical Membrane-type Surface stress Sensor (MSS) for gas sensing. Laser treatment of bulk flakes of GO, MoS_2 and WS_2 dispersed in water or ethanol:water solution results in the creation of defects and addition of functional groups from the solvent. The solution is then casted as the receptor layer (green) on the MSS. The coated membrane is physically deflected in the presence of a gaseous analyte imparting a strain on the piezoresistors (red) placed at the four fixed ends of the membrane. Detailed schematic of the MSS has been previously shown elsewhere [19, 20].

different analytes was measured electrically using a Wheatstone bridge circuit resulting in a millivolt output signal.

The coated sensors were placed in a sealed Teflon enclosure and were tested with the following analytes: water, ethanol, hexanol, hexanal, heptane, methylcyclohexane, toluene, ethyl acetate and acetone. Vapors of the analytes were produced by bubbling with a nitrogen carrier gas and injected into the enclosure in ON/OFF intervals of 10 seconds each for 10 cycles. The analyte concentration in the chamber was controlled by varying the flow rate of the carrier gas to achieve analyte relative vapor pressures 2%, 5% and 10%. The concentration in parts per million (ppm) of each analyte is listed in Table B.1 in Appendix B. Figure 7.2 shows the sensor response of the coated sensors exposed to water, ethanol, and acetone vapors at 10% relative vapor pressure. In all cases, an uncoated MSS was measured under identical conditions for comparison (black lines in Figure 7.2). Figure B.2-B.9 inAppendix B show the response data for each receptor layer, to each analyte, at the three relative vapor pressures tested (2%, 5% and 10%). It is evident that all the receptor materials tested are capable of sensing the analytes studied here, with varying degrees of sensitivity.

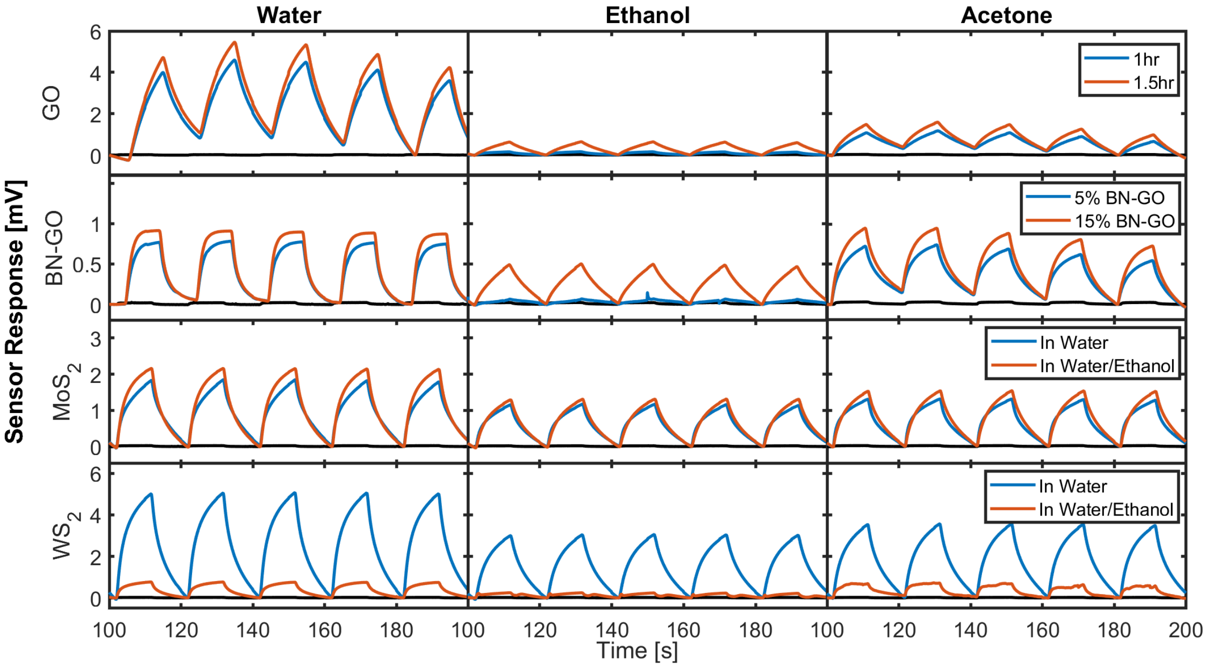

Figure 7.2: Coated MSS response [mV] to water (left column), ethanol (middle column) and acetone (right column) vapors at 10% relative vapor pressure, response to other tested analytes are included in Appendix B. The response to the analytes is compared between: graphene oxides (top row) treated for 1 hr (blue) and 1.5hrs (red), boron nitride doped graphene oxide (2nd row) doped with 5% (blue) and 15% (red) boron nitride, molybdenum disulfide (3rd row) treated in water (blue) and ethanol:water (red) solutions, and tungsten disulfide (last row) treated in water (blue) and ethanol:water (red) solutions. All results are compared to the uncoated MSS response (black).

The estimated sensitivity ($\Delta\mu V \Delta ppm^{-1}$) of the coated sensors was calculated by plotting the amplitude of the response signal at each analyte concentration (ppm) and determining the slope by linear regression [255]. The estimated sensitivities are listed in Table 7.1 with the standard error of the regression shown in Table B.2 in Appendix B. The sensitivities (s) and standard deviation (σ_{std}) from the linear regression analysis were used to estimate the limit of detection (LOD) as $3\sigma_{std}/s$ [229]. Table B.3 in Appendix B lists these calculated LODs (ppm). The 2D materials utilized in this work demonstrate a large range of sensitivities from 0.01 µV ppm^{-1} for the detection of ethanol with 5% BN-GO to 43.40 µV ppm^{-1} for the detection of hexanol with WS_2 laser treated in water. The sensitivity to a particular analyte varied considerably depending on the 2D material that was used as the receptor material. In general, the largest sensitivities were obtained for the detection of hexanol which range from 6.90 to 43.40 µV ppm^{-1}. The lowest sensitivities were obtained for acetone which range from 0.04 to 0.20 µV ppm^{-1}. As listed in Table B.1 in Appendix B, hexanol has the lowest vapor pressure while acetone has the highest vapor pressure. Here, the vapor pressure corresponds to the amount of analyte that can exist in the gas phase in the sensing chamber. Therefore, the high sensitivities to hexanol can be partially attributed to its relatively low abundance in the gas phase and similarly, the low sensitivities to acetone is partially attributed to its high abundance [256]. WS_2 treated in water had the highest sensitivities to each analyte tested, ranging from 0.20 to 43.40 µV ppm^{-1}. Conversely, the WS_2 treated in the ethanol:water solution had generally the lowest sensitivities ranging from 0.04 to 6.90 µV ppm^{-1}. These results demonstrate the capability of the laser treatment process to tune the gas adsorption behavior of the 2D materials.

Table 7.1: Estimated sensitivities of materials used in this work $[\mu V ppm^{-1}]$. Standard errors are listed in Table B.2 in Appendix B.

Analyte	1 Hr GO	1.5 Hr GO	5% BN-GO	15% BN-GO	MoS_2 in Water	MoS_2 in Ethanol:Water	WS_2 in Water	WS_2 in Ethanol:Water
Water	1.80	2.30	0.49	0.53	1.20	1.40	3.10	0.50
Ethanol	0.04	0.10	0.01	0.10	0.30	0.30	0.70	0.08
Hexanol	19.50	24.90	14.49	16.85	16.20	18.10	43.40	6.90
Hexanal	1.20	1.60	0.79	0.75	1.30	1.70	3.50	0.60
Heptane	0.06	0.20	0.02	0.16	0.40	0.50	1.20	0.20
Methylcyclohexane	0.70	0.80	0.38	0.36	0.60	0.70	1.50	0.30
Toluene	1.60	1.80	0.82	0.82	0.70	0.90	2.20	0.50
Ethyl Acetate	0.20	0.20	0.14	0.16	0.20	0.20	0.50	0.20
Acetone	0.04	0.05	0.04	0.05	0.07	0.08	0.20	0.04

It is difficult to compare the obtained sensitivities with those reported in literature due to the different sensor configurations used (i.e. resistive vs piezoresistive sensors) and the inconsistency in units used to report sensitivity. One report with which a direct comparison can be made is a piezoresistive microbridge structure coated with graphene oxide for relative humidity (%RH) sensing that was reported by Yao et al. [24] When normalized for the applied bridge voltage, the sensitivity of the GO coated sensor in Yao's work was 15.9 µV %RH^{-1}. In comparison, the laser treated GO coated MSS in this work obtained sensitivities of 603 µV %RH^{-1} and 758 µV %RH^{-1} (%RH converted from ppm of water), respectively.

In each study, an enhanced sensor response was obtained due to the laser treatment process affecting the composition and/or structure of the 2D materials. These mechanisms are discussed in detail in the following sections. A relative response intensity for each receptor material towards each analyte was calculated as the amplitude of the coated MSS signal divided by the amplitude of the uncoated MSS signal. The relative response plots allow for evaluation and comparison of gas sensing capabilities of the laser treated 2D materials.

7.3.1 Graphene Oxide

Figure 7.3 shows the relative response intensities of the MSS with laser treated graphene oxides to the analytes tested. It can be seen here that graphene oxide treated for a longer duration (1.5 hrs) consistently had a higher sensor response to the analytes than the 1 hr GO. To investigate these results, materials characterization was done, as shown in Figure 7.4. The Raman spectra of the D and G peaks (located at ≈ 1355 cm^{-1} and ≈ 1595 cm^{-1} respectively) are shown in Figure 7.4(a). The spectra of the laser treated GO solutions were compared to that of untreated GO (black). A ratio of the intensities between the D and G peaks (I_D/I_G) is an indicator of the amount of defect sites in the material [98], including carbon vacancies in the graphene sheet or carbon atoms not bonded in a sp^2 configuration (i.e., functional groups). As shown in the inset of Figure 7.4a, the I_D/I_G ratio increased from 0.85 for untreated GO to 0.9 for 1 hr GO to 1.21 for 1.5 hr GO. Defect sites on graphene and graphene oxide act as suitable adsorption sites for various analytes, and it was reported that an increase in the I_D/I_G ratio generally results in improved gas sensing ability for graphene based sensors [180, 237, 257].

The interplanar distance of the stacked GO sheets was determined by XRD as shown in Figure 7.4b. The 1.5 hr GO has a slightly larger interplanar distance of 0.887 nm compared to 0.845 nm of the 1 hr GO. This is correlated to the increase in defect density,

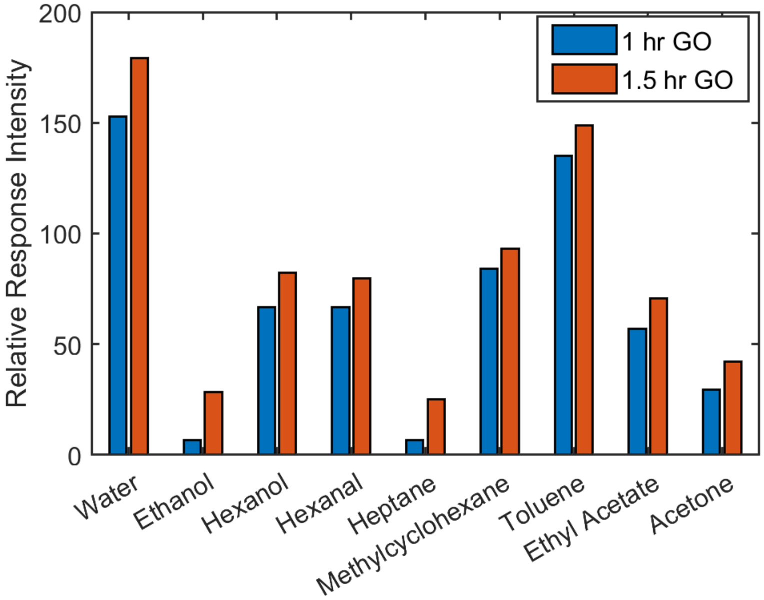

Figure 7.3: Relative response intensity $[mVmV^{-1}]$ of laser treated graphene oxide coated MSS to VOCs at 10% relative vapor pressure. The graphene oxide was laser treated for 1 (blue) or 1.5 (red) hours.

as there is an increase in the number of carbons bonded to functional groups that push the stacked planes away from each other [98]. While the difference in the interplanar distances is fairly small, the slightly larger spacing of the 1.5 hr GO may allow for an increased probability of analyte adsorption in between the planes. The reported and estimated sizes of the analytes [258, 259] are listed in Table B.1 inAppendix B. The sizes varied from 0.277nm (water) to 0.624nm (heptane). This range is of comparable magnitude to the interplanar space of GO such that it is conceivable that an increase in the spacing would allow for higher chance of analyte adsorption and contribute to the higher MSS response. This is in contrast to resistive based sensors, where a larger interplanar spacing between graphene sheets would reduce the conductivity as a result of the charge hopping mechanism (monolayer graphene resistive sensors perform better than multilayer graphene sensors [260]).

XPS was done to determine and quantify the functional groups. Figure 7.4c and d show the deconvoluted C 1s and O 1s spectra, respectively. Table B.4 in Appendix B lists all the peak locations and atomic percentages. The atomic percentage of the sp^2 carbon

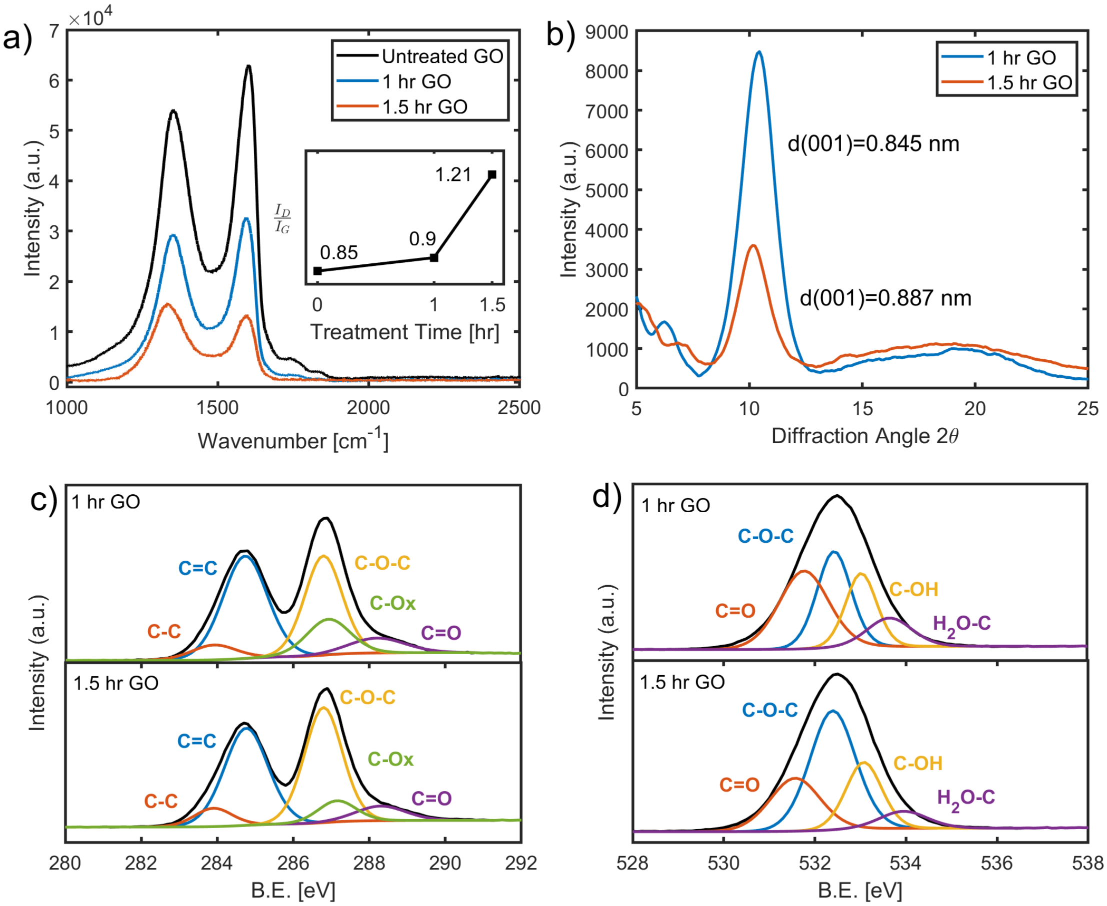

Figure 7.4: Materials characterization of laser treated graphene oxide (GO). a) Raman spectra of the D and G peaks of untreated (black), GO treated for 1-hour (blue) and 1.5-hour (red). The inset figure shows the increase of I_D/I_G ratio as the laser treatment time increases. b) XRD determination of interplanar spacing(d) of 1-hour (blue) and 1.5-hour (red) laser treated GO. c) C 1s XPS spectra of 1-hour (upper panel) and 1.5-hour (lower panel) GO. d) O 1s XPS spectra of 1-hour (upper panel) and 1.5-hour (lower panel) GO. Peak quantities are listed in Appendix B.

bond (C=C) located at 284.8 eV [261], decreased from 40.3 at% for the 1 hr GO to 39.1 at% for the 1.5 hr GO. A decrease in sp^2 carbon bonds indicates an increase in defects and attachment of functional groups with continued laser treatment. The deconvoluted C 1s spectra further revealed the presence of carbon – oxygen bonds at ≈ 286.8 eV, 287 eV and 288.3 eV which were assigned to the epoxy (C-O-C), C-Ox, and carbonyl (C=O) bonds respectively [262–264]. The total amount of carbon-oxygen bonds increased from 53.8 at% to 54.4 at% as the laser treatment time increased from 1 to 1.5 hrs. In the O 1s spectra, peaks located at ≈ 531.8 eV, 532.4 eV and 533 eV were assigned to carbonyl (C=O), epoxy (C-O-C) and hydroxyl (C-OH) bonds, respectively [265, 266]. Here, the increase in laser treatment duration shows an increase in the amount of epoxy and hydroxyl bonds, from 29.0 and 21.0 at% for 1 hr GO to 45.5 and 26.0 at% for 1.5 hr GO, respectively.

The XPS results demonstrate that the increase in laser treatment time resulted in a greater incorporation of oxygen functional groups onto the graphene oxide, consistent with the Raman and XRD data. As previously described, the source of the additional oxygen atoms was the water solvent that the GO flakes were dispersed, and laser treated in [101]. Defects such as oxygen functional groups can act as active adsorption sites on the surface of graphene. Several density functional theory (DFT) studies have demonstrated the enhanced adsorption energy of oxygen functional groups compared to pristine graphene, and that an increase in the number of oxygen atoms would lead to enhanced sensor performance [237, 267]. More specifically, these studies have all singled out the critical importance of hydroxyl groups for improved gas adsorption properties on GO. This was verified experimental by Wang et al. who utilized different reduction techniques to control the amount of hydroxyl, carbonyl and epoxy groups on reduced graphene oxide, and showed the highest gas sensor response was achieved with the GO with the highest amount of hydroxyl groups [268]. This is consistent with the results obtained here, where the GO laser treated for 1.5 hr had a larger C-OH signal in Figure 4d and showed a larger response to all analytes when incorporated in the MSS, as shown in Figure 7.3.

The high relative response to water seen in Figure 7.3 can be attributed to the hydrogen bonding interactions with the oxygen functional groups in the laser treated GO [180, 257, 261]. The second largest response was to toluene, which is an aromatic compound consisting of a benzene ring (six carbons) with a single methyl side group. The high response to this analyte can be attributed to the interaction between the π-bonds of the graphene oxide and the π-bonds of the benzene ring [246], known as the $\pi - \pi$ stacking phenomenon which occurs in aromatic and graphene type materials. This mechanism is supported by the fact that the response to methylcyclohexane, which has an identical structure to toluene but lacks the π-bonds, is lower than the response to toluene.

7.3.2 Boron Nitride doped Graphene Oxide

Figure 7.5 shows the relative response intensities of the 5% and 15% boron nitride doped (by volume) graphene oxides to the analytes tested. The 15% BN doped GO consistently had a higher sensor response than the 5% BN-GO. The Raman spectra of D and G peaks for the two receptor layers is shown in Figure 7.6a. It is seen that the 15% BN-GO sample had a higher I_D/I_G ratio than the 5% BN-GO sample (0.93 vs. 0.88). The higher I_D/I_G ratio can be attributed to a higher incorporation of boron and nitrogen dopants into the GO sheet. XPS analysis of these materials was done with the results summarized in Table B.5 and Table B.6 in Appendix B. The total nitrogen quantity in the doped GO samples was 0.5 at% for the 5% sample, and 0.9 at% for the 15% sample. An increase in performance of graphene based gas sensors as a result of nitrogen doping has been verified theoretically [172, 174, 269, 270] and experimentally [271]. Similar to the role of oxygen functional groups, the incorporated nitrogen in the graphene sheet act as adsorption sites for analytes. The deconvoluted N 1s XPS spectra are shown in Figure 7.6b revealing the C-N-B ($\approx$ 401.4 eV) and pyrrolic nitrogen ($\approx$ 402.5 eV) bonds [253]. The 15% BN-GO sample had a higher content of pyrrolic nitrogen (88.6%) than the 5% BN-GO sample (50.25%). Pyrrolic nitrogen replaces two carbon atoms in the graphene network to create a 5-atom ring. As a result, these bonds have enhanced catalytic activity and have been used as electrocatalysts for oxygen reduction reactions (ORRs) [272–276]. Co-doping with boron, further enhances the catalytic activity as it was shown that the boron atoms can help stabilize the nitrogen atoms and allow them to be located in more suitable sites for ORR [277]. Boron doping also aids in increasing the total nitrogen content incorporated into the GO [278]. Here, the enhanced electrocatalytic activity due to the BN co-doping appears to be beneficial towards gas sensing applications. The highest relative response obtained for the BN doped GO was to toluene (Figure 7.5), which is in contrast to the undoped GO which had the highest response to water (Figure 7.3). This may be attributed to the incorporation of pyrrolic nitrogen which retains the π-bonds of the graphene oxide to further promote the adsorption of toluene.

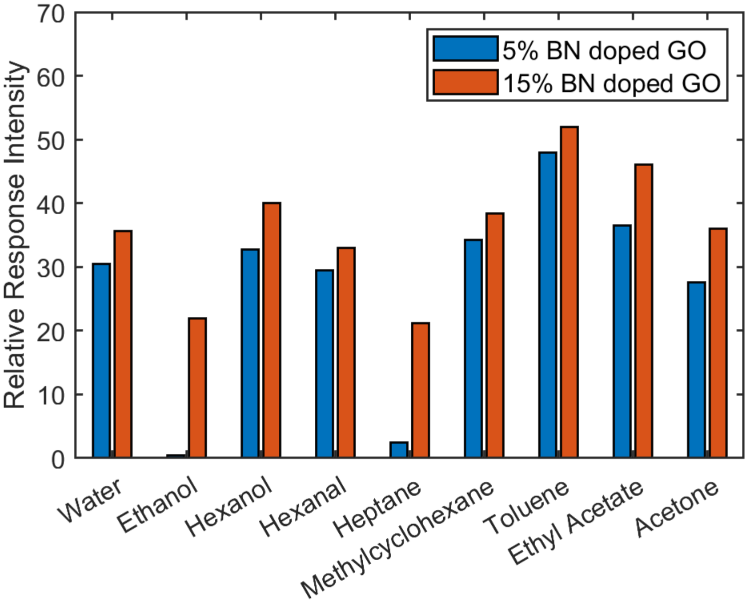

Figure 7.5: Relative response intensity of laser treated boron nitride doped graphene oxide coated MSS to VOCs at 10% relative vapor pressure. The graphene oxide was doped with 5% (blue) and 15% (red) boron nitride.

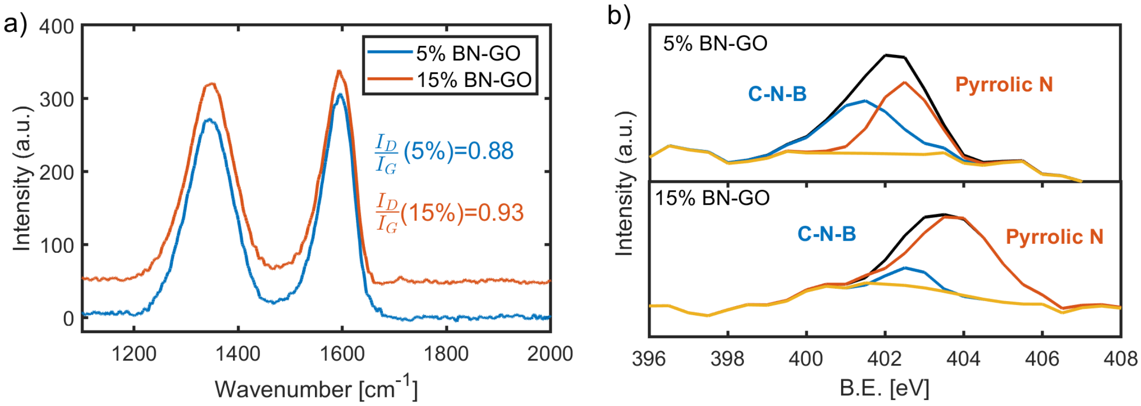

Figure 7.6: Materials characterization of boron nitride doped graphene oxide. a) Raman spectra of 5% (blue) and 15% (red) BN doped graphene oxide. The I_D/I_G ratios are listed in the inset. b) N 1s XPS spectra of 5% (upper panel) and 15% (lower panel) BN doped graphene oxide. The yellow line represents the background. Peak quantities are listed in Appendix B.

7.3.3 Molybdenum Disulfide and Tungsten Disulfide

The relative response intensity of the MoS_2 and WS_2 receptor layers is shown in Figure 7.7. The materials were laser treated in two different solvents (water and an ethanol:water mixture) and their MSS responses were compared. It was previously shown that the laser treatment of these 2D materials in water results in the incorporation of oxygen, whereas treatment in an ethanol:water solution also results in the attachment of carbon atoms from the ethanol to the periphery of the treated 2D flakes [101]. As shown in Figure 7.7a, the sensor response was consistently higher when the MoS_2 was treated in ethanol:water. The opposite effect was observed for the WS_2 receptor layers, where a much higher sensor response was achieved with the water solvent, as shown in Figure 7.7b. Additionally, both MoS_2 and WS_2 do not appear to be selective towards toluene, which is supported by the absence of π -bonds in these materials, unlike the graphene oxides discussed in the previous sections. The Mo 3d and W 4f XPS spectra are shown in Figure B.10, with the atomic percentages quantified in Table B.7 in Appendix B. The presence of oxygen bonds in all four solutions was evident with peaks at $\approx$ 233.5 eV and 236 eV assigned to MoOx [279–281], and $\approx$ 38.45 eV and 41.94 eV assigned to WO_3 [282] and WO [101, 280], respectively. The MoS_2 and WS_2 laser treated in water had higher atomic percentages of oxygen bonds than the MoS_2 and WS_2 treated in the ethanol:water solution. As previously discussed, an increase in oxygen atoms or functional groups tends to enhance the gas adsorption properties of graphene oxide, however for MoS_2 this does not appear to be the case. Ultimately, the analysis of the Mo 3d and W 4f XPS spectra was inconclusive. The Mo and W atoms of the basal plane generally have low surface energy and are chemically inert [173]. DFT studies have shown that gas adsorption primarily occurs on the sulfur atoms in MoS_2 and WS_2 materials [92].

The S 2p XPS spectra of the MoS_2 and WS_2 treated in water and an ethanol:water are shown in Figure 7.8 with a complete list of peak locations and atomic percentages included in Table B.8 in Appendix B. As shown in the figure, the S 2p spectra can be divided into two groups of peaks. Peaks in the range of 160-167 eV are attributed to sulfide bonds, while peaks in the range of 167-175 eV are attributed to sulphate bonds

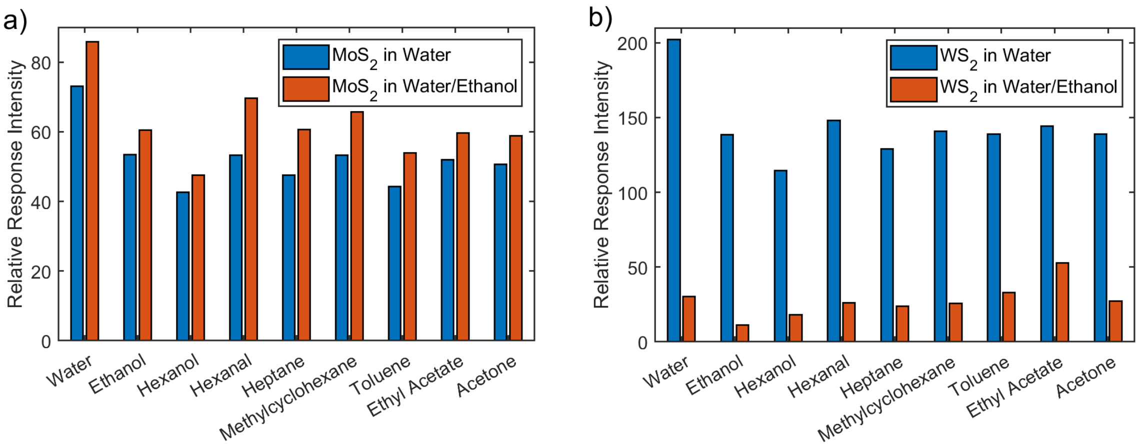

Figure 7.7: Relative response intensity of laser treated MoS_2 and WS_2 MSS to VOCs at 10% relative vapor pressure. a) The response of MoS_2 treated in water (blue) and ethanol:water (red) solution. b) The response of WS_2 treated in water (blue) and ethanol:water (red) solution.

[283, 284]. The sulfide groups are deconvoluted into two sets of doublets both consisting of a S $2p_{1/2}$ and S $2p_{3/2}$ peak. The higher energy doublet represents bridging or apical sulfur while the lower energy doublet represents unsaturated or terminal sulfur [285–288]. For example, the MoS_2 in ethanol:water spectrum (lower panel of Figure 7.8a) showed peaks at 162.67 eV (S $2p_{3/2}$) and 163.93 eV (S $2p_{1/2}$) which were assigned to terminal/unsaturated sulfur, while the peaks at 165.38 eV(S $2p_{3/2}$) and 166.82 eV (S $2p_{1/2}$) were assigned to bridging/apical sulfur. The sulphate peaks are deconvoluted into various forms of oxidized sulfur (sulfates/sulfonates) that take the form $S(O_x)$ where x=2,3,4 [283, 289–291]. For reference, the untreated MoS_2 and WS_2 used in this study have no bridging/apical or sulphate character [101] and hence, these bonds were created by the laser treatment process.

Table 7.2 lists the total sulfide and sulphate contributions for the four materials, calculated as the sum of the atomic percentages of the peaks in each group. A higher sulfide character is seen in MoS_2 in ethanol:water and in WS_2 in water. These two materials also had the higher sensor response as seen in Figure 7.7, suggesting a correlation between the sulfide bonds and enhanced gas sensing properties. Furthermore, these two materials also had larger quantities of high energy bridging/apical sulfur bonds, whereas the MoS_2 in water and WS_2 in ethanol:water had smaller proportions or none of these bonds Notably, the WS_2 in ethanol:water, which showed the lowest relative response intensity in Figure 7.7,

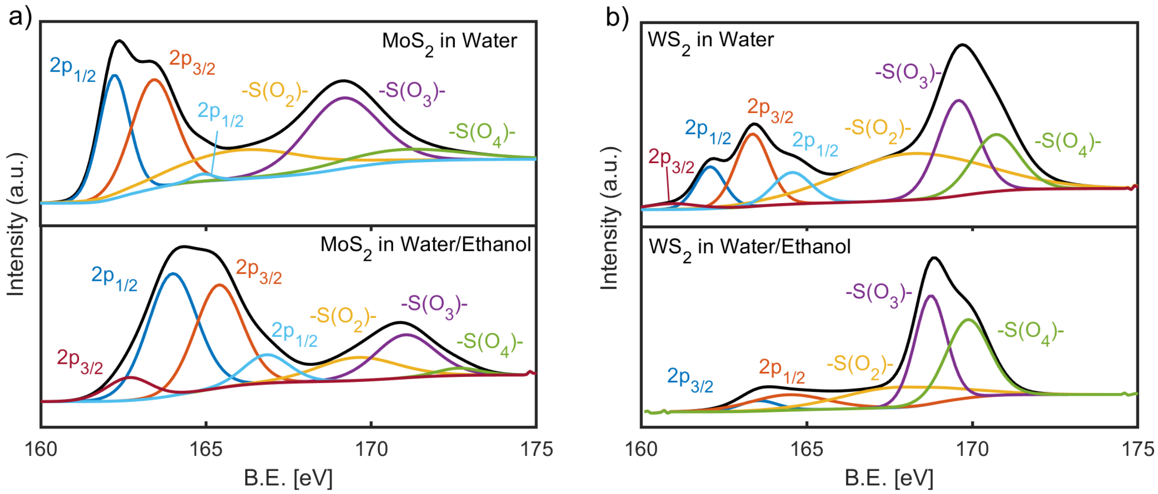

Figure 7.8: S 2p XPS characterization of laser treated MoS_2 and WS_2. a) S 2p spectra of MoS_2 treated in water (upper panel) and MoS_2 treated in ethanol:water solution (lower panel). b) S 2p spectra of WS_2 treated in water (upper panel) and WS_2 treated in ethanol:water solution (lower panel). Peak quantities are listed in Appendix B.

has the smallest sulfide component (Table 2) and no bridging/apical sulfur bonds in its S 2p XPS spectra (Figure 7.8). It was previously shown that bridging/apical sulfur have high catalytic activity for application in electrochemical hydrogen evolution reactions [286,292] and therefore, have benefits for gas sensing applications.

Table 7.2: Sum of sulfide and sulphate contributions for the MoS_2 and WS_2 materials.

Sulfur Composition	MoS_2 in Water [%]	MoS_2 in ethanol:water[%]	WS_2 in Water[%]	WS_2 in ethanol:water[%]
Sulfide	42.75	73.77	71.79	14.90
Sulphate	54.24	26.33	28.21	85.07

7.3.4 Sensing Mechanism

Material characterization data presented in the previous sections have identified the mechanisms that contribute to increased gas adsorption on the 2D materials utilized in this work, however, the origin of the piezoresistive sensing signal has not yet been discussed. The casted 2D-material coating is expected to be a randomly orientated network of overlapping monolayer and multilayer flakes. When exposed to an analyte gas, the analyte molecules penetrate this structure and adsorb onto the active adsorption sites (e.g.: oxygen functional groups on graphene oxide) resulting in an increase in the interlayer distance of the stacked 2D sheets, which causes an overall film expansion or "swelling". The swelling of graphene oxide films upon exposure to water and various alcohols has been reported previously. [23, 24, 180, 181] The same swelling behavior is expected for MoS_2 and WS_2 films due to their flat 2D structure similar to graphene. The expansion of the receptor layer induces a surface stress on the underlying membrane causing it to deflect upwards [19, 20]. This deflection imparts a strain on the four piezoresistors embedded at the fixed ends of the membrane and produces a change in their resistance, which is measured electrically.

The measured piezoresistive signal is proportional to the surface stress on the membrane. In a theoretical model presented by Wenzel et al. for coated microcantilevers (Equation 7.1), the surface stress (σ) is proportionally dependent on the elastic modulus of the receptor material (E_R), specific volume of the adsorbed gas (V_a), partition coefficient of the gas (K_p) and the concentration of the gas in the vapor phase (C_g) [252, 293, 294].

$$\sigma = \frac{-E_R V_a K_p C_g}{3} \tag{7.1}$$

As described earlier, 2D materials typically have high E_R which is advantageous for MSS receptor materials as it results in a high induced surface stress. As observed in Figure B.2-B.9, the MSS response increased as the relative vapor pressure of the analyte gas increased, which is proportional to its concentration C_g. V_a and K_p relate to the interaction between the analyte molecules and the receptor layer and are therefore dependent on the laser treatment of the 2D materials to promote increased adsorption. For example, the increased number of oxygen functional groups and defects on the laser treated GO would increase the proportion of analyte molecules in the solid phase that are adsorbed onto the surface of the GO resulting in high K_p and V_a [252]. Furthermore, the unique properties of each analyte such as their molecule size, saturation vapor pressure and intramolecular bonds are accounted for in K_p and generate unique MSS signal response intensities. Through this model and sensing mechanism it is evident that laser treated 2D materials are suitable for use as receptor layers in MSS devices.

Finally, it is important to note that the responses obtained in Chapter 5 with the reflectance screening technique are widely different than the responses observed in this chapter for the same analytes tested. This may be because the laser treatment times of the 2D materials used in Chapter 5, where different than the ones used in this chapter. For example, the GO solution tested with the reflectance screening technique, had a different laser treatment time of 20 minutes compared to the 1 and 1.5 hour treatment times used here. The different laser treatment times likely resulted in a set of unique material properties (e.g., amount of defects and functional groups) that may have changed their interaction with the analytes. Nonetheless, the reflectance screening technique is still valid, as it showed that the laser treated 2D materials did interact with the analytes to varying degrees.

7.4 Conclusion

Nanomechanical Membrane-type Surface stress Sensors (MSS) were coated with laser treated 2D materials to observe their ability to sense various volatile compounds. Utilizing the MSS configuration instead of a resistive sensor configuration is advantageous as it does not rely on the electrical properties of the sensing material. The 2D materials were laser treated in water and an ethanol:water to introduce defects, dopants, and functional groups to improve their gas adsorption properties, without concern about the impact on the electrical properties. The results showed that a longer laser treatment time for graphene oxide in water increased the sensor response as a result of the increase in defects and oxygen functional groups. The opposite effect may have occurred if the laser treated graphene oxide were used in a resistive sensor configuration where the increase in defects and oxygen functional groups would be expected to reduce the conductivity of the material, which may result in a lower resistive sensor response. Furthermore, the increased interplanar spacing of the GO may have contributed to higher analyte adsorption and increased MSS signal. This most likely would not have been the case in a resistive sensor where the larger interplanar spacing would be expected to reduce conduction. Doping of graphene oxide with boron nitride improved sensor response, which is attributed to the introduction of pyrrolic nitrogen with high catalytic activity. Laser treated MoS_2 and WS_2

showed improved sensor response attributed to a higher content of sulfide bonds and the formation of apical or bridging sulfur bonds with enhanced catalytic activity. Here, laser treatment is expected to produce multilayered particles of these 2D materials. The multiple layers increase the available surface area for analyte adsorption but would decrease the conductivity of a resistive sensor, whereas this is not a concern for the MSS. Additionally, 2D materials used in resistive sensors ideally need large flake sizes to retain conductivity by reducing the number of grain boundaries and a reliance on the charge hopping mechanism. In an MSS it is ideal to have smaller flake sizes for an increase in overall surface area for improved analyte adsorption and higher MSS signal.

The 2D material coated MSS demonstrated a large range of sensitivities to several VOCs, ranging from 0.01 µV ppm^{-1} for the detection of ethanol by 5% BN GO to 43.40 µV ppm^{-1} for the detection of hexanol with WS_2 treated in water. All sensors demonstrated high response for the detection of water, most likely due to its small molecule size and stronger adsorption capability due to hydrogen bonding. The sensor response to the aromatic molecule toluene was the highest in the BN doped graphene oxides and second highest for the undoped graphene oxides. This was attributed to the $\pi-\pi$ stacking interactions between the π -bonds in the toluene and the π-bonds in the graphene oxides. The response of the MoS_2 and WS_2 coated sensors to toluene was not prominent compared to the other analytes and therefore it is evident that the graphene oxides demonstrate some degree of selectivity towards toluene. The detection of other aromatic compounds may result in high GO sensor response as well and therefore warrants further investigation to verify the $\pi-\pi$ stacking mechanism. This is particularly relevant for the sensing of air pollutants such as BTEX compounds [60] (benzene, toluene, ethylbenzene and xylene) which occur naturally in crude oil and are released in the air through motor vehicle emissions and cigarette smoke.

To avoid the influence of humidity on sensor performance, several approaches exist. One approach is to use a filter that can eliminate the moisture from the sample gas. A second approach is to utilize a microheater to raise the temperature in the vicinity of the sensor to slightly higher than the ambient temperature [295]. By doing so, the effects of relative humidity changes are eliminated. A third approach is to compensate for the effect of humidity at the data processing stage. An example of this was demonstrated by using principle component analysis (PCA) and an artificial neural network as described by Mumyakmaz et al. [296] An array of MSS devices coated with different 2D materials can be used to overcome challenges in selectivity. Using various data analysis techniques including a basic principal component analysis and advanced machine learning algorithms [245, 297], the unique relative response intensities of the receptors to each analyte form a characteristic pattern that can be used to identify an unknown VOCs.

"Part of the journey is the end."

— Tony Stark

Chapter 8

Conclusions

In this body of work, reflectometry was used to generate useful insights towards the development of new materials and novel architectures for MEMS gas sensors. Two main applications of the reflectometry technique were demonstrated, which led to the development of two unique MEMS gas sensor devices. The first application was the use of in-situ reflectance spectroscopy to study the growth behavior and property evolution of metal oxide thin films grown by atmospheric pressure-spatial atomic layer deposition (Chapter 3). The in-situ technique revealed a two stage growth mechanism for metal oxides, comprised of a initial non-linear nucleation period followed by linear growth. Real time monitoring of the growth by in-situ reflectance spectroscopy is therefore crucial to enable the accurate open-air deposition of metal oxide thin films with desired thicknesses, as linear growth rates cannot be assumed from the start. In Chapter 4, the in-situ reflectometry technique was further expanded to monitor the growth behavior of metal oxide films on various non-conventional surfaces such as metals, flexible substrates, fabrics, polymer layers and films of 2D nanoparticles. The nucleation period of ZnO deposited on the different substrates varied greatly. Hence, it is beneficial to use the in-situ reflectometry technique to achieve accurate ZnO thicknesses. This became particularly relevant for the accurate deposition of ZnO on photoresist, which was required for the fabrication of a novel ZnO resonant cantilever gas sensor (Chapter 6). In this novel MEMS architecture, a ZnO thin film layer serves as both the cantilever structural layer as well as the gas sensitive receptor layer. Doing so reduces the number of layers on the cantilever to minimize damping effects. More importantly the use of a 200 nm ZnO thin film, reduces the size of the cantilever and its overall mass, which was instrumental to achieving comparatively high sensitivity towards low relative humidity levels.

The second application of reflectometry, was to evaluate the suitability of various receptor material candidates for use in static deflection type MEMS gas sensors (Chapter 5). The reflectance intensity of receptor materials was monitored as they were exposed to analyte gases. Changes in reflectance intensity indicated that the receptor material was interacting with the analyte gas. More specifically, the receptor materials were expanding in the presence of the analyte gas, which makes them suitable for their integration into nanomechanical membrane-type surface stress sensors(MSS) for gas sensing (Chapter 7). Hence, the reflectometry technique can be used to screen for those materials that are suitable for MSS. The screening technique showed that laser treated 2D materials such as graphene oxide, molybdenum disulfide and tungsten disulfide were indeed excellent receptor material candidates. These materials were coated onto MSS to observe their ability to sense a select group of volatile organic compounds with a wide range of sensitivities. Furthermore, materials characterization revealed that the laser treatment of the 2D materials was beneficial to attaining high sensor response and sensitivity, as it introduced defects, dopants and functional groups to the 2D materials to promote gas adsorption.

Further improvements to the ZnO resonant cantilever structure were identified. This included removal of the top aluminum layer to minimize residual stresses, as well as the use of piezoresistive readout instead of laser vibrometry. Furthermore, it was shown that the morphology of the ZnO layer could be altered by varying the AP-SALD process parameters, and that some morphologies may be preferred for enhanced gas adsorption. However, achieving those morphologies may come at the expense of the structural integrity of the layer itself thus not making it not suitable to be a cantilever structural layer. Here, reflectance spectroscopy may be able to determine if the cantilever is structurally suitable by determining the refractive index of the layer, which is related to the compactness and density of the material. For MSS based gas sensors, novel receptor material candidates can be synthesized and optimized with the femtosecond laser treatment technique. The reflectance screening technique can be used to screen those new materials for their suitability. Furthermore screening can be done at IR wavelengths to observe the change in the materials electrical properties upon exposure to an analyte gas. This would enable this technique to screen for potential receptor materials for chemiresistive gas sensors as well.

While the focus of this work as been towards MEMS devices. The outcomes of the in-situ reflectance spectroscopy of film growth with AP-SALD, are applicable to other opto-electronic devices such as MIM diodes, LEDS, thin film solar cells and chemiresistive sensors. The open-air growth of metal oxides by the AP-SALD technique is very promising for the large scale, high volume manufacturing of thin films. Thus reflectance spectroscopy becomes a crucial tool for online process monitoring and error analysis. In conclusion, reflectometry may be a relatively simple technique, but it can be a very powerful tool not only for the development of MEMS gas sensors but also the next generation of nanoscale devices.

References

[1] "Global MEMS Gas Sensor Market Expected to Reach USD 233.9 Billion by 2026: Facts & Factors," 11 2020. [Online]. Available: https://www.globenewswire.com/news-release/2020/11/18/2129222/0/en/Global-MEMS-Gas-Sensor-Market-Expected-to-Reach-USD-233-9-Billion-by-2026-Facts-Factors.html

[2] C. Monn, "Chapter 4 Exposure assessment of air pollutants: a review on spatial heterogeneity and indoor/outdoor/personal exposure to suspended particulate matter, nitrogen dioxide and ozone," *Developments in Environmental Science*, vol. 1, no. C, pp. 117–182, 2002. [Online]. Available: http://linkinghub.elsevier.com/retrieve/pii/S1474817702800079

[3] C. Turner, C. Walton, S. Hoashi, and M. Evans, "Breath acetone concentration decreases with blood glucose concentration in type i diabetes mellitus patients during hypoglycaemic clamps," *Journal of Breath Research*, vol. 3, no. 4, 2009.

[4] A. Boisen, S. Dohn, S. S. Keller, S. Schmid, and M. Tenje, "Cantilever-like micromechanical sensors," *Reports on Progress in Physics*, vol. 74, no. 3, p. 036101, 3 2011. [Online]. Available: https://iopscience.iop.org/article/10.1088/0034-4885/74/3/036101

[5] C. Marichy and N. Pinna, "Atomic Layer Deposition to Materials for Gas Sensing Applications," *Advanced Materials Interfaces*, vol. 3, no. 21, p. 1600335, 2016. [Online]. Available: http://doi.wiley.com/10.1002/admi.201600335

[6] F. Battiston, J.-P. Ramseyer, H. Lang, M. Baller, C. Gerber, J. Gimzewski, E. Meyer, and H.-J. Güntherodt, "A chemical sensor based on a microfabricated cantilever array with simultaneous resonance-frequency and bending readout," *Sensors and Actuators B: Chemical*, vol. 77, no. 1-2, pp. 122–131, 6 2001. [Online]. Available: https://linkinghub.elsevier.com/retrieve/pii/S0925400501006839

[7] M. Sepaniak, P. Datskos, N. Lavrik, and C. Tipple, "Peer Reviewed: Microcantilever Transducers: A new Approach in Sensor Technology," *Analytical Chemistry*, vol. 74, no. 21, pp. 568 A–575 A, 11 2002. [Online]. Available: https://pubs.acs.org/doi/10.1021/ac022156i

[8] M. I. Younis, *MEMS Linear and Nonlinear Statics and Dynamics*, ser. Microsystems. Boston, MA: Springer US, 2011, vol. 20. [Online]. Available: http://link.springer.com/10.1007/978-1-4419-6020-7

[9] H. Debéda and I. Dufour, "Resonant microcantilever devices for gas sensing," *Advanced Nanomaterials for Inexpensive Gas Microsensors: Synthesis, Integration and Applications*, pp. 161–188, 2019.

[10] A. K. Naik, M. S. Hanay, W. K. Hiebert, X. L. Feng, and M. L. Roukes, "Towards single-molecule nanomechanical mass spectrometry," *Nature Nanotechnology*, vol. 4, no. 7, pp. 445–450, 7 2009. [Online]. Available: http://www.nature.com/articles/nnano.2009.152

[11] R. Raiteri, M. Grattarola, H. J. Butt, and P. Skládal, "Micromechanical cantilever-based biosensors," *Sensors and Actuators, B: Chemical*, vol. 79, no. 2-3, pp. 115–126, 2001.

[12] N. V. Lavrik, M. J. Sepaniak, and P. G. Datskos, "Cantilever transducers as a platform for chemical and biological sensors," *Review of Scientific Instruments*, vol. 75, no. 7, pp. 2229–2253, 2004.

[13] R. Ibbotson, R. Dunn, V. Djakov, P. K. Ferrigno, and S. Huq, "Polyimide microcantilever surface stress sensor using low-cost, rapidly-interchangeable, spring-

loaded microprobe connections," *Microelectronic Engineering*, vol. 85, no. 5-6, pp. 1314–1317, 5 2008. [Online]. Available: https://linkinghub.elsevier.com/retrieve/pii/S0167931707008313

[14] G. Yoshikawa, H. P. Lang, T. Akiyama, L. Aeschimann, U. Staufer, P. Vettiger, M. Aono, T. Sakurai, and C. Gerber, "Sub-ppm detection of vapors using piezoresistive microcantilever array sensors," *Nanotechnology*, vol. 20, no. 1, p. 015501, 2009.

[15] M. E. Franke, T. J. Koplin, and U. Simon, "Metal and metal oxide nanoparticles in chemiresistors: Does the nanoscale matter?" *Small*, vol. 2, no. 1, pp. 36–50, 2006.

[16] J. K. Gimzewski, C. Gerber, E. Meyer, and R. R. Schlittler, "Observation of a chemical reaction using a micromechanical sensor," *Chemical Physics Letters*, vol. 217, no. 5-6, pp. 589–594, 1994.

[17] H. Jensenius, J. Thaysen, A. A. Rasmussen, L. H. Veje, O. Hansen, and A. Boisen, "A microcantilever-based alcohol vapor sensor-application and response model," *Applied Physics Letters*, vol. 76, no. 18, pp. 2615–2617, 5 2000. [Online]. Available: http://aip.scitation.org/doi/10.1063/1.126426

[18] L. A. Pinnaduwage, D. L. Hedden, A. Gehl, V. I. Boiadjiev, J. E. Hawk, R. H. Farahi, T. Thundat, E. J. Houser, S. Stepnowski, R. A. McGill, L. Deel, and R. T. Lareau, "A sensitive, handheld vapor sensor based on microcantilevers," *Review of Scientific Instruments*, vol. 75, no. 11, pp. 4554–4557, 2004.

[19] G. Yoshikawa, T. Akiyama, S. Gautsch, P. Vettiger, and H. Rohrer, "Nanomechanical membrane-type surface stress sensor," *Nano Letters*, vol. 11, no. 3, pp. 1044–1048, 2011.

[20] G. Yoshikawa, T. Akiyama, F. Loizeau, K. Shiba, S. Gautsch, T. Nakayama, P. Vettiger, N. F. de Rooij, and M. Aono, "Two dimensional array of piezoresistive nanomechanical Membrane-type Surface stress Sensor(MSS) with improved sensitivity," *Sensors (Switzerland)*, vol. 12, no. 11, pp. 15 873–15 887, 2012.

[21] K. Shiba, T. Takei, G. Yoshikawa, and M. Ogawa, "Deposition of a titania layer on spherical porous silica particles and their nanostructure-induced vapor sensing properties," *Nanoscale*, vol. 9, no. 43, pp. 16 791–16 799, 2017. [Online]. Available: http://xlink.rsc.org/?DOI=C7NR06086F

[22] I. Osica, G. Imamura, K. Shiba, Q. Ji, L. K. Shrestha, J. P. Hill, K. J. Kurzydłowski, G. Yoshikawa, and K. Ariga, "Highly Networked Capsular Silica-Porphyrin Hybrid Nanostructures as Efficient Materials for Acetone Vapor Sensing," *ACS Applied Materials and Interfaces*, vol. 9, no. 11, pp. 9945–9954, 3 2017. [Online]. Available: http://pubs.acs.org/doi/10.1021/acsami.6b15680

[23] Y. Yao, X. Chen, H. Guo, and Z. Wu, "Graphene oxide thin film coated quartz crystal microbalance for humidity detection," *Applied Surface Science*, vol. 257, no. 17, pp. 7778–7782, 6 2011. [Online]. Available: https://linkinghub.elsevier.com/retrieve/pii/S0169433211005629

[24] Y. Yao, X. Chen, H. Guo, Z. Wu, and X. Li, "Humidity sensing behaviors of graphene oxide-silicon bi-layer flexible structure," *Sensors and Actuators, B: Chemical*, vol. 161, no. 1, pp. 1053–1058, 2012. [Online]. Available: http://dx.doi.org/10.1016/j.snb.2011.12.007

[25] T. Thundat, E. A. Wachter, S. L. Sharp, and R. J. Warmack, "Detection of mercury vapor using resonating microcantilevers," *Applied Physics Letters*, vol. 66, no. 13, pp. 1695–1697, 3 1995. [Online]. Available: http://aip.scitation.org/doi/10.1063/1.113896

[26] M. Maute, S. Raible, F. E. Prins, D. P. Kern, H. Ulmer, U. Weimar, and W. Göpel, "Detection of volatile organic compounds (VOCs) with polymer-coated cantilevers," *Sensors and Actuators, B: Chemical*, vol. 58, no. 1-3, pp. 505–511, 1999.

[27] D. Then, A. Vidic, and C. Ziegler, "A highly sensitive self-oscillating cantilever array for the quantitative and qualitative analysis of organic vapor mixtures," *Sensors and Actuators, B: Chemical*, vol. 117, no. 1, pp. 1–9, 2006.

[28] Y. Lv, P. Xu, H. Yu, J. Xu, and X. Li, "Ni-MOF-74 as sensing material for resonant-gravimetric detection of ppb-level CO," *Sensors and Actuators, B: Chemical*, vol. 262, pp. 562–569, 2018. [Online]. Available: https://doi.org/10.1016/j.snb.2018.02.058

[29] H. Yamagiwa, S. Sato, T. Fukawa, T. Ikehara, R. Maeda, T. Mihara, and M. Kimura, "Detection of volatile organic compounds by weight-detectable sensors coated with metal-organic frameworks," *Scientific Reports*, vol. 4, pp. 1–6, 2014.

[30] M. A. Urbiztondo, I. Pellejero, M. Villarroya, J. Sesé, M. P. Pina, I. Dufour, and J. Santamaría, "Zeolite-modified cantilevers for the sensing of nitrotoluene vapors," *Sensors and Actuators, B: Chemical*, vol. 137, no. 2, pp. 608–616, 2009.

[31] K. S. Hwang, M. H. Lee, J. Lee, W. S. Yeo, J. H. Lee, K. M. Kim, J. Y. Kang, and T. S. Kim, "Peptide receptor-based selective dinitrotoluene detection using a microcantilever sensor," *Biosensors and Bioelectronics*, vol. 30, no. 1, pp. 249–254, 2011. [Online]. Available: http://dx.doi.org/10.1016/j.bios.2011.09.021

[32] N. V. Lavrik, C. A. Tipple, M. J. Sepaniak, and P. G. Datskos, "Enhanced chemi-mechanical transduction at nanostructured interfaces," *Chemical Physics Letters*, vol. 336, no. 5-6, pp. 371–376, 2001.

[33] J. J. Headrick, M. J. Sepaniak, N. V. Lavrik, and P. G. Datskos, "Enhancing chemi-mechanical transduction in microcantilever chemical sensing by surface modification," *Ultramicroscopy*, vol. 97, no. 1-4, pp. 417–424, 2003.

[34] C. A. Tipple, N. V. Lavrik, M. Culha, J. Headrick, P. Datskos, and M. J. Sepaniak, "Nanostructured microcantilevers with functionalized cyclodextrin receptor phases: Self-assembled monolayers and vapor-deposited films," *Analytical Chemistry*, vol. 74, no. 13, pp. 3118–3126, 2002.

[35] I. Bargatin, E. B. Myers, J. S. Aldridge, C. Marcoux, P. Brianceau, L. Duraffourg, E. Colinet, S. Hentz, P. Andreucci, and M. L. Roukes, "Large-scale integration of nanoelectromechanical systems for gas sensing applications," *Nano Letters*, vol. 12, no. 3, pp. 1269–1274, 2012.

[36] P. Clément, E. Del Castillo Perez, O. Gonzalez, R. Calavia, C. Lucat, E. Llobet, and H. Debéda, “Gas discrimination using screen-printed piezoelectric cantilevers coated with carbon nanotubes,” *Sensors and Actuators, B: Chemical*, vol. 237, pp. 1056–1065, 2016. [Online]. Available: http://dx.doi.org/10.1016/j.snb.2016.07.163

[37] K. Jensen, K. Kim, and A. Zettl, “An atomic-resolution nanomechanical mass sensor,” *Nature Nanotechnology*, vol. 3, no. 9, pp. 533–537, 9 2008. [Online]. Available: http://www.nature.com/articles/nnano.2008.200

[38] M. Li, H. X. Tang, and M. L. Roukes, “Ultra-sensitive NEMS-based cantilevers for sensing, scanned probe and very high-frequency applications,” *Nature Nanotechnology*, vol. 2, no. 2, pp. 114–120, 2 2007. [Online]. Available: http://www.nature.com/articles/nnano.2006.208

[39] W. Li, S. Ma, Y. Li, G. Yang, Y. Mao, J. Luo, D. Gengzang, X. Xu, and S. Yan, “Enhanced ethanol sensing performance of hollow ZnO-SnO2 core-shell nanofibers,” *Sensors and Actuators, B: Chemical*, vol. 211, pp. 392–402, 2015. [Online]. Available: http://dx.doi.org/10.1016/j.snb.2015.01.090

[40] S. Roy and S. Basu, “Improved zinc oxide film for gas sensor applications,” *Bulletin of Materials Science*, vol. 25, no. 6, pp. 513–515, 2002.

[41] C. Nayral, E. Viala, P. Fau, F. Senocq, J. C. Jumas, A. Maisonnat, and B. Chaudret, “Synthesis of tin and tin oxide nanoparticles of low size dispersity for application in gas sensing,” *Chemistry - A European Journal*, vol. 6, no. 22, pp. 4082–4090, 2000.

[42] X. Li, R. Ramasamy, and P. K. Dutta, “Study of the resistance behavior of anatase and rutile thick films towards carbon monoxide and oxygen at high temperatures and possibilities for sensing applications,” *Sensors and Actuators, B: Chemical*, vol. 143, no. 1, pp. 308–315, 2009.

[43] K. Galatsis, Y. Li, W. Wlodarski, E. Comini, G. Sberveglieri, C. Cantalini, S. Santucci, and M. Passacantando, “Comparison of single and binary oxide MoO3, TiO2 and WO3 solgel gas sensors,” *Sensors and Actuators*

B: Chemical, vol. 83, no. 1-3, pp. 276–280, 3 2002. [Online]. Available: https://linkinghub.elsevier.com/retrieve/pii/S0925400501010723

[44] Z.-P. Sun, L. Liu, L. Zhang, and D.-Z. Jia, "Rapid synthesis of ZnO nano-rods by one-step, room-temperature, solid-state reaction and their gas-sensing properties," *Nanotechnology*, vol. 17, no. 9, pp. 2266–2270, 5 2006. [Online]. Available: https://iopscience.iop.org/article/10.1088/0957-4484/17/9/032

[45] H. Gómez-Pozos, E. J. L. Arredondo, A. M. Álvarez, R. Biswal, Y. Kudriavtsev, J. V. Pérez, Y. L. Casallas-Moreno, and M. d. l. L. O. Amador, "Cu-Doped ZnO thin films deposited by a sol-gel process using two copper precursors: Gas-sensing performance in a propane atmosphere," *Materials*, vol. 9, no. 2, 2016.

[46] H. Nanto, T. Minami, and S. Takata, "Zinc-oxide thin-film ammonia gas sensors with high sensitivity and excellent selectivity," *Journal of Applied Physics*, vol. 60, no. 2, pp. 482–484, 1986.

[47] F. Paraguay D., M. Miki-Yoshida, J. Morales, J. Solis, and W. Estrada L., "Influence of Al, In, Cu, Fe and Sn dopants on the response of thin film ZnO gas sensor to ethanol vapour," *Thin Solid Films*, vol. 373, no. 1-2, pp. 137–140, 2000.

[48] N. Kilinc, O. Cakmak, A. Kosemen, E. Ermek, S. Ozturk, Y. Yerli, Z. Z. Ozturk, and H. Urey, "Fabrication of 1D ZnO nanostructures on MEMS cantilever for VOC sensor application," *Sensors and Actuators, B: Chemical*, vol. 202, pp. 357–364, 2014. [Online]. Available: http://dx.doi.org/10.1016/j.snb.2014.05.078

[49] J. Yang, J. Xu, W. Wu, M. Bertke, H. S. Wasisto, and E. Peiner, "Piezoresistive Silicon Cantilever Covered by ZnO Nanorods for Humidity Sensing," *Procedia Engineering*, vol. 168, pp. 1114–1117, 2016. [Online]. Available: http://dx.doi.org/10.1016/j.proeng.2016.11.361

[50] J. Xu, M. Bertke, X. Li, H. Mu, H. Zhou, F. Yu, G. Hamdana, A. Schmidt, H. Bremers, and E. Peiner, "Fabrication of ZnO nanorods and Chitosan@ZnO nanorods on MEMS piezoresistive self-actuating silicon microcantilever for humidity

sensing," *Sensors and Actuators, B: Chemical*, vol. 273, no. January, pp. 276–287, 2018. [Online]. Available: https://doi.org/10.1016/j.snb.2018.06.017

[51] J. Xu, A. Setiono, and E. Peiner, "Piezoresistive Microcantilever with SAM-Modified ZnO-Nanorods@Silicon-Nanopillars for Room-Temperature Parts-per-Billion NO 2 Detection," *ACS Applied Nano Materials*, vol. 3, no. 7, pp. 6609–6620, 7 2020. [Online]. Available: https://pubs.acs.org/doi/10.1021/acsanm.0c01055

[52] L. Aprilia, R. Nuryadi, R. D. Mayasari, D. Gustiono, Masmui, J. Raharjo, Y. Deni, B. Yuliarto, M. Iqbal, and D. Hartanto, "Growth of zinc oxide sensitive layer on microcantilever surface for gas sensor application," *14th International Conference on QiR (Quality in Research), QiR 2015 - In conjunction with 4th Asian Symposium on Material Processing, ASMP 2015 and International Conference in Saving Energy in Refrigeration and Air Conditioning, ICSERA 2015*, pp. 151–154, 2016.

[53] L. Aprilia, R. Nuryadi, D. Gustiono, Nurmahmudi, A. Udhiarto, D. Hartanto, B. Yuliarto, M. Hosoda, Y. Neo, and H. Mimura, "CO Gas-Induced Resonance Frequency Shift of ZnO-Functionalized Microcantilever in Humid Air," *Journal of Nanomaterials*, vol. 2017, pp. 1–7, 2017. [Online]. Available: https://www.hindawi.com/journals/jnm/2017/4824607/

[54] R. Nuryadi, L. Aprilia, M. Hosoda, M. A. Barique, A. Udhiarto, D. Hartanto, M. B. Setiawan, Y. Neo, and H. Mimura, "Observation of CO Detection Using Aluminum-Doped ZnO Nanorods on Microcantilever," *Sensors*, vol. 20, no. 7, p. 2013, 4 2020. [Online]. Available: https://www.mdpi.com/1424-8220/20/7/2013

[55] X. H. Wang, Y. F. Ding, J. Zhang, Z. Q. Zhu, S. Z. You, S. Q. Chen, and J. Zhu, "Humidity sensitive properties of ZnO nanotetrapods investigated by a quartz crystal microbalance," *Sensors and Actuators, B: Chemical*, vol. 115, no. 1, pp. 421–427, 2006.

[56] A. Erol, S. Okur, B. Comba, O. Mermer, and M. C. Arikan, "Humidity sensing properties of ZnO nanoparticles synthesized by sol-gel process," *Sensors and Actuators, B: Chemical*, vol. 145, no. 1, pp. 174–180, 2010.

[57] A. Erol, S. Okur, N. Yagmurcukardes, and M. C. Arikan, "Humidity-sensing properties of a ZnO nanowire film as measured with a QCM," *Sensors and Actuators, B: Chemical*, vol. 152, no. 1, pp. 115–120, 2011.

[58] N. Asar, A. Erol, S. Okur, and M. C. Arikan, "Morphology-dependent humidity adsorption kinetics of ZnO nanostructures," *Sensors and Actuators, A: Physical*, vol. 187, pp. 37–42, 2012. [Online]. Available: http://dx.doi.org/10.1016/j.sna.2012.08.019

[59] J. Xie, H. Wang, and M. Duan, "QCM chemical sensor based on ZnO colloid spheres for the alcohols," *Sensors and Actuators, B: Chemical*, vol. 203, pp. 239–244, 2014. [Online]. Available: http://dx.doi.org/10.1016/j.snb.2014.06.119

[60] S. Ozturk, A. Kösemen, Z. A. Kösemen, N. Kilinç, Z. Z. Öztürk, and M. Penza, "Electrochemically growth of Pd doped ZnO nanorods on QCM for room temperature VOC sensors," *Sensors and Actuators, B: Chemical*, vol. 222, pp. 280–289, 1 2016. [Online]. Available: https://linkinghub.elsevier.com/retrieve/pii/S0925400515302616

[61] J. Xie, H. Wang, Y. Lin, Y. Zhou, and Y. Wu, "Highly sensitive humidity sensor based on quartz crystal microbalance coated with ZnO colloid spheres," *Sensors and Actuators, B: Chemical*, vol. 177, pp. 1083–1088, 2013. [Online]. Available: http://dx.doi.org/10.1016/j.snb.2012.12.033

[62] S. M. George, "Atomic layer deposition: An overview," *Chemical Reviews*, vol. 110, no. 1, pp. 111–131, 1 2010. [Online]. Available: http://pubs.acs.org/doi/abs/10.1021/cr900056bhttps://pubs.acs.org/doi/10.1021/cr900056b

[63] R. L. Puurunen, "Surface chemistry of atomic layer deposition: A case study for the trimethylaluminum/water process," *Journal of Applied Physics*, vol. 97, no. 12, p. 121301, 6 2005. [Online]. Available: http://aip.scitation.org/doi/10.1063/1.1940727

[64] P. Poodt, D. C. Cameron, E. Dickey, S. M. George, V. Kuznetsov, G. N. Parsons, F. Roozeboom, G. Sundaram, and A. Vermeer, "Spatial atomic layer deposition:

A route towards further industrialization of atomic layer deposition," *Journal of Vacuum Science & Technology A: Vacuum, Surfaces, and Films*, vol. 30, no. 1, p. 010802, 1 2012. [Online]. Available: http://avs.scitation.org/doi/10.1116/1.3670745

[65] D. Muñoz-Rojas, V. H. Nguyen, C. Masse de la Huerta, S. Aghazadehchors, C. Jiménez, and D. Bellet, "Spatial Atomic Layer Deposition (SALD), an emerging tool for energy materials. Application to new-generation photovoltaic devices and transparent conductive materials," *Comptes Rendus Physique*, vol. 18, no. 7-8, pp. 391–400, 9 2017. [Online]. Available: http://dx.doi.org/10.1016/j.crhy.2017.09.004

[66] R. L. Z. Hoye, D. Muñoz-Rojas, K. P. Musselman, Y. Vaynzof, and J. L. MacManus-Driscoll, "Synthesis and Modeling of Uniform Complex Metal Oxides by Close-Proximity Atmospheric Pressure Chemical Vapor Deposition," *ACS Applied Materials & Interfaces*, vol. 7, no. 20, pp. 10 684–10 694, 5 2015. [Online]. Available: https://pubs.acs.org/doi/10.1021/am5073589

[67] P. Poodt, J. van Lieshout, A. Illiberi, R. Knaapen, F. Roozeboom, and A. van Asten, "On the kinetics of spatial atomic layer deposition," *Journal of Vacuum Science & Technology A: Vacuum, Surfaces, and Films*, vol. 31, no. 1, p. 01A108, 2013. [Online]. Available: http://avs.scitation.org/doi/10.1116/1.4756692

[68] P. Poodt, B. Kniknie, A. Branca, H. Winands, and F. Roozeboom, "Patterned deposition by plasma enhanced spatial atomic layer deposition," *Physica Status Solidi - Rapid Research Letters*, vol. 5, no. 4, pp. 165–167, 2011.

[69] P. Poodt, R. Knaapen, A. Illiberi, F. Roozeboom, and A. van Asten, "Low temperature and roll-to-roll spatial atomic layer deposition for flexible electronics," *Journal of Vacuum Science & Technology A: Vacuum, Surfaces, and Films*, vol. 30, no. 1, p. 01A142, 2012. [Online]. Available: http://avs.scitation.org/doi/10.1116/1.3667113

[70] D. H. Levy, S. F. Nelson, and D. Freeman, "Oxide Electronics by Spatial Atomic Layer Deposition," *Journal of Display Technology*, vol. 5, no. 12, pp. 484–494, 12 2009. [Online]. Available: http://ieeexplore.ieee.org/document/5332034/

[71] P. Poodt, A. Lankhorst, F. Roozeboom, K. Spee, D. Maas, and A. Vermeer, "High-Speed Spatial Atomic-Layer Deposition of Aluminum Oxide Layers for Solar Cell Passivation," *Advanced Materials*, vol. 22, no. 32, pp. 3564–3567, 8 2010. [Online]. Available: http://doi.wiley.com/10.1002/adma.201000766

[72] C. R. Ellinger and S. F. Nelson, "Selective area spatial atomic layer deposition of ZnO, Al2O 3, and aluminum-doped ZnO using poly(vinyl pyrrolidone)," *Chemistry of Materials*, vol. 26, no. 4, pp. 1514–1522, 2 2014. [Online]. Available: https://pubs.acs.org/doi/10.1021/cm402464z

[73] A. Illiberi, F. Roozeboom, and P. Poodt, "Spatial Atomic Layer Deposition of Zinc Oxide Thin Films," *ACS Applied Materials & Interfaces*, vol. 4, no. 1, pp. 268–272, 1 2012. [Online]. Available: www.acsami.orghttp://pubs.acs.org/doi/10.1021/am2013097

[74] A. Illiberi, I. Katsouras, S. Gazibegovic, B. Cobb, E. Nekovic, W. van Boekel, C. Frijters, J. Maas, F. Roozeboom, Y. Creyghton, P. Poodt, and G. Gelinck, "Atmospheric plasma-enhanced spatial-ALD of InZnO for high mobility thin film transistors," *Journal of Vacuum Science & Technology A: Vacuum, Surfaces, and Films*, vol. 36, no. 4, p. 04F401, 7 2018. [Online]. Available: http://avs.scitation.org/doi/10.1116/1.5008464

[75] R. L. Hoye, M. R. Chua, K. P. Musselman, G. Li, M. L. Lai, Z. K. Tan, N. C. Greenham, J. L. MacManus-Driscoll, R. H. Friend, and D. Credgington, "Enhanced performance in fluorene-free organometal halide perovskite light-emitting diodes using tunable, low electron affinity oxide electron injectors," *Advanced Materials*, vol. 27, no. 8, pp. 1414–1419, 2015.

[76] A. Illiberi, R. Scherpenborg, F. Roozeboom, and P. Poodt, "Atmospheric Spatial Atomic Layer Deposition of In-Doped ZnO," *ECS Journal of Solid State Science and Technology*, vol. 3, no. 5, pp. P111–P114, 3 2014. [Online]. Available: http://pubs.acs.org/doi/10.1021/am404137e

[77] A. Illiberi, C. Frijters, M. Ruth, D. Bremaud, P. Poodt, F. Roozeboom, and P. J. Bolt, " Atmospheric spatial atomic layer deposition of ZnOS buffer layers for flexible Cu(In,Ga)Se 2 solar cells ," *Journal of Vacuum Science & Technology A*, vol. 36, no. 5, p. 051511, 2018. [Online]. Available: http://avs.scitation.org/doi/10.1116/1.5040457

[78] D. Muñoz-Rojas, M. Jordan, C. Yeoh, A. T. Marin, A. Kursumovic, L. A. Dunlop, D. C. Iza, A. Chen, H. Wang, and J. L. MacManus Driscoll, "Growth of 5 cm 2 V 1 s 1 mobility, p-type Copper(I) oxide (Cu2O) films by fast atmospheric atomic layer deposition (AALD) at 225C and below," *AIP Advances*, vol. 2, no. 4, p. 042179, 12 2012. [Online]. Available: http://aip.scitation.org/doi/10.1063/1.4771681

[79] D. Muñoz-Rojas and J. MacManus-Driscoll, "Spatial atmospheric atomic layer deposition: a new laboratory and industrial tool for low-cost photovoltaics," *Mater. Horiz.*, vol. 1, no. 3, pp. 314–320, 2014. [Online]. Available: http://xlink.rsc.org/?DOI=C3MH00136A

[80] L. Hoffmann, K. O. Brinkmann, J. Malerczyk, D. Rogalla, T. Becker, D. Theirich, I. Shutsko, P. Görrn, and T. Riedl, "Spatial Atmospheric Pressure Atomic Layer Deposition of Tin Oxide as an Impermeable Electron Extraction Layer for Perovskite Solar Cells with Enhanced Thermal Stability," *ACS Applied Materials & Interfaces*, vol. 10, no. 6, pp. 6006–6013, 2 2018. [Online]. Available: http://pubs.acs.org/doi/10.1021/acsami.7b17701https://pubs.acs.org/doi/10.1021/acsami.7b17701

[81] D. Bellet, M. Lagrange, T. Sannicolo, S. Aghazadehchors, V. H. Nguyen, D. P. Langley, D. Muñoz-Rojas, C. Jiménez, Y. Bréchet, and N. D. Nguyen, "Transparent electrodes based on silver nanowire networks: From physical considerations towards device integration," *Materials*, vol. 10, no. 6, 2017.

[82] R. L. Z. Hoye, D. Muñoz-Rojas, S. F. Nelson, A. Illiberi, P. Poodt, F. Roozeboom, and J. L. MacManus-Driscoll, "Research Update: Atmospheric pressure spatial atomic layer deposition of ZnO thin films: Reactors, doping, and

devices," *APL Materials*, vol. 3, no. 4, p. 040701, 4 2015. [Online]. Available: http://dx.doi.org/10.1063/1.4916525

[83] A. H. Alshehri, K. Mistry, V. H. Nguyen, K. H. Ibrahim, D. Muñoz-Rojas, M. Yavuz, and K. P. Musselman, "Quantum-Tunneling Metal-Insulator-Metal Diodes Made by Rapid Atmospheric Pressure Chemical Vapor Deposition," *Advanced Functional Materials*, vol. 29, no. 7, p. 1805533, 2 2019. [Online]. Available: http://doi.wiley.com/10.1002/adfm.201805533

[84] A. Mameli, F. J. van den Bruele, C. K. Ande, M. A. Verheijen, W. M. M. Kessels, and F. Roozeboom, "On the growth, percolation and wetting of silver thin films grown by atmospheric-plasma enhanced spatial atomic layer deposition," *ECS Transactions*, vol. 75, no. 6, pp. 129–142, 2016.

[85] I. Nasution, A. Velasco, and H.-j. j. Kim, "Atmospheric pressure chemical vapor deposition mechanism of Al2O3 film from AlCl3 and O2," *Journal of Crystal Growth*, vol. 311, no. 2, pp. 429–434, 1 2009. [Online]. Available: https://linkinghub.elsevier.com/retrieve/pii/S0022024808013110

[86] T. W.-k. Yeow, K. Mistry, A. Shahin, M. Yavuz, and K. P. Musselman, "Atmospheric-pressure spatial chemical vapor deposition of tungsten oxide," *Journal of Vacuum Science & Technology A*, vol. 38, no. 5, p. 052411, 9 2020. [Online]. Available: http://avs.scitation.org/doi/10.1116/6.0000347

[87] K. P. Musselman, K. H. Ibrahim, and M. Yavuz, "Research update: Beyond graphenesynthesis of functionalized quantum dots of 2d materials and their applications," *APL Materials*, vol. 6, no. 12, p. 120701, 2018.

[88] X. Wang, G. Sun, N. Li, and P. Chen, "Quantum dots derived from two-dimensional materials and their applications for catalysis and energy," *Chemical Society Reviews*, vol. 45, no. 8, pp. 2239–2262, 2016.

[89] Y. Xu, X. Wang, W. L. Zhang, F. Lv, and S. Guo, "Recent progress in two-dimensional inorganic quantum dots," *Chemical Society Reviews*, vol. 47, no. 2, pp. 586–625, 2018.

[90] X. Zhang, H. Cheng, and H. Zhang, "Recent progress in the preparation, assembly, transformation, and applications of layer-structured nanodisks beyond graphene," *Advanced Materials*, vol. 29, no. 35, p. 1701704, 2017.

[91] S. Yang, C. Jiang, and S.-h. h. Wei, "Gas sensing in 2D materials," *Applied Physics Reviews*, vol. 4, no. 2, p. 021304, 6 2017. [Online]. Available: http://aip.scitation.org/doi/10.1063/1.4983310

[92] M. Donarelli and L. Ottaviano, "2d materials for gas sensing applications: A review on graphene oxide, mos2, ws2 and phosphorene," *Sensors (Switzerland)*, vol. 18, no. 11, p. 3638, 10 2018. [Online]. Available: http://www.mdpi.com/1424-8220/18/11/3638

[93] W. Yang, L. Gan, H. Li, and T. Zhai, "Two-dimensional layered nanomaterials for gas-sensing applications," *Inorganic Chemistry Frontiers*, vol. 3, no. 4, pp. 433–451, 2016.

[94] T. H. Kim, Y. H. Kim, S. Y. Park, S. Y. Kim, and H. W. Jang, "Two-dimensional transition metal disulfides for chemoresistive gas sensing: Perspective and challenges," *Chemosensors*, vol. 5, no. 2, p. 15, 2017. [Online]. Available: http://www.mdpi.com/2227-9040/5/2/15

[95] U. Latif and F. L. Dickert, "Graphene hybrid materials in gas sensing applications," *Sensors (Switzerland)*, vol. 15, no. 12, pp. 30 504–30 524, 2015. [Online]. Available: http://www.mdpi.com/1424-8220/15/12/29814

[96] S. S. Varghese, S. H. Varghese, S. Swaminathan, K. K. Singh, and V. Mittal, "Two-dimensional materials for sensing: Graphene and beyond," *Electronics (Switzerland)*, vol. 4, no. 3, pp. 651–687, 2015. [Online]. Available: http://www.mdpi.com/2079-9292/4/3/651/

[97] X. Liu, T. Ma, N. Pinna, and J. Zhang, "Two-Dimensional Nanostructured Materials for Gas Sensing," *Advanced Functional Materials*, vol. 27, no. 37, pp. 1–30, 2017.

[98] K. H. Ibrahim, M. Irannejad, M. Hajialamdari, A. Ramadhan, K. P. Musselman, J. Sanderson, and M. Yavuz, "A Novel Femtosecond Laser-Assisted Method for the Synthesis of Reduced Graphene Oxide Gels and Thin Films with Tunable Properties," *Advanced Materials Interfaces*, vol. 3, no. 14, p. 1500864, 7 2016. [Online]. Available: http://doi.wiley.com/10.1002/admi.201500864

[99] D. Alsaedi, M. Irannejad, K. H. Ibrahim, A. Almutairi, O. Ramahi, and M. Yavuz, "High-responsivity reduced graphene oxide gel photodetectors for visible-light detection with a large detection area and an end-contact interface," *Journal of Materials Chemistry C*, vol. 5, no. 4, pp. 882–888, 2017.

[100] I. Novodchuk, M. Irannejad, B. Wales, K. Ibrahim, J. Sanderson, M. Bajcsy, and M. Yavuz, "Controlled volume production of simultaneously B/N co-doped reduced graphene oxide nanoflakes using femtosecond laser ablation," *Materials Research Bulletin*, vol. 111, no. November 2018, pp. 80–86, 2019. [Online]. Available: https://doi.org/10.1016/j.materresbull.2018.10.039

[101] K. H. Ibrahim, M. Irannejad, B. Wales, J. Sanderson, M. Yavuz, and K. P. Musselman, "Simultaneous Fabrication and Functionalization of Nanoparticles of 2D Materials with Hybrid Optical Properties," *Advanced Optical Materials*, vol. 1701365, no. 11, pp. 1–7, 6 2018. [Online]. Available: http://doi.wiley.com/10.1002/adom.201701365

[102] M. Quinten, *A Practical Guide to Optical Metrology for Thin Films*. Weinheim, Germany: Wiley-VCH Verlag GmbH & Co. KGaA, 10 2012. [Online]. Available: http://doi.wiley.com/10.1002/9783527664344

[103] D. T. Larson, L. A. Lott, and D. L. Cash, "Surface Film Thickness Determination By Reflectance Measurements." *Applied Optics*, vol. 12, no. 6, pp. 1271–1275, 1973. [Online]. Available: http://www.ncbi.nlm.nih.gov/pubmed/20125509

[104] E. Langereis, S. B. S. Heil, H. C. M. Knoops, W. Keuning, M. C. M. van de Sanden, and W. M. M. Kessels, “In situ spectroscopic ellipsometry as a versatile tool for studying atomic layer deposition,” *Journal of Physics D: Applied Physics*, vol. 42, no. 7, p. 073001, 4 2009. [Online]. Available: https://iopscience.iop.org/article/10.1088/0022-3727/42/7/073001

[105] G. E. Jellison and F. A. Modine, “Parameterization of the optical functions of amorphous materials in the interband region,” *Applied Physics Letters*, vol. 69, no. 3, pp. 371–373, 7 1996. [Online]. Available: http://aip.scitation.org/doi/10.1063/1.118064

[106] A. S. Ferlauto, G. M. Ferreira, J. M. Pearce, C. R. Wronski, R. W. Collins, X. Deng, and G. Ganguly, “Analytical model for the optical functions of amorphous semiconductors from the near-infrared to ultraviolet: Applications in thin film photovoltaics,” *Journal of Applied Physics*, vol. 92, no. 5, pp. 2424–2436, 9 2002. [Online]. Available: http://aip.scitation.org/doi/10.1063/1.1497462

[107] W. G. Breiland and K. P. Killeen, “A virtual interface method for extracting growth rates and high temperature optical constants from thin semiconductor films using in situ normal incidence reflectance,” *Journal of Applied Physics*, vol. 78, no. 11, pp. 6726–6736, 12 1995. [Online]. Available: http://aip.scitation.org/doi/10.1063/1.360496

[108] K. P. Killeen and W. G. Breiland, “In situ spectral reflectance monitoring of III-V epitaxy,” *Journal of Electronic Materials*, vol. 23, no. 2, pp. 179–183, 1994.

[109] A. S. Yersak, Y. C. Lee, J. A. Spencer, and M. D. Groner, “ Atmospheric pressure spatial atomic layer deposition web coating with in situ monitoring of film thickness ,” *Journal of Vacuum Science & Technology A: Vacuum, Surfaces, and Films*, vol. 32, no. 1, p. 01A130, 2014. [Online]. Available: http://scitation.aip.org/content/avs/journal/jvsta/32/1/10.1116/1.4850176

[110] D. Degler, N. Barz, U. Dettinger, H. Peisert, T. Chassé, U. Weimar, and N. Barsan, “Extending the toolbox for gas sensor research: Operando UV/vis diffuse reflectance

spectroscopy on SnO2-based gas sensors," *Sensors and Actuators, B: Chemical*, vol. 224, pp. 256–259, 2016.

[111] A. Elger and C. Hess, "Elucidating the Mechanism of Working SnO 2 Gas Sensors Using Combined Operando UV/Vis, Raman, and IR Spectroscopy," *Angewandte Chemie International Edition*, vol. 58, no. 42, pp. 15 057–15 061, 10 2019. [Online]. Available: https://onlinelibrary.wiley.com/doi/10.1002/anie.201908871

[112] K. Mistry, A. Jones, M. Kao, T. W.-k. Yeow, M. Yavuz, and K. P. Musselman, "In-situ observation of nucleation and property evolution in films grown with an atmospheric pressure spatial atomic layer deposition system," *Nano Express*, vol. 1, no. 1, p. 010045, 6 2020. [Online]. Available: https://iopscience.iop.org/article/10.1088/2632-959X/ab976c

[113] K. P. Musselman, D. Muñoz-Rojas, R. L. Z. Hoye, H. Sun, S.-L. Sahonta, E. Croft, M. L. Böhm, C. Ducati, and J. L. MacManus-Driscoll, "Rapid open-air deposition of uniform, nanoscale, functional coatings on nanorod arrays," *Nanoscale Horizons*, vol. 2, no. 2, pp. 110–117, 2017. [Online]. Available: http://xlink.rsc.org/?DOI=C6NH00197A

[114] D. Muñoz-rojas, H. Sun, D. C. Iza, J. Weickert, L. Chen, H. Wang, L. Schmidt-Mende, and J. L. MacManus-Driscoll, "High-speed atmospheric atomic layer deposition of ultra thin amorphous TiO 2 blocking layers at 100 °C for inverted bulk heterojunction solar cells," *Progress in Photovoltaics: Research and Applications*, vol. 9, no. 11, pp. n/a–n/a, 4 2013. [Online]. Available: http://doi.wiley.com/10.1002/pip.2380

[115] R. L. Z. Hoye, B. Ehrler, M. L. Böhm, D. Muñoz-rojas, R. M. Altamimi, A. Y. Alyamani, Y. Vaynzof, A. Sadhanala, G. Ercolano, N. C. Greenham, R. H. Friend, J. L. MacManus-Driscoll, and K. P. Musselman, "Improved Open- Circuit Voltage in ZnO-PbSe Quantum Dot Solar Cells by Understanding and Reducing Losses Arising from the ZnO Conduction Band Tail," *Advanced Energy Materials*, vol. 4, no. 8, pp. 1–6, 6 2014. [Online]. Available: http://doi.wiley.com/10.1002/aenm.201301544

[116] C. H. Hsu, C. W. Huang, Y. S. Cho, W. Y. Wu, D. S. Wuu, X. Y. Zhang, W. Z. Zhu, S. Y. Lien, and C. S. Ye, “Efficiency improvement of PERC solar cell using an aluminum oxide passivation layer prepared via spatial atomic layer deposition and post-annealing,” *Surface and Coatings Technology*, vol. 358, no. November 2018, pp. 968–975, 2019.

[117] B. Ehrler, K. P. Musselman, M. L. Böhm, F. S. F. Morgenstern, Y. Vaynzof, B. J. Walker, J. L. MacManus-Driscoll, and N. C. Greenham, “Preventing Interfacial Recombination in Colloidal Quantum Dot Solar Cells by Doping the Metal Oxide,” *ACS Nano*, vol. 7, no. 5, pp. 4210–4220, 5 2013. [Online]. Available: https://pubs.acs.org/doi/10.1021/nn400656n

[118] H. Choi, S. Shin, H. Jeon, Y. Choi, J. Kim, S. Kim, S. C. Chung, and K. Oh, “Fast spatial atomic layer deposition of Al2O3 at low temperature (100 °C) as a gas permeation barrier for flexible organic light-emitting diode displays,” *Journal of Vacuum Science & Technology A: Vacuum, Surfaces, and Films*, vol. 34, no. 1, p. 01A121, 1 2016. [Online]. Available: http://dx.doi.org/10.1116/1.4934752

[119] D. Di, L. Yang, J. M. Richter, L. Meraldi, R. M. Altamimi, A. Y. Alyamani, D. Credgington, K. P. Musselman, J. L. MacManus-Driscoll, and R. H. Friend, “Efficient Triplet Exciton Fusion in Molecularly Doped Polymer Light-Emitting Diodes,” *Advanced Materials*, vol. 29, no. 13, p. 1605987, 4 2017. [Online]. Available: http://doi.wiley.com/10.1002/adma.201605987

[120] V. H. Nguyen, U. Gottlieb, A. Valla, D. Muñoz, D. Bellet, and D. Muñoz-Rojas, “Electron tunneling through grain boundaries in transparent conductive oxides and implications for electrical conductivity: The case of ZnO:Al thin films,” *Materials Horizons*, vol. 5, no. 4, pp. 715–726, 2018. [Online]. Available: http://xlink.rsc.org/?DOI=C8MH00402A

[121] E. B. Yousfi, J. Fouache, and D. Lincot, “Study of atomic layer epitaxy of zinc oxide by in-situ quartz crystal microgravimetry,” *Applied Surface*

Science, vol. 153, no. 4, pp. 223–234, 1 2000. [Online]. Available: http://dx.doi.org/10.2134/agronj1971.00021962006300050023x

[122] A. Rahtu, T. Alaranta, and M. Ritala, "In situ quartz crystal microbalance and quadrupole mass spectrometry studies of atomic layer deposition of aluminum oxide from trimethylaluminum and water," *Langmuir*, vol. 17, no. 21, pp. 6506–6509, 2001.

[123] G. Koster, "Reflection high-energy electron diffraction (RHEED) for in situ characterization of thin film growth," in *In Situ Characterization of Thin Film Growth*, G. Koster and G. Rijnders, Eds. Elsevier, 2011, ch. 1, pp. 3–28. [Online]. Available: https://linkinghub.elsevier.com/retrieve/pii/B9781845699345500011http://www.sciencedirect.com/science/article/pii/B9781845699345500011

[124] R. Bankras, J. Holleman, J. Schmitz, M. Sturm, A. Zinine, H. Wormeester, and B. Poelsema, "In Situ Reflective High-Energy Electron Diffraction Analysis During the Initial Stage of a Trimethylaluminum/Water ALD Process," *Chemical Vapor Deposition*, vol. 12, no. 5, pp. 275–279, 5 2006. [Online]. Available: http://doi.wiley.com/10.1002/cvde.200506433

[125] M. A. Mione, R. Engeln, V. Vandalon, W. M. M. Kessels, and F. Roozeboom, "Infrared and optical emission spectroscopy study of atmospheric pressure plasma-enhanced spatial ALD of Al2O3," *Applied Physics Letters*, vol. 115, no. 8, p. 083101, 8 2019. [Online]. Available: http://aip.scitation.org/doi/10.1063/1.5113753

[126] M. Kao, "An Intelligent Neural Network Controlled Atmospheric Pressure Spatial Atomic Layer Deposition System for Tunable Metal Oxide Thin Films by," Ph.D. dissertation, University of Waterloo, 2018. [Online]. Available: http://hdl.handle.net/10012/13642

[127] mathworks., "Solve Nonlinear Curve-Fitting (Data-Fitting) Problems in Least-Square sense - MATLAB lsqcurvefit," 2013. [Online]. Available: mathworks.com/help/optim/ug/lsqcurvefit.html

[128] C. Yim, M. O'Brien, N. McEvoy, S. Winters, I. Mirza, J. G. Lunney, and G. S. Duesberg, "Investigation of the optical properties of MoS 2 thin films using spectroscopic ellipsometry," *Applied Physics Letters*, vol. 104, no. 10, p. 103114, 3 2014. [Online]. Available: http://aip.scitation.org/doi/10.1063/1.4868108

[129] J. Tauc, "Optical properties and electronic structure of amorphous Ge and Si," *Materials Research Bulletin*, vol. 3, no. 1, pp. 37–46, 1 1968. [Online]. Available: http://www.sciencedirect.com/science/article/pii/0025540868900238https://linkinghub.elsevier.com/retrieve/pii/0025540868900238

[130] M. Guo, C. Yang, M. Zhang, Y. Zhang, T. Ma, X. Wang, and X. Wang, "Effects of preparing conditions on the electrodeposition of well-aligned ZnO nanorod arrays," *Electrochimica Acta*, vol. 53, no. 14, pp. 4633–4641, 5 2008. [Online]. Available: https://linkinghub.elsevier.com/retrieve/pii/S0013468608001382

[131] M. Caglar, S. Ilican, Y. Caglar, and F. Yakuphanoglu, "Electrical conductivity and optical properties of ZnO nanostructured thin film," *Applied Surface Science*, vol. 255, no. 8, pp. 4491–4496, 2 2009. [Online]. Available: https://linkinghub.elsevier.com/retrieve/pii/S016943320802415X

[132] J. Lim, K. Shin, H. Kim, and C. Lee, "Enhancement of ZnO nucleation in ZnO epitaxy by atomic layer epitaxy," *Thin Solid Films*, vol. 475, no. 1-2 SPEC. ISS., pp. 256–261, 2005.

[133] Z. Baji, Z. Lábadi, Z. E. Horváth, G. Molnár, J. Volk, I. Bársony, and P. Barna, "Nucleation and growth modes of ALD ZnO," *Crystal Growth and Design*, vol. 12, no. 11, pp. 5615–5620, 2012.

[134] H. Makino, S. Kishimoto, T. Yamada, A. Miyake, N. Yamamoto, and T. Yamamoto, "Effects of surface pretreatment on growth of ZnO on glass substrate," *Physica Status Solidi (A) Applications and Materials Science*, vol. 205, no. 8, pp. 1971–1974, 2008.

[135] C. Biswas, Z. Ma, X. Zhu, T. Kawaharamura, and K. L. Wang, "Atmospheric growth of hybrid ZnO thin films for inverted polymer solar cells," *Solar Energy*

Materials and Solar Cells, vol. 157, pp. 1048–1056, 2016. [Online]. Available: http://dx.doi.org/10.1016/j.solmat.2016.08.022

[136] J. Hu and R. G. Gordon, "Textured aluminum-doped zinc oxide thin films from atmospheric pressure chemical-vapor deposition," *Journal of Applied Physics*, vol. 71, no. 2, pp. 880–890, 1 1992. [Online]. Available: http://aip.scitation.org/doi/10.1063/1.351309

[137] S. Ratzsch, E.-B. Kley, A. Tünnermann, and A. Szeghalmi, "Influence of the oxygen plasma parameters on the atomic layer deposition of titanium dioxide," *Nanotechnology*, vol. 26, no. 2, p. 024003, 1 2015. [Online]. Available: http://dx.doi.org/10.1088/0957-4484/26/2/024003

[138] E. Janocha and C. Pettenkofer, "ALD of ZnO using diethylzinc as metal-precursor and oxygen as oxidizing agent," *Applied Surface Science*, vol. 257, no. 23, pp. 10 031–10 035, 9 2011. [Online]. Available: https://linkinghub.elsevier.com/retrieve/pii/S0169433211010099

[139] R. W. Johnson, A. Hultqvist, and S. F. Bent, "A brief review of atomic layer deposition: from fundamentals to applications," *Materials Today*, vol. 17, no. 5, pp. 236–246, 6 2014. [Online]. Available: https://linkinghub.elsevier.com/retrieve/pii/S1369702114001436

[140] S. Tan, W. Yang, K. J. Kanarik, T. Lill, V. Vahedi, J. Marks, and R. A. Gottscho, "Highly Selective Directional Atomic Layer Etching of Silicon," *ECS Journal of Solid State Science and Technology*, vol. 4, no. 6, pp. N5010–N5012, 2015. [Online]. Available: http://jss.ecsdl.org/lookup/doi/10.1149/2.0031506jss

[141] G. S. Oehrlein, D. Metzler, and C. Li, "Atomic Layer Etching at the Tipping Point: An Overview," *ECS Journal of Solid State Science and Technology*, vol. 4, no. 6, pp. N5041–N5053, 3 2015. [Online]. Available: http://jss.ecsdl.org/lookup/doi/10.1149/2.0061506jss

[142] J. S. Jur and G. N. Parsons, “Atomic layer deposition of Al 2O 3 and ZnO at atmospheric pressure in a flow tube reactor,” *ACS Applied Materials and Interfaces*, vol. 3, no. 2, pp. 299–308, 2011.

[143] M. B. M. Mousa, C. J. Oldham, and G. N. Parsons, “Atmospheric pressure atomic layer deposition of Al2O3 using trimethyl aluminum and ozone,” *Langmuir*, vol. 30, no. 13, pp. 3741–3748, 4 2014. [Online]. Available: https://pubs.acs.org/doi/10.1021/la500796r

[144] M. Caglar, Y. Caglar, S. Aksoy, and S. Ilican, “Temperature dependence of the optical band gap and electrical conductivity of solgel derived undoped and Li-doped ZnO films,” *Applied Surface Science*, vol. 256, no. 16, pp. 4966–4971, 6 2010. [Online]. Available: http://dx.doi.org/10.1016/j.apsusc.2010.03.010

[145] P. B. Allen and V. Heine, “Theory of the temperature dependence of electronic band structures,” *Journal of Physics C: Solid State Physics*, vol. 9, no. 12, pp. 2305–2312, 6 1976. [Online]. Available: http://stacks.iop.org/0022-3719/9/i=12/a=013?key=crossref.3c65ed24780cc9940d0f68b0a2f7d8a7

[146] V. H. Nguyen, J. Resende, C. Jiménez, J.-L. L. Deschanvres, P. Carroy, D. Muñoz, D. Bellet, and D. Muñoz-Rojas, “Deposition of ZnO based thin films by atmospheric pressure spatial atomic layer deposition for application in solar cells,” *Journal of Renewable and Sustainable Energy*, vol. 9, no. 2, p. 021203, 2017. [Online]. Available: http://aip.scitation.org/doi/10.1063/1.4979822

[147] R. E. Marotti, P. Giorgi, G. Machado, and E. A. Dalchiele, “Crystallite size dependence of band gap energy for electrodeposited ZnO grown at different temperatures,” *Solar Energy Materials and Solar Cells*, vol. 90, no. 15, pp. 2356–2361, 2006.

[148] Y. V. Vorobiev, P. P. Horley, J. Hernández-Borja, H. E. Esparza-Ponce, R. Ramírez-Bon, P. Vorobiev, C. Pérez, and J. González-Hernández, “The effects of porosity on optical properties of semiconductor chalcogenide films obtained by the chemical bath deposition,” *Nanoscale Research Letters*, vol. 7, no. 1, p. 483,

12 2012. [Online]. Available: https://nanoscalereslett.springeropen.com/articles/10.1186/1556-276X-7-483

[149] I. Sagnes, A. Halimaoui, G. Vincent, and P. A. Badoz, "Optical absorption evidence of a quantum size effect in porous silicon," *Applied Physics Letters*, vol. 62, no. 10, pp. 1155–1157, 1993.

[150] G. Luka, T. Krajewski, L. Wachnicki, B. Witkowski, E. Lusakowska, W. Paszkowicz, E. Guziewicz, and M. Godlewski, "Transparent and conductive undoped zinc oxide thin films grown by atomic layer deposition," *Physica Status Solidi (A) Applications and Materials Science*, vol. 207, no. 7, pp. 1568–1571, 2010. [Online]. Available: http://doi.wiley.com/10.1002/pssa.200983709

[151] J. Iqbal, A. Jilani, P. M. Ziaul Hassan, S. Rafique, R. Jafer, and A. A. Alghamdi, "ALD grown nanostructured ZnO thin films: Effect of substrate temperature on thickness and energy band gap," *Journal of King Saud University - Science*, vol. 28, no. 4, pp. 347–354, 10 2016. [Online]. Available: https://linkinghub.elsevier.com/retrieve/pii/S1018364715301105

[152] Y. P. Varshni, "Temperature dependence of the energy gap in semiconductors," *Physica*, vol. 34, no. 1, pp. 149–154, 1967.

[153] M. Maleki and S. M. Rozati, "Dependence of ZnO nanostructured thin films properties on growth temperature by APCVD method," *Acta Physica Polonica A*, vol. 128, no. 3, pp. 367–372, 2015.

[154] M. D. Groner, F. H. Fabreguette, J. W. Elam, and S. M. George, "Low-Temperature Al2O3 Atomic Layer Deposition," *Chemistry of Materials*, vol. 16, no. 4, pp. 639–645, 2004.

[155] K. Kukli, M. Ritala, M. Leskelä, and J. Jokinen, "Atomic layer epitaxy growth of aluminum oxide thin films from a novel Al(CH3)2Cl precursor and H2O," *Journal of Vacuum Science & Technology A: Vacuum, Surfaces, and Films*, vol. 15, no. 4, pp. 2214–2218, 1997.

[156] S. Behzadinasab, A. Chin, M. Hosseini, L. Poon, and W. A. Ducker, "A surface coating that rapidly inactivates sars-cov-2," *ACS applied materials & interfaces*, vol. 12, no. 31, pp. 34 723–34 727, 2020.

[157] K. Sunada, M. Minoshima, and K. Hashimoto, "Highly efficient antiviral and antibacterial activities of solid-state cuprous compounds," *Journal of hazardous materials*, vol. 235, pp. 265–270, 2012.

[158] A. Verbič, M. Gorjanc, and B. Simončič, "Zinc oxide for functional textile coatings: Recent advances," *Coatings*, vol. 9, no. 9, pp. 17–23, 2019.

[159] A. J. Karttunen, L. Sarnes, R. Townsend, J. Mikkonen, and M. Karppinen, "Flexible Thermoelectric ZnOOrganic Superlattices on Cotton Textile Substrates by ALD/MLD," *Advanced Electronic Materials*, vol. 3, no. 6, 2017.

[160] N. L. Pomerantz, E. E. Anderson, N. P. Dugan, N. F. Hoffman, H. F. Barton, D. T. Lee, C. J. Oldham, G. W. Peterson, and G. N. Parsons, "Air, Water Vapor, and Aerosol Transport through Textiles with Surface Functional Coatings of Metal Oxides and Metal-Organic Frameworks," *ACS Applied Materials and Interfaces*, vol. 11, no. 27, pp. 24 683–24 690, 2019.

[161] N. N. Greenwood and A. Earnshaw, "Chemistry of the elements," 1984.

[162] M. D. Groner, J. W. Elam, F. H. Fabreguette, and S. M. George, "Electrical characterization of thin Al2O3 films grown by atomic layer deposition on silicon and various metal substrates," *Thin Solid Films*, vol. 413, no. 1-2, pp. 186–197, 2002.

[163] Q. Peng, X. Y. Sun, J. C. Spagnola, G. K. Hyde, R. J. Spontak, and G. N. Parsons, "Atomic layer deposition on electrospun polymer fibers as a direct route to Al2O3 microtubes with precise wall thickness control," *Nano Letters*, vol. 7, no. 3, pp. 719–722, 2007.

[164] G. N. Parsons, S. E. Atanasov, E. C. Dandley, C. K. Devine, B. Gong, J. S. Jur, K. Lee, C. J. Oldham, Q. Peng, J. C. Spagnola, and P. S.

Williams, “Mechanisms and reactions during atomic layer deposition on polymers,” *Coordination Chemistry Reviews*, vol. 257, no. 23-24, pp. 3323–3331, 2013. [Online]. Available: http://dx.doi.org/10.1016/j.ccr.2013.07.001

[165] J. S. Jur, W. J. Sweet, C. J. Oldham, and G. N. Parsons, “Atomic layer deposition of conductive coatings on cotton, paper, and synthetic fibers: Conductivity analysis and functional chemical sensing using ”all-fiber” capacitors,” *Advanced Functional Materials*, vol. 21, no. 11, pp. 1993–2002, 2011.

[166] E. Lee, Y. S. Yoon, and D. J. Kim, “Two-Dimensional Transition Metal Dichalcogenides and Metal Oxide Hybrids for Gas Sensing,” *ACS Sensors*, vol. 3, no. 10, pp. 2045–2060, 2018.

[167] N. Justh, B. Berke, K. László, L. P. Bakos, A. Szabó, K. Hernádi, and I. M. Szilágyi, “Preparation of graphene oxide/semiconductor oxide composites by using atomic layer deposition,” *Applied Surface Science*, vol. 453, no. December 2017, pp. 245–251, 2018. [Online]. Available: https://doi.org/10.1016/j.apsusc.2018.05.064

[168] H. Mu, Z. Zhang, X. Zhao, F. Liu, K. Wang, and H. Xie, “High sensitive formaldehyde graphene gas sensor modified by atomic layer deposition zinc oxide films,” *Applied Physics Letters*, vol. 105, no. 3, 2014. [Online]. Available: http://dx.doi.org/10.1063/1.4890583

[169] T. N. Walter, S. Lee, X. Zhang, M. Chubarov, J. M. Redwing, T. N. Jackson, and S. E. Mohney, “Atomic layer deposition of ZnO on MoS 2 and WSe 2,” *Applied Surface Science*, vol. 480, no. December 2018, pp. 43–51, 2019.

[170] H. Zhang, D. Chiappe, J. Meersschaut, T. Conard, A. Franquet, T. Nuytten, M. Mannarino, I. Radu, W. Vandervorst, and A. Delabie, “Nucleation and growth mechanisms of Al2O3 atomic layerdeposition on synthetic polycrystalline MoS2,” *Journal of Chemical Physics*, vol. 146, no. 5, 2017. [Online]. Available: http://dx.doi.org/10.1063/1.4967406

[171] A. Jones, K. Mistry, M. Kao, A. Shahin, M. Yavuz, and K. P. Musselman, "In-situ spatial and temporal electrical characterization of ZnO thin films deposited by atmospheric pressure chemical vapour deposition on flexible polymer substrates," *Scientific Reports*, vol. 10, no. 1, pp. 1–10, 2020. [Online]. Available: https://doi.org/10.1038/s41598-020-76993-4

[172] Y.-H. Zhang, Y.-B. Chen, K.-G. Zhou, C.-H. Liu, J. Zeng, H.-L. Zhang, and Y. Peng, "Improving gas sensing properties of graphene by introducing dopants and defects: a first-principles study," *Nanotechnology*, vol. 20, no. 18, p. 185504, 5 2009. [Online]. Available: https://iopscience.iop.org/article/10.1088/0957-4484/20/18/185504

[173] S.-Y. Cho, S. J. Kim, Y. Lee, J.-S. Kim, W.-B. Jung, H.-W. Yoo, J. Kim, and H.-T. Jung, "Highly Enhanced Gas Adsorption Properties in Vertically Aligned MoS 2 Layers," *ACS Nano*, vol. 9, no. 9, pp. 9314–9321, 9 2015. [Online]. Available: https://pubs.acs.org/doi/10.1021/acsnano.5b04504

[174] Q. Zhou, L. Yuan, X. Yang, Z. Fu, Y. Tang, C. Wang, and H. Zhang, "DFT study of formaldehyde adsorption on vacancy defected graphene doped with B, N, and S," *Chemical Physics*, vol. 440, pp. 80–86, 2014.

[175] A. Shokri and N. Salami, "Gas sensor based on MoS2 monolayer," *Sensors and Actuators, B: Chemical*, vol. 236, pp. 378–385, 11 2016. [Online]. Available: http://linkinghub.elsevier.com/retrieve/pii/S0925400516308851

[176] J. Wang, S. Gao, C. Zhang, Q. Zhang, Z. Li, and S. Zhang, "A high throughput platform screening of ppb-level sensitive materials for hazardous gases," *Sensors and Actuators, B: Chemical*, vol. 276, no. August, pp. 189–203, 2018. [Online]. Available: https://doi.org/10.1016/j.snb.2018.08.079

[177] T. J. Koplin, M. Siemons, C. Océn-Valéntin, D. Sanders, and U. Simon, "Workflow for high throughput screening of gas sensing materials," *Sensors*, vol. 6, no. 4, pp. 298–307, 2006.

[178] M. Siemons, T. J. Koplin, and U. Simon, "Advances in high throughput screening of gas sensing materials," *Applied Surface Science*, vol. 254, no. 3, pp. 669–676, 2007.

[179] W. Ogieglo, H. Wormeester, K. J. Eichhorn, M. Wessling, and N. E. Benes, "In situ ellipsometry studies on swelling of thin polymer films: A review," *Progress in Polymer Science*, vol. 42, pp. 42–78, 2015. [Online]. Available: http://dx.doi.org/10.1016/j.progpolymsci.2014.09.004

[180] Q. Fatima, A. A. Haidry, Z. Yao, Y. He, Z. Li, L. Sun, and L. Xie, "The critical role of hydroxyl groups in water vapor sensing of graphene oxide," *Nanoscale Advances*, vol. 1, no. 4, pp. 1319–1330, 2019. [Online]. Available: http://xlink.rsc.org/?DOI=C8NA00135A

[181] S. Zheng, Q. Tu, J. J. Urban, S. Li, and B. Mi, "Swelling of Graphene Oxide Membranes in Aqueous Solution: Characterization of Interlayer Spacing and Insight into Water Transport Mechanisms," *ACS Nano*, vol. 11, no. 6, pp. 6440–6450, 2017.

[182] A. Iakunkov, J. Sun, A. Rebrikova, M. Korobov, A. Klechikov, A. Vorobiev, N. Boulanger, and A. V. Talyzin, "Swelling of graphene oxide membranes in alcohols: Effects of molecule size and air ageing," *Journal of Materials Chemistry A*, vol. 7, no. 18, pp. 11 331–11 337, 2019.

[183] E. Dickey and W. A. Barrow, "High rate roll to roll atomic layer deposition, and its application to moisture barriers on polymer films," *Journal of Vacuum Science & Technology A: Vacuum, Surfaces, and Films*, vol. 30, no. 2, p. 021502, 2012.

[184] N. Shiraishi, T. Ikehara, D. V. Dao, S. Sugiyama, and Y. Ando, "Fabrication and testing of polymer cantilevers for VOC sensors," *Sensors and Actuators, A: Physical*, vol. 202, pp. 233–239, 2013. [Online]. Available: http://dx.doi.org/10.1016/j.sna.2013.01.011

[185] Y. Li, "Challenges and Issues of Using Polymers as Structural Materials in MEMS: A Review," *Journal of Microelectromechanical Systems*, vol. 27, no. 4, pp. 581–598, 2018.

[186] D. Bhatia, H. Sharma, R. Meena, and V. Palkar, "A novel ZnO piezoelectric microcantilever energy scavenger: Fabrication and characterization," *Sensing and Bio-Sensing Research*, vol. 9, pp. 45–52, 7 2016. [Online]. Available: https://linkinghub.elsevier.com/retrieve/pii/S221418041630054X

[187] N. Y. Yuan, S. Y. Wang, C. B. Tan, X. Q. Wang, G. G. Chen, and J. N. Ding, "The influence of deposition temperature on growth mode, opticaland mechanical properties of ZnO films prepared by the ALD method," *Journal of Crystal Growth*, vol. 366, pp. 43–46, 2013.

[188] . Özgür, Y. I. Alivov, C. Liu, A. Teke, M. A. Reshchikov, S. Doan, V. Avrutin, S. J. Cho, and H. Morko, "A comprehensive review of ZnO materials and devices," *Journal of Applied Physics*, vol. 98, no. 4, pp. 1–103, 2005.

[189] F. Fitriana, N. L. W. Septiani, I. Irzaman, F. Ferdiansjah, M. Z. Fahmi, D. R. Adhika, S. Suyatman, N. Nugraha, and B. Yuliarto, "Preparation of (002)-oriented ZnO for CO gas sensor," *Materials Research Express*, vol. 6, no. 6, p. 064003, 3 2019. [Online]. Available: https://iopscience.iop.org/article/10.1088/2053-1591/ab0d6b

[190] H. H. Tawfik, M. Y. Elsayed, F. Nabki, and M. N. El-Gamal, "Hard-baked photoresist as a sacrificial layer for sub-180 °C surface micromachining processes," *Micromachines*, vol. 9, no. 5, pp. 1–8, 2018.

[191] C. P. Green and J. E. Sader, "Frequency response of cantilever beams immersed in viscous fluids near a solid surface with applications to the atomic force microscope," *Journal of Applied Physics*, vol. 98, no. 11, 2005.

[192] X. Xu and A. Raman, "Comparative dynamics of magnetically, acoustically, and Brownian motion driven microcantilevers in liquids," *Journal of Applied Physics*, vol. 102, no. 3, 2007.

[193] Z. Chai, X. Lu, and D. He, "Atomic layer deposition of zinc oxide films: Effects of nanocrystalline characteristics on tribological performance," *Surface and Coatings*

Technology, vol. 207, no. June 2018, pp. 361–366, 2012. [Online]. Available: http://dx.doi.org/10.1016/j.surfcoat.2012.07.021

[194] W. M. Haynes, *CRC handbook of chemistry and physics*. CRC press, 2014.

[195] P. Tsai and Y. Yan, "The influence of fiber and fabric properties on nonwoven performance," in *Applications of nonwovens in technical textiles*. Elsevier, 2010, pp. 18–45.

[196] Y. Yang, G. Wang, and X. Li, "Water Molecule-Induced Stiffening in ZnO Nanobelts," *Nano Letters*, vol. 11, no. 7, pp. 2845–2848, 7 2011. [Online]. Available: https://pubs.acs.org/doi/10.1021/nl201237x

[197] D. Mata-Hernandez, D. Fernández, S. Banerji, and J. Madrenas, "Resonant mems pressure sensor in 180 nm cmos technology obtained by beol isotropic etching," *Sensors*, vol. 20, no. 21, p. 6037, 2020.

[198] Z. Zheng, Y. Yao, J. A. Liu, Y. Sun, and J. T. Yeow, "Highly sensitive CMUT-based humidity sensors built with nitride-to-oxide wafer bonding technology," *Sensors and Actuators, B: Chemical*, vol. 294, no. March, pp. 123–131, 2019. [Online]. Available: https://doi.org/10.1016/j.snb.2019.05.003

[199] L. Sheng, C. Dajing, and C. Yuquan, "A surface acoustic wave humidity sensor with high sensitivity based on electrospun MWCNT/Nafion nanofiber films," *Nanotechnology*, vol. 22, no. 26, 2011.

[200] X. Cha, F. Yu, Y. Fan, J. Chen, L. Wang, Q. Xiang, Z. Duan, and J. Xu, "Superhydrophilic ZnO nanoneedle array: Controllable in situ growth on QCM transducer and enhanced humidity sensing properties and mechanism," *Sensors and Actuators, B: Chemical*, vol. 263, pp. 436–444, 2018. [Online]. Available: https://doi.org/10.1016/j.snb.2018.01.110

[201] T. Addabbo, A. Fort, M. Mugnaini, V. Vignoli, A. Baldi, and M. Bruzzi, "Quartz-Crystal Microbalance Gas Sensors Based on TiO2 Nanoparticles," *IEEE Transactions on Instrumentation and Measurement*, vol. 67, no. 3, pp. 722–730, 2018.

[202] S. N. Hidayat, T. Julian, A. Rianjanu, A. Kusumaatmadja, K. Triyana, and Roto, "Quartz crystal microbalance coated by PAN nanofibers and PEDOT: PSS for humidity sensor," *Proceedings - 2017 International Seminar on Sensor, Instrumentation, Measurement and Metrology: Innovation for the Advancement and Competitiveness of the Nation, ISSIMM 2017*, vol. 2017-Janua, no. August, pp. 119–123, 2017.

[203] Z. Yuan, H. Tai, Z. Ye, C. Liu, G. Xie, X. Du, and Y. Jiang, "Novel highly sensitive QCM humidity sensor with low hysteresis based on graphene oxide (GO)/poly(ethyleneimine) layered film," *Sensors and Actuators, B: Chemical*, vol. 234, pp. 145–154, 2016. [Online]. Available: http://dx.doi.org/10.1016/j.snb.2016.04.070

[204] Y. Yao, X. h. Huang, B. y. Zhang, Z. Zhang, D. Hou, and Z. k. Zhou, "Facile fabrication of high sensitivity cellulose nanocrystals based QCM humidity sensors with asymmetric electrode structure," *Sensors and Actuators, B: Chemical*, vol. 302, no. September 2019, pp. 1–9, 2020.

[205] P. Qi, T. Zhang, J. Shao, B. Yang, T. Fei, and R. Wang, "A QCM humidity sensor constructed by graphene quantum dots and chitosan composites," *Sensors and Actuators, A: Physical*, vol. 287, pp. 93–101, 2019.

[206] H. J. Lee, K. K. Park, M. Kupnik, N. A. Melosh, and B. T. Khuri-Yakub, "Mesoporous thin-film on highly-sensitive resonant chemical sensor for relative humidity and CO 2 detection," *Analytical Chemistry*, vol. 84, no. 7, pp. 3063–3066, 2012.

[207] H. J. Lee, K. K. Park, . Oralkan, M. Kupnik, and B. T. Khuri-Yakub, "A multichannel oscillator for a resonant chemical sensor system," *IEEE Transactions on Industrial Electronics*, vol. 61, no. 10, pp. 5632–5640, 2014.

[208] C. Sun, Q. Shi, M. S. Yazici, C. Lee, and Y. Liu, "Development of a highly sensitive humidity sensor based on a piezoelectric micromachined ultrasonic transducer array functionalized with graphene oxide thin film," *Sensors (Switzerland)*, vol. 18, no. 12, pp. 1–12, 2018.

[209] W. Xuan, M. Cole, J. W. Gardner, S. Thomas, F. H. Villa-López, X. Wang, S. Dong, and J. Luo, “A film bulk acoustic resonator oscillator based humidity sensor with graphene oxide as the sensitive layer,” *Journal of Micromechanics and Microengineering*, vol. 27, no. 5, 2017.

[210] X. Qiu, R. Tang, J. Zhu, J. Oiler, C. Yu, Z. Wang, and H. Yu, “Experiment and theoretical analysis of relative humidity sensor based on film bulk acoustic-wave resonator,” *Sensors and Actuators, B: Chemical*, vol. 147, no. 2, pp. 381–384, 2010.

[211] X. L. He, D. J. Li, J. Zhou, W. B. Wang, W. P. Xuan, S. R. Dong, H. Jin, and J. K. Luo, “High sensitivity humidity sensors using flexible surface acoustic wave devices made on nanocrystalline ZnO/polyimide substrates,” *Journal of Materials Chemistry C*, vol. 1, no. 39, pp. 6210–6215, 2013.

[212] P. Xu, X. Li, H. Yu, and T. Xu, “Advanced nanoporous materials for micro-gravimetric sensing to trace-level bio/chemical molecules,” *Sensors (Switzerland)*, vol. 14, no. 10, pp. 19 023–19 056, 2014.

[213] X. Le, X. Wang, J. Pang, Y. Liu, B. Fang, Z. Xu, C. Gao, Y. Xu, and J. Xie, “A high performance humidity sensor based on surface acoustic wave and graphene oxide on AlN/Si layered structure,” *Sensors and Actuators, B: Chemical*, vol. 255, pp. 2454–2461, 2018.

[214] Y. Liu, H. Huang, L. Wang, D. Cai, B. Liu, D. Wang, Q. Li, and T. Wang, “Electrospun CeO2 nanoparticles/PVP nanofibers based high-frequency surface acoustic wave humidity sensor,” *Sensors and Actuators, B: Chemical*, vol. 223, pp. 730–737, 2016.

[215] S. Alam, T. Islam, and U. Mittal, “A Sensitive Inexpensive SAW Sensor for Wide Range Humidity Measurement,” *IEEE Sensors Journal*, vol. 20, no. 1, pp. 546–551, 2020.

[216] Y. Su, C. Li, M. Li, H. Li, S. Xu, L. Qian, and B. Yang, “Surface acoustic wave humidity sensor based on three-dimensional architecture graphene/PVA/SiO2 and

its application for respiration monitoring," *Sensors and Actuators, B: Chemical*, vol. 308, no. September 2019, 2020.

[217] J. Verd, M. Sansa, A. Uranga, F. Perez-Murano, J. Segura, and N. Barniol, "Metal microelectromechanical oscillator exhibiting ultra-high water vapor resolution," *Lab on a Chip*, vol. 11, no. 16, pp. 2670–2672, 2011.

[218] S. Kim, B. Lee, Y. Toon, T. Thundat, and J. Lee, "Static and dynamic operation of metal-coated hydrogel cantilever humidity sensors based on hygroscopic mismatch," *TRANSDUCERS 2017 - 19th International Conference on Solid-State Sensors, Actuators and Microsystems*, pp. 300–302, 2017.

[219] D. M. Karabacak, S. H. Brongersma, and M. Crego-Calama, "Enhanced sensitivity volatile detection with low power integrated micromechanical resonators," *Lab on a Chip*, vol. 10, no. 15, p. 1976, 2010. [Online]. Available: http://xlink.rsc.org/?DOI=b926170b

[220] X. Le, L. Peng, J. Pang, Z. Xu, C. Gao, and J. Xie, "Humidity sensors based on AlN microcantilevers excited at high-order resonant modes and sensing layers of uniform graphene oxide," *Sensors and Actuators, B: Chemical*, vol. 283, no. July 2018, pp. 198–206, 2019. [Online]. Available: https://doi.org/10.1016/j.snb.2018.12.021

[221] N. Sakly, A. Haj Said, and H. Ben Ouada, "Humidity-sensing properties of ZnO QDs coated QCM: Optimization, modeling and kinetic investigations," *Materials Science in Semiconductor Processing*, vol. 27, no. 1, pp. 130–139, 2014. [Online]. Available: http://dx.doi.org/10.1016/j.mssp.2014.06.027

[222] R. I. Masel, *Principles of adsorption and reaction on solid surfaces.* John Wiley & Sons, 1996, vol. 3.

[223] H. Freundlich, *Kapillarchemie: eine Darstellung der Chemie der Kolloide und verwandter Gebiete.* akademische Verlagsgesellschaft, 1922.

[224] S. Brunauer, P. H. Emmett, and E. Teller, "Adsorption of gases in multimolecular layers," *Journal of the American chemical society*, vol. 60, no. 2, pp. 309–319, 1938.

[225] O. M. Ylivaara, X. Liu, L. Kilpi, J. Lyytinen, D. Schneider, M. Laitinen, J. Julin, S. Ali, S. Sintonen, M. Berdova *et al.*, "Aluminum oxide from trimethylaluminum and water by atomic layer deposition: The temperature dependence of residual stress, elastic modulus, hardness and adhesion," *Thin Solid Films*, vol. 552, pp. 124–135, 2014.

[226] Z. Zhu, E. Salmi, and S. Virtanen, "Residual stress study of thin films deposited by atomic layer deposition," in *2017 IEEE 12th International Conference on ASIC (ASICON)*. IEEE, 2017, pp. 233–236.

[227] K. Mistry, K. H. Ibrahim, I. Novodchuk, H. T. Ngo, G. Imamura, J. Sanderson, M. Yavuz, G. Yoshikawa, and K. P. Musselman, "Nanomechanical Gas Sensing with Laser Treated 2D Nanomaterials," *Advanced Materials Technologies*, vol. 5, no. 12, p. 2000704, 12 2020. [Online]. Available: https://onlinelibrary.wiley.com/doi/10.1002/admt.202000704

[228] S. Sethi, R. Nanda, and T. Chakraborty, "Clinical application of volatile organic compound analysis for detecting infectious diseases," *Clinical Microbiology Reviews*, vol. 26, no. 3, pp. 462–475, 2013.

[229] W. Zheng, Y. Xu, L. Zheng, C. Yang, N. Pinna, X. Liu, and J. Zhang, "MoS2 Van der Waals pn Junctions Enabling Highly Selective RoomTemperature NO 2 Sensor," *Advanced Functional Materials*, vol. 30, no. 19, p. 2000435, 5 2020. [Online]. Available: https://onlinelibrary.wiley.com/doi/abs/10.1002/adfm.202000435

[230] A. Lipatov, A. Varezhnikov, P. Wilson, V. Sysoev, A. Kolmakov, and A. Sinitskii, "Highly selective gas sensor arrays based on thermally reduced graphene oxide," *Nanoscale*, vol. 5, no. 12, pp. 5426–5434, 2013.

[231] S. L. Zhang, H. H. Choi, H. Y. Yue, and W. C. Yang, "Controlled exfoliation of molybdenum disulfide for developing thin film humidity sensor," *Current Applied Physics*, vol. 14, no. 3, pp. 264–268, 2014.

[232] C. Ahn, J. Lee, H. U. Kim, H. Bark, M. Jeon, G. H. Ryu, Z. Lee, G. Y. Yeom, K. Kim, J. Jung, Y. Kim, C. Lee, and T. Kim, "Low-Temperature Synthesis of Large-Scale Molybdenum Disulfide Thin Films Directly on a Plastic Substrate Using Plasma-Enhanced Chemical Vapor Deposition," *Advanced Materials*, vol. 27, no. 35, pp. 5223–5229, 9 2015. [Online]. Available: http://doi.wiley.com/10.1002/adma.201501678

[233] A. S. Pawbake, R. G. Waykar, D. J. Late, and S. R. Jadkar, "Highly Transparent Wafer-Scale Synthesis of Crystalline WS2 Nanoparticle Thin Film for Photodetector and Humidity-Sensing Applications," *ACS Applied Materials and Interfaces*, vol. 8, no. 5, pp. 3359–3365, 2016.

[234] R. K. Jha and P. K. Guha, "Liquid exfoliated pristine WS2 nanosheets for ultrasensitive and highly stable chemiresistive humidity sensors," *Nanotechnology*, vol. 27, no. 47, 2016.

[235] T. Kavinkumar, D. Sastikumar, and S. Manivannan, "Effect of functional groups on dielectric, optical gas sensing properties of graphene oxide and reduced graphene oxide at room temperature," *RSC Advances*, vol. 5, no. 14, pp. 10 816–10 825, 2015. [Online]. Available: http://dx.doi.org/10.1039/C4RA12766H

[236] B. Chen, H. Liu, X. Li, C. Lu, Y. Ding, and B. Lu, "Fabrication of a graphene field effect transistor array on microchannels for ethanol sensing," *Applied Surface Science*, vol. 258, no. 6, pp. 1971–1975, 2012. [Online]. Available: http://dx.doi.org/10.1016/j.apsusc.2011.05.101

[237] C. R. Minitha, V. S. Anithaa, V. Subramaniam, R. T. Rajendra Kumar, R. Thangavelu, R. Kumar, R. T. Rajendra Kumar, R. Thangavelu, and R. Kumar, "Impact of Oxygen Functional Groups on Reduced Graphene Oxide-Based Sensors for Ammonia and Toluene Detection at Room Temperature," *ACS Omega*, vol. 3, no. 4, pp. 4105–4112, 2018.

[238] W. Y. Chen, C. C. Yen, S. Xue, H. Wang, and L. A. Stanciu, "Surface Functionalization of Layered Molybdenum Disulfide for the Selective Detection of Volatile Organic

Compounds at Room Temperature," *ACS Applied Materials and Interfaces*, vol. 11, no. 37, pp. 34 135–34 143, 2019.

[239] K. Y. Ko, J.-g. G. Song, Y. Kim, T. Choi, S. Shin, C. W. Lee, K. Lee, J. Koo, H. Lee, J. Kim, T. Lee, J. Park, and H. Kim, "Improvement of Gas-Sensing Performance of Large-Area Tungsten Disulfide Nanosheets by Surface Functionalization," *ACS Nano*, vol. 10, no. 10, pp. 9287–9296, 10 2016. [Online]. Available: http://pubs.acs.org/doi/10.1021/acsnano.6b03631

[240] J. Dai, J. Yuan, and P. Giannozzi, "Gas adsorption on graphene doped with B, N, Al, and S: A theoretical study," *Applied Physics Letters*, vol. 95, no. 23, pp. 8–11, 2009.

[241] S. Basu and P. Bhattacharyya, "Recent developments on graphene and graphene oxide based solid state gas sensors," *Sensors and Actuators, B: Chemical*, vol. 173, pp. 1–21, 10 2012. [Online]. Available: http://dx.doi.org/10.1016/j.snb.2012.07.092https://linkinghub.elsevier.com/retrieve/pii/S092540051200785X

[242] D. Ma, W. Ju, T. Li, X. Zhang, C. He, B. Ma, Z. Lu, and Z. Yang, "Applied Surface Science The adsorption of CO and NO on the MoS 2 monolayer doped with Au , Pt , Pd , or Ni : A first-principles study," *Applied Surface Science*, vol. 383, pp. 98–105, 10 2016. [Online]. Available: http://dx.doi.org/10.1016/j.apsusc.2016.04.171https://linkinghub.elsevier.com/retrieve/pii/S0169433216309606

[243] F. Schedin, A. K. Geim, S. V. Morozov, E. W. Hill, P. Blake, M. I. Katsnelson, and K. S. Novoselov, "Detection of individual gas molecules adsorbed on graphene," *Nature Materials*, vol. 6, no. 9, pp. 652–655, 2007.

[244] Z. Liu, S. P. Lau, and F. Yan, "Functionalized graphene and other two-dimensional materials for photovoltaic devices: device design and processing," *Chemical Society Reviews*, vol. 44, no. 15, pp. 5638–5679, 2015.

[245] K. Shiba, R. Tamura, T. Sugiyama, Y. Kameyama, K. Koda, E. Sakon, K. Minami, H. T. Ngo, G. Imamura, K. Tsuda, and G. Yoshikawa, "Functional Nanoparticles-

Coated Nanomechanical Sensor Arrays for Machine Learning-Based Quantitative Odor Analysis," *ACS Sensors*, vol. 3, no. 8, pp. 1592–1600, 2018.

[246] H. T. Ngo, K. Minami, G. Imamura, K. Shiba, and G. Yoshikawa, "Effects of Center Metals in Porphines on Nanomechanical Gas Sensing," *Sensors (Switzerland)*, vol. 18, no. 5, pp. 1–14, 5 2018. [Online]. Available: http://www.mdpi.com/1424-8220/18/5/1640

[247] I. Osica, A. F. A. A. Melo, F. C. D. A. Lima, K. Shiba, G. Imamura, F. N. Crespilho, J. Betlej, K. J. Kurzydowski, G. Yoshikawa, and K. Ariga, "Nanomechanical Recognition and Discrimination of Volatile Molecules by Au Nanocages Deposited on Membrane-Type Surface Stress Sensors," *ACS Applied Nano Materials*, vol. 3, no. 5, pp. 4061–4068, 5 2020. [Online]. Available: https://pubs.acs.org/doi/10.1021/acsanm.0c00115

[248] H. H.-M. Yeung, G. Yoshikawa, K. Minami, and K. Shiba, "Strain-based chemical sensing using metalorganic framework nanoparticles," *Journal of Materials Chemistry A*, 2020. [Online]. Available: http://xlink.rsc.org/?DOI=D0TA07248F

[249] S. Zhuang, E. S. Lee, L. Lei, B. B. Nunna, L. Kuang, and W. Zhang, "Synthesis of nitrogen-doped graphene catalyst by high-energy wet ball milling for electrochemical systems," *International Journal of Energy Research*, vol. 40, no. 15, pp. 2136–2149, 12 2016. [Online]. Available: http://doi.wiley.com/10.1002/er.3595

[250] D. Akinwande, C. J. Brennan, J. S. Bunch, P. Egberts, J. R. Felts, H. Gao, R. Huang, J.-S. Kim, T. Li, Y. Li, K. M. Liechti, N. Lu, H. S. Park, E. J. Reed, P. Wang, B. I. Yakobson, T. Zhang, Y.-W. Zhang, Y. Zhou, and Y. Zhu, "A review on mechanics and mechanical properties of 2D materialsGraphene and beyond," *Extreme Mechanics Letters*, vol. 13, pp. 42–77, 5 2017. [Online]. Available: http://dx.doi.org/10.1016/j.eml.2017.01.008

[251] G. Yoshikawa, "Mechanical analysis and optimization of a microcantilever sensor coated with a solid receptor film," *Applied Physics Letters*, vol. 98, no. 17, pp. 98–101, 2011.

[252] G. Imamura, K. Minami, K. Shiba, K. Mistry, K. P. Musselman, M. Yavuz, G. Yoshikawa, K. Saiki, and S. Obata, "Graphene Oxide as a Sensing Material for Gas Detection Based on Nanomechanical Sensors in the Static Mode," *Chemosensors*, vol. 8, no. 3, p. 82, 9 2020. [Online]. Available: https://www.mdpi.com/2227-9040/8/3/82

[253] I. Novodchuk, M. Kayaharman, K. Ibrahim, S. Al-Tuairqi, M. Irannejad, E. Abdel-Rahman, J. Sanderson, M. Bajcsy, and M. Yavuz, "B/N co-doped graphene oxide gel with extremely-high mobility and ION/IOFF for large-area field effect transistors," *Carbon*, vol. 158, pp. 624–630, 3 2020. [Online]. Available: https://linkinghub.elsevier.com/retrieve/pii/S0008622319311595

[254] K. Ibrahim, I. Novodchuk, K. Mistry, M. Singh, C. Ling, J. Sanderson, M. Bajcsy, M. Yavuz, and K. P. Musselman, "LaserDirected Assembly of Nanorods of 2D Materials," *Small*, vol. 15, no. 46, p. 1904415, 11 2019. [Online]. Available: https://onlinelibrary.wiley.com/doi/abs/10.1002/smll.201904415

[255] G. Korotcenkov and B. K. Cho, "Engineering approaches for the improvement of conductometric gas sensor parameters: Part 1. Improvement of sensor sensitivity and selectivity (short survey)," *Sensors and Actuators, B: Chemical*, vol. 188, pp. 709–728, 2013. [Online]. Available: http://dx.doi.org/10.1016/j.snb.2013.07.101

[256] K. Minami, K. Shiba, and G. Yoshikawa, "Discrimination of structurally similar odorous molecules with various concentrations by using a nanomechanical sensor," *Analytical Methods*, vol. 10, no. 30, pp. 3720–3726, 2018. [Online]. Available: http://xlink.rsc.org/?DOI=C8AY01224E

[257] Q. Huang, D. Zeng, S. Tian, and C. Xie, "Synthesis of defect graphene and its application for room temperature humidity sensing," *Materials Letters*, vol. 83, pp. 76–79, 9 2012. [Online]. Available: http://dx.doi.org/10.1016/j.matlet.2012.05.074https://linkinghub.elsevier.com/retrieve/pii/S0167577X12007525

[258] Y. Marcus, "The sizes of molecules - Revisited," *Journal of Physical Organic Chemistry*, vol. 16, no. 7, pp. 398–408, 2003.

[259] B. Zheng, L. L. Wang, L. Du, Y. Pan, Z. Lai, K. W. Huang, and H. L. Du, "Diffusion as a function of guest molecule length and functionalization in flexible metal-organic frameworks," *Materials Horizons*, vol. 3, no. 4, pp. 355–361, 2016.

[260] R. Pearce, T. Iakimov, M. Andersson, L. Hultman, A. L. Spetz, and R. Yakimova, "Epitaxially grown graphene based gas sensors for ultra sensitive NO 2 detection," *Sensors and Actuators, B: Chemical*, vol. 155, no. 2, pp. 451–455, 2011. [Online]. Available: http://dx.doi.org/10.1016/j.snb.2010.12.046

[261] K. Muthoosamy, R. Geetha Bai, I. B. Abubakar, S. M. Sudheer, H. N. Lim, H. S. Loh, N. M. Huang, C. H. Chia, and S. Manickam, "Exceedingly biocompatible and thin-layered reduced graphene oxide nanosheets using an eco-friendly mushroom extract strategy," *International Journal of Nanomedicine*, vol. 10, pp. 1505–1519, 2015.

[262] L. Zhang, Y. Li, L. Zhang, D. W. Li, D. Karpuzov, and Y. T. Long, "Electrocatalytic oxidation of NADH on graphene oxide and reduced graphene oxide modified screen-printed electrode," *International Journal of Electrochemical Science*, vol. 6, no. 3, pp. 819–829, 2011.

[263] K. Dave, K. H. Park, and M. Dhayal, "Two-step process for programmable removal of oxygen functionalities of graphene oxide: functional, structural and electrical characteristics," *RSC Advances*, vol. 5, no. 116, pp. 95 657–95 665, 2015.

[264] G. Sobon, J. Sotor, J. Jagiello, R. Kozinski, M. Zdrojek, M. Holdynski, P. Paletko, J. Boguslawski, L. Lipinska, and K. M. Abramski, "Graphene Oxide vs Reduced Graphene Oxide as saturable absorbers for Er-doped passively mode-locked fiber laser," *Optics Express*, vol. 20, no. 17, p. 19463, 2012.

[265] B. Gupta, N. Kumar, K. Panda, V. Kanan, S. Joshi, and I. Visoly-Fisher, "Role of oxygen functional groups in reduced graphene oxide for lubrication," *Scientific Reports*, vol. 7, pp. 1–14, 2017.

[266] S. Muralikrishna, K. Sureshkumar, T. S. Varley, D. H. Nagaraju, and T. Ramakrishnappa, "In situ reduction and functionalization of graphene oxide with l-cysteine

for simultaneous electrochemical determination of cadmium(ii), lead(ii), copper(ii), and mercury(ii) ions," *Analytical Methods*, vol. 6, no. 21, pp. 8698–8705, 2014.

[267] L. Guo, H.-B. B. Jiang, R.-Q. Q. Shao, Y.-L. L. Zhang, S.-Y. Y. Xie, J.-N. N. Wang, X.-B. B. Li, F. Jiang, Q.-D. D. Chen, T. Zhang, and H.-B. B. Sun, "Two-beam-laser interference mediated reduction, patterning and nanostructuring of graphene oxide for the production of a flexible humidity sensing device," *Carbon*, vol. 50, no. 4, pp. 1667–1673, 4 2012. [Online]. Available: https://linkinghub.elsevier.com/retrieve/pii/S0008622311009560

[268] X. Wang, X. Li, Y. Zhao, Y. Chen, J. Yu, and J. Wang, "The influence of oxygen functional groups on gas-sensing properties of reduced graphene oxide (rGO) at room temperature," *RSC Advances*, vol. 6, no. 57, pp. 52 339–52 346, 2016.

[269] C. Ma, X. Shao, and D. Cao, "Nitrogen-doped graphene as an excellent candidate for selective gas sensing," *Science China Chemistry*, vol. 57, no. 6, pp. 911–917, 2014.

[270] L. Shao, G. Chen, H. Ye, Y. Wu, Z. Qiao, Y. Zhu, and H. Niu, "Sulfur dioxide adsorbed on graphene and heteroatom-doped graphene: A first-principles study," *European Physical Journal B*, vol. 86, no. 2, pp. 2–6, 2013.

[271] F. Niu, J. M. Liu, L. M. Tao, W. Wang, and W. G. Song, "Nitrogen and silica co-doped graphene nanosheets for NO2 gas sensing," *Journal of Materials Chemistry A*, vol. 1, no. 20, pp. 6130–6133, 2013.

[272] Y. Zhang, K. Fugane, T. Mori, L. Niu, and J. Ye, "Wet chemical synthesis of nitrogen-doped graphene towards oxygen reduction electrocatalysts without high-temperature pyrolysis," *Journal of Materials Chemistry*, vol. 22, no. 14, pp. 6575–6580, 2012. [Online]. Available: http://xlink.rsc.org/?DOI=c2jm00044j

[273] Y. Liu, J. Li, W. Li, Y. Li, F. Zhan, H. Tang, and Q. Chen, "Exploring the nitrogen species of nitrogen doped graphene as electrocatalysts for oxygen reduction reaction in Al-air batteries," *International Journal of Hydrogen Energy*, vol. 41, no. 24, pp. 10 354–10 365, 2016.

[274] Y. F. Lu, S. T. Lo, J. C. Lin, W. Zhang, J. Y. Lu, F. H. Liu, C. M. Tseng, Y. H. Lee, C. T. Liang, and L. J. Li, "Nitrogen-doped graphene sheets grown by chemical vapor deposition: Synthesis and influence of nitrogen impurities on carrier transport," *ACS Nano*, vol. 7, no. 8, pp. 6522–6532, 2013.

[275] L. M. Ombaka, P. G. Ndungu, and V. O. Nyamori, "Pyrrolic nitrogen-doped carbon nanotubes: Physicochemical properties, interactions with Pd and their role in the selective hydrogenation of nitrobenzophenone," *RSC Advances*, vol. 5, no. 1, pp. 109–122, 2015.

[276] E. Luo, M. Xiao, J. Ge, C. Liu, and W. Xing, "Selectively doping pyridinic and pyrrolic nitrogen into a 3D porous carbon matrix through template-induced edge engineering: Enhanced catalytic activity towards the oxygen reduction reaction," *Journal of Materials Chemistry A*, vol. 5, no. 41, pp. 21 709–21 714, 2017.

[277] S. F. Huang, K. Terakura, T. Ozaki, T. Ikeda, M. Boero, M. Oshima, J. I. Ozaki, and S. Miyata, "First-principles calculation of the electronic properties of graphene clusters doped with nitrogen and boron: Analysis of catalytic activity for the oxygen reduction reaction," *Physical Review B - Condensed Matter and Materials Physics*, vol. 80, no. 23, pp. 1–12, 2009.

[278] C. H. Choi, S. H. Park, and S. I. Woo, "Binary and ternary doping of nitrogen, boron, and phosphorus into carbon for enhancing electrochemical oxygen reduction activity," *ACS Nano*, vol. 6, no. 8, pp. 7084–7091, 2012.

[279] Q. Gao, X. Zhao, Y. Xiao, D. Zhao, and M. Cao, "A mild route to mesoporous Mo2C-C hybrid nanospheres for high performance lithium-ion batteries," *Nanoscale*, vol. 6, no. 11, pp. 6151–6157, 2014.

[280] J. Gao, B. Li, J. Tan, P. Chow, T. M. Lu, and N. Koratkar, "Aging of Transition Metal Dichalcogenide Monolayers," *ACS Nano*, vol. 10, no. 2, pp. 2628–2635, 2016.

[281] D. Ganta, S. Sinha, and R. T. Haasch, "2-D Material Molybdenum Disulfide Analyzed by XPS," *Surface Science Spectra*, vol. 21, no. 1, pp. 19–27, 2014. [Online]. Available: http://dx.doi.org/10.1116/11.20140401

[282] R. Bhandavat, L. David, and G. Singh, "Synthesis of surface-functionalized WS 2 nanosheets and performance as li-ion battery anodes," *Journal of Physical Chemistry Letters*, vol. 3, no. 11, pp. 1523–1530, 2012.

[283] M. Fantauzzi, B. Elsener, D. Atzei, A. Rigoldi, and A. Rossi, "Exploiting XPS for the identification of sulfides and polysulfides," *RSC Advances*, vol. 5, no. 93, pp. 75 953–75 963, 2015. [Online]. Available: http://dx.doi.org/10.1039/C5RA14915K

[284] J. Zhu, H. Xian, X. Lin, H. Tang, R. Du, Y. Yang, R. Zhu, X. Liang, J. Wei, H. H. Teng, and H. He, "Surface structure-dependent pyrite oxidation in relatively dry and moist air: Implications for the reaction mechanism and sulfur evolution," *Geochimica et Cosmochimica Acta*, vol. 228, no. March, pp. 259–274, 2018. [Online]. Available: https://doi.org/10.1016/j.gca.2018.02.050

[285] M. R. Gao, J. X. Liang, Y. R. Zheng, Y. F. Xu, J. Jiang, Q. Gao, J. Li, and S. H. Yu, "An efficient molybdenum disulfide/cobalt diselenide hybrid catalyst for electrochemical hydrogen generation," *Nature Communications*, vol. 6, 2015.

[286] C. H. Lin, C. H. Tsai, F. G. Tseng, Y. Y. Yu, H. C. Wu, and C. K. Hsieh, "Low-Temperature Thermally Reduced Molybdenum Disulfide as a Pt-Free Counter Electrode for Dye-Sensitized Solar Cells," *Nanoscale Research Letters*, vol. 10, no. 1, pp. 1–10, 2015. [Online]. Available: http://dx.doi.org/10.1186/s11671-015-1156-0

[287] L. R. L. Ting, Y. Deng, L. Ma, Y.-J. J. Zhang, A. A. Peterson, and B. S. Yeo, "Catalytic Activities of Sulfur Atoms in Amorphous Molybdenum Sulfide for the Electrochemical Hydrogen Evolution Reaction," *ACS Catalysis*, vol. 6, no. 2, pp. 861–867, 2 2016. [Online]. Available: https://pubs.acs.org/doi/10.1021/acscatal.5b02369

[288] H. Vrubel, D. Merki, and X. Hu, “Hydrogen evolution catalyzed by MoS 3 and MoS 2 particles,” *Energy and Environmental Science*, vol. 5, no. 3, pp. 6136–6144, 2012. [Online]. Available: http://xlink.rsc.org/?DOI=c2ee02835b

[289] H. Huang, Y. C. Lu, A. J. Wang, J. H. Liu, J. R. Chen, and J. J. Feng, “A facile, green, and solvent-free route to nitrogen-sulfur-codoped fluorescent carbon nanoparticles for cellular imaging,” *RSC Advances*, vol. 4, no. 23, pp. 11 872–11 875, 2014.

[290] Y. Zhang, Y. Wang, Y. Guan, and L. Feng, “Uncovering the pKa dependent fluorescence quenching of carbon dots induced by chlorophenols,” *Nanoscale*, vol. 7, no. 14, pp. 6348–6355, 2015.

[291] L. Qie, W. Chen, X. Xiong, C. Hu, F. Zou, P. Hu, and Y. Huang, “Sulfur-Doped Carbon with Enlarged Interlayer Distance as a High-Performance Anode Material for Sodium-Ion Batteries,” *Advanced Science*, vol. 2, no. 12, 2015.

[292] T. R. Hellstern, J. Kibsgaard, C. Tsai, D. W. Palm, L. A. King, F. Abild-Pedersen, and T. F. Jaramillo, “Investigating catalyst-support interactions to improve the hydrogen evolution reaction activity of thiomolybdate [Mo 3 S 13] 2- Nanoclusters,” *ACS Catalysis*, vol. 7, no. 10, pp. 7126–7130, 2017.

[293] M. J. Wenzel, F. Josse, S. M. Heinrich, E. Yaz, and P. G. Datskos, “Sorption-induced static bending of microcantilevers coated with viscoelastic material,” *Journal of Applied Physics*, vol. 103, no. 6, 2008.

[294] G. Imamura, K. Shiba, G. Yoshikawa, and T. Washio, “Analysis of nanomechanical sensing signals; physical parameter estimation for gas identification,” *AIP Advances*, vol. 8, no. 7, p. 075007, 7 2018. [Online]. Available: http://aip.scitation.org/doi/10.1063/1.5036686

[295] N. Gupta, H. M. Fahad, M. Amani, X. Song, M. Scott, and A. Javey, “Elimination of response to relative humidity changes in chemical-sensitive field-effect transistors,” *ACS Sensors*, vol. 4, no. 7, pp. 1857–1863, 2019.

[296] B. Mumyakmaz, A. Özmen, M. A. Ebeoğlu, C. Taşaltn, and . Gürol, "A study on the development of a compensation method for humidity effect in QCM sensor responses," *Sensors and Actuators B: Chemical*, vol. 147, no. 1, pp. 277–282, 5 2010. [Online]. Available: https://linkinghub.elsevier.com/retrieve/pii/S0925400510002315

[297] K. Shiba, R. Tamura, G. Imamura, and G. Yoshikawa, "Data-driven nanomechanical sensing: Specific information extraction from a complex system," *Scientific Reports*, vol. 7, no. 1, pp. 1–12, 2017.

[298] S. Drewniak, R. Muzyka, A. Stolarczyk, T. Pustelny, M. Kotyczka-Morańska, and M. Setkiewicz, "Studies of reduced graphene oxide and graphite oxide in the aspect of their possible application in gas sensors," *Sensors (Switzerland)*, vol. 16, no. 1, 2016.

[299] A. Ganguly, S. Sharma, P. Papakonstantinou, and J. Hamilton, "Probing the thermal deoxygenation of graphene oxide using high-resolution in situ X-ray-based spectroscopies," *Journal of Physical Chemistry C*, vol. 115, no. 34, pp. 17 009–17 019, 2011.

[300] C. Zhang, Z. Wang, S. Bhoyate, T. Morey, B. Neria, V. Vasiraju, G. Gupta, S. Palchoudhury, P. Kahol, S. Mishra, F. Perez, and R. Gupta, "MoS2 Decorated Carbon Nanofibers as Efficient and Durable Electrocatalyst for Hydrogen Evolution Reaction," *C*, vol. 3, no. 4, p. 33, 2017.

[301] T. Polcar, F. Gustavsson, T. Thersleff, S. Jacobson, and A. Cavaleiro, "Complex frictional analysis of self-lubricant W-S-C/Cr coating," *Faraday Discussions*, vol. 156, pp. 383–401, 2012.

APPENDICES

Appendix A

Supplementary Material for Chapter 3

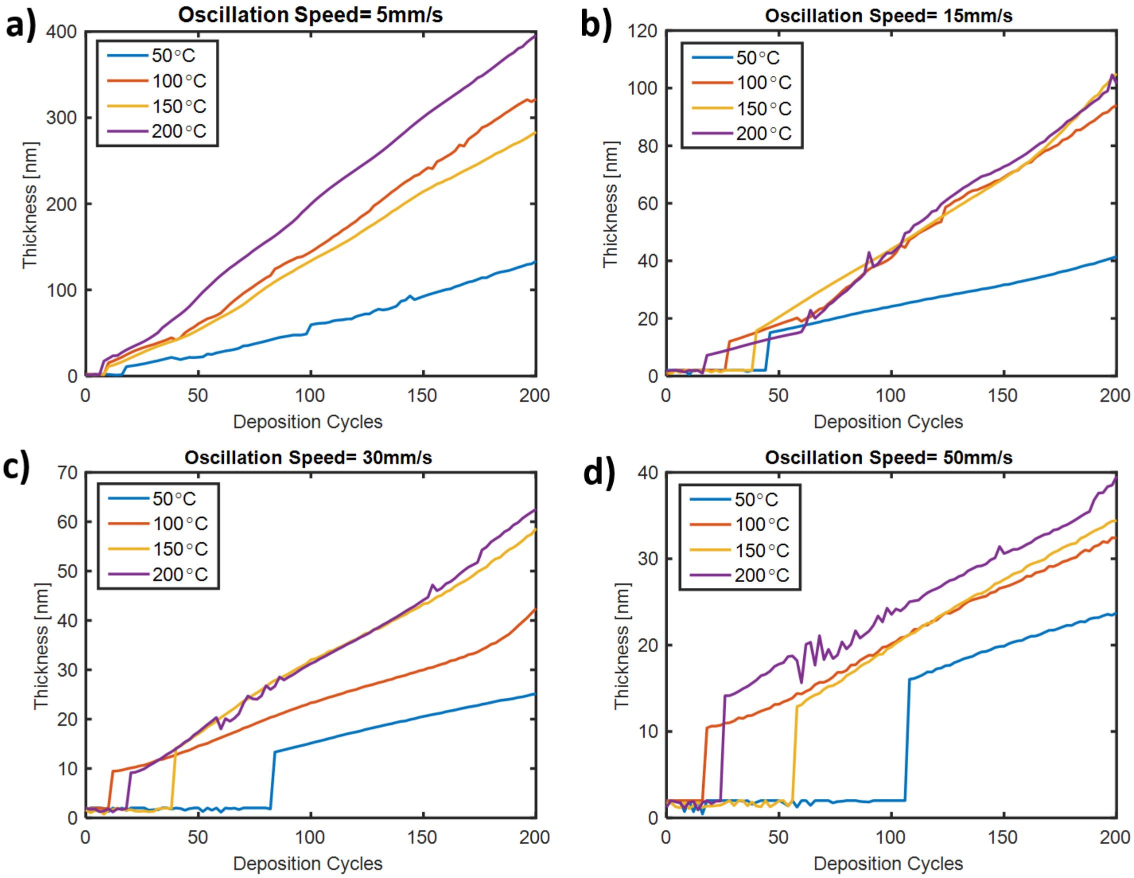

Figure A.1: Thickness of deposited Zinc Oxide (ZnO) films at varying temperatures and substrate oscillation speeds: a) 5 mm/s, b) 15 mm/s, c) 30 mm/s and d) 50 mm/s

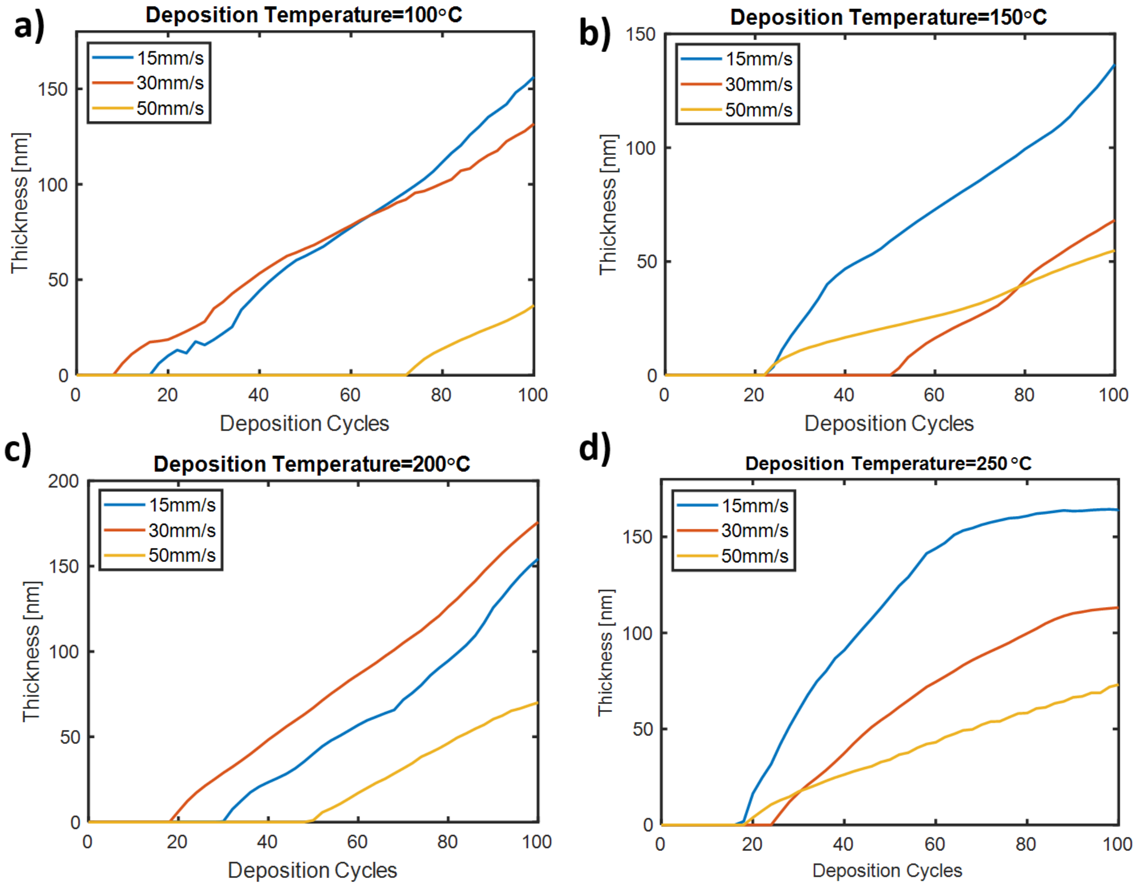

Figure A.2: Thickness of deposited Aluminum Oxide (Al_2O_3) films at varying substrate oscillation speeds and deposition temperatures : a)100°C, b) 150°C, c) 200°C and d) 250°C.

Appendix B

Supplementary Material for Chapter 7

Table B.1: Relevant properties of the analytes used in this work.

Analyte	Vapor Pressure @ 15°C [*mmHg*]	Saturated Concentration[c] [*ppm*]	Molecule Size/Length [*nm*]	Estimated Cubic Length[b] [*nm*]
Water	12.79	1682.63	0.277 [258]	0.310
Ethanol	32.91	4329.71	0.433 [258]	0.459
Hexanol[a]	0.34	45.55	-	0.592
Hexanal[a]	9.83	647.27	-	0.588
Heptane	27.15	3572.48	0.625 [258]	0.624
Methylcyclohexane	28.05	3691.16	0.590 [258]	0.596
Toluene	16.57	2180.63	0.564 [258]	0.560
Ethyl Acetate	57.01	7500.50	0.460 [259]	0.545
Acetone	147.62	19423.90	0.476 [258]	0.497

[a] Sizes of hexanol and hexanal molecules were not found in literature.

[b] Since the size of hexanol and hexanal were not reported in literature, an estimate for the length of the molecules was determined from its molar mass and density using a cubic volume approximation.

[c] Concentrations[ppm] of analytes at 2%, 5% and 10% relative pressures were determined by multiplying the saturated concentration by 0.02, 0.05 and 0.1, respectively.

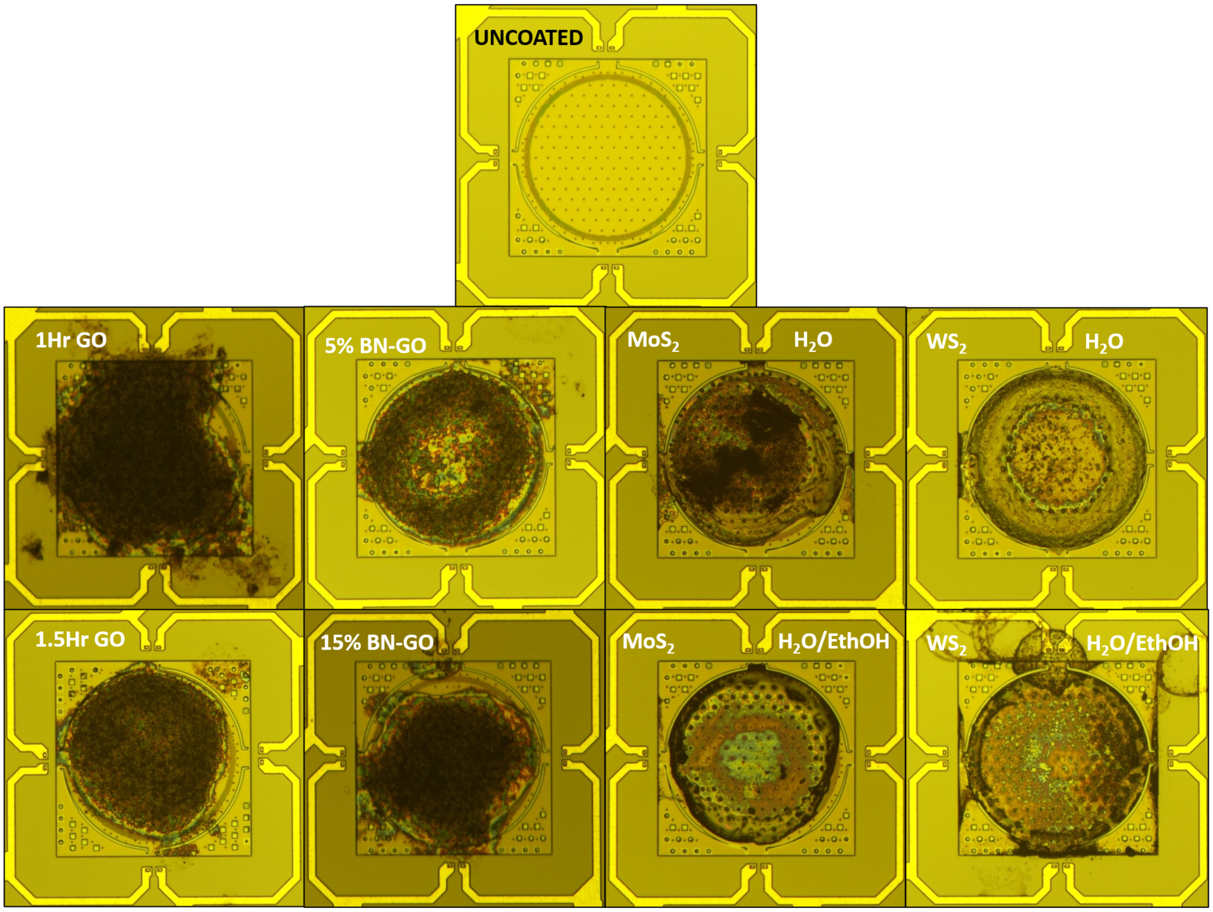

Figure B.1: Microscopic images of uncoated and coated MSS devices.

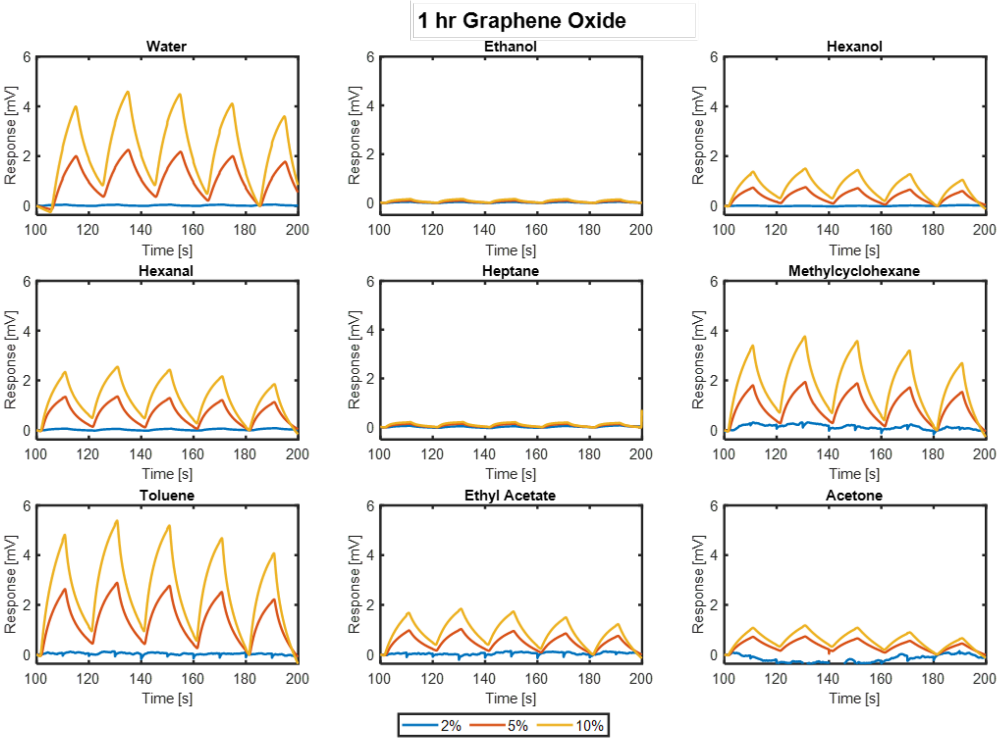

Figure B.2: Response [mV] of MSS coated with graphene oxide (laser treated for 1 hour) to analytes present at 2%, 5%, and 10% relative vapor pressures.

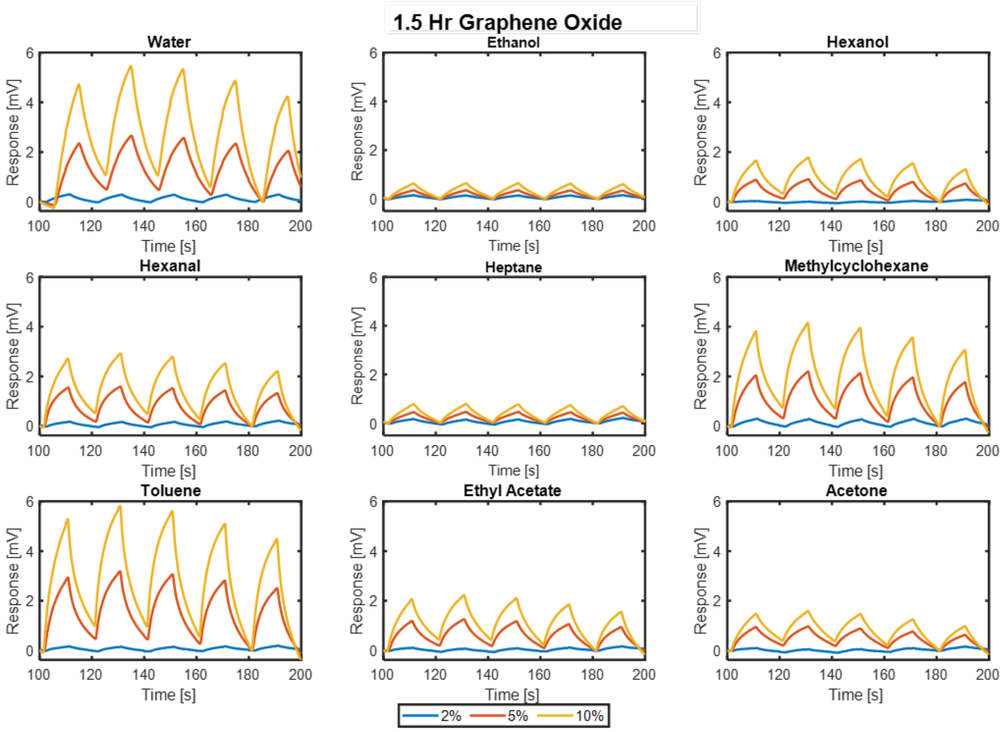

Figure B.3: Response [mV] of MSS coated with graphene oxide (laser treated for 1.5 hour) to analytes present at 2%, 5%, and 10% relative vapor pressures.

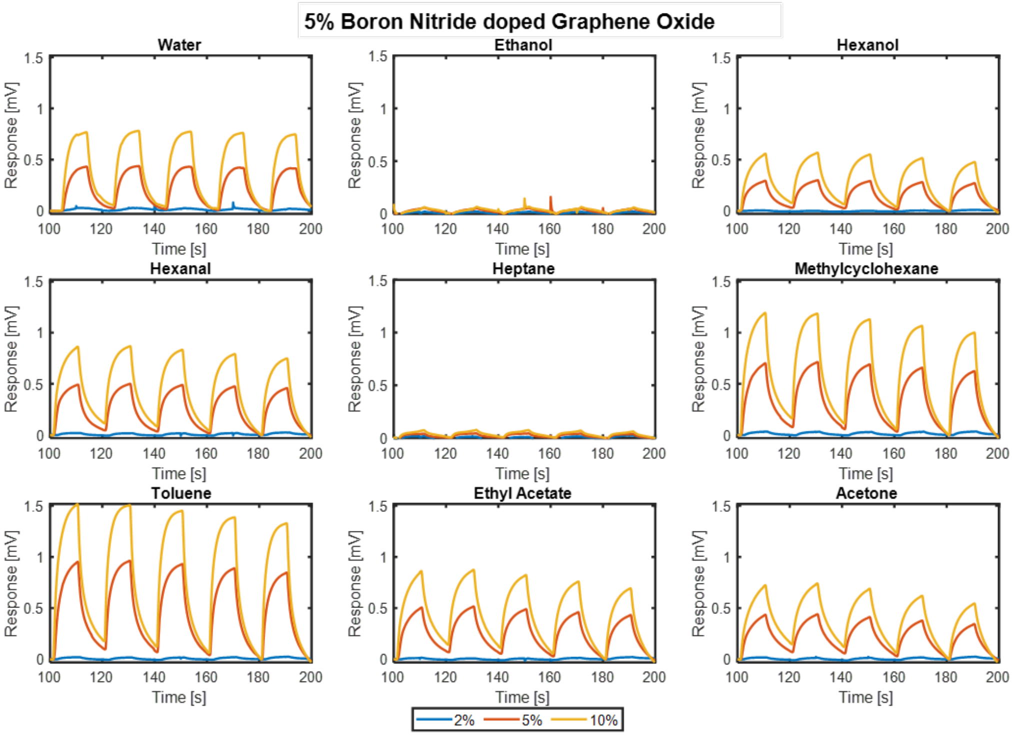

Figure B.4: Response [mV] of MSS coated with 5% boron nitride doped graphene oxide to analytes present at 2%, 5%, and 10% relative vapor pressures.

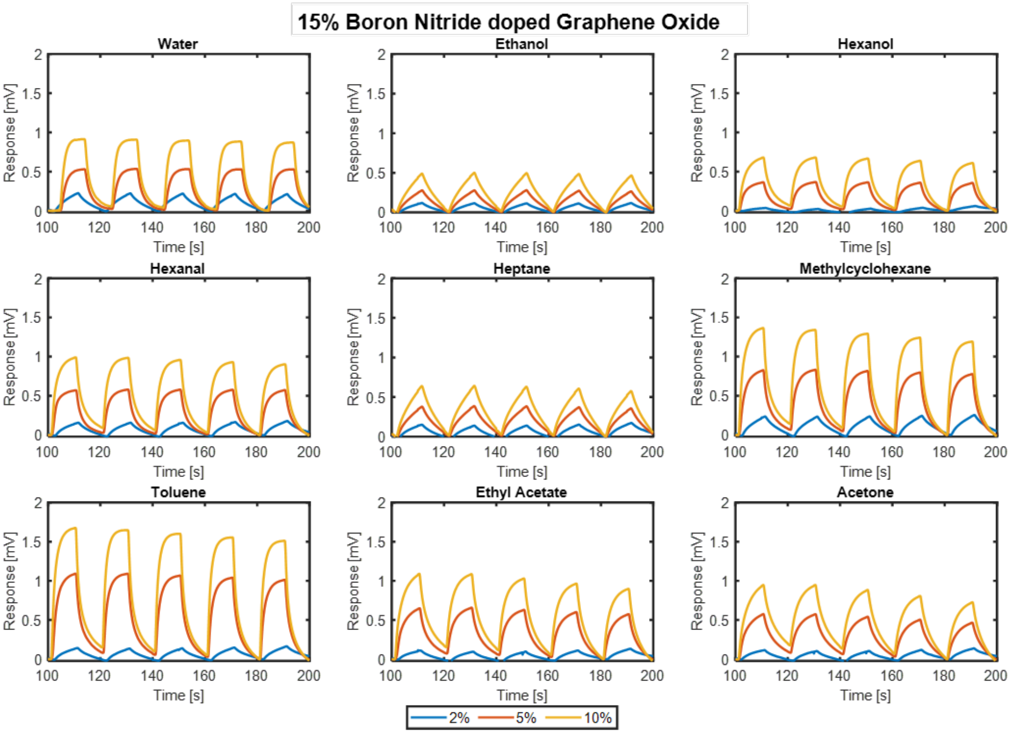

Figure B.5: Response [mV] of MSS coated with 15% boron nitride doped graphene oxide to analytes present at 2%, 5%, and 10% relative vapor pressures.

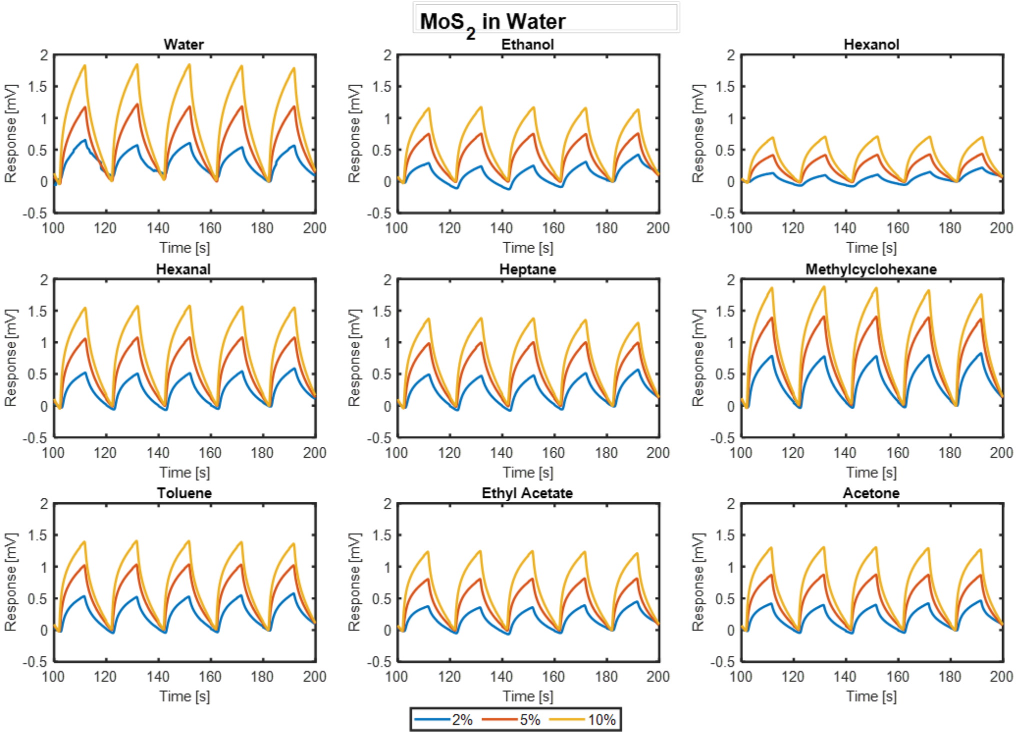

Figure B.6: Response [mV] of MSS coated with molybdenum disulfide (laser treated in water) to analytes present at 2%, 5%, and 10% relative vapor pressures.

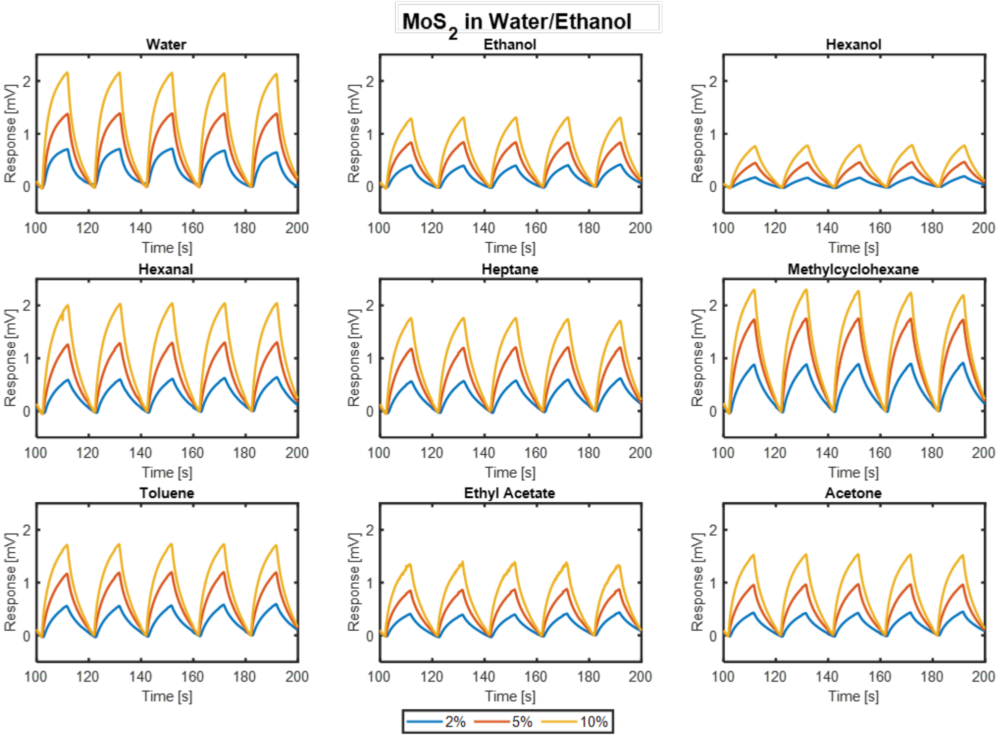

Figure B.7: Response [mV] of MSS coated with molybdenum disulfide (laser treated in water/ethanol solution) to analytes present at 2%, 5%, and 10% relative vapor pressures.

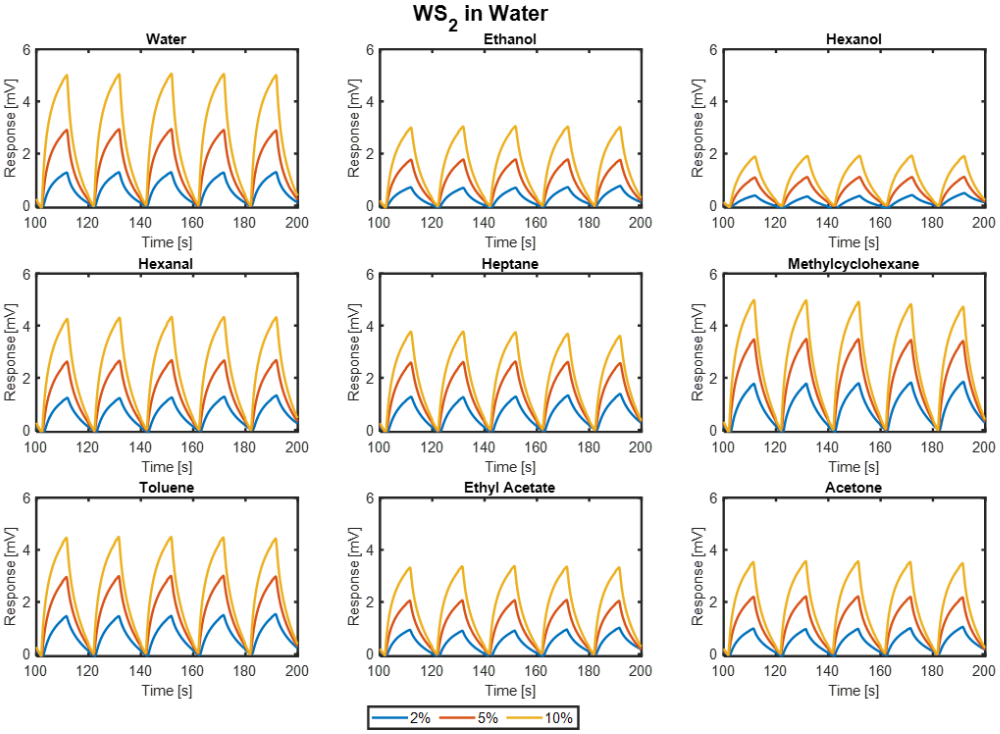

Figure B.8: Response [mV] of MSS coated with tungsten disulfide (laser treated in water) to analytes present at 2%, 5%, and 10% relative vapor pressures.

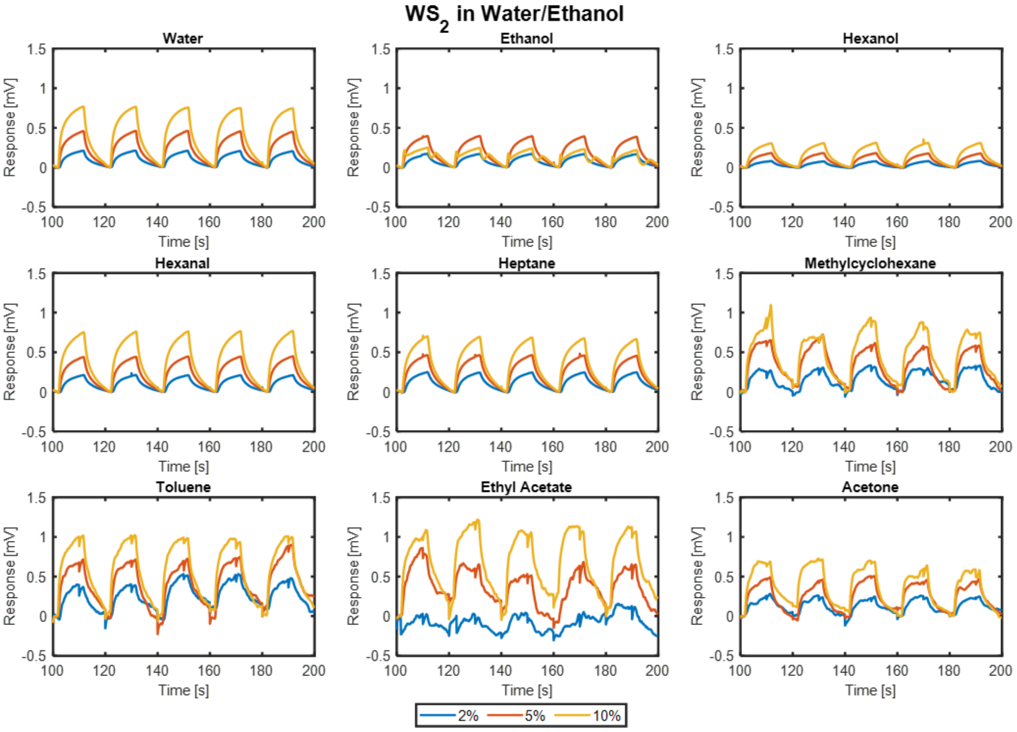

Figure B.9: Response [mV] of MSS coated with tungsten disulfide (laser treated in water/ethanol solution) to analytes present at 2%, 5%, and 10% relative vapor pressures.

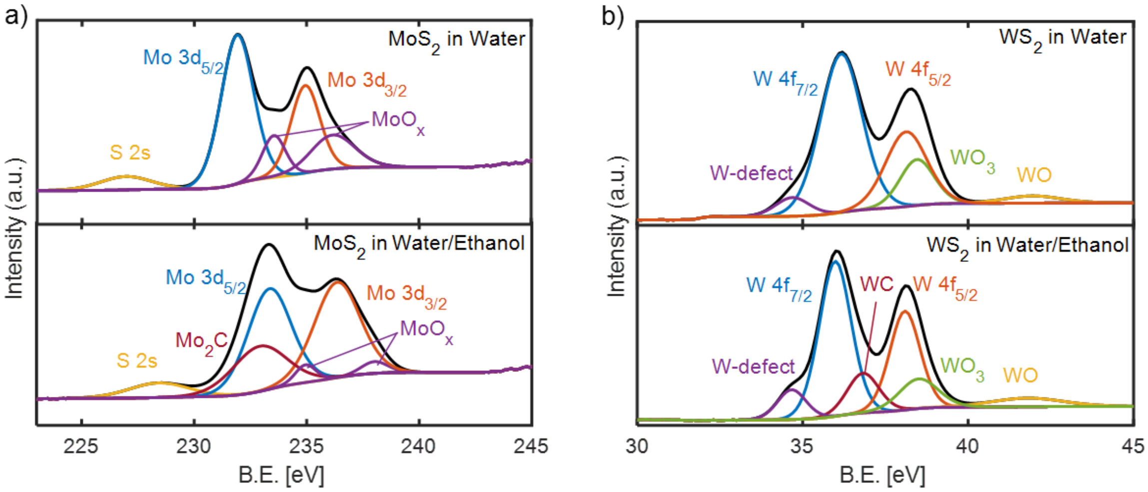

Figure B.10: XPS characterization of laser treated MoS_2 and WS_2. a) Mo 3d spectra of MoS_2 treated in water (upper panel) and MoS_2 treated in water/ethanol solution (lower panel). b) W 4f spectra of WS_2 treated in water (upper panel) and WS_2 treated in water/ethanol solution (lower panel). Table B.7 lists the peak quantities.

Table B.2: Estimated sensitivities of materials used in this work [$\mu V ppm^{-1}$]. Standard error of the linear regression is displayed in parenthesis.

Analyte	1 Hr GO	1.5 Hr GO	5% BN-GO	15% BN-GO	MoS_2 in Water	MoS_2 in Ethanol:Water	WS_2 in Water	WS_2 in Ethanol:Water
Water	1.80 (0.55)	2.30 (0.46)	0.49 (0.01)	0.53 (0.01)	1.20 (0.18)	1.40 (0.24)	3.10 (0.29)	0.50 (0.05)
Ethanol	0.04 (0.16)	0.10 (0.02)	0.01 (0.03)	0.10 (0.03)	0.30 (0.13)	0.30 (0.15)	0.70 (0.18)	0.08 (0.18)
Hexanol	19.50 (0.33)	24.90 (0.36)	14.49 (0.01)	16.85 (0.01)	16.20 (0.04)	18.10 (0.04)	43.40 (0.09)	6.90 (0.01)
Hexanal	1.20 (0.55)	1.60 (0.44)	0.79 (0.01)	0.75 (0.02)	1.30 (0.24)	1.70 (0.22)	3.50 (0.40)	0.60 (0.04)
Heptane	0.06 (0.03)	0.20 (0.06)	0.02 (0.01)	0.16 (0.04)	0.40 (0.25)	0.50 (0.25)	1.20 (0.60)	0.20 (0.09)
Methylcyclohexane	0.70 (0.71)	0.80 (0.06)	0.38 (0.01)	0.36 (0.06)	0.60 (0.40)	0.70 (0.46)	1.50 (0.81)	0.30 (0.15)
Toluene	1.60 (0.51)	1.80 (0.58)	0.82 (0.01)	0.82 (0.03)	0.70 (0.27)	0.90 (0.24)	2.20 (0.63)	0.50 (0.34)
Ethyl Acetate	0.20 (0.22)	0.20 (0.32)	0.14 (0.05)	0.16 (0.01)	0.20 (0.15)	0.20 (0.13)	0.50 (0.21)	0.20 (0.08)
Acetone	0.04 (0.10)	0.05 (0.14)	0.04 (0.02)	0.05 (0.02)	0.07 (0.17)	0.08 (0.15)	0.20 (0.33)	0.04 (0.12)

Table B.3: Estimated limit of detection (LOD) of materials used in this work [ppm].

Analyte	1 Hr GO	1.5 Hr GO	5% BN-GO	15% BN-GO	MoS_2 in Water	MoS_2 in Ethanol:Water	WS_2 in Water	WS_2 in Ethanol:Water
Water	0.915	0.604	0.085	0.084	0.469	0.518	0.285	0.337
Ethanol	11.993	0.843	9.845	0.903	1.320	1.510	0.801	6.754
Hexanol	0.052	0.044	0.002	0.001	0.008	0.007	0.007	0.009
Hexanal	1.380	0.833	0.032	0.091	0.573	0.396	0.349	0.245
Heptane	1.563	0.908	2.265	0.863	1.928	1.522	1.512	1.455
Methylcyclohexane	3.072	0.228	0.039	0.543	2.005	1.993	1.638	1.576
Toluene	0.968	0.974	0.028	0.130	1.161	0.822	0.862	2.049
Ethyl Acetate	3.291	4.814	1.093	0.160	2.359	2.065	1.270	1.231
Acetone	7.815	8.940	2.018	1.240	7.354	5.854	5.096	9.70

Table B.4: XPS analysis of laser treated graphene oxide (1 and 1.5 hours).

Material	Spectra	Peak Identity	Peak Position [eV]	Atomic Percentage %
1-Hour Graphene Oxide	C 1s	C-C (sp3) [298]	284.0	5.9
		C=C (sp2) [261]	284.8	40.3
		C-O-C (epoxy) [262]	286.8	30.8
		C-Ox (x=1,2,3) [263]	287.0	14.6
		C=O (carbonyl) [264]	288.3	8.4
	O 1s	C=O (carbonyl) [265]	531.8	40.0
		C-O-C (epoxy) [266]	532.4	29.0
		C-OH [265]	533.0	21.0
		H_2O-C [299]	533.7	9.0
1.5-Hour Graphene Oxide	C 1s	C-C (sp3)	283.9	6.4
		C=C (sp2)	284.8	39.2
		C-O-C (epoxy)	286.8	40.3
		C-Ox (x=1,2,3)	287.2	7.4
		C=O (carbonyl)	288.4	6.7
	O 1s	C=O (carbonyl)	531.6	24.0
		C-O-C (epoxy)	532.4	45.5
		C-OH	533.1	26.0
		H_2O-C	534.0	4.5

Table B.5: Total elemental composition as determined by XPS analysis of 5% and 15% boron nitride doped graphene oxide.

Material	C 1S (at%)	O 1S (at%)	N 1S (at%)	B 1S (at%)
5% BN doped GO	70.3	28.5	0.5	0.7
15% BN doped GO	66.2	31.5	0.9	1.4

Table B.6: Analysis of N 1s XPS spectra of 5% and 15% boron nitride doped graphene oxide.

Material	Peak Identity	Peak Position [eV]	Atomic Percentage %
5% BN doped GO	C-N-B [253]	401.41	49.75
	Pyrrolic N	402.48	50.25
15% BN doped GO	C-N-B	402.71	11.37
	Pyrrolic N	403.82	88.64

Table B.7: Quantification of peaks shown in Figure B.10 (XPS analsis of Mo 3d and W 4f).

Material	Peak Identity	Peak Position [eV]	Atomic Percentage %
MoS2 in Water	S 2s [101, 300]	226.94	6.59
	Mo $3d_{5/2}$ [101, 300]	231.90	45.95
	Mo $3d_{3/2}$ [101, 300]	234.93	24.13
	MoOx [279–281]	233.54, 236.16	9.22, 14.12
MoS2 in Water/Ethanol	S 2s	228.41	6.90
	Mo $3d_{5/2}$	233.34	34.35
	Mo $3d_{3/2}$	236.35	34.28
	MoOx	234.95, 238	2.86, 2.47
	Mo2C [101, 279]	232.9	19.14
WS2 in Water	W-defect[18]	34.68	5.12
	W $4f_{7/2}$ [101]	36.16	53.58
	W $4f_{5/2}$ [101]	38.12	25.16
	WO3 [282]	38.45	12.83
	WO [101, 280]	41.94	3.31
WS2 in Water/Ethanol	W-defect	34.66	7.22
	W $4f_{7/2}$	35.98	41.73
	W $4f_{5/2}$	38.09	25.37
	WO3	38.49	9.36
	WO	41.78	5.22
	WC [101, 301]	36.82	10.70

Table B.8: Quantification of peaks shown in Figure 7.8 (XPS analysis of S 2p

Material	Peak identity	Peak Position[eV]	Atomic Percentage %	Sulfur composition
MoS_2 in Water	S $2p_{1/2}$ (Terminal/Unsaturated) [285–288]	162.23	19.64	Sulfide = 42.75%
	S $2p_{3/2}$ (Apical/bridging) [285–288]	163.42	25.25	
	S $2p_{1/2}$ (Apical/bridging) [285–288]	164.91	0.86	
	-S(O_2)- (Oxidized Sulfur) [283, 289–291]	166.12	19.46	Sulphate= 54.24%
	-S(O_3)- (Oxidized Sulfur) [283, 289–291]	169.12	26.69	
	-S(O_4)- (Oxidized Sulfur) [283, 289–291]	170.88	8.09	
MoS_2 in Water/Ethanol	S $2p_{1/2}$ (Terminal/Unsaturated) [2124]	163.98	33.59	Sulfide = 73.77%
	S $2p_{3/2}$ (Apical/bridging) [285–288]	165.38	27.27	
	S $2p_{3/2}$ (Terminal/Unsaturated) [285–288]	162.67	5.73	
	S $2p_{1/2}$ (Apical/bridging) [285–288]	166.82	7.18	
	-S(O_2)- (Oxidized Sulfur)	169.57	10.26	Sulphate= 26.33%
	-S(O_3)- (Oxidized Sulfur)	172.63	1.73	
	-S(O_4)- (Oxidized Sulfur)	171.02	14.24	
WS_2 in Water	S $2p_{3/2}$ (Terminal/Unsaturated)	160.96	1.62	Sulfide= 71.79%
	S $2p_{1/2}$ (Terminal/Unsaturated)	162.08	6.60	
	S $2p_{3/2}$ (Apical/bridging)	164.56	6.65	
	S $2p_{1/2}$ (Apical/bridging)	163.36	13.34	
	-S(O_2)- (Oxidized Sulfur)	169.57	21.49	Sulphate = 28.21%
	-S(O_3)- (Oxidized Sulfur)	168.16	35.63	
	-S(O_4)- (Oxidized Sulfur)	170.70	14.67	
WS_2 in Water/Ethanol	S $2p_{1/2}$ (Terminal/Unsaturated)	164.45	11.22	Sulfide = 14.9%
	S $2p_{3/2}$ (Terminal/Unsaturated)	163.53	3.77	
	-S(O_2)- (Oxidized Sulfur)	169.86	31.93	Sulphate= 85.07%
	-S(O_3)- (Oxidized Sulfur)	167.72	20.72	
	-S(O_4)- (Oxidized Sulfur)	168.74	32.42	

Glossary

bandgap Refers to the energy difference between the top of the valence band and the bottom of the conduction band in insulators and semiconductors. xvi, xvii, 65, 68–70, 77–80

bimorph A bimorph is a cantilever used for actuation or sensing which consists of two active layers. 12

chemiresistive Sensor based on change of electrical properties such as resistance. 5, 31, 109, 111, 112, 114, 115, 128

conductor A material that allows the flow of charge. 54

COVID-19 Severe acute respiratory syndrome coronavirus 2 (SARS-CoV-2) first identified in 2019 responsible for the global health pandemic throughout 2020. 82, 93

extinction coefficient Imaginary part of refractive index, indicates the amount of attenuation (absorption) when an electromagnetic wave propagates through a material. xvi, 53–55, 66–68

grain boundaries The interface between two grains, or crystallites, in a polycrystalline material. Grain boundaries are 2D defects in the crystal structure, and tend to decrease the electrical and thermal conductivity of the material. 64

gravimetric Resonant frequency shift based sensors. x, 31, 148, 149

insulator A material in which the electron does not flow freely. 54

operando Refers to an experimental procedure or measurement performed in operating conditions. 104

receptor A material that interacts with a gas in a quantifiable way. xxi, 2, 103, 104, 116, 157, 158, 161–165, 169, 171, 174

refractive index A dimensionless number(n) that describes how fast light travels through a material, relative to vacuum. It is defined as $n = c/v$, where c is the speed of light in a vacuum and v is the phase velocity of light in the medium. xvi, xvii, 53, 55, 59, 64–70, 78–80

semiconductor A material has an electrical conductivity value falling between that of a conductor and an insulator. 54

sorption Absorption and adsorption considered as a single process. 5, 6, 8, 20, 37, 39, 108, 141, 151

transduction Conversion of a signal from one form of energy to another. 5, 102

trap Any location within a solid (generally a semiconductor or an insulator) that restricts the movement of electrons and holes. 64

wheatstone bridge An electrical circuit used to measure an unknown electrical resistance by balancing two legs of a bridge circuit, one leg of which includes the unknown component. xiii, 19, 21, 25